

Volume 65D

Number 5

Sept.-Oct. 1961

ST 2  
SCIENCE

# Radio

# Propagation

SEP 18 1961

SEP 18 1961



---

U.S. DEPARTMENT  
OF COMMERCE



## SECTION D

# JOURNAL OF RESEARCH NATIONAL BUREAU OF STANDARDS

MIAMI UNIVERSITY LIBRARY

**Journal of Research**  
of the  
**National Bureau of Standards**

**D. RADIO PROPAGATION**

SEPT.-OCT. • 1961

VOLUME • 65D

NUMBER • 5



Editor: James R. Wait  
Central Radio Propagation Laboratory,  
National Bureau of Standards, Boulder,  
Colo.

Associate Editors: T. N. Gautier, J. W.  
Herbstreit, R. C. Kirby, C. G. Little, A. G.  
McNish, R. A. Helliwell, W. E. Gordon,  
A. D. Wheeler, S. Silver

IRE Advisors: A. H. Waynick, K. M. Siegel

Publication dates:  
Jan. 15, Mar. 15, May 15, July 15, Sept. 15, Nov. 15, 1961

**JOURNAL OF RESEARCH**

The National Bureau of Standards Journal of Research reports research and development in the fields of activity shown at right. Also included from time to time are survey articles related to the Bureau's scientific and technical program.

The Journal is published in four separate sections as follows:

**A. Physics and Chemistry**

Contains papers of interest primarily to scientists working in these fields. Issued six times a year. Annual subscription: domestic, \$4.00; foreign, \$4.75.

**B. Mathematics and Mathematical Physics**

Presents studies and compilations designed mainly for the mathematician and the theoretical physicist. Issued quarterly. Annual subscription: domestic, \$2.25; foreign, \$2.75.

**C. Engineering and Instrumentation**

Reports research and development results of interest chiefly to the engineer and the applied scientist. Issued quarterly. Annual subscription: domestic, \$2.25; foreign, \$2.75.

**D. Radio Propagation**

Reports research in radio propagation, atmospheric physics, and communications. Issued six times a year. Annual subscription: domestic, \$4.00; foreign, \$4.75.

**Functions and Activities**

The functions of the National Bureau of Standards are set forth in the Act of Congress, March 3, 1901, as amended. These include the development and maintenance of the national standards of measurement and the provision of means and methods for making measurements consistent with these standards; the determination of physical constants and properties of materials; the development of methods and instruments for testing materials, devices, and structures; advisory services to government agencies on scientific and technical problems; invention and development of devices to serve special needs of the Government; and the development of standard practices, codes, and specifications. The work includes basic and applied research, development, engineering, instrumentation, testing, evaluation, calibration services, and various consultation and information services. The Bureau also serves as the Federal technical research center in a number of specialized fields. The scope of activities of the National Bureau of Standards is suggested in the following listing of the divisions and sections engaged in technical work.

**Washington, D.C.**

**Electricity.** Resistance and Reactance. Electrochemistry. Electrical Instruments. Magnetic Measurements. Dielectrics.

**Metrology.** Photometry and Colorimetry. Refractometry. Photographic Research. Length. Engineering Metrology. Mass and Scale. Volumetry and Densimetry.

**Heat.** Temperature Physics. Heat Measurement. Cryogenic Physics. Equation of State. Statistical Physics.

**Radiation Physics.** X-Ray. Radioactivity. Radiation Theory. High Energy Radiation. Radiological Equipment. Nucleonic Instrumentation. Neutron Physics.

**Analytical and Inorganic Chemistry.** Pure Substances. Spectrochemistry. Solution Chemistry. Analytical Chemistry. Inorganic Chemistry.

**Mechanics.** Sound. Pressure and Vacuum. Fluid Mechanics. Engineering Mechanics. Rheology. Combustion Controls.

**Organic and Fibrous Materials.** Rubber. Textiles. Paper. Leather. Testing and Specifications. Polymer Structure. Plastics. Dental Research.

**Metallurgy.** Thermal Metallurgy. Chemical Metallurgy. Mechanical Metallurgy. Corrosion. Metal Physics.

**Mineral Products.** Engineering Ceramics. Glass. Refractories. Enamelled Metals. Crystal Growth. Constitution and Microstructure.

**Building Research.** Structural Engineering. Fire Research. Mechanical Systems. Organic Building Materials. Codes and Safety Standards. Heat Transfer. Inorganic Building Materials.

**Applied Mathematics.** Numerical Analysis. Computation. Statistical Engineering. Mathematical Physics.

**Data Processing Systems.** Components and Techniques. Digital Circuitry. Digital Systems. Analog Systems. Applications Engineering.

**Atomic Physics.** Spectroscopy. Radiometry. Solid State Physics. Electron Physics. Atomic Physics.

**Instrumentation.** Engineering Electronics. Electron Devices. Electronic Instrumentation. Mechanical Instruments. Basic Instrumentation.

**Physical Chemistry.** Thermochemistry. Surface Chemistry. Organic Chemistry. Molecular Spectroscopy. Molecular Kinetics. Mass Spectrometry. Molecular Structure and Radiation Chemistry.

**• Office of Weights and Measures**

**Boulder, Colo.**

**Cryogenic Engineering.** Cryogenic Equipment. Cryogenic Processes. Properties of Materials. Gas Liquefaction.

**Ionosphere Research and Propagation.** Low Frequency and Very Low Frequency Research. Ionosphere Research. Prediction Services. Sun-Earth Relationships. Field Engineering. Radio Warning Services.

**Radio Propagation Engineering.** Data Reduction Instrumentation. Radio Noise. Tropospheric Measurements. Tropospheric Analysis. Propagation-Terrain Effects. Radio-Meteorology. Lower Atmospheric Physics.

**Radio Standards.** High-Frequency Electrical Standards. Radio Broadcast Service. Radio and Microwave Materials. Atomic Frequency and Time Interval Standards. Electronic Calibration Center. Millimeter-Wave Research. Microwave Circuit Standards.

**Radio Systems.** High Frequency and Very High Frequency Research. Modulation Research. Antenna Research. Navigation Systems. Space Telecommunications.

**Upper Atmosphere and Space Physics.** Upper Atmosphere and Plasma Physics. Ionosphere and Exosphere Scatter. Airglow and Aurora. Ionospheric Radio Astronomy.

**U.S. DEPARTMENT OF COMMERCE**  
Luther H. Hodges, Secretary

**NATIONAL BUREAU OF STANDARDS**  
A. V. Astin, Director

Order all publications from the Superintendent of Documents,  
U.S. Government Printing Office, Washington 25, D.C.

Use of funds for printing this publication approved by the Director of the Bureau of the Budget (June 19, 1961).





# Frequency Dependence of *D*-Region Scattering at VHF

J. C. Blair, R. M. Davis, Jr., and R. C. Kirby

Contribution from Central Radio Propagation Laboratory, National Bureau of Standards, Boulder, Colo.

(Received March 30, 1961)

Results are given of a one-year program of observation of frequency dependence of system loss for *D*-region scattering at VHF. Continuous simultaneous observations were made at five frequencies from 30 to 108 Mc/s, using narrow beam antennas scaled in dimensions and height according to wavelength; the path was from Long Branch, Ill., to Boulder, Colo., a distance of 1,300 km. Hourly values of system loss closely followed the relationship  $p_s/p_{s0} \propto f^n$ . The value of  $n$  varied with time of day and season, with 90 percent of all observations lying in the range 7 to  $9\frac{1}{2}$  for scaled antenna systems. Diurnal and seasonal variation of  $n$  are attributed to changing relative roles of turbulence and meteoric reflections. Effects of normal ionospheric absorption are not apparent. A special analysis is made of frequency dependence during weak signal conditions. Results are also given of studies of the frequency dependence of fading characteristics, the effect of beamwidth, and SID behavior.

## 1. Introduction

Continuous radio-wave scattering at very high frequencies, from turbulent irregularities and meteoric ionization in the *D*-region of the ionosphere, has been intensively investigated [Bailey, Bateman and Kirby, 1955] since 1951, and has been exploited for communication systems in several areas of the world [JTAC, 1960]. This paper reports an experimental study of the frequency dependence in the range 30 to 108 Mc/s. One of the authors has already published preliminary data [Blair, 1959].

Frequency dependence is of considerable engineering importance in the design of ionospheric-scatter communication systems. The higher the frequency one can use, the greater the freedom from interference, especially that propagated to great distances by the *F*2-layer and sporadic-*E* ionization. To raise the frequency, however, increases propagation losses until, in spite of the accompanying decrease of the background level of galactic noise, excessive transmitter power is required for a needed transmission capacity. For design purposes one is especially interested in the frequency dependence characteristic of weak-signal conditions.

Interpretation of the physics of the scattering process also requires knowledge of the frequency dependence. In studying the role of turbulence, under the usual assumptions of single isotropic scattering at an average angle  $\theta$ , observations of frequency dependence serve to evaluate the spectrum of sizes of irregularities,  $S(k)$ . The scattering process acts like a narrow band filter, emphasizing the sizes of irregularities which have wavenumbers equal to

$$k = \frac{4\pi}{\lambda} \sin \frac{\theta}{2} \quad (1)$$

where

$\lambda$  = wavelength

$\theta$  = scattering angle, shown in figure 1.

Wheelon [1960a] has recently summarized turbulence theory for *D*-region scatter. He treats the single scattering description of electromagnetic response of electron density irregularities in time and space, and discusses several theories for turbulent mixing of electron density.

Neglecting absorption, the total received power in VHF scatter propagation is the resultant of components due to turbulent scattering, meteor reflections, and noise, which may be expressed as a function of frequency:

$$p_a(f) = p_s(f) + p_m(f) + p_N(f) \quad (2)$$

where

$p_a$  = available power at terminal of receiving antenna

$p_s$  = component of available power from scattering

from turbulent irregularities

$p_m$  = component of available power from meteor reflections

$p_N$  = component of available power from external noise usually mainly galactic

$f$  = carrier frequency, megacycles per second

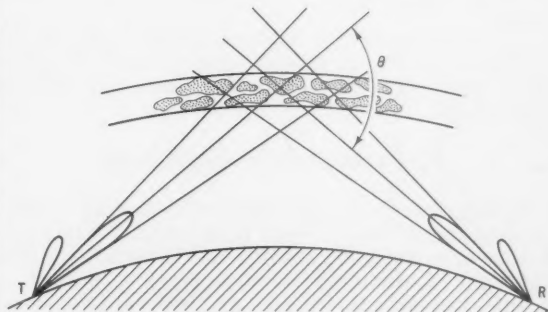


FIGURE 1. Geometry of *D*-region scattering.

Other modes which sometimes occur, such as  $E_s$ , auroral echoes,  $F2$ -propagated ground backscatter, are recognizable by the abnormal character of the recording, and such data are not used in the analysis of frequency dependence. Adequate power is used in the experiment to keep the signal-to-noise ratio large, usually greater than 10, so that  $p_N$  can be neglected. The effect of absorption can be indicated:

$$p_a(f) = p_i(f) \exp \left[ \frac{-2}{(f+f_H)^2} \int_0^{h_s} \alpha \sec \theta dh \right] + p_m(f) \exp \left[ \frac{-2}{(f+f_H)^2} \int_0^{h_m} \alpha \sec \theta dh \right] \quad (3)$$

where

$f_H$  is the gyrofrequency, megacycles per second  
 $\alpha$  is absorption coefficient, per element thickness,  $dh$ , of absorbing region  
 $h_s$  is the effective scattering height  
 $h_m$  is the height of meteoric reflection

for the oblique transmission through the absorbing region enroute to and from the scattering region or meteor reflection.

This is the first published report of comprehensive results of simultaneous observations at a series of frequencies, rather than a pair at a time, throughout the range of interest. The frequency dependence is expressed in terms of  $n$  in the relation

$$p_i/p_a \propto f^n$$

where

$p_i$  = power to transmitting antenna  
 $p_a$  = available power at receiving antenna  
 $f$  = frequency

Earlier experiments showed a variation of  $n$ . The Bailey, Bateman and Kirby [1955] measurements, obtained in two nonsimultaneous tests, indicated lower values of  $n$  in the frequency range below 50 Mc/s than in the range above 50 Mc/s. This led Wheelon [1957] to suggest a theoretical explanation for a dichotomy in the scaling law; he emphasized at the same time the need of carefully scaled simultaneous measurements over the whole frequency range.

Some interpretation is given in this report of the variation in relative contribution of meteoric reflections and turbulent scattering, and the role of absorption.

## 2. Experimental Conditions

System loss,  $p_i/p_a$ , has been compared at a series of frequencies, using a fixed path length. The angle  $\theta$  is nearly constant; diurnal and seasonal changes in height of scattering introduce slight variations.

Identical antenna patterns and gains are preserved at all frequencies by scaling antenna dimensions and height. Thus, the scattering volume is illuminated

and viewed uniformly throughout the frequency range. As a consequence of scaling antennas, an extra power of 2 is contained in the exponent,  $n$ , for system loss, because the aperture of the receiving antenna varies as  $\lambda^2$ . One must subtract a power of 2 from the values of  $n$  (divide system loss by  $f^2$ ) for scaled antennas given in this paper,<sup>1</sup> to make comparison with theoretical frequency dependence of scattering cross section  $\sigma$ , or with  $S(k)$  values.

Figure 2 shows the geographical layout of the experimental path. Continuous transmissions were maintained at five frequencies from near 30 Mc/s to near 108 Mc/s. Narrow-beam rhombic antennas were used, scaled in dimensions and height; the leg length was 25 wavelengths, one-half the obtuse angle was 80.2° and the horizontal half-power beamwidth was 6°. The elevation of the axes of the main lobes was 4.6°; the beams were directed to intersect at the path midpoint at an ionospheric height of 85 km. Losses in transmitting and receiving transmission line systems were measured, and observed data at each frequency corrected accordingly. Finally, aircraft measurements of antenna gains and radiation patterns were carried out. The average value of gain was 18.8 db relative to a halfwave reference dipole at the same height; measured values of gain for all antennas were found to be within  $\pm 0.8$  db of the average value. The sites were nearly ideally flat over at least the first Fresnel zone for ground reflection, and the aircraft measurements of radiation patterns confirmed the uniformity of the main lobes at all frequencies.

Transmitter power supplied to the antennas ranged from a nominal value of 2 kw at 30 Mc/s to 20 kw at 108 Mc/s; the power at each frequency was calibrated and records were kept so that the received signal intensity could be adjusted to a standard reference level. Receiver noise bandwidths were 300 c/s at all frequencies except 108 Mc/s, for which a 25 c/s band was used.

<sup>1</sup> This use of  $n$  is at variance with its use in the references, including previous publications of the authors; it has been adopted because of the convenience of the system loss concept. Furthermore, one can effectively measure or interpret data only for the scaled antenna situation. Even in communication practice the concept of scaled (or constant gain) antennas is more convenient than that of constant-aperture antennas.

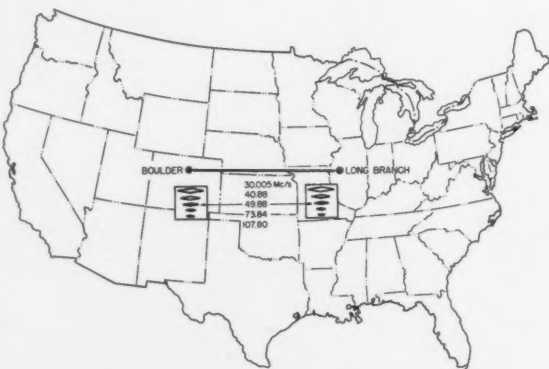


FIGURE 2. Experimental transmission path and frequencies.

In the long-term recording program a detector-AGC circuit with an integration time constant of 12 sec was used; the recorder response was proportional to logarithm of the average signal voltage. For the short-term signal distributions encountered, comparison with fast-response recorder and totalizer measurements showed that median values given by the long-time constant record, scaled for periods of 5 min or so, corresponded with true median values of the distributions within a decibel. The use of integration considerably facilitated manual reduction of the records. Studies of short-term statistics were carried out separately.

The average signal voltage thus measured was equated to the rms value for computation of received power. Earlier tests [Boggs and Hekimian, 1953] showed that using the time average of the signal in this way may introduce up to 3 db or more error in estimation of absolute power, but that little error is made in relative power ratios.

### 3. Results

#### 3.1. Short-Term Signal Statistics

It was considered important to establish whether the statistical description of the short-term behaviors of the signals were sufficiently alike throughout the frequency band to warrant the assumption: (a) that the same propagation process was being observed at

all frequencies and, to be assured (b) that the receiver was integrating signals alike at all frequencies. A number of fast-response recordings (receiver bandwidth 300 c/s, recorder response 25 c/s) were made of the fading signal received simultaneously at all frequencies.

Figure 3 shows cumulative distributions of signal envelopes at all frequencies, for typical daytime and nighttime conditions. The data shown were obtained from 10-min sampling periods. It is seen from the figure that:

a. The distributions are similar at all frequencies.

b. The distributions approximate a Rayleigh distribution during the midday hours, and are somewhat peaked at the "high-signal" end during the late night and early morning hours.

Wheelon [1960] has recently discussed the amplitude distribution for a received signal containing effects of many meteor bursts, and obtains theoretical distributions similar to those shown for the night hours in figure 3.

Median crossings per second of positive slope,  $N$ , were obtained from these records. These fading rates were observed to vary over a wide range of values. For short periods (of the order of 30 sec) the value of  $N$  may be from 0.2 c/s to 1.0 c/s at 30 Mc/s, with corresponding values of 1.0 c/s to 3 c/s at 108 Mc/s. When signals are influenced by

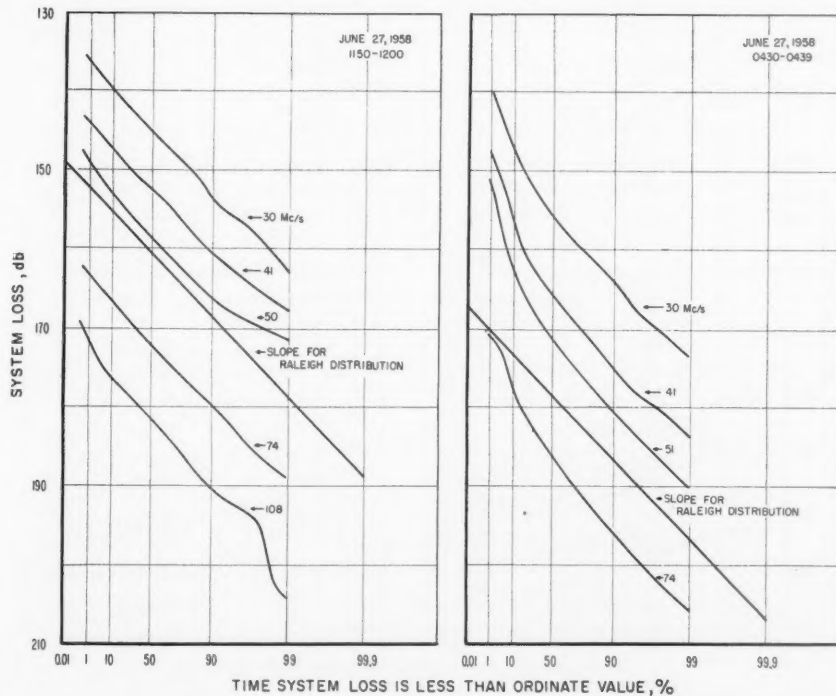


FIGURE 3. Cumulative distribution of fading envelope at five frequencies for ten minute periods; typical daytime and nighttime observations.

sporadic-*E* ionization, the fading rate may remain very low for several minutes. Figure 4 shows typical values of *N* versus carrier frequency, averaged over 10-min periods.

Most of the observations show *N* proportional to carrier frequency to a power between 3/4 and 5/4. One would expect to observe linear dependence of fading rate on carrier frequency if the drift speed of the scattering region were high compared to the speed of change of structure of irregularities. Linear dependence of *N* and good correlation of fading structure at all the frequencies would be expected if a single intense scatterer in motion, such as a meteor, were propagating the dominant signal, or if the signal were made up of an ensemble of such reflections. *Departure from linear dependence of *N* on frequency and poor frequency correlation almost certainly implies fading dominated by changing structure within the scattering region.*

### 3.2. Hourly System Loss

Continuous recording, using the receiver integration discussed in section 2 above, was carried out from October 1, 1958 through September 30, 1959. Hourly median values of the average signal trace were scaled for each hour of observation to obtain system loss values at the five frequencies.

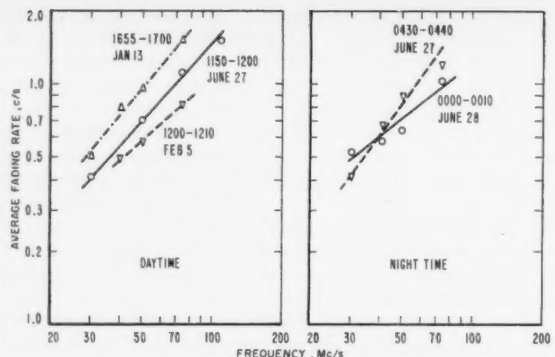


FIGURE 4. Observations of fading rate versus frequency; median crossings (one sign of slope) observed in ten minute period; typical daytime and nighttime observations.

Cumulative distributions of the hourly system loss values at all frequencies are plotted in figure 5 for 4 months of data representing conditions observed during summer, winter, and equinoxes. The solid curves represent the scatter signal data, with hours of identifiable sporadic-*E* eliminated, and including some hourly values interpolated through short periods. One notes that the frequency dependence is a little lower at the weak-signal end of the distribution. This is discussed later.

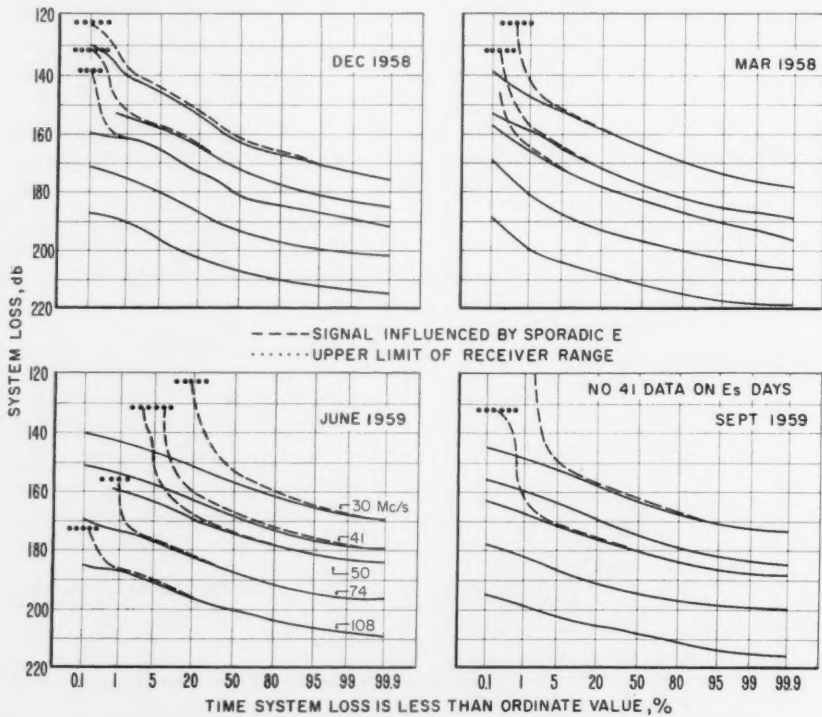


FIGURE 5. Monthly cumulative distributions of hourly values of system loss at five frequencies for months representative of winter, equinox and summer.

Figure 6 shows the characteristic diurnal variation of the scatter signal at all frequencies for the same months as above. Monthly median values of the system loss for each hour of the day are plotted. One notes that the diurnal variation is consistently greater at lower frequencies than it is at higher frequencies. The effect, especially noticeable in the December and June curves, is progressive through the frequency range. This corresponds to diurnal variation of the frequency dependence which will be shown more explicitly later.

### 3.3. Frequency Dependence of Hourly System Loss

Using hourly median values of signal intensity observed at the five frequencies, linear least-squares regression lines of system loss in decibels versus log frequency were computed on an electronic computer for each hour's data for the 1-year observing period. The slope of this line is proportional to the hourly value of  $n$ . Standard error of  $n$  was computed for each hour to check the goodness of fit of the straight line to the data. Median values of 0.30 for March 1959 and 0.34 for June 1959 are examples of the standard error.

Figure 7 is a representative plot of the observed hourly frequency dependence of system loss. Observed signal intensity at each frequency is plotted relative to that observed at the highest frequency, 108 Mc/s. The lines are indicative of individual hourly observations but the plotted points in the figure are actually median values of all hourly observations in July 1959, for hours near midday and

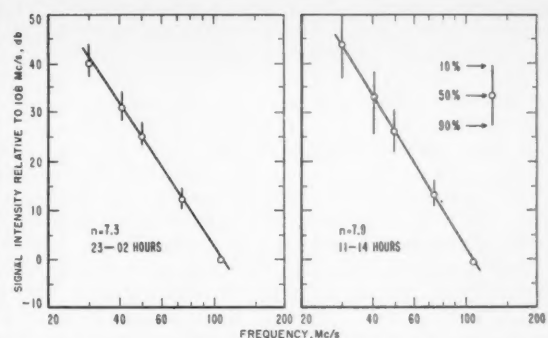


FIGURE 7. Frequency dependence of system loss; observed signal intensity at each frequency plotted relative to that observed at 108 Mc/s; values shown in plot represent all hourly values near midday and midnight during July 1959.

near midnight. The spread of hourly observations is indicated by the vertical lines through the points, the extremities of which represent the values observed 10 and 90 percent of the time. Because of the goodness of the fit of the points to straight lines at all hours, the spread shown is also nearly representative of the computed regression lines.

The actual correspondence of results with this "straight line" law is the most striking departure of the present results from earlier work. Though  $n$  varies from about 6 to 11, with characteristic diurnal and seasonal variation, received power is always closely represented by the strict power law,  $p_t/p_a \propto f^n$ ,

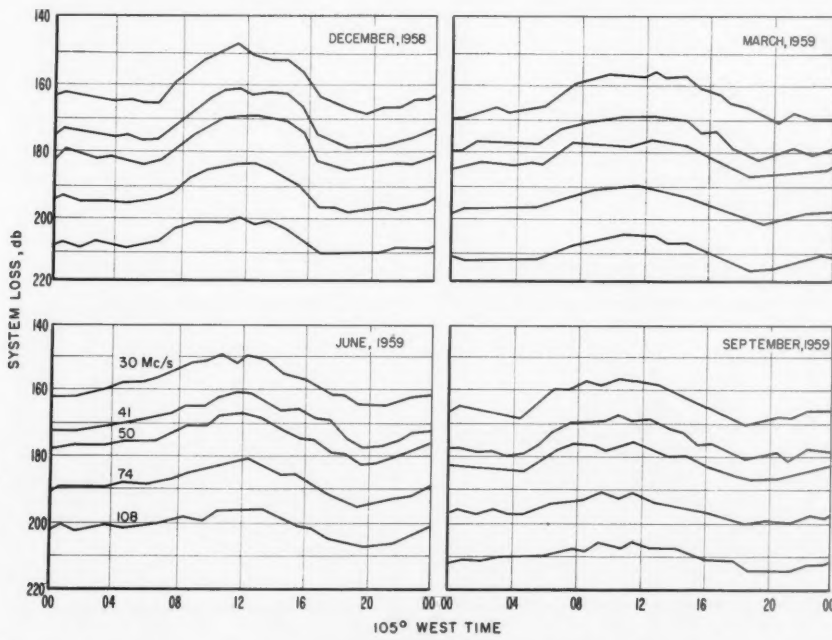


FIGURE 6. Monthly median plots of hourly values of system loss, showing diurnal variation at five frequencies in winter, equinox and summer.

over the range of frequencies observed. The earlier NBS results [Bailey, Bateman and Kirby, 1955] had been interpreted as giving a lower value of  $n$  for the lower part of the frequency range (28 to 50 Mc/s) than was obtained for the higher part (50 to 108 Mc/s). The two pairs of frequencies had not been observed simultaneously, and later studies of the siting and antenna characteristics also raised some questions about the idealness of the radiation patterns. It is felt that the careful siting and calibration of antennas and power in the present experiment, together with the feature of simultaneous comparison at frequencies throughout the whole range, fully justifies revision of the earlier conclusion and adoption of the idea of a strict power law. It thus appears valid to express the turbulent spectrum function  $S(k)$  as a power relationship  $k^{-(n-2)}$ .

The straight-line law also has implications as to absorption effects. During the course of the VHF measurements, attenuation data over the same path were obtained from a continuous 5 Mc/s transmission. Sufficient sensitivity was achieved to permit continuous day and night observation at the single frequency, so that information was obtained on diurnal and seasonal variation of nondeviative  $D$ -region attenuation. The observed values of attenuation at 5 Mc/s were extrapolated to VHF by the relation

$$Adb \propto \frac{1}{(f_H + f)^2}. \quad (4)$$

This indicated that if the scatter signal suffered full  $D$ -region attenuation, the noon values at 30 Mc/s would be reduced by 3 to 4 db and *noticeable curvature would be introduced into the scaling law*. Alter-

natively, if the observed straight line law included the effect of daytime absorption, then the absence of absorption at night would introduce curvature. But the experimental results gave a greater value of  $n$  by day than at night and a straight line at all times *except* during abnormal absorption events such as are associated with solar flares. It appears that under normal conditions the VHF scatter signal does not encounter measurable attenuation and therefore must not traverse a significant part of the absorbing region.

### 3.4. Diurnal and Seasonal Variation of Frequency Dependence

Figure 8 shows that the value of  $n$ , varying over a range from about 6 to 11, is characteristically maximum during the daytime. This figure shows values of  $n$  exceeded 90 percent, 50 percent, and 10 percent of the days for each of four months representing all seasons. Diurnally  $n$  usually varies  $\pm 1$ , though July shows less.

Figure 9 shows systematic seasonal variation of  $n$ . The median of all daytime values (hours 0900 to 1400) and nighttime values (hours 2100 to 0200) is plotted for each month; despite the spread of values in each month, indicated by the vertical lines, the seasonal variation seems clear. A summer minimum is distinct and there is a suggestion in the daytime values of a secondary winter minimum.

It is of interest to inquire whether the summer minimum represents absorption effects; i.e., whether greater summer  $D$ -region absorption tends to reduce the net frequency exponent of the scatter signals.

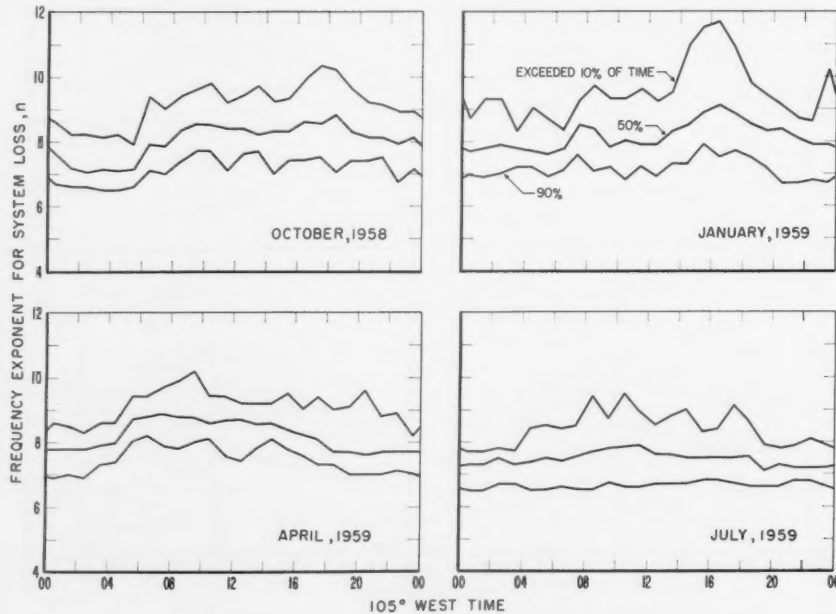


FIGURE 8. Diurnal variation of  $n$  during four seasons.

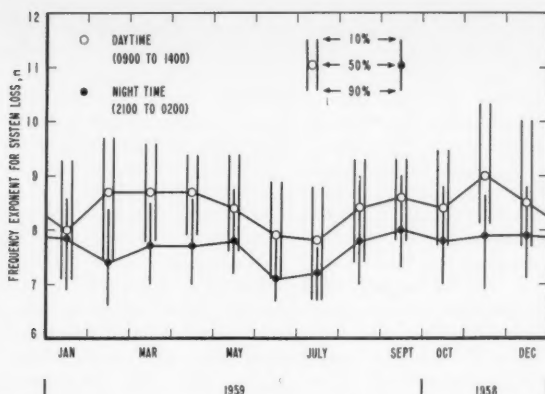


FIGURE 9. Seasonal variation of  $n$  for daytime and nighttime observations.

However, the seasonal depression of values of  $n$  is about as great at night as during the day, and  $n$  is greater during the day. These observations again tend to rule out absorption as a factor. It seems more likely that the diurnal and seasonal variation of  $n$  represents changing relative roles of meteoric reflections and turbulence.

A frequency exponent of 7 has been estimated for scatter signals that are composed entirely of meteoric echoes [Villard, Eshleman, Manning, and Peterson, 1955]. Thus, the value of 7 could be expected to prevail at times when the signal is mostly dominated by meteoric reflections. Higher values are provided

by turbulence theory. Comparison of  $n$  for broad-beam and narrow-beam systems discussed in 3.6 also strengthens the idea that variation of the relative role of meteor reflections may account for part of the diurnal and seasonal variation of  $n$ . It is also possible that the  $S(k)$  for turbulence varies with time of day and season, though the theories have not suggested this.

Figure 10 shows cumulative distributions of hourly values of  $n$  observed during each month of the program. For the year, the median value of all observations of  $n$  was 8. Ninety-five percent of the observations exceeded 6.9 and five percent exceeded 9.7.

### 3.5. Weak-Signal Conditions

It is of interest to the design engineer to know the frequency dependence of system loss during conditions of weakest signals, which generally govern the limitations of the system capacity. Values of  $n$  associated with signal levels exceeded large percentages of the time can be obtained by comparing the cumulative distributions of system loss for a year's observations at each frequency. The following values are obtained:

Value of $n$	Obtained for system loss corresponding to signal level exceeded:
8.1	50% of time
7.6	90%
7.4	99%

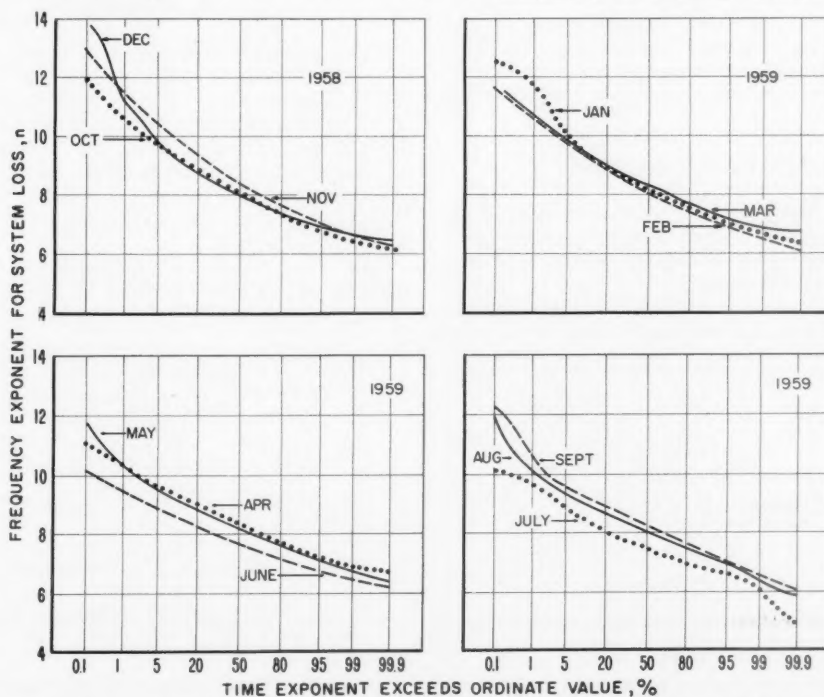


FIGURE 10. Cumulative distribution of values of  $n$  observed during each month of the year.

A value  $n=7.4$  may thus be taken for engineering computations concerned with weak signal conditions. If galactic noise is limiting at the receiver, the net signal-to-noise ratio may be taken to vary as  $\sim f^{-n}$ , allowing for the frequency dependence of the noise.

### 3.6. Effect of Beam Width

A parallel experimental system, using horizontal Yagi transmitting and receiving antennas with azimuthal beam widths of  $56^\circ$ , was available over the same path as the narrow-beam systems. This broad-beam system provided the opportunity for simultaneous frequency-dependence observations at two frequencies, near 30 and 50 Mc/s.

Figure 11 compares monthly median values of  $n$  at all hours of the day for the two systems for September 1959. The broad-beam system values of  $n$  range from  $\frac{1}{2}$  to 1 lower than the narrow-beam values. The diurnal variation of  $n$  is more pronounced for the broad-beam system, and distinct minimums are observed during early evening and early morning hours.

These results are interpreted as additional evidence that a lower value of  $n$  is associated with the meteoric contribution more effectively than with the narrow-beam system directed along the Great Circle, especially during early morning and evening hours, for geometrical reasons discussed in the literature. More noticeable absorption effects in the broad-beam system might also tend to reduce the effective exponent, as transmission off the Great Circle must traverse a longer path in the  $D$ -region. These absorption effects have manifested themselves during at least one intense absorption event associated with a solar flare, when signals in the broad-beam system were attenuated much more severely than the narrow-beam system signals.

### 3.7. Abnormal $D$ Ionization

A number of observations were made during abnormal events such as daylight occurrences of sudden ionospheric disturbances associated with solar flares, and magnetic disturbances.

During SID's attenuation was characteristically observed at the lowest frequencies, and an increase

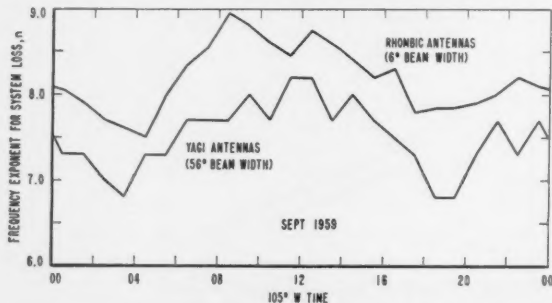


FIGURE 11. Comparison of values and diurnal variation of  $n$  for narrow and broad beam systems (measurements made simultaneously).

of scattered signal intensity was observed at the highest frequencies. Attenuation of as much as 30 db has been observed at 30 Mc/s, but the signal never dropped below the threshold of observability. Usually, the attenuation was overtaken by increased scattering to produce a net enhancement within 10 to 30 min. Attenuation is rarely observed at 50 Mc/s; usually an enhancement is noticeable.

Figure 12 shows signal behavior at five frequencies during an SID of March 29, 1958. Absorption is severe at 30 Mc/s, and is noticeable at 41 Mc/s. Note that a signal enhancement is observed at all frequencies, somewhat greater and later at the lower frequencies. The initial rise in signal intensity at 108 Mc/s is essentially simultaneous with the onset of the absorption at 30 Mc/s. As time progresses increased scattering develops at the lower frequencies, eventually overtaking the attenuation effects at 30 Mc/s.

It is of interest that during the same event for which the narrow-beam system data is given in figure 12, approximately twice as much attenuation (in decibels) was observed on the broad-beam Yagi system at 30 Mc/s, and transmission at frequencies as high as 74 Mc/s suffered noticeable attenuation. This is attributed to the greater path length through the absorbing  $D$ -region for the energy propagated off the Great Circle; it is also likely that dependence of the broad beam propagation on meteoric echoes at higher ionospheric heights than the absorbing  $D$ -region tends to increase the effective attenuation.

### 4. Summary

The frequency dependence of system loss has been found to follow a strict power law  $p_t/p_0 \propto f^n$  over the frequency range of the experiment, 30 to 108 Mc/s, at all times except during abnormal ionospheric absorption. Thus, it seems the spectrum of turbulence  $S(k)$  may be characterized by an  $\lambda^{n-2}$  dependence. Figure 13 compares the distribution of  $n$  with theoretical values from Wheelon's [1960a] summary of spectral models.

The value of  $n$  varies diurnally and seasonally; 90 percent of all observations lie in the range 7 to

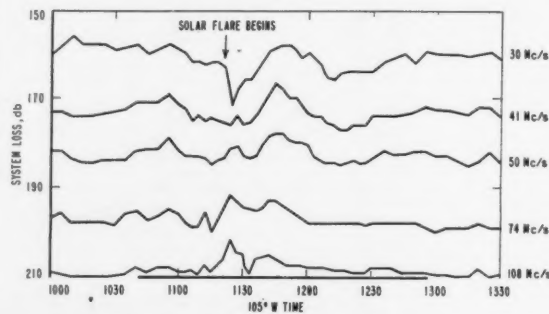


FIGURE 12. Signal behavior at five frequencies during an intense ionospheric absorption event associated with a solar flare, March 29, 1958.

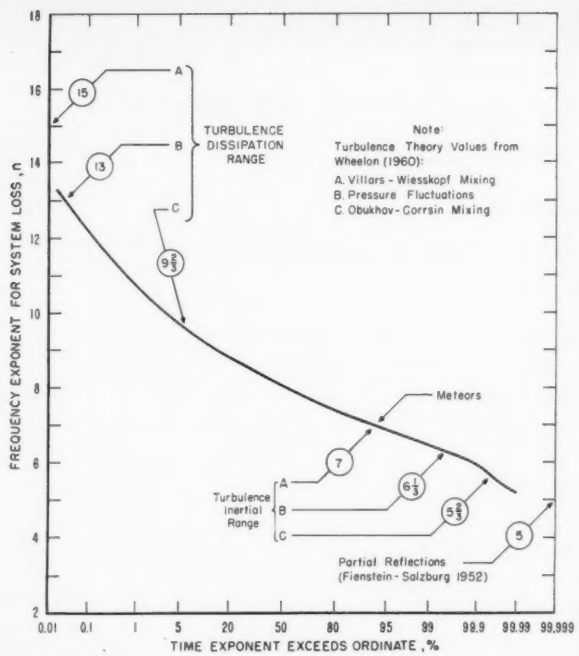


FIGURE 13. Cumulative distribution of all hourly values of  $n$  measured during the year, with theoretical values noted for comparison.

9 $\frac{1}{2}$ . The median value of the observations is 8. These values, for scaled antenna systems, include the  $f^2$  factor, which is the effect of variation of receiving antenna aperture with frequency. Daytime exponents are characteristically greater than nighttime values by 1 or 2; summer values are lower than those observed at other seasons, though winter daytime values are also lower than equinoctial daytime values. For system design, a value of 7.4 may be taken to characterize weakest signal periods. Since galactic noise varies as about  $f^{-5/2}$ , the resultant signal/noise ratio varies as  $f^{-5}$ .

Systematic temporal variation of  $n$  is accounted for by (a) diurnal and seasonal variation in the relative contributions of meteoric reflections and turbulent scattering, as well as (b) possible diurnal and seasonal variation of  $S(k)$ . The latter possibility has not yet been suggested by the theories.

It is concluded that normal ionospheric absorption does not affect the scattered signal, so the scattering would appear to occur mostly below the absorbing region. During abnormal intense absorption events associated with solar flares or other disturbances, attenuation is observed at frequencies below 40 Mc/s. Enhancement of signal is characteristic at all frequencies during such events, but is observed at the lowest frequencies only after the initial absorption effects no longer dominate.

A broad-beam system yields lower values of  $n$  than are obtained with a narrow-beam system. In the experiment, the system having an azimuthal beam width of  $56^\circ$  gave values of  $n$  lower by  $\frac{1}{2}$  to 1 than the system using  $6^\circ$  beam width. The broad-beam system exhibited more pronounced minimums in the diurnal variation of  $n$  during the early morning and early evening hours, and susceptibility to greater attenuation during absorption events.

A. D. Wheeler and K. L. Bowles contributed valuable suggestions on the initiation and conduct of the program. E. F. Florman designed the antenna systems and P. P. Viezbicke supervised the calibration of antennas and measurement of radiation patterns. J. L. Green supervised the transmitting station; R. P. Fitzpatrick and C. H. Johnson were principal observers and data analysts at the receiving station.

## 5. References

- Bailey, D. K., R. Bateman, and R. C. Kirby, Radio transmission at VHF by scattering and other processes in the lower ionosphere, Proc. IRE **43**, 1181-1231 (Oct. 1955).
- Blair, J. C., Frequency dependence of VHF ionospheric scattering, NBS Tech. Note 9 (April 1959).
- Boggs, G. E., and N. C. Hekimian, Determination of frequency dependence exponent by true power measurements, Unpublished NBS report (1953).
- Villard, O. G., Jr., V. R. Eshleman, L. A. Manning, and A. M. Peterson, The role of meteors in extended-range VHF propagation, Proc. IRE **43**, 1473-1481 (Oct. 1955).
- Wheeler, A. D., Relation of turbulence theory to ionospheric forward scatter propagation experiments, J. Research NBS **64D** (Radio Prop.) No. 4, 301-309 (July-Aug. 1960).
- Wheeler, A. D., Radio frequency and scattering angle dependence of ionospheric scatter propagation at VHF, J. Geophys. Research **62**, 93-112 (March 1957).
- Wheeler, A. D., The amplitude distribution for radio signals reflected by meteor trails, J. Research NBS **64D** (Radio Prop.) No. 5, 449-453 (Sept.-Oct. 1960).
- Report of the IRE-EIA Joint Technical Advisory Committee, Radio transmission by ionospheric and tropospheric scattering, Proc. IRE **48**, 3-46 (Jan. 1960).

(Paper 65D5-146)

f  
f  
f  
f  
r  
i  
c  
g

t  
u  
t  
a

T  
n  
a  
r

p

—  
c

# Theoretical Scattering Coefficient for Near Vertical Incidence From Contour Maps<sup>1</sup>

H. S. Hayre and R. K. Moore

Contribution from the Electrical Engineering Department, University of New Mexico, Albuquerque, N. Mex.

(Received January 30, 1961; revised April 10, 1961)

In calculation of the theoretical scattering coefficient for a terrain, previous authors tentatively assumed the normalized autocovariance function  $\rho(r) = e^{-4r^2}$  for the ground elevation as a function of distance from a given point. Recently autocorrelation studies were made using maps with contours ranging from one to twenty-five feet. These resulted in curves of  $\rho(r)$ , which are approximated by  $\exp(-|r|/B)$ . The theoretical scattering cross section ( $\sigma_0$ ) of many such terrains can be expressed as

$$\sigma_0 = 4\sqrt{2} \frac{\pi B^2}{\lambda^2} \left( \frac{\theta}{\sin \theta} \right) e^{-4k^2 \sigma^2 \cos^2 \theta} \sum_{n=1}^{\infty} \frac{(4k^2 \sigma^2)^n (\cos^2 \theta)^{n+1}}{(n-1)! (2k^2 B^2 \sin^2 \theta + n^2)^{3/2}}, \quad (1)$$

where  $\sigma$ ,  $\lambda$ ,  $k$ , and  $\theta$  are standard deviation of the target terrain, wavelength, wavenumber ( $2\pi/\lambda$ ) and the angle of incidence respectively. For the case where  $1/B$  is small as compared to  $k$ , the above expression becomes

$$\sigma_0 = \frac{4\sigma^2}{\lambda B} (\theta \cot^4 \theta) \quad \text{for } \theta \neq 0^\circ. \quad (2)$$

These expressions, when normalized, are in agreement with experimental results of other authors. It is also noteworthy that the results obtained with an acoustic simulator model compared very well with this theoretical expression. This work is based on the property that the ground is conducting and has random elevation variations. Theoretical results calculated on the basis of varying ground impedance rather than its elevation are also in agreement with this expression.

## 1. Introduction

In recent years, the calculation of backscatter from a rough surface, with very obvious extension and application to the radar return from the moon, has attracted considerable attention. Here we follow the basic approach of Davies [1954] as modified by Moore [1957] and Cooper [1958]. The modified Kirchhoff-Huygens' principle is employed in the calculation using modified spherical variables of integration. The ground model used assumes "facets," of variable size and height above mean ground level, whose position is described statistically.

Instead of assuming a correlation model for terrain, as is usually done, the present approach used contour maps of different terrain samples in the United States to calculate the terrain-elevation autocovariance and other statistical properties. The overall approach to the problem is an approximation, but the results so obtained are very reasonable indeed, insofar as the comparison with terrain return and moon-echo data reported in various publications [Briggs, 1960; Hughes, 1960; Nielson, 1960] is concerned.

## 2. Statistical Properties of Terrain

Various autocovariance [Ament, 1953; Davies, 1954; Moore, 1957b; Daniels, 1960] functions for rough terrain have so far been assumed. In some instances [Cohen, 1948] an effort was made to derive an approximate expression for the autocorrelation from actual data on terrain elevation. A general expression [Norton, 1960] for space correlation function  $\rho(\bar{r})$  describing the random variation of the refractive index over space is given here:

$$\rho(\bar{r}) = \left[ \frac{2}{\Gamma(\mu)} \right] \left( \frac{r}{2l_0} \right)^\mu K_\mu \left( \frac{r}{l_0} \right), \quad (2.1)$$

where

$l_0$ =characteristic scale

$\mu$ =constant

$\Gamma(\mu)$ =gamma function

$K_\mu \left( \frac{r}{l_0} \right)$ =modified Bessel function of the second kind.

It seems to cover some of the most commonly assumed [Wheelon, 1959] expressions for correlation functions.

A search of the literature shows that small-scale perturbations of the terrain elevation have not so far been used to calculate an experimental autocovari-

<sup>1</sup> This work was sponsored by the Naval Ordnance Test Station, China Lake, Calif., under contract No. N123(60530)18138A.

TABLE 1. Location of terrain samples and the surface characteristic constant,  $B$

Sample	General location	Average elevation	Standard deviation	Sampling interval	Surface characteristic constant, $(1/B)$
1	Lawrence, Kans.	853.5	ft	5.63	ft
2	Tees Nos, Ariz.	5254	49	5	$0.1193 \times 10^{-3}$
3	Turtle Mountain, N. Dak.	1990	8.2	5	$1.3213 \times 10^{-3}$
4	Gila River, Ariz.	2617	13.6	5	$0.7070 \times 10^{-3}$
5	White River, Ariz.	5028	5.18	5	$0.9236 \times 10^{-3}$
6	Mountain Park, N. Mex.	7530	1030	62.5	$1.3610 \times 10^{-3}$
7	Sandia Park, N. Mex.	6780	250	20	$0.2729 \times 10^{-3}$

ance function. For this reason, contour maps for seven different terrains in the United States were selected, as listed in table 1. This set included relatively flat land, rolling plains and some rugged mountain areas. The average elevation (above sea level) and standard deviation of these samples varied from 850 to 7,530 ft and 5 to 1,030 ft, respectively. Three distinctly different but random lines were drawn on each of these contour maps. Along these lines, the elevation of the terrain was read to within one tenth of a foot (by interpolation) on 1-ft contour maps, and within 5 ft on 20- and 25-ft contour maps. Using a reasonable compromise between resolution and confidence level [Blackman and Tukey, 1958], and due to the unavailability of less-than-one-foot contour maps, horizontal sampling intervals of 5, 20, 30, and 62.5 ft were used. The number of points for a subsample varied from 58 to 610. The autocovariance was calculated using a CRC-102 computer. The resulting curves were averaged for each type of terrain. A simple theoretical approximation of these curves for high confidence level portions was found to be

$$\rho(r) \approx e^{-|r|/B} \quad (2.2)$$

where

$B$ =characteristic constant  
 $r$ =distance between points

Seven cases for the experimental autocovariance are shown in figure 1.

In figure 1 the autocorrelation curves for samples 1 and 3 seem to slope off faster than the rest. In case of sample 1 this is caused by the lag distance for a given number of lags being greater than for samples 2 through 5 and 7. In view of this, if all these curves were plotted on a semilog paper (as in fig. 1), for a given lag distance rather than for a fixed number of lags, these would plot approximately as straight lines over limited distances. These two curves can also be approximated as  $\rho(r) = e^{-|r|/B} \cos cr$ , where  $c$  was found to be 0.2188 and 0.7931 deg/ft for samples 1 and 3, respectively. For near vertical incidence, the distances involved are rather short, and therefore  $\cos cr$  is approximately unity. It is felt that the apparent cosine factor in the autocovariance appears because of the relatively short length of the sample used in this case. This seems to indicate that the autocovariance function  $\rho(r)$  often varies as  $e^{-|r|/B}$ .

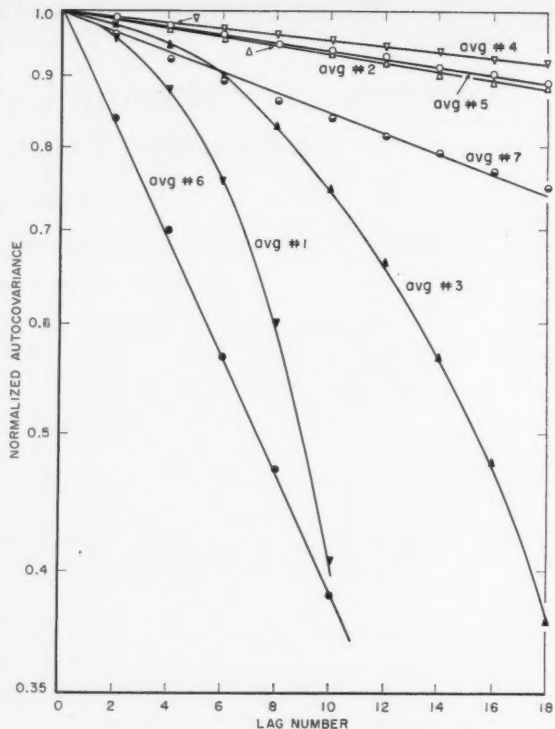


FIGURE 1. Normalized autocovariance curves—(portions with highest confidence level).

Sample No. and type of terrain	Length of data (points in each subsample)	Sampling interval
1 (relatively flat)	58, 101, 079	ft, 30
2 (rolling and flat)	252, 276, 215	5
3 (rolling)	189, 194, 144	5
4 (irregular, sloping)	226, 196, 261	5
5 (flat, slight slope)	287, 264, 272	5
6 (very rugged mtn.)	216, 187, 187	62.5
7 (rugged mountain)	187, 187, 187	20

It is known [Cohen, 1948; Isakovitch, 1952] that the slope of  $\rho(r)$  at  $r$  equal to zero should be zero unless the ground elevation function has infinite slopes. In this instance,  $\rho(r)$  has a slope of  $-1/B$  which is in most cases believed to be of the order of  $10^{-3}$  (see table 1). Considering the minute size (in the general range of  $10^{-3}$  to  $10^{-4}$  m) of the earth particles, this may be quite a reasonable approximation to the exact description of the terrain roughness.

It was also found that the ground elevations generally are normally distributed. For a certain type of terrain, the ground elevation data along a random line is most probably a random function belonging to a large, approximately stationary ensemble. It is further suspected that the expressions obtained for the scales of roughness covered in this study when reduced by a scale factor, might well describe extremely minute variations of ground roughness as seen by very high frequency waves.



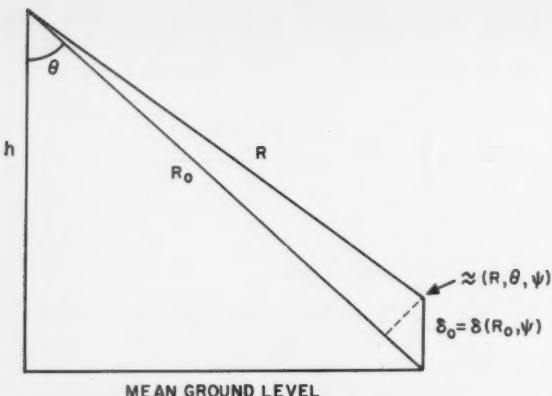


FIGURE 3. A typical point, at a random height  $\delta_0$  above mean ground level.

where  $E^*$  stands for complex conjugate of  $E$  and  $\mathcal{R}$  is the symbol for 'real part of' the expression following it. The difference in ranges of two points on ground located at  $(R, \theta, \psi)$  and  $(R', \theta', \psi')$  can be expressed as follows with the help of figure 3,

$$\begin{aligned} R - R' &= [R_0 - \delta(R_0, \psi) \cos \theta] - [R'_0 - \delta(R'_0, \psi') \cos \theta'] \\ &= -s + [\delta(R_0 + s, \psi + \alpha) \cos \theta' - \delta(R_0, \psi) \cos \theta] \\ &= -s + (\delta - \delta_0) \cos \theta \end{aligned} \quad (3.5)$$

where  $\theta \approx \theta'$  (assumed)

$$\delta = \delta(R_0 + s, \psi + \alpha)$$

$$\delta_0 = \delta(R_0, \psi)$$

$$R'_0 \approx R_0 + s$$

The substitution of (3.3) in (3.4) results in

$$P_r = \frac{1}{32\pi^2} \mathcal{R} e \int \frac{P_r G^2 \cos \theta \cos \theta'}{R^2 R'^2} e^{-j2k(R-R')} dA dA'. \quad (3.6)$$

where the primed quantities refer to a point at  $(R', \theta', \psi')$ .

The average received power can now be expressed in terms of  $R$ ,  $s$ ,  $\psi$ , and  $\alpha$  by substituting (3.5) in (3.6) as

$$\begin{aligned} \bar{P}_r &= \frac{1}{32\pi^2} \int_{-\pi}^{\pi} \int_{-2\theta_0}^{2\theta_0} \int_{-(R_0-h)}^{\infty} \int_{R_0 - \frac{cr}{2}}^{R_0} \frac{P_r G^2 \cot \theta \cot \theta'}{R R'} \\ &\quad \exp [j2k\{s + (\delta_0 - \delta) \cos \theta\}] dR ds d\psi d\alpha \end{aligned} \quad (3.7)$$

where primed quantities refer to values at a point different from that for unprimed quantities. The limits  $-2\theta_0$  to  $2\theta_0$  on the variable  $\psi$  are used to cover the entire  $360^\circ$  of the azimuth angle.

It is apparent from the statistical studies of contour maps that the probability density function for terrain elevation above the mean (say  $\delta$ ) can be written as

$$p(\delta) = \frac{1}{(2\pi\sigma^2)^{1/2}} e^{-\delta^2/(2\sigma^2)}, \quad (3.8)$$

The conditional (normal) density function for the elevations  $\delta$  given  $\delta_0$  at two points on the ground, a distance  $r$  apart, is given by

$$p(\delta; \delta_0, r) = \frac{1}{[2\pi\sigma^2(1-\rho^2)]^{1/2}} e^{-\frac{(\delta-\delta_0)^2}{2\sigma^2(1-\rho^2)}}. \quad (3.9)$$

The expression  $\exp [j2k\{s + (\delta_0 - \delta) \cos \theta\}]$  in (3.7) is first averaged over  $\delta$  using (3.8) and the result is

$$\exp [j2ks - a^2 k^2 \cos^2 \theta + j2k\delta_0(1-\rho) \cos \theta], \quad (3.10)$$

where

$$a^2 = 2\sigma^2(1-\rho^2).$$

Now (3.10) is averaged over  $\delta_0$  using (3.9), and it becomes,

$$\exp [j2ks - 4k^2\sigma^2(1-\rho) \cos^2 \theta]. \quad (3.11)$$

One can deduce from Davies' [1954] approximation  $r^2 \approx R^2 \alpha^2 + s^2 \operatorname{cosec}^2 \theta$  (see fig. 2) that

$$r \approx R\alpha + \frac{s^2 \operatorname{cosec}^2 \theta}{2R\alpha}. \quad (3.12)$$

It can be now shown that the integration of (3.7) after substituting (3.11), (3.12), and (2.2) results in an expression, which when rearranged, becomes

$$\begin{aligned} \bar{P}_r &= \frac{\lambda^2}{32\pi^2} \int \left( \frac{P_r G^2}{R^3} \right) \left[ \frac{4\sqrt{2}\pi}{B\lambda^2} \left( \frac{\theta}{\sin \theta} \right) \right. \\ &\quad \left. e^{-4k^2\sigma^2 \cos^2 \theta} \sum_{n=1}^{\infty} \frac{(4k^2\sigma^2)^n (\cos^2 \theta)^{n+1}}{(n-1)! \left[ 2k^2 \sin^2 \theta + \frac{n^2}{B^2} \right]^{3/2}} \right] dR. \end{aligned} \quad (3.13)$$

Here it has again been assumed that  $R'$  and  $\theta'$  are approximately equal to  $R$  and  $\theta$  respectively, for near-vertical incidence. From the comparison of (3.1) with (3.13) it is clear that the scattering coefficient,  $\sigma_0$ , is given by

$$\sigma_0 = \frac{4\sqrt{2}\pi B^2}{\lambda^2} \left( \frac{\theta}{\sin \theta} \right)$$

$$e^{-4k^2\sigma^2 \cos^2 \theta} \sum_{n=1}^{\infty} \frac{(4k^2\sigma^2)^n (\cos^2 \theta)^{n+1}}{(n-1)! [2k^2 B^2 \sin^2 \theta + n^2]^{3/2}}. \quad (3.14)$$

The value of  $1/B$  is far less than  $k$  for *nearly smooth* surfaces, and hence the scattering coefficient for such surfaces can be approximated from (3.14) as

$$\sigma_0 \text{ (for nearly smooth surfaces)} \approx \frac{4\sigma^2}{B\lambda} (\theta \cot^4 \theta) \quad (3.15)$$

for  $\theta \neq 0^\circ$ .

#### 4. Experimental Verification

For *nearly smooth* surfaces, the surface characteristic constant  $1/B \approx 0$ , and (3.15) gives the scattering coefficient. This result compares very closely with published results [Nielson, 1960] for new ice as shown in table 2.

For rough (not *nearly smooth*) surfaces, (3.14) describes the relationship of the scattering coefficient  $\sigma_0$  and other variables such as the angle of incidence  $\theta$ , wavelength  $\lambda$ , standard deviation  $\sigma$  and surface covariance constant  $B$ , etc. Two curves of the scattering coefficient  $\sigma_0$  versus  $\theta$  for each of the three values of  $\lambda/B$ , 0.1, 0.5, and 1.0 for  $\sigma/\lambda$  equal to 0.05, and 0.1 are shown in figure 4. It may be noticed that as the surface becomes rougher, or as  $\lambda/B$  increases for a specified  $\lambda$ , the scattering coefficient curve becomes flatter, showing the relative importance of the contribution of the power return from the surface at angles other than those near zero. As expected, when the surface becomes smoother or  $1/B$  decreases, the received power seems to come primarily from near-zero angles. These curves are quite similar to those recently published [Campbell, 1959; Dye, 1959; Edison, 1960]. The experimental data [Nielson, 1960] on desert and new ice also seems to follow the pattern of these theoretical curves described above.

TABLE 2. Comparison of theoretical versus experimental scattering coefficient (Normalized)

$\theta^\circ$	$\sigma_0$ Theoretical	$\sigma_0$ Experimental
30	1.000	1.000
40	0.291	0.308
50	0.088	0.089
60	0.022	0.021
70	0.004	0.004

Similar results<sup>2</sup> obtained by an acoustic simulator at the University of New Mexico also verify these theoretical conclusions. It is interesting to note that an experimental expression ( $\sigma_0 = \sigma_1 e^{-100}$  for  $\theta$  in radians) for the scattering coefficient [Hughes, 1960] of the Moon, verified by photographic astronomical [Briggs, 1960] calculations, is a very close fit to the graph of eq (3.14) for  $\sigma/\lambda = 0.1$  and  $\lambda/B = 1.0$  in the range of incidence angles of 3 to 14 deg. The authors believe that other values of  $B$  and  $\sigma$  may well be appropriate, as only a limited set has been tried to date.

<sup>2</sup> A. R. Edison and R. K. Moore, Preliminary report on an acoustic simulator for investigation of backscatter of E.M. waves, unpublished report of the University of New Mexico, Albuquerque, N. Mex. (1961).

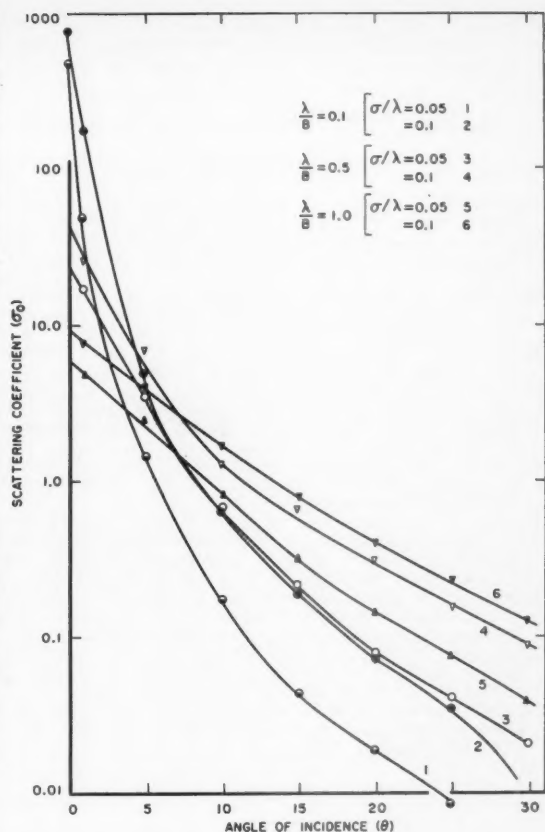


FIGURE 4. Scattering coefficient versus the angle of incidence.

#### 5. Conclusions

The scattering coefficient ( $\sigma_0$ ) for *nearly smooth* surfaces is inversely proportional to the wavelength, but varies directly with  $(\sigma^2)$ ,  $(\theta \cot^4 \theta)$  and  $1/B$ , where  $\sigma$ ,  $\theta$ ,  $B$  are standard deviation, angle of incidence, and the terrain characteristic constant respectively. For rough surfaces it has a negative exponential factor, where the exponent is made up of  $\frac{\sigma^2 \cos^2 \theta}{\lambda^2}$  times a constant. The surface characteristic constants  $B$  and  $\sigma$  can be calculated from the radar return data. Although approximate, the theoretical results agree well with the experimental data; and therefore, suggest the usefulness of the approach. The application of these results may be extended to the moon-echo data, with proper corrections for Faraday and libration effects, etc. This investigation has established that for near-vertical incidence, the normalized autocovariance for the terrain elevation is more often of the exponential form  $\exp(-|r|/B)$  rather than the Gaussian form,  $\exp(-r^2/B)$ . The former may well be more appropriate for finer terrain irregularities than those considered in this

paper. It may also be representative of the normalized autocovariance of the moon surface. An exact theoretical, but usable, expression for the scattering coefficient has been very reasonably approximated by the results of this study.

## 6. References

Ament, W. L., Toward a theory of reflection by a rough surface, *Proc. IRE* **41**, No. 1, 142-146 (Jan. 1953).

Bendat, J. S., Principles and applications of random noise theory, 189-218 (John Wiley & Sons, New York, N.Y., 1958).

Blackman, R. B. and J. W. Tukey, The measurement of power spectra, 22-25, 30-32, 147-149 (Dover Publication, Inc., New York, N.Y., 1958).

Briggs, B. H., Roughness of the moon as a radar reflector, *Nature* **187**, No. 4736, 490 (Aug. 6, 1960).

Campbell, J. P., Backscattering characteristics of land and sea at X-band, *Transactions of the 1959 Symposium on Radar Return*, Univ. of New Mexico, pt. 1, unclassified, 277 (fig. 6) (May 11-12, 1959).

Cohen, R., Some analytical and practical aspects of Wiener's theory of prediction, Thesis for M.S.E.E., Massachusetts Institute of Technology (May 1948).

Cooper, J. A., Comparison of observed and calculated near vertical radar ground return intensities and fading spectra, M.S. Thesis, Univ. of New Mexico, Albuquerque, also *Engng. Exper. Station Tech. Rep. EE-10* (May 1958).

Daniels, F. B., Radar determination of the surface structure of the moon, U.S. Army Signal Res. & Dev. Lab., Fort Monmouth, N.J., Tech. Rep. 2110 (April 1960).

Davenport, W. B., and William L. Root, An introduction to the theory of random signals and noise, 45-75, 147-150 (McGraw-Hill Book Co., New York, N.Y., 1958).

Davies, H., The reflection of electromagnetic waves from a rough surface, *J. Inst. Elec. Engrs. (London)*, pt. 4, **101**, 209-215 (Aug. 1954).

Dye, J. E., Ground and sea return signal characteristics of microwave pulse altimeters, *Transactions of the 1959 Symposium on Radar Return*, pt. 1, unclassified, Univ. of New Mexico, Slide II, 111, (May 11-12, 1959).

Edison, A. R., R. K. Moore, and B. D. Warner, Radar terrain return measured at near-vertical incidence, *IRE PGAP-8*, No. 3, 246-254 (May 1960).

Hughes, V. A., Roughness of the moon as a radar reflector, *Nature* **187**, No. 4728, 873 (June 11, 1960).

Isakovitch, M. A., The scattering and radiation of waves by statistically oscillating surfaces, *J. Exptl. Theoret. Phys. U.S.S.R.* 23-305 (1952).

Katz, I., and L. M. Spetner, Two statistical models for radar terrain return, *IRE-PGAP*, **AP-8**, No. 3, 242-246 (May 1960).

Moore, R. K., and C. S. Williams, Jr., Radar return at near vertical incidence, *Proc. IRE* **45**, No. 2, 228-238 (Feb. 1957).

Moore, R. K., Resolution of vertical incidence radar return into random and specular components, *Univ. of New Mexico Engineering Experiment Station Tech. Report EE-6* (July 1957).

Nelson, D., et al., An investigation of the backscatter of high-frequency radio waves from land, sea water, and ice, *SRI Project 2909*, Stanford Research Inst., Menlo Park, Calif., 129-135 (May 1960).

Norton, K. A., Carrier-frequency dependence of the basic transmission loss in tropospheric forward scatter propagation, *J. Geophys. Research* **65**, No. 7, 2029-2045 (July 1960).

Wheelon, A. D., Radio-wave scattering by tropospheric irregularities, *J. Research NBS* **63D**, No. 2, 205-234 (Sept.-Oct. 1959).

Wolfgang, G., and Nikolaus Hofreiter, *Integraltafel*, 64-65 Springer-Verlag, Wien 1950.

(Paper 65D5-147)

# Mutual Interference Between Surface and Satellite Communication Systems<sup>1</sup>

William J. Hartman and Martin T. Decker

(Received April 27, 1961)

Contribution from Central Radio Propagation Laboratory, National Bureau of Standards, Boulder, Colo.

Estimates of the mutual interference expected to occur between the ground terminals of space communications systems and surface point-to-point systems are presented in a fashion suitable for engineering applications. These estimates are obtained from recently developed methods for predicting the transmission loss over tropospheric paths in terms of parameters such as geographic separation, elevation angle of the antenna, antenna patterns and frequency. It is concluded that these systems can share the same frequency assignment under suitable conditions.

## 1. Introduction

Many of the problems of mutual interference between proposed satellite communications systems and surface communications systems can be investigated in terms of presently available theories. The prediction method used here is that developed by Rice, Longley, and Norton [1959], for tropospheric scatter propagation. The method is designed to predict the median value of hourly median basic transmission loss,  $L_b$ , and to give a distribution of the medians about this value; the median basic transmission loss is defined in terms of the ratio of the power,  $p_r$ , radiated from the transmitting antenna to the available power,  $p_a$ , at the receiving antenna, when isotropic antennas are used at both ends of the path. The method is applicable for any path configuration. The median transmission loss,  $L$ , is obtained from this by subtracting the path antenna gain,  $G_p$ , [Hartman and Wilkerson, 1959] from the basic transmission loss. It should be noted that these methods give excellent agreement with data measured over a frequency range from 100 Mc/s to 10,000 Mc/s. Most of these data were taken over conventional scatter paths with the antennas directed at the horizon in the great circle plane, although some preliminary data obtained using elevated beams are shown later in the paper.

Tolerable interference will depend not only on the relative levels of the desired and undesired signals, but also on the type of modulation used for both of these signals and in most cases must be determined experimentally, in some cases subjectively (for example, subjective rating of television pictures). Further, neither desired nor interfering signals will be steady signals, but will be represented by a distribution of values. Because of this, satisfactory operation should usually be specified in terms of an hourly-median-desired-signal to an hourly-median-undesired-signal ratio required to

provide a given grade of service or better for some percentage of the hours. A discussion of this problem is given by Norton [1959]; and Miller, Ports, and Savage [1960]. However, in view of the many unknowns the actual problem has been somewhat simplified by relating the hourly-median-interfering-signal power to the noise power of the receiver under consideration. Thus the question answered here is what separation distances and antenna elevation angles are required so that the interfering hourly-median-signal power is equal to or less than the receiver noise power for a given percent of the hours.

## 2. Path Parameters

The following values of the path parameters are used here to illustrate the methods of a more general treatment [JTAC, 1961].

It is assumed that the satellite ground terminal has an antenna with the general characteristics of a 60-ft parabolic dish, and that the surface system antennas are at most 10-ft dishes. The satellite terminal antenna beam will be directed above the horizon at an angle  $\psi$  as shown in figure 1, and the

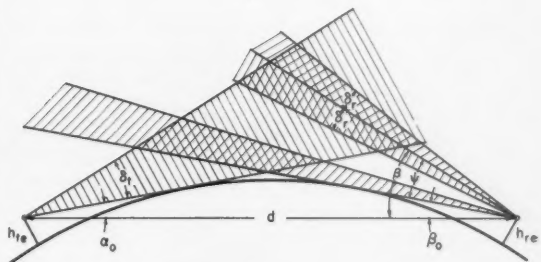


FIGURE 1. Geometry.

<sup>1</sup> This is a résumé of work sponsored by the Joint Technical Advisory Committee of the Electronic Industries Association and the Institute of Radio Engineers.

surface system antenna will be directed at the horizon. Both antennas are to be located 30 ft above a smooth spherical earth. Because antenna heights, terrain effects, and diffraction become increasingly important for shorter path lengths, a distance of 100 miles is chosen as a minimum for which calculations of this type will give representative values of transmission loss. At any distance a careful selection of the terminal site is necessary, and in some cases it will be possible to use terrain to give protection at distances shorter than those shown in this paper. If the specific path parameters are known, the transmission loss can be predicted accurately for any distance using the methods of the references given above [Hartman and Wilkerson, 1959; Rice, Longley, and Norton, 1959]. Both antenna axes are centered in the great circle plane. Although this situation usually results in the maximum interference, it may be impossible to avoid it if the satellite systems share frequencies with existing systems.

Figure 2 shows values of hourly median transmission loss which will be exceeded by 99.9 percent of the hourly medians for a 10-ft dish at one end, and the main beam, a side lobe with the same half-power beamwidth as the main beam and 20 db down from the main beam, and an isotropic portion of the antenna pattern for a 60-ft dish at the other end. These are plotted versus the elevation angle,  $\psi$ , for the main beam of the 60-ft dish. Examples of this type of calculation for median values are shown in figure 3. Also shown in this figure are the results of some preliminary measurements. These data points represent 5-minute medians measured over a 165-mile test path from Boulder to Haswell, Colo. The pertinent parameters for this path are as follows: Frequency, 409.9 Mc/s, the angular distances with both antennas directed at their respective horizons is 33 milliradians, the fixed transmitting antenna is a 14-ft parabolic dish, and the receiving antenna being elevated is a 60-ft dish.

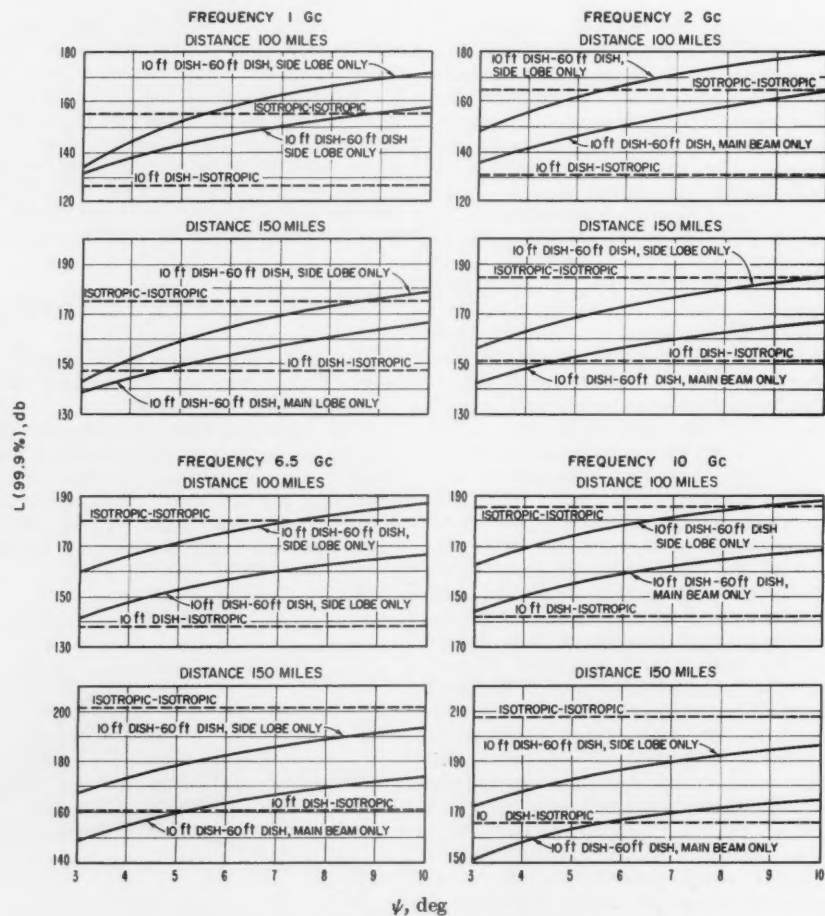


FIGURE 2. Transmission loss exceeded 99.9 percent of the time.

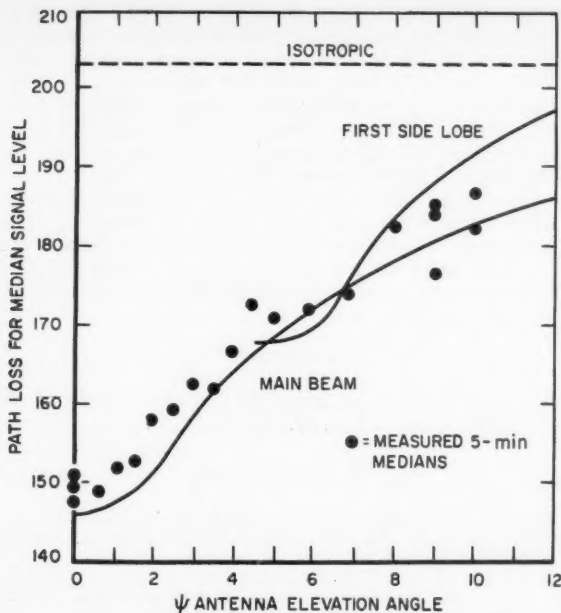


FIGURE 3. *Boulder-Haswell Test Path, transmission loss exceeded 50 percent of the time.*

The following procedure is used to determine the required separation distance for which the undesired signal is less than the receiver noise power at the receiver intermediate frequency for 99.9 percent of the hours.

Compute the value of transmission loss required to make the interfering signal equal to the noise power. This value is

$$L_{req} = P_t - L_c - M - P_n$$

where  $P_t$  is the power, in decibels, of the interfering transmitter,  $L_c$  represents coupling losses in the system and may include transmission line losses, cross-polarization losses, etc.,  $M$  is a term to allow for the situation in which the transmitted energy is spread over a frequency band different from that which will be accepted by the receiver. It will depend on the type of modulation as well as the bandwidths, but an estimate is made here by letting  $M = 10 \log b_t/b_r$ , where  $b_t$  and  $b_r$  are the transmitter and receiver bandwidths, respectively.  $P_n$  is the available noise power in decibels at the receiver terminals and is given by

$$P_n = NF + 10 \log k T_0 b = 10 \log k T_r b$$

where  $NF$  is the effective noise figure [Norton, 1959; Hogg, 1960] of the receiving system,  $k$  is Boltzmann's constant,  $b$  is the noise bandwidth of the receiver in cycles per second,  $T_0$  is a reference temperature,  $288.48^{\circ}\text{K}$ , and  $T_r$  is the effective noise temperature of the receiver and antenna combination.  $T_r$  should not be confused with the effective antenna tempera-

ture. This value of  $L_{req}$  is then compared with the curves for the frequency under consideration to determine if  $L_{req} \leq L'$  where  $L'$  is the smallest of the transmission loss values using the main beam or the side lobe or the isotropic part of the antenna pattern.

### 3. Examples

1. Consider first the case of interference from the earth terminal transmitter to a point-to-point relay receiver. The receiver noise power is determined as above assuming a bandwidth of 20 Mc/s and a noise figure of 10 db. Then

$$P_n = NF + 10 \log b - 204 = -121 \text{ dbw.}$$

Assume a transmitter power of 1 kw, coupling losses of 4 db, including line and polarization losses, and a transmitted bandwidth of 20 Mc/s. Then

$$L_{req} = P_t - L_c - M - P_n = 147 \text{ db.}$$

This transmission loss value is now used with figure 2 to determine whether the above condition,  $L_{req} \leq L'$  can be met. It is clear that for a separation distance of 100 miles and for all four frequencies the transmission loss from the isotropic portion of the transmitting antenna is less than the 147 db required loss. For a separation of 150 miles the energy transmitted by way of the main beam becomes significant and the required conditions can be met at all frequencies if the main beam of the 60-ft antenna is elevated above the horizon by approximately  $5^{\circ}$ .

This analysis assumes that the antenna of the surface point-to-point system is directed toward the earth terminal. Rotating this antenna so that the main beam does not point directly toward the earth terminal would increase the transmission loss. When the pattern of the 10-ft dish is at the isotropic level in the direction of the earth terminal the "isotropic-isotropic" curves of figure 2 will apply rather than the "10-ft dish-isotropic" curves. The transmission loss via main and side lobes will of course increase by approximately the same amount. Therefore, the requirement could be met at 100 miles and at all frequencies by orienting the 10-ft dish to reduce the interfering signal by 10 db at 1 Ge and by lesser amounts at the other frequencies.

Other earth terminal to satellite systems might require more or less transmitter power. Suggested systems [FCC hearing] range from approximately 3 to 36 dbw. The effect of changing this parameter in the above example would give a range of  $L_{req}$  from 120 to 153 db at the 99.9 percent level.

If instead of a 60-ft dish, a 120-ft dish or a 30-ft dish were used for the transmitter, the only noticeable effect would be in the calculations for  $L(p)$  for the main beam. In the former case  $L(p)$  for the main beam would be decreased by less than 6 db and in the latter case,  $L(p)$  would be increased by approximately 6 db. This can alter the conclusions only by increasing (or decreasing) the required elevation angle of the transmitter by at most  $2^{\circ}$ .

2. Consider next the case of interference from a point-to-point microwave relay transmitter to the earth-terminal receiver of a satellite system. It is assumed that a wide deviation FM system is used in the satellite to earth link, so that the earth terminal receiver has an RF bandwidth of 100 Mc/s. With the use of a low noise antenna and maser amplifier, we assume that the effective noise temperature of the receiver is reduced to 30 °K.

$$P_n = 10 \log T_e b - 228.6 = -134 \text{ dbw.}$$

Compute the transmission loss,  $L_{req}$ , assuming a transmitter power of 1 w, coupling losses of 4 db and a transmitted bandwidth of 20 Mc/s. Then

$$L_{req} = P_t - L_c - M - P_n = 137.$$

This value of  $L_{req}$  is compared with figure 2 to determine whether the requirement can be met. It is seen that under these assumptions the point-to-point antenna could not be directed toward the earth-terminal at a distance of 100 miles. As in the previous example the curves indicate that the requirements could be met by not allowing the 10-ft dish to be directed toward the earth terminal.

The effects of varying the transmitter antenna size and the transmitted power were noted in example 1. Similar statements can be made about varying the receiver antenna size and transmitted power in this example. Values of the power for typical point-to-point microwave relays range from -3 dbw to +7 dbw.

#### 4. Conclusions

Our theoretical analysis indicates that space communications systems and surface systems of the conventional microwave relay type can share the same frequencies if care is used in locating the possible interfering sources. As seen in the examples,

separation distances of from 100 miles to 150 miles usually suffice, and under ideal conditions, distances of less than 100 miles could give adequate protection. Estimates have been made for other systems such as high-powered radar and these indicate that harmful interference should not be experienced if the radar and earth terminals are separated by distances of 500 miles or more [JTAC, 1961].

The data shown in figure 3 represent samples during times when aircraft were not present in the propagation path, and although the data agree with the predicted values for the stated conditions, the estimates may not be accurate for some paths where aircraft are present.

The measurements reported here were made under the supervision of A. F. Barghausen.

#### 5. References

- Federal Communications Commission hearing, Allocation of frequencies in the bands above 890 Mc, F.C.C. Docket No. 11866 (undated).
- Hartman, W. J., and R. E. Wilkerson, Path antenna gain in an exponential atmosphere, *J. Research NBS 63D* (Radio Prop.), No. 3, 273-286 (Nov.-Dec. 1959).
- Hogg, D. C., Problems in low-noise reception of microwaves, *Trans. IRE, Fifth National Symposium on Space Electronics and Telemetry*, Part 8-2, pp 1-11 (Sept. 1960).
- Joint Technical Advisory Committee of IRE-EIA, a report on frequency allocations for space communications, F.C.C. Docket No. 13522 (March, 1961).
- Miller, C. R., D. C. Ports, and J. W. Savage, Receiver analysis for interference prediction purposes, *IRE International Convention Record*, Part 8 (1960).
- Norton, Kenneth A., System loss in radio wave propagation, *J. Research NBS 63D* (Radio Prop.), No. 1, 53-73 (July-Aug. 1959).
- Rice, P. L., A. G. Longley, and K. A. Norton, Prediction of the cumulative distribution with time of ground wave and tropospheric wave transmission loss, Part 1—The prediction formula, *NBS Tech. Note 15* (1959).

(Paper 65D5-148)

# VHF and UHF Signal Characteristics Observed on a Long Knife-Edge Diffraction Path

A. P. Barsis and R. S. Kirby

(Received April 6, 1961)

Contribution from Central Radio Propagation Laboratory, National Bureau of Standards, Boulder, Colo.

During 1959 and 1960 long-term transmission loss measurements were performed over a 223 kilometer path in Eastern Colorado using frequencies of 100 and 751 megacycles per second. This path intersects Pikes Peak which forms a knife-edge type obstacle visible from both terminals. The transmission loss measurements have been analyzed in terms of diurnal and seasonal variations in hourly medians and in instantaneous levels. As expected, results show that the long-term fading range is substantially less than expected for tropospheric scatter paths of comparable length. Transmission loss levels were in general agreement with predicted knife-edge diffraction propagation when allowance is made for rounding of the knife edge. A technique for estimating long-term fading ranges is presented and the results are in good agreement with observations. Short-term variations in some cases resemble the space-wave fadeouts commonly observed on within-the-horizon paths, although other phenomena may contribute to the fading. Since the foreground terrain was rough, there was no evidence of direct and ground-reflected lobe structure.

In most cases comparatively high correlation exists between signals received simultaneously on two antennas with 8.3 and 14 meters vertical separation. These separations were chosen as being representative for practical space diversity systems designed for eliminating the effects of fading arising from direct and ground-reflected phase interference phenomena. The comparatively high correlation observed suggests that space diversity will be relatively less successful in mountain obstacle paths with rough terrain near the terminals than on tropospheric scatter paths or on line-of-sight paths over smooth terrain.

The enhancement of field strength associated with propagation over mountain ridges may cause concern in applications where mountains are being counted on to shield unwanted radio waves. Some radio astronomy installations have been located in mountain valleys for this reason, and it is possible that obstacle-gain effects may aggravate rather than alleviate interference.

## 1. Introduction

It is generally known that mountain ridges can act as diffracting knife-edges in point-to-point communication circuits on VHF and UHF frequencies. The mathematical approach has been developed using the Fresnel-Kirchhoff diffraction theory [Schelleng, Burrows, and Ferrell, 1933]. Substantial reductions in transmission loss as compared to scatter circuits of similar length, and relatively fading-free signals were reported by several workers, both in this country and abroad [Dickson, Egl, Herbstreit, and Wickizer, 1953; Kirby, Dougherty, and McQuate, 1955; Kono and Hirai, 1955; Crysdale, Day, Cook, Psutka, and Robillard, 1957; Nishikori, Kurihara, Fukushima, and Ikeda, 1957; Hirai, Fujii and Saito, 1958]. More recently, additional work in Japan [Kakita, Iwai, and Ieiri, 1959], and so far unpublished data from Alaskan knife-edge diffraction paths<sup>1</sup> have shown that some paths exhibit considerable fading at carrier frequencies in the 900 Mc/s range. Much of the time the fading encountered resembles the "space-wave fadeout" phenomena observed commonly on within-the-horizon paths at comparable frequencies [Bean, 1954]. It consists of relatively deep and slow fades, and the occurrence of these fades may show marked

diurnal trends and correlation with meteorological phenomena as well as with simultaneous ducting on paths just beyond the horizon.

To obtain a better understanding of the long-term signal and fading characteristics, NBS established a test path in Colorado to study knife-edge type diffraction phenomena. This path extends in a roughly north-south direction along the Front Range of the Colorado Rockies, and uses Pikes Peak as the diffracting knife-edge. An outline map of the path with the locations of the terminals at Beulah and Table Mesa, Colo., is shown on figure 1. Pertinent path and equipment data are given in table 1, below. The path profile is shown on figure 2, based on an equivalent earth radius of 9,000 km. This is 1.41 times the actual earth's radius and corresponds to a surface refractivity of 316 N-units.

Operation on 751 Mc/s commenced in December 1959, and terminated in September 1960. Data were recorded continuously during 5-day periods at the rate of one each month with more frequent operation in June and August. Operation on 100 Mc/s started in August 1960, on the same basis. During two 5-day periods in August 1960, an additional site was operated on top of Pikes Peak, using horizontal half-wave dipole receiving antennas on both frequencies. These antennas were mounted about 6 m above ground. The length of this auxiliary line-of-sight path was 77 km.

<sup>1</sup> Private communication from Western Electric Co.

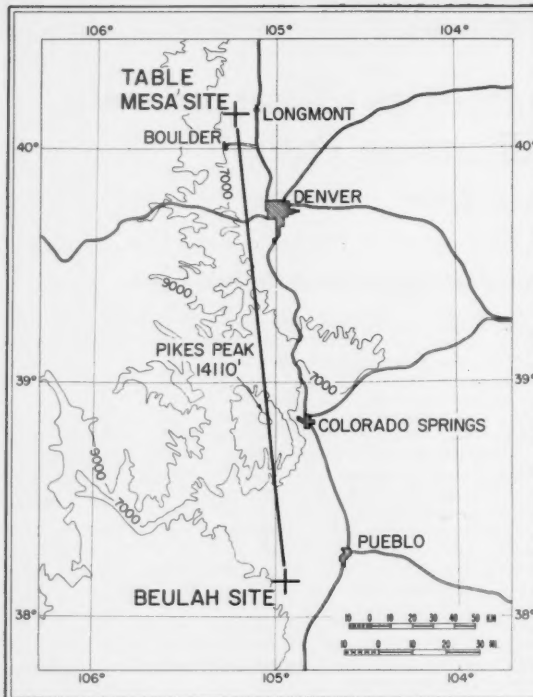


FIGURE 1. Outline map for Colorado obstacle gain path.

TABLE 1. Path and equipment data  
Pikes Peak obstacle gain path

Path distance.....	223 km.
Angular distance.....	64.4 milliradians.
Terminal elevations above mean sea level:	
Transmitter.....	(Beulah) 1905 m.
Receiver.....	(Table Mesa) 1666 m.
Height of obstruction above mean sea level:	
(Pikes Peak).....	4292 m.
Height of obstruction above mean terminal elevation.....	2507 m.
Antenna heights above ground:	
Transmitter.....	7.3 m for 751 Mc/s, 12.4 m for 100 Mc/s.
Receiver.....	8.2, 16.5 and 22.3 m for 751 Mc/s, 13.7 m for 100 Mc/s.
Polarization.....	Horizontal.
Antennas:	
Transmitting.....	751 Mc/s 4.3 m Dish
Receiving.....	100 Mc/s 3 m Dish Yagi
Modulation.....	continuous wave.

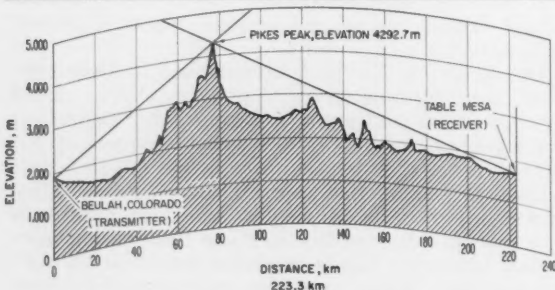


FIGURE 2. Terrain profile of Colorado obstacle gain propagation path.

The receiver outputs were recorded on strip charts and multichannel magnetic tape. Transmitter power output values were also recorded on strip charts, so that a continuous record of the transmitter power is available for both frequencies. The receivers were calibrated by signal generators checked against laboratory standards.

## 2. Characteristics of the Received Signal and Variation of Hourly Median Values

### 2.1. Signal Characteristics

Figure 3 shows sample recordings of both frequencies at the two sites taken on the morning of August 10, 1960. The 751 Mc/s record at the Table Mesa receiving site shows more rapid small signal variations superimposed on a much slower fading pattern, which includes a fade in excess of 15 db lasting several minutes. There appears to be substantial correlation between the signal recorded simultaneously on the two antennas on 751 mc/s. The slow fading pattern is absent on the Table Mesa 100 Mc/s record; only the more rapid variations are present, and they are superimposed on a virtually constant signal. It is believed that these rapid signal variations of small amplitude are due to a component of scattered field superimposed on the more slowly varying diffracted field. For the line-of-sight path with the terminal on the top of Pikes Peak this scattered component is not noticeable, as

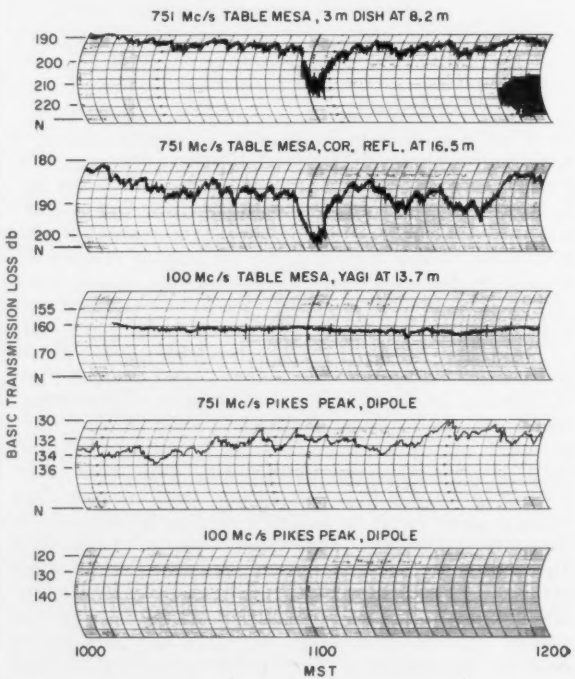


FIGURE 3. Simultaneous chart recordings for Colorado obstacle gain and line-of-sight propagation paths, August 10, 1960.

expected. However, the slower variations are still present on 751 Mc/s, and they do not appear correlated with the slow fading observed at the Table Mesa site.

The slow signal variations which are similar to the "space-wave fadeouts" commonly observed on line-of-sight paths will be discussed in more detail later on.

## 2.2. Variations of Hourly Medians

A typical sample of diurnal variations of hourly medians is shown on figure 4 for the period August 8 to 12, 1960, at the Table Mesa receiving site. Each open circle denotes an hourly median of basic transmission loss for the hour given by the abscissa. The distribution of the points and the median curve shows no pronounced diurnal trend. This is in contrast to (smooth earth) diffraction or scatter paths of similar length where usually a substantial diurnal trend of hourly median values is observed.

Similarly, the absence of a pronounced seasonal trend is shown by figure 5. Here, the median of all hourly medians recorded during each 5-day period is plotted versus time. The maximum variation is about 5 db. The overall medians obtained for the two antennas appear well correlated, and there seems

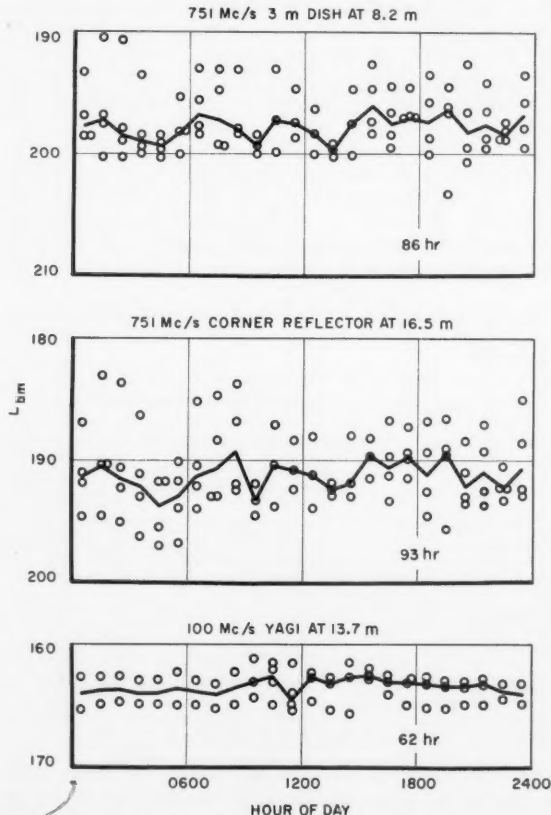


FIGURE 4. Diurnal variations of hourly median transmission loss levels for August 8-12, 1960.

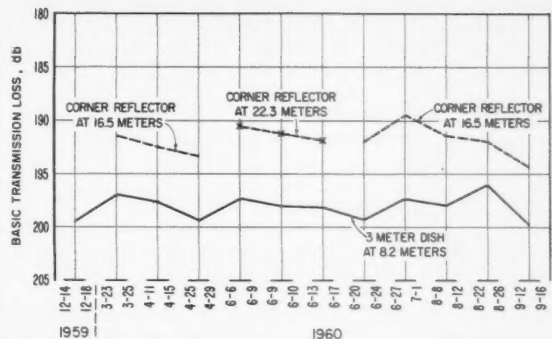


FIGURE 5. Seasonal trend of overall weekly medians, 751 Mc/s.

to be no significant difference between the results obtained at the two heights used for the corner reflector antenna. During the three recording periods in June when the corner reflector antenna was at the 22.3 m elevation, the overall medians follow the trend given by the rest of the data, when the 16.5 m height was used.

The 100 Mc/s data at Table Mesa and the Pikes Peak data were not included in this study, because they are only available for August and September—not enough to study seasonal trends.

It should be recognized that the time periods on figure 5 are consecutive as far as recorded data are concerned. Weeks with no recordings have been omitted.

Diurnal and seasonal variations may also be studied by obtaining distributions of hourly medians for eight time blocks as previously defined [Norton, Rice, and Vogler, 1955]. For this purpose, the hours of the day are divided into four blocks for summer as well as winter months, as follows:

TABLE 2. Time blocks

No.	Months	Hours
1	November to April	0600 to 1300
2	November to April	1300 to 1800
3	November to April	1800 to 2400
4	May to October	0600 to 1300
5	May to October	1300 to 1800
6	May to October	1800 to 2400
7	May to October	0000 to 0600
8	November to April	0000 to 0600

Cumulative distributions of the hourly basic transmission loss medians are calculated for each individual time block, or for combinations of time blocks, and plotted on log-normal graph paper. Thus it is possible to obtain an estimate of the range of observed hourly medians which is the long-term fading range. This will be compared with theoretical estimates, or with similar data obtained from other paths.

The cumulative distributions of all measured hourly median transmission loss values are shown on figure 6 separately for all time blocks, and for both 751 Mc/s antennas, with the corner reflector at the 16.5 m elevation. All curves are bunched

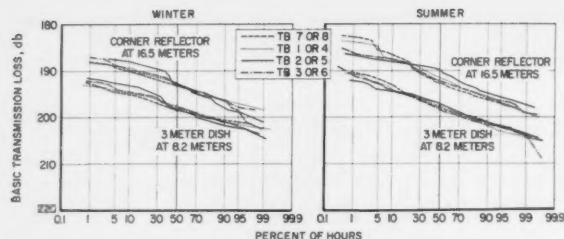


FIGURE 6. Distributions of hourly median basic transmission loss values for Colorado obstacle gain path on 751 Mc/s.

and nearly parallel, indicating very little diurnal or seasonal variation. Table 3, below, shows a comparison of the overall median values and the long-term fading range. Here the overall median is the median of all hourly medians within a time block, and the long-term fading range is defined as the difference between hourly median values exceeded 1 percent and 99 percent of all hours.

Even though the cumulative distributions of hourly medians plotted by time blocks on figure 6 appear quite similar, table 3 indicates some seasonal effect in the long-term fading range. The range is larger during summer, and is also larger for the corner reflector at the higher elevation than for the dish. There is very little variation in the overall median values between time blocks, and the difference between the dish and the corner reflector appears to be slightly higher in summer.

TABLE 3. Comparison of winter and summer results

Time block No.	Overall median decibels		Difference of overall medians db	Long-term fading range, decibels (1% to 99%)	
	3 m dish	Corner reflector		3 m dish	Corner reflector
<i>Winter:</i>					
8 (0000 to 0600)	198.4	193.2	5.2	8.9	14.8
1 (0600 to 1300)	197.6	192.6	5.0	8.9	10.5
2 (1300 to 1800)	198.3	192.8	5.5	12.4	14.0
3 (1800 to 2400)	197.9	192.7	5.2	11.5	11.6
<i>Summer:</i>					
7 (0000 to 0600)	198.1	192.7	5.4	13.5	16.2
4 (0600 to 1300)	197.6	191.4	6.2	13.8	14.4
5 (1300 to 1800)	197.3	189.9	7.4	11.4	10.7
6 (1800 to 2400)	198.5	192.3	6.2	13.0	12.9

### 2.3. Comparative Studies of Median Distributions

Although tropospheric scatter is not primarily involved in these experiments, it is of interest to compare first the measured distributions with theoretically expected values and with data from tropospheric scatter paths having similar path parameters. For this purpose, two hypothetical paths and the measured results obtained from two actual tropospheric scatter paths were used. The two hypothetical paths were considered to have the same antenna height as the actual path. One was assumed to have an angular distance which a tropospheric scatter path of the same length would have over a smooth earth, and the other would have a path length corresponding to a smooth earth path having the same angular

distance as the obstacle gain path. The actually measured paths were selected to correspond closely to these assumptions in path geometry and frequency. Table 4, below, shows the path constants used:

TABLE 4. Path constants for comparative study

	Path distance	Angular distance
	km	Milliradians
Hypothetical path A	223	24.0
Hypothetical path B	566	64.4
<i>Actual paths:</i>		
Pikes Peak obstacle gain (751 Mc/s)	223	64.4
Cheyenne Mt. to Garden City (1046 Mc/s)	364	26.7
Cheyenne Mt. to Anthony (1046 Mc/s)	633	59.8

Overall time block medians and the long-term fading ranges for the hypothetical paths were determined from a consideration of the expected long-term variation of hourly medians. These distributions are obtained from the empirical  $V(p, \theta)$  curves, which were determined from a large amount of experimental data representing a number of different geographical and climatic regions within the United States [Rice, Longley, and Norton, 1959]. The time block medians and long-term fading ranges given there are measured relative to a calculated reference value of basic transmission loss, which is the median of all hourly median values in time block 2 (winter afternoon). The curves are assumed to be valid for all frequencies in the 70 to 4000 Mc/s range.

A comparison of the long-term fading range determined in this manner for the hypothetical paths with the ones measured on the Pikes Peak obstacle gain path is shown as table 5 for all time blocks separately, for all hours during summer and winter, and for all hours of the year.

TABLE 5. Comparison of hypothetical tropospheric propagation paths data with measured data from Pikes Peak obstacle gain path

Time block	Long term fading range, db (1% to 99%)		
	Hypothetical path A, 223 km, $\theta=24$ milliradians	Hypothetical path B, 566 km, $\theta=64.4$ milliradians	Pikes Peak obstacle gain path, 223 km, $\theta=64.4$ milliradians (3 m dish)
8 (winter)	42.1	21.1	8.9
1	37.6	13.9	8.9
2	32.9	14.0	12.4
3	39.2	16.3	11.5
7 (summer)	42.2	21.4	13.5
4	37.7	28.1	13.8
5	25.1	18.2	11.4
6	36.5	19.0	13.0
All hours, winter	38.8	19.3	11.7
All hours, summer	41.9	26.0	13.4
All year	39.7	26.4	14.3

It is seen that the actually observed long-term fading ranges were considerably smaller than the ones predicted on the basis of scatter propagation, although the fading predicted for a scatter path

having the same angular distance is a somewhat better estimate.

In order to provide a more valid basis for estimating long-term fading ranges and the distribution of hourly medians for knife-edge diffraction paths, use is made of a method suggested by K. A. Norton. The results of this method as applied to the Pikes Peak obstacle gain path will be compared with the actual measurements in what follows.

For the purpose of studying variations in hourly median field strength or transmission loss values a knife-edge diffraction path is considered to consist of two line-of-sight paths in tandem. The diffracting knife-edge constitutes a common terminal for the two paths. If the hourly median signal for each of the two line-of-sight paths is subject to random variations,  $V_1$  and  $V_2$ , then the random variation  $V$  expected on the mountain obstacle path would be  $V = V_1 + V_2$ , where  $V$ ,  $V_1$ , and  $V_2$ ,

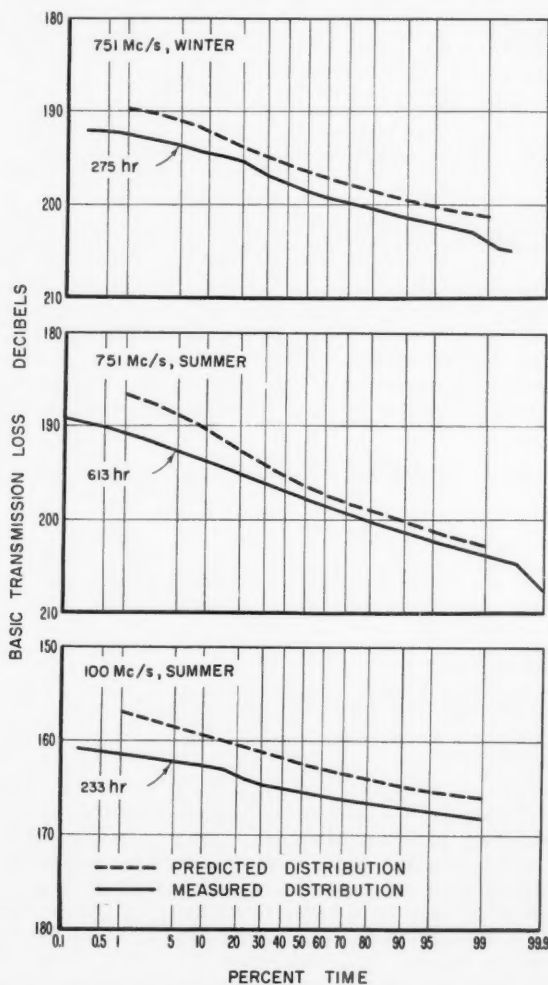


FIGURE 7. Predicted and measured cumulative distributions of basic transmission loss hourly medians, December 1959 to September 1960.

are random variables expressed in decibels. The resulting cumulative distribution of hourly medians for the entire path may be determined by the convolution of the distributions of  $V_1$  and  $V_2$  [Davenport and Root, 1958].

The cumulative distributions of hourly medians for the two individual line-of-sight paths may be calculated by empirical formulas as functions of the path distance, the effective antenna heights, the carrier frequency, the horizon elevation angles, and season, summer or winter. The methods used are unpublished empirical methods communicated to the authors by P. L. Rice. This material will be described in detail in forthcoming NBS Technical Notes and in a U.S. Air Force Technical Order dealing with design procedures for tropospheric communication circuits. Results are shown on figure 7, where the empirical distributions are compared with the actually measured distributions. Comparison is made for the data on 751 Mc/s obtained using the 3-m dish separately for all hours during the summer and during the winter months, and for the 100 Mc/s data for the summer months.

Calculation of the empirical distributions of hourly medians shown on figure 7 includes determination of the overall median reference value by Fresnel diffraction and ray optics methods which will be discussed in more detail in section 3 below. What is primarily important here is the comparison of the slopes of the actually measured and the empirically predicted distribution curve shown on figure 7, rather than their absolute position on the basic transmission loss scale.

The comparison of measured and predicted fading ranges from figure 7 is summarized in table 6 below.

TABLE 6. Comparison of actually measured fading ranges with empirical predictions for Pikes Peak obstacle gain path

	Long-term fading range, in decibels (1% to 99%)	
	Actually measured	Empirical prediction
751 Mc/s:		
All hours, winter.....	11.7	11.5
All hours, summer.....	13.4	16.2
100 Mc/s:		
All hours, summer.....	7.0	9.0

Table 6 shows that the empirical method just described provides much better estimates of the long-term fading range than the assumption of a tropospheric scatter path of the same linear or angular distance. This conclusion applies to this specific knife-edge diffraction path, and should be tested against data obtained from other knife-edge paths in order to arrive at an estimate of the uncertainty inherent in the prediction process. However, agreement of the predicted 1 to 99 percent long-term fading ranges is well within the sampling error of the empirical data on which this prediction is based and this suggests that the proposed method of predicting long-term fading ranges is a reliable one.

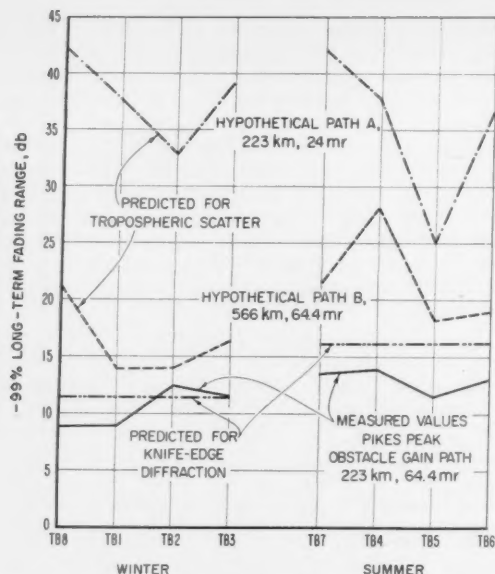


FIGURE 8. Comparison of predicted and measured diurnal and seasonal variations of the long-term fading range.

The data in tables 5 and 6 have been plotted on figure 8 to obtain a better picture of the comparison between predicted and measured long-term fading ranges and their diurnal trends. As the empirical prediction method just mentioned does not distinguish between individual time blocks, it is represented by a straight line for all summer and winter time blocks, respectively. In spite of the large discrepancy between the measured fading ranges and the ones predicted on the basis of scatter propagation, it is of interest to note that the predicted diurnal trend is evident in the measured data for the summer time blocks, although to a considerably lesser degree. This is not the case for the winter time blocks due to the relatively large measured Time Block 2 long-term fading range.

An additional comparison of the measurement results was made with similar data obtained from two actually measured tropospheric propagation paths which represent a geographical location similar to the Pikes Peak obstacle gain path. In addition thereto, these paths correspond most closely to the hypothetical paths described above in path distance and angular distance, and at the same time, represent a similar carrier frequency. The hourly median distributions for these two paths were taken from unpublished reports. A description of the paths and the various experiments conducted have been published by NBS [Barsis, Herbstreit, and Hornberg, 1955].

Figure 9 compares the distribution of hourly medians measured during the summer months over the Pikes Peak obstacle gain path, with the two paths between Cheyenne Mountain and points in the eastern plains. It is seen that the long-term fading range is smallest for the obstacle gain path;

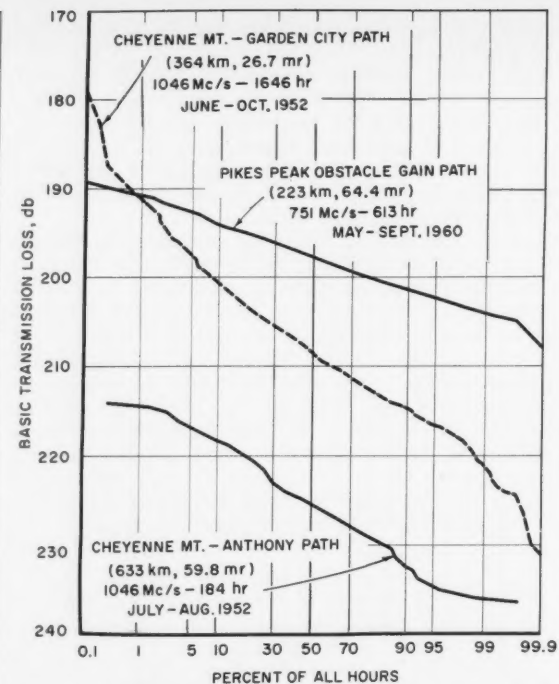


FIGURE 9. Cumulative distributions of hourly median basic transmission loss values for Colorado-Kansas propagation paths.

it is quite large for the Garden City path which represents the same linear path distance, and slightly larger for the Anthony path which represents the same angular distance, but a substantially greater linear path distance. Table 7 shows the comparison of overall median values and ranges taken from figure 9.

TABLE 7. Comparison of long tropospheric propagation path results

Path	Frequency Mc/s	Time period	No. of hours	Basic transm. loss overall median db	Long-term fading range, db (1% to 99%)
Pikes Peak obstacle gain.	751	Summer 1960	613	198.7	13.4
Cheyenne Mt. Garden City.	1046	Summer 1952	1646	208.9	30.5
Cheyenne Mt. Anthony.	1046	Summer 1952 (July to August)	184	225.5	21.5

The overall medians have been added for completeness of the information. It is quite clear that transmission loss tends to be smaller for a knife-edge diffraction path as compared to tropospheric scatter paths of similar length. Perhaps even more significant is the substantial reduction in the long-term fading range. Although there are fewer hours of measurements available for the Cheyenne Mountain-Anthony path, table 6 shows that a tropospheric scatter path of comparable linear distance has a

substantially greater long-term fading range than an obstacle gain path, whereas a scatter path of similar *angular* distance has only a moderately greater long-term fading range. This agrees well with the results obtained by the application of empirical methods for determining fading range—the method based on scatter propagation paths yielding substantially greater fading ranges than the method based on line-of-sight paths.

#### 2.4. Frequency Dependence of the Distributions of Hourly Medians

Figure 10 shows a comparison of all measured data on 100 Mc/s and 751 Mc/s during the two weekly periods when the receiver site on Pikes Peak was operated. These are overall summer-time distributions; they have not been separated into time blocks because of the comparatively few hours available. As expected, the long-term fading range is smaller for the line-of-sight path to the top of the

peak than for the obstacle gain path. Overall median and ranges for this period are given in table 8 below.

TABLE 8. Data from distributions of hourly medians

Path and frequency	Basic transmission loss overall Median, db	Long-term fading range, db (1% to 99%)
Beulah-Pikes Peak, 100 Mc/s	128.2	5.7
Beulah-Pikes Peak, 751 Mc/s	132.0	6.3
Beulah-Table Mesa, 100 Mc/s	165.3	7.0
Beulah-Table Mesa, 751 Mc/s (dish)	197.0	13.0
Beulah-Table Mesa, 751 Mc/s (corner)	191.6	14.7

This tabulation shows a substantial frequency dependence of the fading range for the obstacle gain path—more than doubled when comparing 100 Mc/s with either one of the 751 Mc/s antennas. There is not nearly that much frequency dependence on the line-of-sight path. It has already been shown that the  $V(p, \theta)$  distributions are not appropriate for use in predicting the performance of knife-edge diffraction paths, and that much better agreement is obtained by the use of a different empirical method taking into account carrier frequency and horizon elevation angles.

#### 3. Height Gain Studies

Previous measurements made of obstacle diffraction over Pikes Peak [Kirby, Dougherty, and McQuate, 1955] showed marked agreement between the predicted and observed variation of transmission loss with height. These measurements were made using a shorter path and with a relatively smooth terrain area in the immediate foreground of the antenna whose height was varied.

The 751 Mc/s equipment installed on Table Mesa permitted the collection of similar data for antenna heights up to 100 ft using a telescopic tower with dual receivers and recorders. However, the Table Mesa site differs from the receiving site previously used in that the terrain is very rough except for a small flat area immediately in front of the receiver site, which is only large enough for approximately one-third of the first Fresnel-zone ellipse. It has been previously shown that the cumulative distributions of hourly basic transmission loss medians for the two antenna heights on 751 Mc/s have approximately the same dispersion and the medians are separated by approximately 5 db in winter, and up to 7.4 db in summer. Using a small stored-program electronic computer the height distribution of field strength or basic transmission loss was calculated by methods of geometrical optics using the vector sum of four rays [Dickson, Egli, Herbstreit, and Wickizer, 1953; Crysdale, Day, Cook, Psutka, and Robillard, 1957]. Each of the rays has a magnitude and phase value determined by reflections from the ground and diffraction by the knife-edge type obstacle. The reflecting planes were assumed to be parallel to a smooth earth's surface, and to pass through the bases of the antenna towers. Reflection

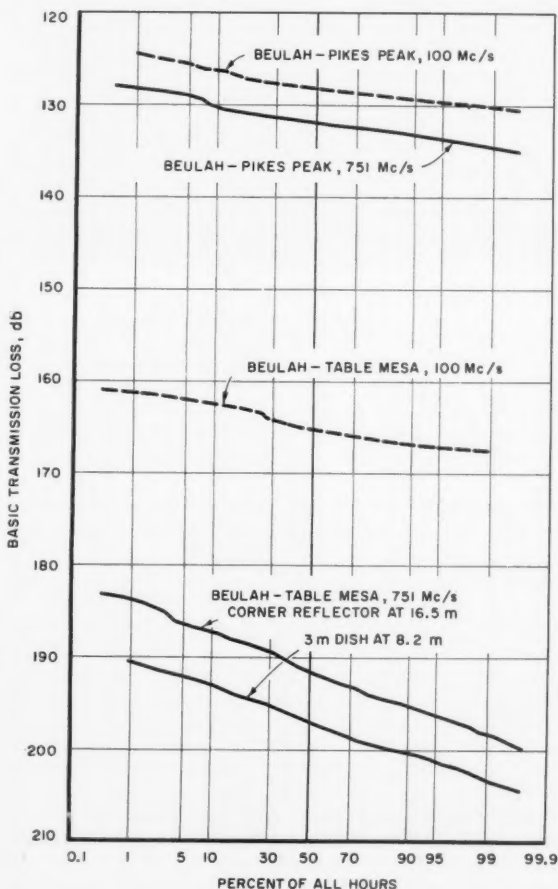


FIGURE 10. Measured distributions of hourly median basic transmission loss values for August 8-12 and 22-26, 1960.

coefficients of 0.5 and 0.9 were assumed, with a phase shift of  $180^\circ$  occurring at the reflecting planes. The attenuation and phase-shift at the obstacle were calculated using the asymptotic expansions for Fresnel integrals [Schelleng, Burrows, and Ferrell, 1933]. This was justified due to the magnitude of the parameters involved. For all calculations a refractivity value  $N_s = 290$  was assumed, which corresponds to average winter afternoon for the geographical region where the measurements were made. Changes in the  $N_s$  value within the range 240 to 320  $N$ -units did not materially affect the relative height dependence of basic transmission loss.

A height-gain run was performed in the morning hours of March 25, 1960. For each position of the corner reflector antenna (mounted on the telescopic tower) the basic transmission loss was determined for both receiving antennas, so that the values measured could be corrected for changes recorded on the fixed antennas. The results are plotted versus receiving antenna height on the subsequent figures in order to permit comparison with calculated values using various parameters.

Figure 11 shows the comparison of the measured height dependence with calculated values, using reflection coefficients of 0.9 and 0.5. There is no agreement in the magnitude of the transmission loss or in the number of lobes. The measured data show only one lobe with a maximum at approximately 21 m above ground, whereas the theoretical calculations predict 4 to 5 lobes within the height interval measured. A change in the reflection coefficient only changes the magnitude of the maxima and minima. Similarly, any change in the assumed

elevation of the transmitting antenna has little or no effect upon the position and number of lobes at the receiver, but can modify the transmission loss approximately the same amount at all heights. Height-gain experiments using the transmitting antenna were not performed.

Studies were also made assuming the cross section along the profile of the refracting knife-edge to be rounded. The terrain profile cross section through the top of Pikes Peak can be approximated by a circular arc with a radius of roughly 11.5 km. Following, in general, the rounded knife-edge procedure [Wait and Conda, 1959], the resultant diffracted field as a function of receiving antenna height was calculated again as the vector sum of four rays, each of which is affected by the rounded obstacle and by reflections from the terrain in the foreground of the antennas. These results are shown on figure 12, together with the measured height-gain run and the theoretical curve for the ideal knife-edge. Both theoretical curves are based on a reflection coefficient of 0.9. It is seen that only the absolute values of transmission loss are affected by "rounding" the knife-edge; the number and position of the lobes with antenna height remains the same. Additional calculations show that the change in transmission loss depends on the radius of curvature assumed; as this is somewhat arbitrary for this terrain configuration, the assumption of 11.5 km depends on how much of the profile the arc is fitted to.

Figure 11 shows that the long-term median values of transmission loss observed on the dish at 8.2 m and the corner reflector at 16.5 m have approximately the same difference as is indicated by the

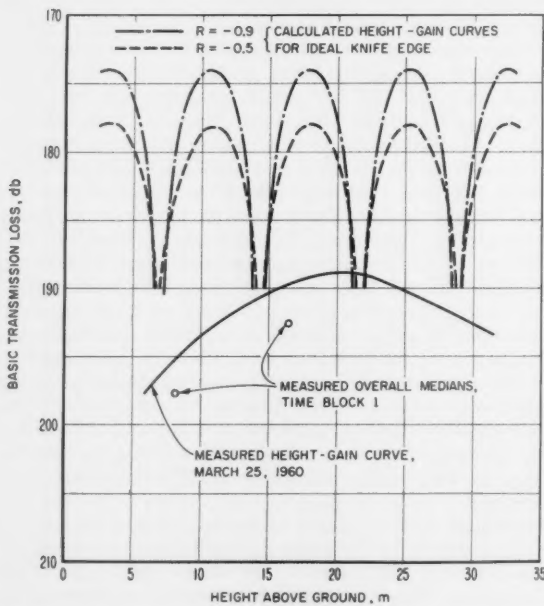


FIGURE 11. Comparison of calculated and measured height-gain curves for Colorado obstacle gain path.

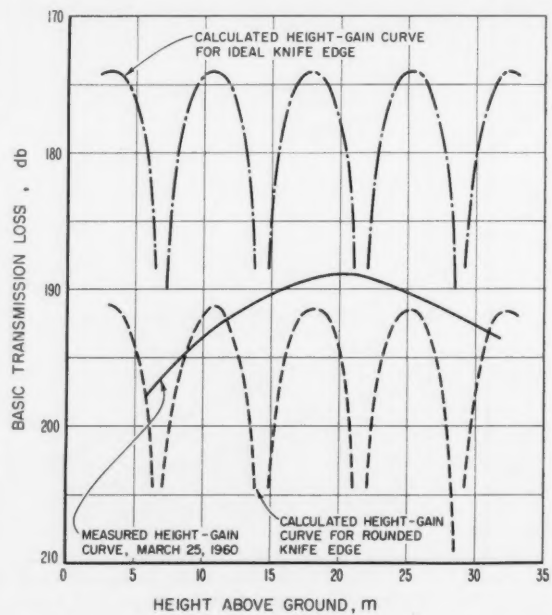


FIGURE 12. Comparison of calculated and measured height-gain curves for Colorado obstacle gain path.



FIGURE 13. Transverse profile through Pikes Peak as seen from transmitter site.

measured height gain curve. For the two different heights used for the higher antenna (corner reflector at 16.5 and 22.3 m) there is little difference in the values of transmission loss observed. This tends to confirm the similarity of long-term transmission loss values observed at the two heights as shown in figure 5.

It is quite clear from the above discussion that the basic transmission loss dependence on antenna height cannot be represented in this case by the simple four-ray knife-edge model, even if the knife-edge is assumed to be rounded. The reason becomes evident if the transverse profile through the obstacle is studied, which is a terrain profile drawn through the obstacle at right angles to the propagation path. Figure 13 is a photograph of the visual horizon as seen from the transmitting antenna with various visible ridge lines emphasized. A grid is superimposed which shows the angles subtended from the transmitting site. It is seen that the transmitting antenna beam, with a  $7.7^\circ$  half-power beam width sees a substantial portion of the ridge line on either side of the principal obstacle. Similar conditions exist if the transverse profile is viewed from the receiving terminal. Thus field contributions may exist from the ridges and other terrain features between the terminals and Pikes Peak

illuminated by the antenna beams. It has so far not been possible to make a quantitative study of these contributions in order to use them for field computations. The effect of a transverse triangular mountain profile was studied by Matsuo in [1950]. Numerical results for a specific example were given but no comparison was made with actual measured results.

#### 4. Vertical Space Diversity and Fading Characteristics

A detailed study of the short-term fading characteristics observed on this path is contained in another paper [Barsis and Johnson, 1961]. A number of possible mechanisms appear responsible for the fading. These include those associated with prolonged space-wave fadeouts, which resemble phenomena observed on within-the-horizon paths, as well as those associated with scattering components. Other mechanisms appear to be due to the terrain configuration and may be the cause of an intermediate type of fading, characterized by fadeouts on the order of 5 db which last less than a few minutes.

In view of the apparent positive correlation between the 751 Mc/s signals recorded simulta-

neously on the two receiving antennas, studies were performed to determine the correlation coefficient between instantaneous envelope values for various sample periods. For this purpose, the transmission loss information recorded on magnetic tape was digitized and fed into a computer program. The tape contained adequate timing signals to insure proper evaluation without time lag. Table 9, below, contains the time and duration of each sample, the separation of the receiving antennas, and the resulting correlation coefficient. For purpose of digitizing, the magnetic tape was sampled once per second. The correlation coefficients listed apply to basic transmission loss in decibels; a check revealed that results were not materially different if receiver input voltages (proportional to field strength) were correlated.

TABLE 9. Results of envelope correlation studies for Pikes Peak obstacle gain path

Date and time of sample (1960)	Length	Antenna spacing	Correlation coefficient
June 13, 1745 to 1800	15	14.1	0.491
June 13, 2120 to 2125	5	14.1	.503
June 13, 2200 to 2220	20	14.1	.625
June 14, 1010 to 1020	20	14.1	.204
June 15, 0738 to 0748	10	14.1	.242
June 15, 1200 to 1210	10	14.1	.033
June 15, 1800 to 1805	5	14.1	.537
June 15, 0350 to 0400	10	14.1	.656
September 15, 1700 to 1710	10	8.3	.555
September 15, 1920 to 1930	10	8.3	.677
September 15, 2126 to 2146	20	8.3	.685
September 16, 0255 to 0305	10	8.3	.331
September 16, 1015 to 1025	10	8.3	.780
September 16, 1120 to 1130	10	8.3	.450

The samples were picked to represent different types of the signal as it appeared on the visual recording charts for the two antennas. They are not to be considered taken at random in a statistical sense; therefore they serve only to illustrate the phenomenon, and cannot be used to establish a time or spacing dependence, or similar results. They show, however, that moderately high correlation exists between simultaneous envelope values of the signal received on vertically spaced antennas, and that the correlation coefficient seems to be higher at nighttime and for closer spaced antennas, and that these results make the effectiveness of vertical space diversity questionable for a path of this type. A more complete analysis using many more samples evenly distributed over the recording period would be necessary to draw final conclusions on the diurnal variation and other characteristics of the correlation coefficient.

A visual representation of the instantaneous envelope correlation may be obtained by applying the tape-recorded signals to an *x-y* plotter. Figure 14 shows two such samples, and a good qualitative idea of the magnitude of the correlation coefficient may be obtained thereby.

Figure 15 shows examples of the correlation coefficient between hourly median values of basic transmission loss. In general, hourly medians tend to be more highly correlated than instantaneous

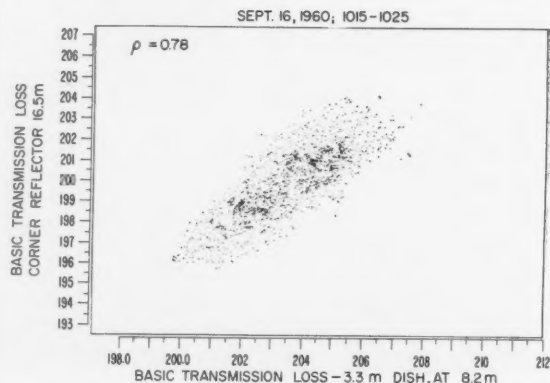
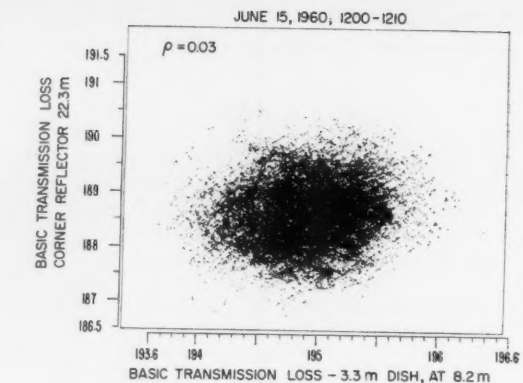


FIGURE 14. Instantaneous envelope correlation for Colorado obstacle gain path on 751 Mc/s.

values. The two graphs shown represent the two antenna separations used. The correlation coefficient is substantially higher for the closer spaced antennas (8.3 m). It cannot be determined, however, if this is entirely due to the spacing, as the two samples were taken at different times. The graphs indicate the antenna spacing, the number of hours, the standard deviations of hourly medians for each antenna, and the correlation coefficient. Hourly medians determined with the 3 m dish are plotted along the *y*-axis, whereas the corner reflector data are plotted along the *x*-axis.

Finally, a new analysis of fade durations and signal distributions is shown on figure 16. Four periods of record ranging from 6 hr to more than 200 hr each were analyzed to determine the distribution of fades as well as high signal of various levels and duration periods. Each curve shown corresponds to one of these levels, and the points plotted are the percentages of the total time the signal remained either above or below the indicated level for the duration given by the ordinate. The median is the dividing line; for each graph curves to the left of the median represent fades, and the ones to the right represent periods of signal higher than the median. The asymptotic extensions of the curves toward a zero

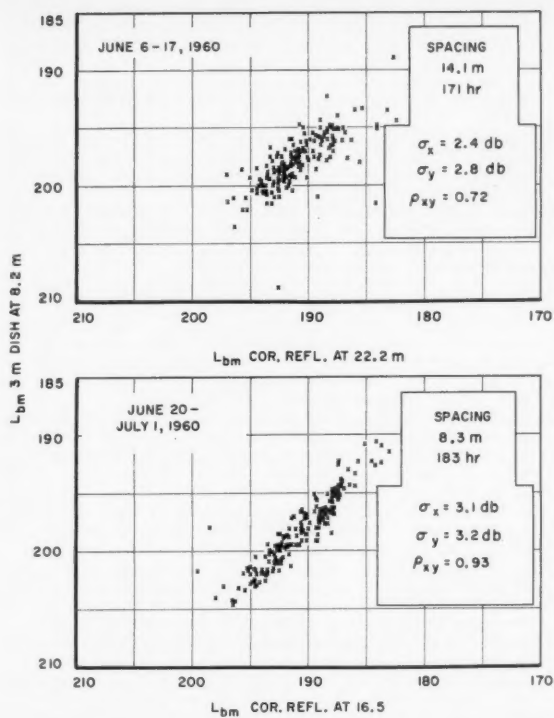


FIGURE 15. Correlation of hourly medians for vertically spaced antennas at 751 Mc/s.

fade or signal duration become the distribution of instantaneous signal levels for each period in the limit. As an example, in the upper right hand graph (period August 8 to 12), the curve labelled "202" indicates the distribution of durations when the basic transmission loss exceeded 202 db: 1 percent of all "fades" to 202 db was of at least 8 min duration.

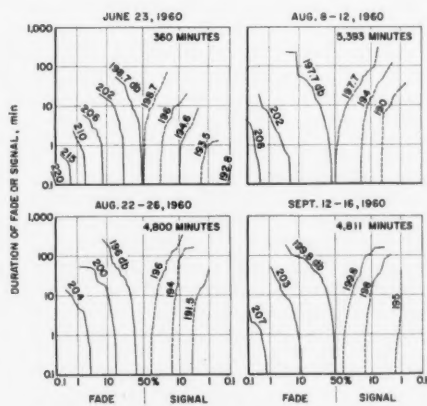


FIGURE 16. 751 Mc/s fading characteristics observed on 3 meter dish.

This type of representation permits an analysis of fades or short-term variations in terms of basic transmission loss levels, which may be easily related to any arbitrary reference, like the overall median of the period considered. This type of presentation can be used to determine, at least statistically, the characteristics of individual fades. For example it might be of interest to know how many fades occurred whose duration was between 1 and 2 min. The difference between the percentage of the total time the signal fell below the specified level for durations of 1 and 2 min respectively can be read from this type of presentation. From this information the number of fades within this range of duration can easily be determined for the entire period of the analysis.

## 5. Conclusions

The analysis of 751 Mc/s data from a long obstacle gain path showed principally that the distribution of hourly medians of field strength or basic transmission loss may be approximated by the convolution of cumulative distributions for two line-of-sight paths in tandem which have the obstacle as a common terminal. As expected, these long-term fading characteristics are quite different from the ones observed for tropospheric scatter propagation over comparable distances. No significant diurnal variation in propagation characteristics was observed on the obstacle-gain path, and the indication is that seasonal variations are small. Due to the limited width of the obstacle, the knife-edge approximation by a semi-infinite plane, or half-cylinder may not be entirely appropriate, although a somewhat arbitrary assumption of curvature leads to theoretical values of transmission loss equivalent to observed values.

Correlation studies of the signal received on vertically spaced antennas suggest that space diversity may not be very effective on circuits utilizing obstacle gain. Transmission loss recordings show slow and deep fades occurring simultaneously on antennas vertically separated by 14.1 and 8.8 m. Correlation was somewhat lower for the greater spacing.

It is hoped that additional diversity experiments can be performed using this path with the antennas spaced horizontally in line with and normal to the path profile.

The outstanding advantages of obstacle gain paths of this type are that the signal level is significantly higher than expected for scatter paths of comparable length, and the amplitude of rapid Raleigh-fading components is substantially reduced. However, the received field strength is lower than values calculated using the idealized knife-edge theory. This is probably due to the profile through the obstacle, which represents a rounded knife-edge, and to reflections and contributions from other terrain features.

These and similar measurements show that relatively high signal strengths are consistently observed behind mountain ridges. Thus it is unlikely that mountain ranges can always be relied upon to shield

potential interference. Special consideration to these phenomena should be given in locating radio astronomy or space communication terminals.

The authors thank all the personnel of the Propagation-Terrain Effects Section who contributed to the installation and operation of the equipment, and the collection and the analysis of the data, and Messrs. K. A. Norton and G. W. Haydon for their review and suggestions. Transmission loss calculations for a "rounded" knife-edge were performed by Messrs. H. T. Dougherty and L. J. Maloney. Drafting work was performed by J. C. Harman and his group, and the manuscript was typed by Mrs. D. J. Hunt.

## 6. References

Barsis, A. P., J. W. Herbstreit, and K. O. Hornberg, Cheyenne Mountain tropospheric propagation experiments, NBS Cir. 554 (Jan. 1955).  
Barsis, A. P., and M. E. Johnson, Prolonged space-wave fadeouts in tropospheric propagation, NBS Tech. Note No. 88 (Feb. 1961).  
Bean, B. R., Prolonged space-wave fadeouts at 1046 Mc/s observed in Cheyenne Mountain propagation program, Proc. IRE 42, 848-853 (May 1954).  
Crysdale, J. M., J. W. B. Day, W. S. Cook, M. E. Psutka, and P. E. Robillard, An experimental investigation of the diffraction of electromagnetic waves by a dominating ridge, IRE Trans. on Antennas and Propagation AP-6, 203-210 (Apr. 1957). See also subsequent discussion by Crysdale in AP-6, 293-295 (July 1958).  
Davenport, W. B. Jr., and W. L. Root, An introduction to the theory of random signals and noise, Chap. 3, 35-37, (McGraw-Hill Book Co., Inc., New York, N.Y., 1958).

Dickson, F. H., J. J. Egli, J. W. Herbstreit, and G. S. Wickizer, Large reductions of VHF transmission loss and fading by the presence of a mountain obstacle in beyond-line-of-sight paths, Proc. IRE 41, 967-969 (Aug. 1953). See also subsequent correspondence by Crysdale, and rebuttal by Dickson, et al, in Proc. IRE 43, 627-628 (May 1955).

Hirai, M., Y. Fujii, and H. Saito, An experimental investigation of the diffraction at VHF and UHF by mountain ridges, Journal of the Radio Research Lab. (Japan) 5, 189-211 (July 1958).

Kakita, K., F. Iwai, and S. Ieiri, Radio transmission beyond-line-of-sight between Kyushu and Anami-Oshima Island, Elec. Commun. Lab. Journal, N.T.T. (Japan) 8, 1183-1213 (1959).

Kirby, R. S., H. T. Dougherty, and P. L. McQuate, Obstacle gain measurements over Pikes Peak at 60 to 1046 Mc/s, Proc. IRE 43, 1467-1472 (Oct. 1955). This paper contains an extensive list of references to previous work.

Kono, T., and M. Hirai, Use of diffraction effect of mountains for VHF radio communication, Journal of the Radio Research Lab. (Japan) 2, 293-309 (July 1955).

Matsuo, Saburo, The method of calculating V.H.F. field intensity and research on its variation, Report 621.39.001 G(047.3), The Electrical Communication Laboratory, Ministry of Telecommunications, Tokyo, Japan (Aug. 1950).

Nishikori, K., Y. Kurihara, M. Fukushima, and M. Ikeda, Broad and narrow beam investigations of SHF diffraction by mountain ridges, Journal of the Radio Research Lab. (Japan) 4, 407-422 (Oct. 1957).

Norton, K. A., P. L. Rice, and L. E. Vogler, The use of angular distance in estimating transmission loss and fading range for propagation through a turbulent atmosphere over irregular terrain, Proc. IRE 43, 1488-1526 (Oct. 1955).

Rice, P. L., A. G. Longley, and K. A. Norton, Prediction of the cumulative distribution with time of ground wave and tropospheric wave transmission loss; Part I-The prediction formula, NBS Tech. Note No. 15 (July 1959).

Schelleng, J. C., C. R. Burrows and E. B. Ferrell, Ultra short-wave propagation, Proc. IRE 21, 427-463 (Mar. 1933).

Wait, J. R., and A. M. Conda, Diffraction of electromagnetic waves by smooth obstacles for grazing angles, J. Research NBS 63D (Radio Prop.), No. 5, 181-197 (Sep.-Oct. 1959).

(Paper 65D5-149)

# Experimental Study of Inverted L-, T-, and Related Transmission-Line Antennas<sup>1</sup>

Sheila Prasad and Ronold W. P. King

Contribution from Gordon McKay Laboratory, Harvard University, Cambridge, Mass.

(Received December 12, 1960; revised January 9, 1961)

An experimental study is made of inverted L-, T-, and related transmission-line antennas and of antennas with two-, three-, and four-element top loads. The apparent measured impedance is corrected for end effects; the approximate theoretical impedances are calculated for very small heights for which measured values cannot be obtained readily. The transmission-line antennas studied are shunt-driven with one open and one closed end or with two closed ends.

## 1. Introduction

The inverted L-antenna and T-antenna, both well known in radio broadcasting, have recently found application in telemetry for missiles. Moreover, a variety of structures that are useful as missile antennas may be analyzed by an appropriate superposition of different inverted L- or T-antennas with images. Theories of the inverted L-antenna and T-antenna with images have been developed by Harrison [1958b; 1958d], and by King and Harrison [1959a; 1959b]; they have been extended to related circuits by Harrison [1958a; 1958c]. Special forms of these structures with low silhouette so that they may be useful as externally carried missile antennas have been studied by King, Harrison, and Denton [1958] in terms of an equivalent shunt-driven transmission line that is terminated at each end in a reactor of arbitrary value.

In order to supplement the extensive theoretical work, an experimental study has been made of the impedances of antennas of these types including especially structures with low silhouette. Antennas with multi-element top loads have also been investigated. The series of measurements was begun with a half dipole over a conducting plane. Antennas with low silhouette were approached by successively folding over larger and larger sections parallel to the ground plane, while the overall length was kept constant.

The driving-point impedances of the antennas were measured with a slotted coaxial line as shown in figure 1 for the inverted L-antenna; the ground screen was of aluminum approximately 10 by 12 feet in size. A 300 Mc/s signal with modulation at 1000 c/s was used. The detecting system included a movable voltage probe and a superheterodyne receiver.

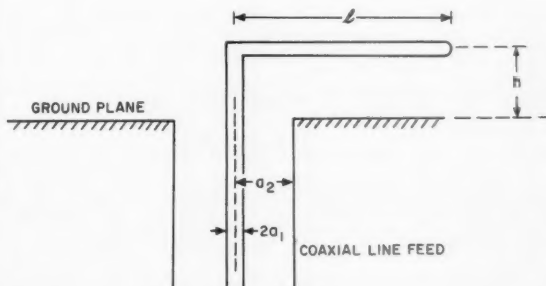


FIGURE 1. Inverted L-antenna.

## 2. Theory of Measurement

The theory of measurement summarized here applies to all of the experimental work described in this paper.

### 2.1. Distribution Curve Method for Determining Apparent Terminal Impedance

The part of the voltage distribution curve near a minimum was plotted and used to locate the minimum accurately. The complex terminal function  $\theta_{sa} = \rho_{sa} + j\Phi_{sa}$  of the load  $Z_{sa}$  is defined [King, 1955, p. 102, eq. 1] as follows:

$$\theta_{sa} = \coth^{-1}(Z_{sa}/Z_c) \quad (1)$$

where  $Z_c$  is the characteristic impedance. The phase function  $\Phi_{sa}$  is determined experimentally from the relation

$$\Phi_{sa} = 2\pi d/\lambda + \pi/2 \quad (2)$$

where  $d$  is the distance between the location of the minimum with a short circuit terminating the coaxial line ( $Z_{sa}=0$ ) and the location of the minimum

<sup>1</sup> This research was supported in part by the Sandia Corporation, Albuquerque, N. Mex., and the Office of Naval Research, under Contract Nonr 1866(26).

This paper first appeared in a more detailed version as a Sandia Corporation Technical Memorandum SCTM 82-60 (14) March 30, 1960.

with the actual load  $Z_{sa}$  terminating the line. The attenuation function  $\rho_{sa}$  is obtained from

$$\sinh^2 \rho_{sa} = \frac{\sin^2(\beta W_2/2) - \frac{p_2^2}{p_1^2} \sin^2(\beta W_1/2)}{\frac{p_2^2}{p_1^2} - 1} \quad (3)$$

where  $W_1$  and  $W_2$  are the widths of the distribution curve minima at the power levels  $p_1^2$  and  $p_2^2$  [King, 1952]. With a square-law detecting system, the power levels  $p_1^2$  and  $p_2^2$  could be read directly on a Ballantine voltmeter. Since  $\rho_{sa}$  is small in all cases, the approximation  $\sinh^2 \rho_{sa} \approx \rho_{sa}$  is valid. From the experimentally determined values of  $\rho_{sa}$  and  $\Phi_{sa}$ , the apparent admittance  $Y_{sa} = G_{sa} + jB_{sa}$  may be calculated with the following formulas [King, 1955, p. 102, eq. 12]:

$$g_{sa} = \frac{\sinh 2\rho_{sa}}{\cosh 2\rho_{sa} + \cos 2\Phi_{sa}} \quad (4)$$

$$b_{sa} = \frac{\sin 2\Phi_{sa}}{\cosh 2\rho_{sa} + \cos 2\Phi_{sa}} \quad (5)$$

where the normalized admittance is

$$y_{sa} = Y_{sa} Z_c = g_{sa} + j b_{sa}.$$

The apparent impedance of the load is  $Z_{sa} = 1/Y_{sa}$ .  $Z_c$  is the characteristic impedance of the coaxial line; its numerical value is  $Z_c = 60.06$  ohms.

## 2.2. End Correction for the Coaxial Line Driving the Antenna Over a Ground Plane

When an antenna is driven over a ground plane by a coaxial line, it is necessary to apply an end correction [King, 1955, p. 430] in order to obtain the theoretical impedance  $Z_0$  from the measured apparent impedance  $Z_{sa}$  terminating the line. This correction consists of a capacitance  $C_{Tc}$  in parallel with  $Z_0 = 1/Y_0$  so that

$$Y_{sa} = Y_0 + j\omega C_{Tc}. \quad (6)$$

A curve of  $C_{Tc}/c_0 a_2$  as a function of  $a_2/a_1$  is given by King [1955, p. 435, fig. 22.4];  $a_2$  and  $a_1$  are the radii of the outer and inner conductors of the coaxial line. For  $a_2/a_1 = 2.762$ ,  $C_{Tc}/c_0 a_2 = -0.25$  or  $C_{Tc} = -0.242 \times 10^{-12}$  farad. It follows from (6) that

$$\begin{aligned} Y_0 &= y_{sa} R_c = (g_{sa} + j b_{sa}) R_c = Y_{sa} - j B_{sa} \\ &= G_{sa} + j(B_{sa} - \omega C_{Tc}). \end{aligned} \quad (7)$$

The normalized theoretical impedance is

$$z_0 = r_0 + j x_0 = Z_0 / R_c = 1/y_0. \quad (8)$$

When  $\beta(h+l)$  is near  $\pi/2$ ,  $\omega C_{Tc}$  is negligible compared with  $B_{sa}$ ; when  $\beta(h+l)$  is near  $\pi$ , the contribution by  $\omega C_{Tc}$  is significant. The theoretical terminal functions  $\rho_0$  and  $\Phi_0$  in  $\theta_0 = \rho_0 + j\Phi_0$  are also computed

from eq (1) with the subscript 0 in place of  $sa$ . Since  $G_0 = G_{sa}$  it follows that  $\rho_0 = \rho_{sa}$ . Since the end effect is purely susceptive and  $b_0$  is small, the terminal function is given by

$$\Phi_0 = \pi + \tan^{-1} b_0 \approx \pi + b_0. \quad (9)$$

## 2.3. End Correction and Theory for Antennas of Small Height

Owing to the finite size of the conductors, it was not practical in the experiment to use antennas with heights  $h$  (fig. 1) less than 2.5 cm ( $\beta h = 2\pi h/\lambda \geq 0.161$ ). Therefore, the experimentally determined curves of  $\rho_0$  and  $\Phi_0$  were extended with theoretical values. These are readily determined since for small heights, the inverted L-antenna with its image is essentially a balanced section of a two-wire transmission line for which the radiation resistance referred to maximum current is given by

$$R^e = 30 \beta^2 (2h)^2 = 120 \beta^2 h^2. \quad (10)$$

When the maximum current is at the driving point,  $\beta(h+l) = \pi/2$ , the input resistance is  $R_{in} = R^e$ . In the case of a T-antenna with image, the resistance is one-half of  $R_{in}$  for the inverted L-antenna with its image since the two equal resistances are in parallel. In general, for the antenna with  $n$ -element top load with image, the resistance is  $1/n$  of  $R_{in}$  for the inverted L-antenna with its image since  $n$  equal resistances are in parallel. When the overall electrical length of the inverted L-antenna is  $\pi$ , the radiation resistance  $R^e$  referred to maximum current must be transformed through an electrical length of line  $\beta w = \pi/2$  to obtain the resistance at the driving point. The relevant formula is [King, 1955, p. 134, eq 9a, b]  $R_{in} = R'_c / R^e$  where  $R'_c$  is the characteristic resistance of the two-wire line formed by the inverted L-antenna and its image. If  $h$  denotes the height of the antenna over the ground plane (one-half the spacing of the two-wire line) and  $a_1$  is the radius of the conductor,  $R'_c$  is given by

$$R'_c = 120 \cosh^{-1} (h/a_1). \quad (11)$$

The theoretical value of the terminal function  $\rho_0$  may be calculated from the general formula [King, 1955, p. 102, eq. 9]. When  $r_0^2 \gg 1$ ,  $r_0^2 \gg x_0^2$  this reduces to

$$\rho_0 \approx 1/2 \tanh^{-1} 2/r_0 \approx 1/r_0. \quad (12)$$

For antennas with overall electrical length (height + one element of top load) equal to approximately  $\pi/2$ ,  $r_0 = R^e / R'_c$  and  $\rho_0 = R'_c / R^e$ . When the overall electrical length is  $\pi$ , the maximum current is a quarter wavelength from the driving point and

$$r_0 = (R'^2 / R^e) (1/R'_c) = R'_c / R^e. \quad (13)$$

It follows that for small values of  $\beta h$ ,

$$\rho_0 = R^e / R'_c. \quad (14)$$

The terminal function  $\Phi_0$  for small  $\beta h$  and when  $\beta(h+l)=\pi/2$  is obtained from that of a transmission line with input reactance  $X_{in}$  in series with the inductive reactance  $X_L=\omega L$  of the short length of conductor of length  $h$  and radius  $a_1$  perpendicular to the ground plane. The inductance of this straight conductor is [King, 1945]

$$L = (\mu_0 h / \pi) [\ln (4h/a_1) + (a_1/2h) - 1]. \quad (15)$$

The input reactance  $X_{in}$  includes a contribution from the end effect at the open end. This is approximately equivalent to a lumped capacitance  $C_{Te}$  that is given by the following formula [King, 1955, p. 367, eq 13]

$$C_{Te} = \frac{\pi \epsilon_0 (2h - a_1)}{2 [\ln (2h/a_1)^2]}. \quad (16)$$

The general formula for transforming a reactance  $X_{Te} = -1/\omega C_{Te}$  from the end of a line of length  $l$  to its driving point is obtained from King [1955, p. 134, eq 9a, b] in the special case when the termination is purely reactive. The sum of the normalized reactances  $x = x_{in} + x_L$  (normalized with respect to  $R'_c$ , the characteristic impedance of the two-wire line) gives the total normalized reactance terminating the coaxial line.  $\Phi_0$  may be obtained for a purely reactive termination from (1) with appropriate change in subscript. With  $x^2 \ll 1$ ,

$$\Phi_0 \doteq \pi/2 + x. \quad (17)$$

The formula gives  $\Phi_0$  for small  $\beta h$  where the overall electrical length of the antenna is  $\beta(h+l) \doteq \pi/2$ .

When the antenna length is  $\beta(h+l) \doteq \pi$ , the current is small at the driving point and the reactance terminating the coaxial line may be assumed to be the input reactance of a section of open-end line of length  $(h+l)$ . The equivalent lumped capacitance of the open end,  $C_{Te}$ , may be transformed to the driving point, so that  $x \doteq x_{Te} = X_{Te}/R'_c$ . In this case, since  $x^2 \gg 1$ ,

$$\Phi_0 \doteq \pi - 1/x = \pi + \omega C_{Te}. \quad (18)$$

In the preceding discussion, approximate corrections have been made for reactive end effects at the load end of the coaxial line and at the open ends of the open-wire lines forming the antennas. It is to be noted that an accurate analysis of end effects when the generator is in the terminal zone is not available. In the case at hand the diameter of the coaxial line is of the same order of magnitude as the smallest heights  $h$  of the antennas so that the electromagnetic field in the vicinity of the driven end of the antennas and the load end of the coaxial line is complicated. An accurate representation in terms of an equivalent lumped load for the coaxial line and equivalent point generator for the antenna is not possible and a close quantitative agreement between theoretical results based on such a representation and measured values cannot be expected in general.

### 3. Experimental Results for Inverted L-, T-, and Multi-Element Top-Loaded Antennas

The measured values of the apparent terminal functions  $\theta_{sa} = \rho_{sa} + j\Phi_{sa}$  are shown in figure 2 for the inverted L-antenna with  $\beta(h+l) = 3.2$ . The corresponding corrected functions  $\theta_0 = \rho_0 + j\Phi_0$  with their theoretically derived extensions to small values of  $\beta h$  are also shown. The apparent terminal impedances  $Z_{sa}$  and the corrected impedances  $Z_0 = R_0 + jX_0$  are shown in figure 3 for the inverted L-antenna with  $\beta(h+l) = 3.2$ . Note that  $Z_{sa}$  is the impedance actually observed as terminating the coaxial line; it includes end effects.  $Z_0$  is the ideal impedance of the antenna in the absence of end effects. Figure 4 shows the impedance of the inverted L-antenna, T-antenna, and antennas with two-, three-, and four-element top loads with  $\beta(h+l) = 1.6$ .

### 4. Antennas of Transmission-Line Types

It has been shown by King, Harrison, and Denton [1958] that antennas of transmission-line types may be treated by transmission line theory corrected for radiation if the height  $h$  of the antenna is sufficiently small. A general formula for the input resistance at the driving point is given by King, Harrison, and Denton [1958]. This formula does not take account of the effect on the driving-point resistance of the conductor of length  $2h$  in series with the generator. Nor is this effect included if the inductive reactance  $X_L = \omega L$  of the section of length  $2h$  is added to the input reactances  $X_{1in}$  and  $X_{2in}$  of the parallel com-

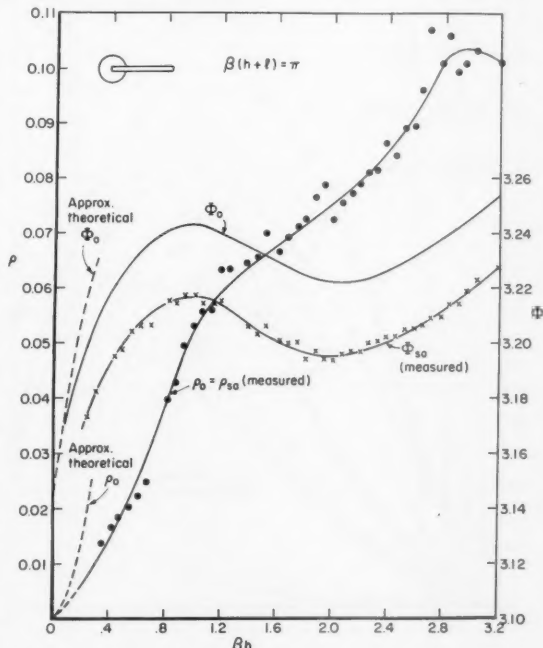


FIGURE 2. Terminal functions for inverted L-antenna,  $\beta(h+l) = 3.2$ .

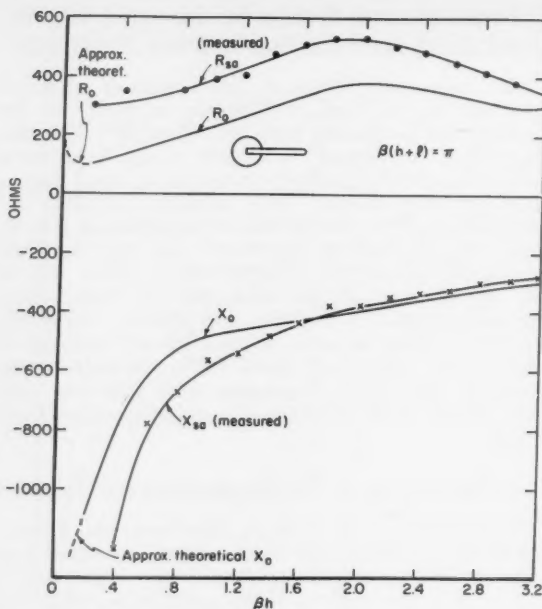


FIGURE 3. Impedances of inverted L-antenna,  $\beta(h+l)=3.2$ .

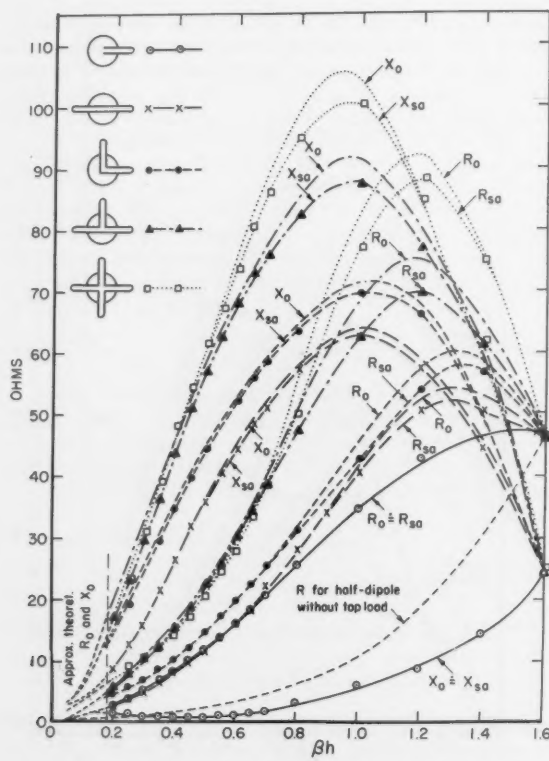


FIGURE 4. Impedances of inverted L-, T-, and multi-element top-loaded antennas,  $\beta(h+l)=1.6$ .

binations of the two transmission-line sections in the form

$$X_{in} = X_L + X_{in}; X'_{in} = \frac{X_{1in}X_{2in}}{X_{1in} + X_{2in}} \quad (19)$$

since the impedance is simply  $Z_{in} = R_{in} + jX_{in}$  where  $R_{in}$  is assumed to be given by King, Harrison, and Denton [1958]. An error due to this effect may be expected whenever  $X_{in}$  becomes large and the current in the generator is not near a maximum. The inclusion of a series inductance  $X_L$  in (19) is itself meaningful only when the current in the generator is near a maximum owing to the fact that there is actually no point generator but rather a distribution of driving field at the end of the coaxial line that extends over the full length  $h$ . For purposes of comparison  $X_{in}$  is calculated both with and without  $X_L$  and curves of both  $X_{in}$  and  $X'_{in}$  are shown.

The shunt driven transmission line with one end open and the other terminated in a straight conductor has three variables  $s_1$ ,  $s_2$  and  $h$ . Figure 5 shows the measured impedances when  $\beta s_2 = \pi/2$  and  $\beta h = 0.161$  and  $0.225$ . In this case the left-hand section is terminated in a straight conductor and the corresponding terminal function is given by King [1955, pp. 123-123]. The right-hand section is adjusted in length to be near a quarter wavelength long. Let  $\beta s_2 = \pi/2 - \beta \delta'$  where  $\delta'$  is a small length. The right end is open but it is not an ideal open end.

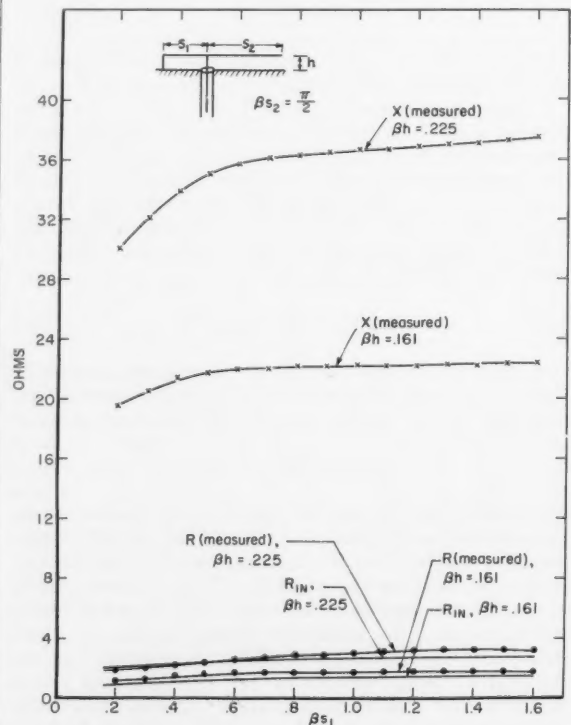


FIGURE 5. Impedances of transmission-line antennas,  $\beta s_2 = \pi/2$ .

The terminal or end effect is equivalent to a lumped capacitance  $C_{re}$  given approximately by eq (16). The corresponding normalized susceptance with  $R'_e = 120 \ln(2h/a_1)$  is  $b_{re} = R'_e \omega C_{re}$ . The corresponding terminal function may be obtained from King [1955, p. 119, eq 8]. The theoretical resistance curves are shown in figure 5. It is seen that there is good agreement between the theoretical and experimental values.

The inductance of a straight section of wire of radius  $a_1$  and length  $2h$  is given by King [1945]. The input reactances of the sections of lossless line are

$$X_{1in} = -R'_e \cot(\beta s_1 + \Phi_0); X_{2in} = -R'_e \cot(\beta s_2 + \Phi_0). \quad (20)$$

For the two cases  $\beta h = 0.161$  and  $0.225$ ,  $X_L$ ,  $X_{1in}$  and  $X_{2in}$  have been calculated and  $X_{in}$  determined. For the antenna over the image plane, the input reactance is  $X_{in}/2$ . The theoretical values are

$$X_{in}/2 = \begin{cases} 22.5 \text{ ohms for } \beta \delta' = 0.0582 \\ 31.4 \text{ ohms for } \beta \delta' = 0 \\ 35.5 \text{ ohms for } \beta \delta' = 0.0735 \\ 48.2 \text{ ohms for } \beta \delta' = 0 \end{cases} \text{ for } \beta h = 0.161$$

$$X_{in}/2 = \begin{cases} 22.3 \text{ ohms for } \beta h = 0.161 \\ 37.0 \text{ ohms for } \beta h = 0.225. \end{cases} \quad (21)$$

The experimentally observed values are

$$X_{in}/2 = \begin{cases} 22.3 \text{ ohms for } \beta h = 0.161 \\ 37.0 \text{ ohms for } \beta h = 0.225. \end{cases} \quad (22)$$

The value for  $\beta h = 0.161$  in (22) corresponds closely to the theoretical value for  $\beta \delta' = 0.0582$  in (21); in this case  $\beta s_2 = 1.511$  or  $s_2 = 0.242 \lambda$ . Similarly the experimental value for  $\beta h = 0.225$  agrees well with the theoretical value for  $s_2 = 0.245 \lambda$ . The input reactance as a function of  $\beta s_1$  is evidently very sensitive to the particular setting of  $s_2$ . A very small change in  $s_2$  alters  $X_{in}$  significantly. The theoretical expressions involve formulas for end effects that provide corrections that are comparable with the line spacing but not comparable with the radius of the conductors. Evidently changes in  $\beta s_2$  of the order of magnitude of  $\beta a_1 = 0.025$  or small multiples thereof are precisely the order of magnitude of the difference between the observed and calculated values.

Figure 6 shows the impedance of the same structure for  $\beta h = 0.161$  and  $\beta s_1 = 0.44$  when  $s_2$  is varied. Resonance occurs near  $\beta(s_1 + s_2) = \pi/2$ . The theoretical resistance  $R_{in}$  and reactance  $X_{in}$  are also shown. Evidently the length  $\beta(s_1 + s_2)$  is a critical quantity in the manner discussed in the preceding special case with  $\beta s_2 = \pi/2$ .

The measured and theoretical impedances of the shunt-driven transmission line antenna with both ends terminated in straight conductors (m-antenna) are shown in figure 7 when  $\beta h = 0.225$  and  $\beta s_2 = \pi/2$ . It is again evident that the setting of  $\beta s_2$  is critical.

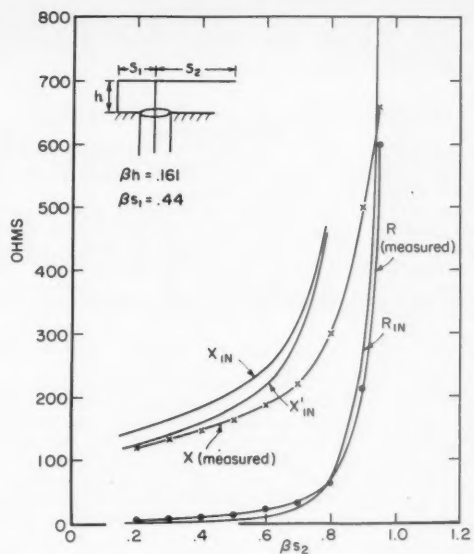


FIGURE 6. Impedances of transmission-line antennas,  $\beta s_1 = 0.44$ ,  $\beta h = 0.161$ .

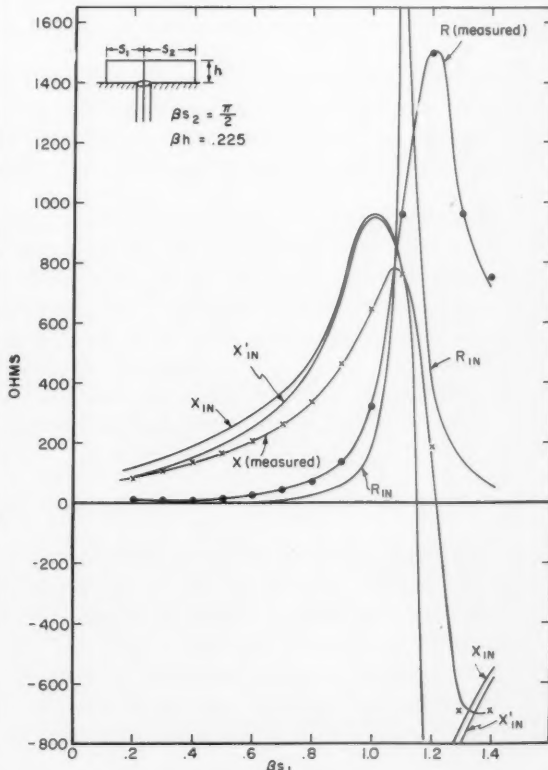


FIGURE 7. Impedances of m-antenna,  $\beta s_2 = \pi/2$ ,  $\beta h = 0.225$ .

A more detailed version of this paper appeared as Technical Report No. 305, Crust Laboratory, Harvard University.

## 5. References

Harrison, C. W., Jr., Antenna synthesis, Sandia Corp. Tech. Memo. 37-58 (14) (March 1958a).  
Harrison, C. W., Jr., Theory of inverted L-antenna with image, Sandia Corp. Tech. Memo. 11-58 (14) (April 1958b).  
Harrison, C. W., Jr., Antenna analysis by circuit superposition, Sandia Corp. Tech. Memo. 250-58 (14) (June 1958c).  
Harrison, C. W., Jr., Impedance of a T-antenna, Sandia Corp. Tech. Memo. 257-58 (14) (July 1958d).

King, D. D., Measurements at Centimeter Wavelength, p. 194 (D. Van Nostrand Co., Inc., New York, N.Y., 1952).  
King, R. W. P., Electromagnetic Engineering, p. 433, eq. 20 (McGraw-Hill Book Co., Inc., New York, N.Y., 1945).  
King, R. W. P., Transmission-line Theory (McGraw-Hill Book Co., Inc., New York, N.Y., 1955).  
King, R. W. P., and C. W. Harrison, Jr., The T-antenna: current and impedance, Sandia Corp. Tech. Memo. 306-59 (14) (Sept. 1959a).  
King, R. W. P., and C. W. Harrison, Jr., The inverted L-antenna: current and impedance, Sandia Corp. Tech. Memo. 353-59 (14) (Nov. 1959b).  
King, R. W. P., C. W. Harrison, Jr., and D. H. Denton, Jr., Transmission-line missile antennas, Sandia Corp. Tech. Memo. 436-58 (14) (Nov. 1958).

(Paper 65D5-150)

# Reflection From a Sharply Bounded Ionosphere for VLF Propagation Perpendicular to the Magnetic Meridian

Douglass D. Crombie<sup>1</sup>

Contribution From Central Radio Propagation Laboratory, National Bureau of Standards, Boulder, Colo.

(Received March 9, 1961; revised March 31, 1961)

There is experimental evidence that VLF signals propagating from west to east suffer less attenuation than from east to west. Earlier work treating the case of nonreciprocal propagation along the magnetic equator is extended in latitude. The nonreciprocity shown by  $||\vec{R}||$  for highly oblique propagation along the magnetic equator persists when the reflection point moves towards a magnetic pole, but at the pole itself  $||\vec{R}||$  is reciprocal. To a first approximation  $\perp R \perp$  is reciprocal at all magnetic latitudes. The conversion coefficients  $||\vec{R} \perp||$ ,  $||\vec{R} \parallel||$ , are greater for east-to-west propagation than for propagation in the opposite direction, except at a magnetic pole where they are equal.

## 1. Introduction

There is now a considerable amount of experimental evidence [Crombie, 1958; Taylor 1960] showing that VLF propagation is nonreciprocal, since VLF signals received from a westerly quarter appear to suffer less attenuation than those received from the east. A qualitative explanation of such behavior in terms of interactions between the longitudinal movements of ionospheric electrons in the plane of incidence, and the transverse component of the earth's magnetic field was given by Crombie [1958].

Subsequently, Barber and Crombie [1959] calculated the reflection coefficient of a sharply bounded ionosphere and showed that this explanation was correct for the special case of waves polarized in the plane of incidence, propagating along the magnetic equator. This special case simplified the calculations since the magnetic field is horizontal and transverse to the plane of incidence.

It has also been shown [Crombie, 1960] that the nonreciprocity which could be expected from the lack of reciprocity exhibited by the reflection coefficient does occur when mode theory is used. Wait [1960, 1961] and Wait and Spies [1960], using some coefficients derived from the numerical data of Johler [1961], have shown that mode propagation depends on the direction of propagation. More recently, Dobrott and Ishimaru [1961] have also concluded that VLF propagation along the magnetic equator may be nonreciprocal.

It is the purpose of this paper to derive formulas for the reflection coefficient of a sharply bounded ionosphere in the rather more general case where plane waves are incident from the west, or from the east at any magnetic latitude.

## 2. Introductory Theory

The starting point of this work is a paper by Yabroff [1957a and b] in which, following an outline by Bremmer [1949], he derives perfectly general relationships between the fields in a sharply bounded ionosphere, and obtains the appropriate boundary equations. Yabroff considered the coordinate system shown in figure 1. The vertical direction is  $x$  and the earth's magnetic field  $H_e$  is contained in the  $xz$  plane. The angle of incidence of the waves is  $\beta_i$ , and the magnetic field of the earth is inclined to the vertical at an angle  $\beta_e$ . The incident, reflected and transmitted waves are described in the coordinate system  $x',y',z'$  in which for a wave

<sup>1</sup> Present address: Dominion Physical Laboratory, Lower Hutt, New Zealand.

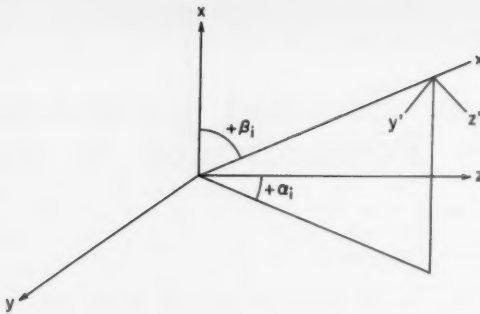


FIGURE 1. Coordinate system.

The positive values of  $\beta_i$  and  $\alpha_i$  are measured clockwise from the positive  $z$  and  $z$  axes respectively.

propagating in the  $\alpha_i, \beta_i$  direction,  $z'$  is in the  $\alpha_i, \beta_i + 90^\circ$  direction;  $y'$  is directed in the  $\alpha_i + 90^\circ$ ,  $90^\circ$  direction and  $x'$  is in the direction  $\alpha_i, \beta_i$ . The lower boundary of the supposedly uniform ionosphere is the  $xy$  plane. If  $z$  is magnetic north, then  $y$  is magnetic east.

The incident plane wave  $F_i$  can be written as

$$F_i = \operatorname{Re} \left\{ F_{oi} \exp \left[ j \frac{\omega}{c} (ct - x \cos \beta_i - y \sin \beta_i \sin \alpha_i - z \sin \beta_i \cos \alpha_i) \right] \right\}$$

in which  $\omega$  = wave angular frequency,  $c$  is the velocity of light and  $t$  is time. Since the boundary conditions must be satisfied it follows that the wave in the ionosphere  $F_m$ , arising from this incident wave, must be of the form

$$F_m = \operatorname{Re} \left\{ F_{om} \exp \left[ j \frac{\omega}{c} (ct - Dx - y \sin \beta_i \sin \alpha_i - z \sin \beta_i \cos \alpha_i) \right] \right\}$$

$D$  may be regarded as the cosine of the (complex) angle of refraction in the ionosphere.

Maxwell's equations and the equations of motion of an electron in a magnetic field can be written as

$$\left. \begin{aligned} \nabla \times \tilde{E} &= -\mu_0 \frac{\partial \tilde{H}}{\partial t} \\ \nabla \times \tilde{H} &= -Ne \tilde{V} + \epsilon_0 \frac{\partial \tilde{E}}{\partial t} \\ m \frac{d\tilde{v}}{dt} &= -e \tilde{E} - m\nu \tilde{V} - \mu_0 (\tilde{V} \times \tilde{H}_e) \end{aligned} \right\} \quad (1)$$

in which,  $-e$ ,  $m$  are the charge and mass of an electron,

$\tilde{V}$  is the electron velocity,

$\nu$  is the collision frequency,

$\epsilon_0$ ,  $\mu_0$  are the permittivity and permeability of free space.

From these three equations the three components of  $\tilde{H}$  and  $\tilde{V}$  may be eliminated giving three equations relating the components of  $\tilde{E}$ . In matrix form these equations are:

$$\begin{bmatrix} 1 - a^2 - \frac{s^2 - h_L^2}{s(s^2 - h^2)} & a_T D - \frac{j h_T}{s^2 - h^2} & a_L D + \frac{h_T h_L}{s(s^2 - h^2)} \\ a_T D + \frac{j h_T}{s^2 - h^2} & 1 - a_L^2 - D^2 - \frac{s}{s^2 - h^2} & a_L a_T - \frac{j h_L}{s^2 - h^2} \\ a_L D + \frac{h_T h_L}{s(s^2 - h^2)} & a_T a_L + \frac{j h_L}{s^2 - h^2} & 1 - D^2 - a_T^2 - \frac{s^2 - h_T^2}{s(s^2 - h^2)} \end{bmatrix} \begin{bmatrix} E_x \\ E_y \\ E_z \end{bmatrix} = 0 \quad (2)$$

where

$$\begin{aligned}
 s &= (1-jZ)/X & h &= Y/X, h_L = h \cos \beta_s, h_T = h \sin \beta_s \\
 X &= Ne^2/m\epsilon_0\omega^2 = (\text{normalized plasma frequency})^2, \\
 Y &= \mu_0\epsilon H_s/\omega m = \text{normalized gyro frequency.} \\
 Z &= \nu/\omega = \text{normalized collision frequency.} \\
 a_L &= \sin \beta_s \cos \alpha_s, a_T = \sin \beta_s \sin \alpha_s, a = \sin \beta_s.
 \end{aligned}$$

In order that  $E$  be finite the determinant of (2) must be zero. Thus

$$b_4 D^4 + b_3 D^3 + b_2 D^2 + b_1 D + b_0 = 0 \quad (3)$$

where

$$\begin{aligned}
 b_4 &= s(s^2 - h^2) - s^2 + h_L^2 \\
 b_3 &= 2a_L h_L h_T \\
 b_2 &= 2s[(1-a^2)h^2 - (s-1)(s-a^2s-1)] - h_T^2(1-a_L^2) - (2-a^2)h_L^2 \\
 b_1 &= -2(1-a^2)a_L h_L h_T \\
 b_0 &= (s-1)\{[(1-a^2)s-1]^2 - (1-a^2)^2 h_T^2 \cos^2 \alpha_s\} \\
 &\quad - (1-a^2)[(1-a^2)s-1](h_T^2 \sin^2 \alpha_s + h_L^2).
 \end{aligned} \quad (3a)$$

The four complex values of  $D$  obtained from this quartic represent the two upgoing and two downgoing characteristic waves which can propagate independently in the medium. Values of  $D$  with positive real and negative imaginary parts represent upgoing waves.

### 2.1. Boundary Equations

Since the total tangential fields  $E_y$ ,  $E_z$ ,  $H_y$ , and  $H_z$  must be continuous across the boundary, the following boundary equations are obtained:

From  $E_y$ :

$$E_{y'1} \cos \alpha_s + E_{z'1} \cos \beta_s \sin \alpha_s + E_{y'2} \cos \alpha_s - E_{z'2} \cos \beta_s \sin \alpha_s = P_1 E_{z1} + P_2 E_{z2} \quad (4a)$$

From  $E_z$ :

$$-E_{y'1} \sin \alpha_s + E_{z'1} \cos \beta_s \cos \alpha_s - E_{y'2} \sin \alpha_s - E_{z'2} \cos \beta_s \cos \alpha_s = E_{z1} + E_{z2} \quad (4b)$$

From  $H_y$ :

$$E_{y'1} \cos \beta_s \sin \alpha_s - E_{z'1} \cos \alpha_s - E_{y'2} \cos \beta_s \sin \alpha_s - E_{z'2} \cos \alpha_s = S_1 E_{z1} + S_2 E_{z2} \quad (4c)$$

From  $H_z$ :

$$E_{y'1} \cos \beta_s \cos \alpha_s + E_{z'1} \sin \alpha_s - E_{y'2} \cos \beta_s \cos \alpha_s + E_{z'2} \sin \alpha_s = T_1 E_{z1} + T_2 E_{z2} \quad (4d)$$

In these equations

$$P = E_y/E_z = M^{-1} \left\{ - \left[ 1 - a^2 - \frac{s^2 - h_L^2}{s(s^2 - h^2)} \right] \left[ a_L a_T - \frac{j h_L}{s^2 - h^2} \right] + \left[ a_T D + \frac{j h_T}{s^2 - h^2} \right] \left[ a_L D + \frac{h_L h_T}{s(s^2 - h^2)} \right] \right\} \quad (5)$$

$$Q = E_x/E_z = M^{-1} \left\{ - \left[ a_L D + \frac{h_L h_T}{s(s^2 - h^2)} \right] \left[ 1 - a_L^2 - D^2 - \frac{s}{s^2 - h^2} \right] + \left[ a_L a_T - \frac{j h_L}{s^2 - h^2} \right] \left[ a_T D - \frac{j h_T}{s^2 - h^2} \right] \right\} \quad (6)$$

where  $M$  is given by

$$M = \left[ 1 - a^2 - \frac{s^2 - h_L^2}{s(s^2 - h^2)} \right] \left[ 1 - a_L^2 - D^2 - \frac{s}{s^2 - h^2} \right] - \left[ a_T D - \frac{j h_T}{s^2 - h^2} \right] \left[ a_T D + \frac{j h_T}{s^2 - h^2} \right] \quad (7)$$

and

$$R = \eta_0 H_x / E_z = a_T - a_L P \quad (8a)$$

$$S = \eta_0 H_y / E_z = a_L Q - D \quad (8b)$$

$$T = \eta_0 H_z / E_z = D P - a_T Q. \quad (8c)$$

In which

$$\eta_0 = \sqrt{\mu_0 / \epsilon_0}.$$

## 2.2. Reflection Coefficient $R$

This can be written in matrix form as

$$R = \begin{bmatrix} R_{||} & R_{\perp} \\ R_{\perp} & R_{||} \end{bmatrix}. \quad (9)$$

The first subscript denotes whether the electric field is parallel (||) or perpendicular ( $\perp$ ) to the plane of incidence, and the second subscript refers in the same way to the electric field of the reflected wave. The components of  $R$  are defined as follows:

$$||R_{||} = E_{z'r}/E_{z'i} \quad (10a). \quad \perp R_{||} = E_{z'r}/E_{y'i}. \quad (10c)$$

$$||R_{\perp} = E_{y'r}/E_{z'i} \quad (10b). \quad \perp R_{\perp} = E_{y'r}/E_{y'i}. \quad (10d)$$

The components of  $R$  are obtained by solution of the boundary eqs (4) for the appropriate pairs of electric fields.

## 3. Application to Propagation Along a Line of Magnetic Latitude

The work of Yabroff given above is perfectly general and expressions for the reflection coefficient could be derived for any direction of propagation, and for any orientation of the magnetic field. The labor involved would be excessive, however, and the resulting expressions cumbersome. The more practical approach to this general case is to use a computer for the solution of the boundary eqs (4). This has been done by Johler and Walters [1960] for propagation in the magnetic meridian. Johler [1961] has also calculated numerically, reflection coefficients for propagation at angles of  $0^\circ, 60^\circ, 120^\circ, 180^\circ, 240^\circ, 300^\circ$  to the magnetic meridian, omitting the directions  $90^\circ$  and  $270^\circ$ , with which this paper is concerned.

However, in the case of propagation along a line of magnetic latitude the expressions obtained for the reflection coefficient are relatively compact as will be shown below, although even in this case the algebra is very tedious.

For magnetic east-to-west or west-to-east propagation  $\alpha_i = 90^\circ$  or  $270^\circ$ . Thus,  $a_L = 0$ . Making this substitution in eqs (4) gives for the boundary equations:

$$Ey: E_{z'i} C - E_{z'r} C = P_1 E_{z1} + P_2 E_{z2} \quad (11a)$$

$$Hz: E_{z'i} + E_{z'r} = T_1 E_{z1} + T_2 E_{z2} \quad (11b)$$

$$Ez: -E_{y'i} - E_{y'r} = E_{z1} + E_{z2} \quad (11c)$$

$$Hy: E_{y'i} C - E_{y'r} C = S_1 E_{z1} + S_2 E_{z2} \quad (11d)$$

where  $C = \cos \beta_i$ .

$$(8b) \text{ and } (8c) \text{ reduce to } T = DP - a_T Q \quad (12)$$

$$S = -D \quad (13)$$

while (5), (6), and (7) reduce to

$$P = P'M^{-1} = M^{-1} \left\{ j \left[ 1 - a^2 - \frac{s^2 - h_L^2}{s(s^2 - h^2)} \right] + \frac{h_T}{s} \left( a_T D + \frac{j h_T}{s^2 - H^2} \right) \right\} \frac{h_L}{s^2 - h^2} \quad (14)$$

$$Q = Q'M^{-1} = M^{-1} \left\{ -j \left( a_T D - \frac{j h_T}{s^2 - h^2} \right) - \frac{h_T}{s} \left( 1 - D^2 - \frac{s}{s^2 - h^2} \right) \right\} \frac{h_L}{s^2 - h^2} \quad (15)$$

$$M = \left[ 1 - a^2 - \frac{s^2 - h_L^2}{s(s^2 - h^2)} \right] \left[ 1 - D^2 - \frac{s}{s^2 - h^2} \right] - \left[ a_T D^2 + \frac{h_T^2}{(s^2 - h^2)^2} \right] \quad (16)$$

The quantities  $M, P, Q, S, T$ , carry the same subscripts as the  $D$  which they contain.

### 3.1. Solution of Boundary Equations

The boundary eqs (11) can be solved in the following way for the components of  $R$ .  $\parallel R_{\parallel}$  is taken as an example. From (11a) and (11b)

$$\parallel R_{\parallel} = E_{z_2}'/E_{z_1}' = \frac{T_1 C - P_1 + (E_{z_2}/E_{z_1})(T_2 C - P_2)}{T_1 C + P_1 + (E_{z_2}/E_{z_1})(T_2 C + P_2)}. \quad (17)$$

From (11c) and (11d), on putting  $E_{y_1}' = 0$  it follows that

$$E_{z_2}/E_{z_1} = -(C + D_1)/(C + D_2). \quad (18)$$

Substitution of (18) in (17) gives

$$\parallel R_{\parallel} = \Delta^{-1} [(T_1 C - P_1)(C + D_2) - (T_2 C - P_2)(C + D_1)], \quad (19)$$

$$\Delta = (T_1 C + P_1)(C + D_2) - (T_2 C + P_2)(C + D_1). \quad (20)$$

Similarly

$$\parallel R_{\perp} = \Delta^{-1} [2C(D_1 - D_2)], \quad (21)$$

$$\perp R_{\parallel} = \Delta^{-1} [2C(T_1 P_2 - T_2 P_1)], \quad (22)$$

$$\perp R_{\perp} = \Delta^{-1} [(T_1 C + P_1)(C - D_2) - (T_2 C + P_2)(C - D_1)]. \quad (23)$$

Substitution for  $T_1, P_1, T_2$  and  $P_2$  in these equations gives, after much work, the following relatively compact expressions for  $\parallel R_{\parallel}$  and  $\perp R_{\perp}$

$$\parallel R_{\parallel} = \Delta_1^{-1} \left[ \left\{ j \left[ \left( 1 - \frac{1}{s} \right) C D_1 D_2 - D_0^2 (C + D_1 + D_2) \right] + \frac{h_T a_T}{s} [C(C + D_1 + D_2) - D_1 D_2] \right\} \left[ \frac{s^2 - h_L^2}{s(s^2 - h^2)} \right. \right. \\ \left. \left. - 1 \right] (D_1 + D_2) + \left[ j \left( 2D_0^2 + \frac{a^2}{s} \right) - \frac{2C a_T h_T}{s} \right] \left[ \left( \frac{s}{s^2 - h^2} - 1 \right) (D_0^2 + D_1 D_2) + \frac{h_T^2 - h_L^2 D_1 D_2}{s(s^2 - h^2)} \right] \right] \quad (24)$$

$$\perp R_{\perp} = \Delta_1^{-1} \left[ \left\{ j \left[ D_0^2 (C - D_1 - D_2) - D_1 D_2 \left( 1 - \frac{1}{s} \right) C \right] - \frac{h_T a_T}{s} [D_1 D_2 - C(C + D_1 + D_2)] \right\} \left[ \frac{s^2 - h_L^2}{s(s^2 - h^2)} \right. \right. \\ \left. \left. - 1 \right] (D_1 + D_2) + \left[ j \left( 2D_0^2 + \frac{a^2}{s} \right) + \frac{2C h_T a_T}{s} \right] \left[ \left( \frac{s}{s^2 - h^2} - 1 \right) (D_0^2 + D_1 D_2) + \frac{h_T^2 - h_L^2 D_1 D_2}{s(s^2 - h^2)} \right] \right], \quad (25)$$

in which

$$\Delta_1 = \Delta / \left[ \frac{h_L}{s^2 - h^2} (D_1 - D_2) \right] = \left\{ j \left[ \left( 1 - \frac{1}{s} \right) C D_1 D_2 + D_0^2 (C + D_1 + D_2) \right] \right. \\ \left. + \frac{h_T a_T}{s} [C(C + D_1 + D_2) + D_1 D_2] \right\} \left[ \frac{s^2 - h_L^2}{s(s^2 - h^2)} - 1 \right] (D_1 + D_2) \\ + j \frac{a^2}{s} \left[ \left( \frac{s}{s^2 - h^2} - 1 \right) (D_0^2 + D_1 D_2) + \frac{h_T^2 - h_L^2 D_1 D_2}{s(s^2 - h^2)} \right] \quad (26)$$

and  $D_0^2 = 1 - a^2 - 1/s$ , the value of  $D^2$  when there is no magnetic field present.

Equation (22) reduces to

$${}_1R_{\parallel} = -\Delta_i^{-1} \frac{2h_L}{s^2 - h^2} \left[ \left(1 - \frac{1}{s}\right) D_0^2 + \frac{h_T^2 a_T^2}{s^2} \right] C. \quad (27)$$

Equation (21) reduces to

$${}_1R_{\perp} = \Delta_i^{-1} \cdot 2CM_1M_2 \left( \frac{s^2 - h_L^2}{h_L} \right). \quad (28)$$

When  $M_1M_2$  is expanded, it is found to contain terms involving  $D_1^2 + D_2^2$  and  $D_1^2 D_2^2$ . These are respectively equal to  $-b_2/b_0$  and  $b_4/b_0$  in eq (3). Substitution of these in (28) gives, after considerable reduction,

$${}_1R_{\perp} = -\Delta_i^{-1} \frac{2h_L}{s^2 - h^2} \left[ \left(1 - \frac{1}{s}\right) D_0^2 + \frac{h_T^2 a_T^2}{s^2} \right] C \quad (29)$$

which is identical to  ${}_1R_{\parallel}$ .

#### 4. Discussion of Reflection Coefficient Formulas

These formulas have been checked under various limiting conditions to ensure that they conform with other published results.

##### 4.1. No Magnetic Field

If the magnetic field is zero then  ${}_1R_{\parallel}$  and  ${}_1R_{\perp}$  reduce to

$${}_1R_{\parallel} = \frac{(D_0^2 + a^2)C - D_0}{(D_0^2 + a^2)C + D_0}$$

$${}_1R_{\perp} = \frac{C - D_0}{C + D_0}$$

while  ${}_1R_{\perp} = {}_1R_{\parallel} = 0$ . These limiting forms were given by Yabroff [1959b].

##### 4.2. Horizontal Magnetic Field

If the magnetic field is horizontal,  $h_L = 0$ ,  $h_T = h$ , and (19) reduces to

$${}_1R_{\parallel} = \frac{\left[ jD_2 \left( 1 - \frac{1}{s} \right) + \frac{h_T a_T}{s} \right] C - \left( jD_1^2 + \frac{h_T a_T D_2}{s} \right)}{\left[ jD_2 \left( 1 - \frac{1}{s} \right) + \frac{h_T a_T}{s} \right] C + \left( jD_1^2 + \frac{h_T a_T D_2}{s} \right)}. \quad (30)$$

From figure 1,  $h_T$  is negative and for west-to-east propagation  $a_T$  is also negative. In Barber and Crombie's paper [1959] their term equivalent to  $h_T a_T$  was taken as negative for west-to-east propagation, because of the different coordinate systems used by them. Bearing this in mind it is possible to show that (30) is identical with their earlier result.

If in (25)  $h_L = 0$  then (25) reduces again to

$${}_1R_{\perp} = \frac{C - D_1}{C + D_1} = \frac{C - D_0}{C + D_0}$$

confirming the result of Barber and Crombie [1959]. It is easily seen from (27) and (29) that when  $h_L = 0$  both  ${}_1R_{\parallel}$  and  ${}_1R_{\perp}$  become zero.

### 4.3. Vertical Incidence, Vertical Magnetic Field

Here  $h_T, a_T, a$  become zero and  $C=1$ .

Substitution in (24), (25), (27), (29), give

$$R_{\parallel} = R_{\perp} = \frac{D_1 D_2 - 1}{(D_1 + 1)(D_2 + 1)}, \quad R_{\parallel} = R_{\perp} = j \frac{D_1 - D_2}{(D_1 + 1)(D_2 + 1)}$$

which are results previously obtained by Bremmer [1949].

### 4.4. Reciprocity

The expressions (24), (25), (27), and (29) all contain  $h_T a_T$ . This is positive for west-to-east propagation and negative for east-to-west propagation. Thus, provided that  $h_T$  is not zero, all the reflection coefficient terms may exhibit nonreciprocity.

## 5. Numerical Work

In order to evaluate the expressions for the reflection coefficients it is necessary first of all to find  $D_1$  and  $D_2$  from (3). For propagation along a line of magnetic latitude  $a_L=0$  and (3) becomes a quadratic in  $D^2$ . Thus

$$b_4 D^4 + b_2 D^2 + b_0 = 0,$$

and

$$D^2 = [-b_2 \pm \sqrt{b_2^2 - 4b_0 b_4}] (2b_4)^{-1}.$$

Substituting  $a_L=0$  into eqs (3a) gives

$$\begin{aligned} b_2 &= 2s [(1-a^2)h^2 - s(s-1)D_0^2] - h_T^2 - (2-a^2)h_L^2 \\ b_1^2 - 4b_0 b_4 &= h^4 - 2(1-a^2)h^2 h_L^2 + 4s(s-1)D_0^2 h_L^2 + (1-a^2)^2 h_L^4 \\ b_4 &= s(s^2 - h^2) - (s^2 - h_L^2). \end{aligned}$$

The values of  $D_1, D_2$  having positive real and negative imaginary parts are chosen since these represent the upgoing "ordinary" and "extraordinary" waves in the ionosphere.

Some special cases are of interest in obtaining the results of section 4.

For  $h=0$ ;  $D_1^2 = D_2^2 = D_0^2 = 1 - a^2 - 1/s$ .

For  $h_L=0$ ;  $h_T=h$  and  $D_1^2 = D_0^2$ ,  $D_2^2 = 1 - a^2 - \frac{s-1}{s^2 - h^2 - s}$ .

For  $h_T=0$ ;  $h_L=h$  and  $a=0$ ,  $D_{1,2}^2 = 1 - \frac{1}{s \pm h}$ .

Some approximate calculations have been made for daytime conditions to show the effect of the angle of dip of the earth's magnetic field on the four reflection coefficient terms using the formulas (24), (25), (27), and (29) developed above. The calculations are based on the following parameters:

$\omega_0 = 10^6$  corresponding to an electron density  $\approx 310/cc$ ,

$\nu = 10^7/\text{sec}$ ,  $\omega = 10^5/\text{sec}$ ,  $\alpha_i \approx 78^\circ 80'$ ,  $C = 0.2$ .

The earth's magnetic field has been taken as 0.5 gauss and the inclination of the field to the vertical  $\beta_e = 90^\circ, 60^\circ, 30^\circ$ , and  $0^\circ$ . The results of these calculations are shown in table 1.

TABLE 1

	$\ R\ $		$\perp R_{\perp}$		$\ R_{\perp} = \perp R\ ^*$		
	West to east	East to west	West to east	East to west	West to east	East to west	
90°	0.72/175°	0.33/175°	0.76/171°	0.76/171°	0.0	0.0	Horizontal field.
60°	.69/176°	.38/176°	.76/162°	.76/162°	.042/136°	.081/102°	-----
30°	.67/179°	.42/183°	.68/162°	.68/160°	.075/145°	.122/177°	-----
0°	.59/180°	.59/180°	.66/150°	.66/150°	.083/153°	.083/153°	Vertical field.

\*For propagation in the Northern Hemisphere the phase angle of  $\|R_{\perp}$  and  $\perp R\|$  should be reduced by 180°.

It is clearly seen from this table that  $\|R\|$ ,  $\|R_{\perp}$  and  $\perp R\|$  all show nonreciprocal properties, whereas  $\perp R_{\perp}$  does not. In the case of  $\|R\|$  the difference between east-to-west and west-to-east propagation is greatest at the magnetic equator where the magnetic field is horizontal, and gradually decreases as the reflection point moves nearer a magnetic pole. Nevertheless, the difference is very appreciable even when the angle of dip is 60° ( $\beta_e = 30^\circ$ ). At the pole, where the magnetic field is vertical the two reflection coefficients are equal, since there is then no transverse field.

At the magnetic equator  $\|R_{\perp}$  and  $\perp R\|$  are zero. When the magnetic field is inclined  $\|R_{\perp}$  and  $\perp R\|$  become finite, but again their values for east-to-west and west-to-east propagation differ. This difference again disappears at the magnetic pole.

Despite the fact that eq (25) for  $\perp R_{\perp}$  contains  $a_r h_T$ , it seems from table 1 that, for the values of the parameters used,  $\perp R_{\perp}$  is essentially reciprocal. Thus in (25) the variations due to the sign of  $a_r h_T$  must, to a first approximation cancel. This presumably will not necessarily occur for other values of the parameters.

The above numerical calculations have been made for highly oblique incidence, since long distance VLF propagation is of interest at present. However, the formulas are applicable at any angle of incidence. Thus the predictions of the formulas could be tested by making observations of  $\|R\|$  and/or  $\|R_{\perp}$  at points situated at equal distances to the west and east of a VLF transmitter. Alternatively, observation of the ground-interference pattern to the west and east of the transmitter could be made with airborne equipment.

## 6. Conclusions

This paper extends the earlier work of Barber and Crombie [1959] to the case of west-to-east and east-to-west propagation at any magnetic latitude. The nonreciprocity shown by  $\|R\|$  for highly oblique propagation along the magnetic equator persists when the reflection point moves towards a magnetic pole, but at the pole itself  $\|R\|$  is reciprocal. To a first approximation at least,  $\perp R_{\perp}$  is reciprocal at all magnetic latitudes. However, the conversion coefficients  $\|R_{\perp}$ ,  $\perp R\|$ , which are shown to be equal, are greater for east-to-west propagation than for propagation in the opposite direction, except at a magnetic pole where they are equal.

The work described in this paper was done while the writer was on a short visit to the Boulder Laboratories of the National Bureau of Standards. The writer wishes to express his appreciation for this opportunity, particularly to Dr. J. R. Wait through whom it was arranged.

## 7. References

- Barber, N. F., and D. D. Crombie, V.L.F. reflections from the ionosphere in the presence of a transverse magnetic field, J.A.T.P. **16**, 37 (1959).
- Bremmer, H., Terrestrial Radio Waves, ch. 11 (Elsevier Publishing Co., New York, N.Y., 1949).
- Crombie, D. D., Differences between east-west and west-east propagation of V.L.F. signals over long distances, J.A.T.P. **12**, 110 (1958).
- Crombie, D. D., On the mode theory of VLF propagation in the presence of a transverse magnetic field, J. Research NBS **64D** (Radio Prop.), No. 3, 265-267 (May-June 1960).

Dobrott, D., and A. Ishimaru, East-west effect on VLF mode transmission across the earth's magnetic field, *J. Research NBS 65D* (Radio Prop.) No. 1, 47-52 (Jan.-Feb. 1961).

Johler, J. Ralph, Magneto-ionic propagation phenomena in low- and very-low-radiofrequency waves reflected by the ionosphere, *J. Research NBS 65D* (Radio Prop.) No. 1, 53-65 (Jan.-Feb. 1961).

Johler, J. R., and L. C. Walters, On the theory of reflection of low and very low frequencies from the ionosphere, *J. Research NBS 64D* (Radio Prop.) 269 (1960).

Taylor, W. L., Daytime attenuation rates in the VLF band using atmospherics, *J. Research NBS 64D* (Radio Prop.) No. 4, 349-355 (July-Aug. 1960).

Wait, James R., Terrestrial propagation of very-low-frequency radio waves, a theoretical investigation, *J. Research NBS 64D* (Radio Prop.) No. 2, 153-204 (March-April 1960).

Wait, James R., A new approach to the mode theory of VLF propagation, *J. Research NBS 65D* (Radio Prop.) No. 1, 37-46 (Jan.-Feb. 1961).

Wait, James R., and Kenneth Spies, Influence of earth curvature and the terrestrial magnetic field on VLF propagation, *J. Geophys. Research 65*, No. 8, 2325-2331 (Aug. 1960).

Yabroff, I. W., Reflection at a sharply bounded ionosphere, *Proc. IRE 45*, 750 (1957a).

Yabroff, I. W., Tech. Report No. I, July 29, 1957. R.P.L. Stanford ASTIA Doc. AD 136, 457 (1957b).

(Paper 65D5-151)



# Resonance of the Space Between Earth and Ionosphere

H. Poeverlein

(Received August 1, 1960; revised March 22, 1961)

Contribution from Propagation Sciences Laboratory, Air Force Cambridge Research Laboratories, Bedford, Mass.

When noise radiation of roughly one or a few kilocycles per second is emitted in the higher atmosphere, part of it (an extraordinary wave) is propagated downward into the space between earth and ionosphere. Reflection at the earth and ionosphere leads then to a standing wave in this space, whose intensity for a given incident power flux varies very much with frequency. Maximum field strength of the standing wave is derived for the resonance frequencies of the space. The incident wave fronts are assumed to be horizontal. Only clearly defined wave fronts being of a sufficiently wide extension and showing no noticeable irregularities will lead to a definite resonance. The space between earth and ionosphere is comparable to an air gap between two parallel plane reflectors. The lower ionosphere is however only a partial reflector, allowing radiation to enter the resonance space and causing at the same time some loss of energy out of the resonance space (leakage). Stratification of the lower ionosphere has some influence on the resonance phenomena. With a *D* layer, an additional resonance at a lower frequency is obtained.

It seems too early to decide whether in any observed noise the resonance spectrum of the space between earth and ionosphere becomes apparent, but it is expected that noise spectra observed on the ground are modified by the resonances. In case of monochromatic emissions, the received intensity depends on the position in the resonance spectrum. The resonance spectrum should be received in case of emission of a white-noise spectrum, provided the wave fronts are appropriate.

## 1. Introduction

### 1.1. Cavity Between Two Plates

In a space between two infinite parallel plates resonance is observed when half a wavelength or multiples of a half-wavelength fit into the space. The electromagnetic field in this case of resonance is that of a standing wave whose wave planes are parallel to the plates. If one of the plates is made partially transparent, a model of the earth and ionosphere is obtained. The semitransparent plate like the ionosphere lets waves enter from outside—or from the higher atmosphere—and still permits resonance oscillations. The phenomena encountered in the case of two semitransparent plates (wire gratings) or one conductor together with a semitransparent plate (grating or dielectric plate) have been described in the literature [Casey and Lewis, 1952; Wait, 1954; von Trentini, 1956].

The field intensity in the resonance space is strongly dependent on the frequency of the incident waves, showing peaks at the resonance frequencies. The partial transparency of one of the reflectors entails imperfect reflection and contributes thus to a limitation of the resonance peaks.

### 1.2. Fundamentals

The ground is a good reflector for frequencies of the order of 1 kc/s. With a conductivity of  $10^{-3}$  mho/m, for example, the amount of the complex refractive index of the ground for 1 kc/s is  $|n|=134$ , a value sufficient for good (almost perfect) reflection in vertical incidence, which is considered exclusively.

The ionosphere is only a partial reflector. The extraordinary wave at very (or extremely) low frequencies finds in the ionosphere (except its lowest part) conditions of free propagation, as is known from the audiofrequency whistlers. The refractive index of the extraordinary wave under these conditions is in general high ( $\gg 1$ ). When the increase to these high values is fairly rapid in terms of wavelengths, we may expect that part of the extraordinary wave passes through the height interval of this rapid increase and part is reflected there. Thus we have for extraordinary waves the combination of an almost perfect reflector (the ground) with a semitransparent reflector that allows waves to enter the resonance space.

The descending wave fronts and consequently also the wave fronts in the resonance space will be assumed as horizontal. An eventual slight inclination of the wave fronts in the ionosphere would, because of the refraction in leaving the ionosphere, cause a considerable inclination of the wave fronts in the resonance space with the result of an essential modification of the resonance spectrum. Random distortion of the wave fronts would correspond to a mixture of propagation directions and consequently lead to a smearing-out of the resonance spectrum. The lateral extension of the wave fronts must be wide enough to have the simple plane-wave theory applicable.

There is some relationship between the resonance effect under consideration and the "tweeks", sequences of pulses caused by multiple reflection of sferics in propagation to a distant location [Potter, 1951]. The lightning flash from which a sferic

originates is nearly a point source. The radiation thus is omnidirectional and the tweek spectrum may not be interpreted as a resonance spectrum corresponding to horizontal (or otherwise simply defined) wave fronts. The asymptotic limit frequency of the tweek spectrum, however, is supposed to relate to horizontal wave fronts and should consequently be identical with our fundamental resonance frequency, at least in case of a well-defined reflection level in the ionosphere. In other respects, the behavior of tweeks and that of our resonance phenomenon are not expected to be the same.

The energy of the resonance oscillations is limited by losses. In our case the losses are due to partial transparency of the lower ionosphere (leakage), absorption on the path in the ionosphere below the reflection level, and imperfect ground reflection. Only the partial transparency is included in the theoretical treatment to follow. At the rather low frequencies the partial transparency is thought of as being the main cause of loss under most conditions. It was noted before that the ground is an almost perfect reflector. An estimate of the absorption in ionospheric propagation is made in appendix 1. The absorption coefficient found for normal daytime conditions may not prevent the resonance oscillations, but we have to be aware that absorption tends to depress the quality factor of the resonances and to smooth the resonance curves. This may preferably happen in daytime and at the higher resonance frequencies.

The refractive index of the ionosphere for our frequencies is in most heights fairly well represented by the "quasi-longitudinal" approximation (eq (14) of appendix 1, slightly simplified)

$$n^2 = 1 \mp \frac{f_0^2}{ff_H |\cos \alpha|} \quad (1)$$

The two signs refer to the ordinary (−) and the extraordinary (+) wave.<sup>1</sup>  $f_0$  is the plasma frequency,  $f_H$  the gyrofrequency of the electrons in the terrestrial magnetic field, and  $\alpha$  the angle between the wave normal and the direction of the terrestrial magnetic field. Equation (1), sometimes further simplified by neglecting unity, has frequently been used to describe whistler propagation [Storey, 1953], (more references given by Poverlein [1959a]). The equation is based on the assumptions:  $f_0 \gg f$ ,  $f \ll f_H$ ,  $\alpha$  not near  $\pi/2$ , and negligible collision frequency. In the lowest ionosphere there is, of course, a height interval in which  $f_0$  is comparable to  $f$ . At our frequencies this height interval is found in a rather low altitude and is obviously narrow in terms of wavelengths (or decay distances). It has therefore no remarkable influence on the propagation and eq (1) may be used throughout. At higher frequencies, at which  $f_0$  is comparable to  $f$  in a significant height interval, the refractive index formula has to be more rigorous and coupling or transition between ordinary

<sup>1</sup> This choice of signs complies with Storey's [1953] classical paper on whistlers and with the conventional definition of ordinary and extraordinary waves on basis of the Appleton-Hartree formula. The opposite notation, however, is occasionally found.

and extraordinary waves has to be taken into consideration. This is known to be the case at frequencies of the order of 10 or 20 kc/s.

Contributions of positive ions to the refractive index become noticeable near the gyrofrequency of the ions (approximately 50 c/s for  $O^+$ ). All derivations from eq (1) are therefore useful only for frequencies well above the ion gyrofrequency.

### 1.3. Objective

This theoretical study is concerned with the modification of noise signals originating in the higher atmosphere by resonance of the space between earth and ionosphere. Frequency response curves of this space will be derived, which show for the frequencies under consideration the amplification or reduction of the signal intensity on the ground compared with the intensity of the incident wave.

First some simplified models of the ionosphere are assumed, exhibiting one or two reflecting boundaries of homogeneous media. Later, samples of nighttime and daytime stratifications of the lower ionosphere are considered. With a simple reflecting boundary, resonance is obviously obtained when multiples of half-wavelengths fit into the resonance space.

The study applies to wide horizontal wave fronts only. A noise emission coherent over a wide area is therefore required. Such an emission may arise from large-scale geophysical processes (e.g., incident corpuscular radiation) rather than from local events.

White noise or short pulses of a sufficient coherence over a wide area would lead to an immediate observation of the derived frequency response curves. Monochromatic noise undergoes an enhancement or reduction of intensity depending on the position of the frequency in the frequency spectrum (response curve). Generally the noise spectrum observable on the ground is the result of the noise emission, eventual propagation effects on the path through the ionosphere, and the response of the resonance space.

Processes of noise generation in the higher atmosphere have been treated to some extent in the literature [Gallet and Helliwell, 1959] (some more references are given by Gustafsson, Egeland, and Aarons [1960]). A survey of any amount of observational material as for indications of our resonance effect has not yet been made.

This study does not show much of a relationship with familiar theories of ELF or VLF propagation. This is mainly due to the consideration of waves that come down from high altitudes and travel vertically. Other investigations are concerned with propagation from a source to a receiver, both between earth and ionosphere. Some remarks on absorption and on a wave theory of propagation that might be of more general use appear in the appendixes.

## 2. Simplified Models

### 2.1. Earth and Sharply Bounded Ionosphere

The earth will be considered as a perfect reflector in all cases that will be discussed. The simplest

model of the ionosphere is a homogeneous medium with a sharp boundary at the bottom. The refractive index of the ionosphere according to eq (1) has a high positive value for the extraordinary wave and in general an imaginary value for the ordinary wave. The extraordinary wave will be dealt with now.

The simple model of the resonance space and the ionosphere is shown in figure 1. The electric field in the resonance space is drawn in for various resonance cases. The field may originate from some noise emission in the ionosphere. A descending wave generated in the ionosphere will reach the bottom of the ionosphere and lead to a standing wave in the resonance space below and to a reflected wave traveling back within the ionosphere. The standing wave in the resonance space may be interpreted as the superposition of a descending and an ascending wave traveling in a vertical direction.

Ascending and descending waves will be denoted by  $F$  and  $G$  respectively. Strictly speaking, the symbols will denote the horizontal electric field strength components of these waves. In the anisotropic ionosphere an additional vertical (longitudinal) field strength component may exist.

Figure 2 is a representation of the horizontal electric field strengths  $F$  and  $G$  in the complex plane. The vectors indicate amplitudes and phases of ascending waves ( $F$ ) and descending waves ( $G$ ). The polarization of the waves (disregarding vertical  $E$  components in the ionosphere) is assumed constant over the entire propagation path. In case of a reflecting artificial dielectric, for example, the polarization may be linear in a fixed direction. In case of the extraordinary wave which is determined by the ionospheric propagation characteristics, the polarization is circular in the quasi-longitudinal approximation that is being used now [Ratcliffe, 1959]. The sense of the rotation is clockwise for an observer looking in the direction of the terrestrial magnetic field.

The construction of figure 2 starts at the earth's surface. The field strengths  $F_1$  and  $G_1$  there are opposite to each other in consequence of the assumed perfect reflection. In traveling upward the two vectors rotate in opposite senses. The rotation in the air space amounts to  $kh$  and is, with a time factor  $\exp(i\omega t)$ , clockwise for the ascending wave ( $F$ ). In traversing the bottom of the ionosphere there is a sudden change from  $F_2$  and  $G_2$  to  $F_3$  and  $G_3$ . The total horizontal field strength components

$$\begin{aligned} E_{\text{hor}} &= F + G \\ H_{\text{hor}} &= H = \sqrt{\frac{\epsilon_0}{\mu_0}} n(F - G) \end{aligned} \quad (2)$$

must be continuous at the boundary.  $E_{\text{hor}}$  there is imaginary,  $H_{\text{hor}}$  real (see fig. 2). In passing the boundary, therefore, the end points of the vectors in figure 2 are shifted symmetrically along a horizontal line with a reduction of the real components by a factor equal to the refractive index ratio ( $n$  of the ionosphere in our case). It may be recalled that  $n$  of the extraordinary wave is assumed to be real and greater than unity.

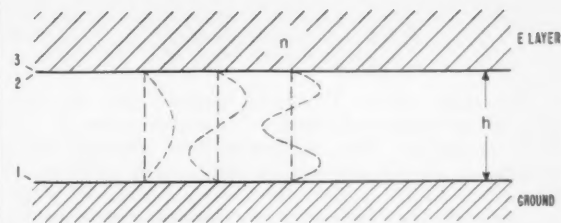


FIGURE 1. Earth and sharply bounded ionosphere.

The broken lines represent the distribution of the electric field strength in various resonance cases. The numbers denote the levels for which field strength vectors are shown in figure 2.

It is superfluous to consider the longitudinal electric field strength components of the waves at the boundary. Continuity of a resulting normal  $D$  component at any boundary is guaranteed by requiring continuity of  $H_{\text{hor}}$ .

From our construction it is easily seen that the reduction of the field vectors  $F$  and  $G$  in going up through the boundary is maximum if the vectors at the boundary are real or

$$kh = \pi, 2\pi, 3\pi, \dots \quad (3)$$

This is the resonance condition. In all cases given by eq (3), a relatively strong field in the space between earth and ionosphere ( $F_1$  and  $G_1$ ) arises from a weak wave incident from above ( $G_3$ ).

Because  $G_3$  is the field of the primary wave, one might like to start the computation or construction of the field strengths with  $G_3$ . This would however necessitate the consideration of multiple reflections between earth and ionosphere, which did not become apparent in the method chosen.

The procedure of figure 2 is also usable for more complicated models of the ionosphere. A multiple layer with several boundaries requires an iterative application of the procedure (section 2.2 deals with a double layer). A step approximation allows us to transfer the method to a continuously varying medium (section 3 and appendix 2).

Figure 2, of course, is nothing but a graphical representation of the analytical expressions describing the waves in the present case. From the figure or from the analytical formulation we derive the ratio between the field strengths arriving at the ground ( $G_1$ ) and incident on the boundary of the ionosphere from above ( $G_3$ )

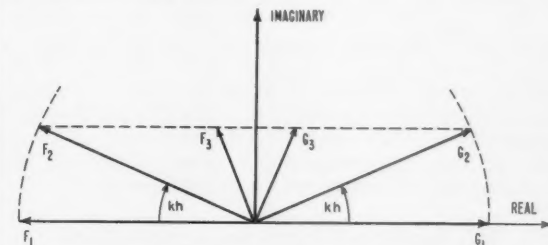


FIGURE 2. Electric field strengths in the complex plane ( $F$  electric field strength of the ascending wave,  $G$  electric field strength of the descending wave).

$$\left| \frac{G_1}{G_3} \right| = \frac{n}{\sqrt{n^2 \sin^2 kh + \cos^2 kh}}. \quad (4)$$

The ratio of the Poynting vectors may be considered as more significant than the ratio of the field strengths. The horizontal field strength component  $G$  of the descending wave in a medium of refractive index  $n$  corresponds to a vertical component of the Poynting vector proportional to  $nG^2$  (cf. eqs (2)). An eventual horizontal component of the Poynting vector is not of interest in this study. The "ratio of the Poynting vectors" in the following always refers to the vertical components of the Poynting vectors which are proportional to  $nG^2$ . The ratio of the Poynting vectors corresponding to the field strength ratio of eq (4) thus is

$$\frac{1}{n} \left| \frac{G_1}{G_3} \right|^2 = \frac{n}{n^2 \sin^2 kh + \cos^2 kh}. \quad (5)$$

Equations (4) and (5) show that *resonance* is obtained under the condition of eq (3), with an enhancement of the Poynting vector

$$\frac{1}{n} \left| \frac{G_1}{G_3} \right|^2 = n. \quad (6)$$

*Maximum reduction* of the Poynting vector is obtained for

$$kh = \frac{1}{2}\pi, \frac{3}{2}\pi, \frac{5}{2}\pi, \dots \quad (7)$$

with a reduction ratio

$$\frac{1}{n} \left| \frac{G_1}{G_3} \right|^2 = \frac{1}{n}. \quad (8)$$

For comparison the results of the Fresnel reflection theory for waves traversing a boundary may be noted: If the waves come from the medium with high-refractive index, a fraction  $2n/(n+1)$  of the electric field strength or a fraction  $4n/(n+1)^2$  of the Poynting vector appears in the second medium. Equation (6) shows that the resonance effect in our case seems to improve the transparency of the boundary (in terms of Poynting vectors) by a factor of approximately  $n^2/4$ . The reduction in the minimum case amounts to approximately  $1/4$  (eq 8).

The enhancement of the Poynting vector in the resonance case does of course not mean a violation of the law of conservation of energy. With perfectly reflecting earth, there is no net power flux in the space between earth and ionosphere. The Poynting vector considered in this space is the Poynting vector of one of the two progressive waves of which the standing wave is supposed to be composed.

## 2.2. Earth and Double-Layer Ionosphere

The single-layer model (fig. 1) may be a fairly good approximation of the lower ionosphere at night.

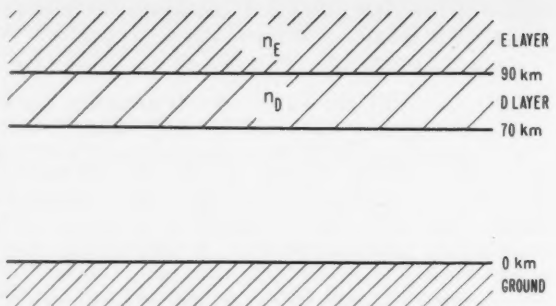


FIGURE 3. Earth and double-layer ionosphere.

The daytime ionosphere in lower heights is better approached by two adjacent dielectrics, representing the  $D$  and the  $E$  layers.<sup>2</sup> This model is shown in figure 3. The heights are chosen in accordance with normal daytime conditions. The refractive indices for the extraordinary wave at a frequency around 500 c/s can be assumed as

$$\left. \begin{aligned} n_D &= 8 \\ n_E &= 50 \end{aligned} \right\}. \quad (9)$$

The vector diagram, figure 2, must now be complemented by a rotation of the vectors corresponding to the phase shift in traveling up through the  $D$  layer and one more horizontal shift of the vector end points corresponding to the transition from the  $D$  to the  $E$  layer. In passing through the boundary between the  $D$  and  $E$  layers, the horizontal components of the field strength vectors in the vector diagram are reduced by the refractive index ratio  $n_E/n_D$ .

In the present case two kinds of resonance may be distinguished, the one resulting from maximum reduction of the electric field strengths  $F$  and  $G$  (fig. 2) at the bottom of the  $D$  layer, the other from maximum reduction at the boundary between  $D$  and  $E$  layers. The first kind of resonance requires that the field vectors  $F$  and  $G$  in reaching the  $D$  layer are real, or in other words, that an integral number of half-wavelengths fits into the space between ground and  $D$  layer. With a height of 70 km for the bottom of the  $D$  layer (fig. 3) this yields the resonance frequencies

$$\left. \begin{aligned} f &= 2.14 \times 10^3 \times m \text{ (c/s)} \\ m &= 1, 2, 3, \dots \end{aligned} \right\}. \quad (10)$$

The minimums between the resonances are found at  $m = \frac{1}{2}, \frac{3}{2}, \frac{5}{2}, \dots$

The second kind of resonance, corresponding to maximum reduction at the boundary between the  $D$  and the  $E$  layer requires real field vectors at this boundary. With the model of figure 3 and the refractive indices of eqs (9) resonance frequencies of 509, 1386,  $\dots$  c/s and minimums at 151, 945,  $\dots$  c/s were derived.

<sup>2</sup> A brief account of a resonance case in the two-layer model was given in an earlier paper [Poeverlein, 1959b].

A simple approximation for the second kind of resonance is obtained by assuming  $n_D \gg 1$ . With large  $n_D$  the horizontal components of  $F$  and  $G$  (fig. 2) in passing the bottom of the  $D$  layer are reduced to almost zero. This means that  $F$  and  $G$  immediately above the bottom of the  $D$  layer become imaginary. A phase shift of  $\frac{1}{2}\pi$ ,  $\frac{3}{2}\pi$ ,  $\frac{5}{2}\pi$ , . . . within the  $D$  layer makes then the vectors  $F$  and  $G$  real at the top of the  $D$  layer. The corresponding resonance frequencies under our conditions are 469, 1406, 2340, . . . c/s.

### 3. Realistic Cases

#### 3.1. E Layer, Extraordinary Wave

A nighttime  $E$  layer profile given by Nertney ([Poeverlein, 1959a] fig. 18) may now be used for the study of resonance of the extraordinary wave. The profile and an approximative step function are shown in figure 4.

The refractive index in the ionosphere (eq 1) depends essentially on the plasma frequency  $f_0$ . Values of  $f_0$  following from

$$f_0^2 = 80.7 \times 10^6 \times N \quad (11)$$

are noted in figure 4 ( $f_0$  in c/s, the electron concentration  $N$  per  $\text{cm}^3$ ). In the refractive index formula,

$$f_H |\cos \alpha| = 1.316 \times 10^6 \text{ c/s} \quad (12)$$

may be assumed (corresponding to some temperate latitude) and hence

$$f_0^2 / (f_H |\cos \alpha|) = 61.3N. \quad (13)$$

The step function of figure 4 similarly to a combination of several dielectrics (sections 2.1 and 2.2) allows the iterative application of the graphical method (fig. 2). The step-by-step construction of the field vectors was begun at the perfectly reflecting ground and conducted up to 104 km height. It appeared that not much contribution to the reflection of the waves comes from heights beyond 104 km, though some inaccuracy may arise from stopping at this somewhat low level and from the large width of the individual steps.

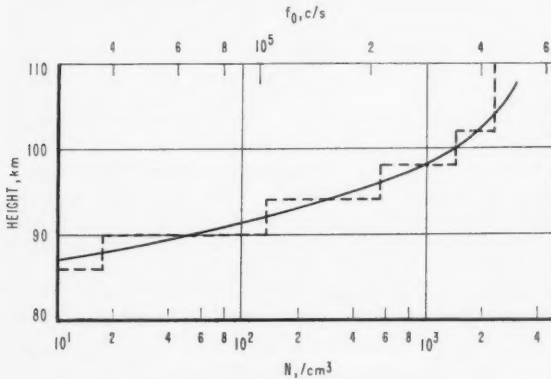


FIGURE 4.  $E$  layer profile.

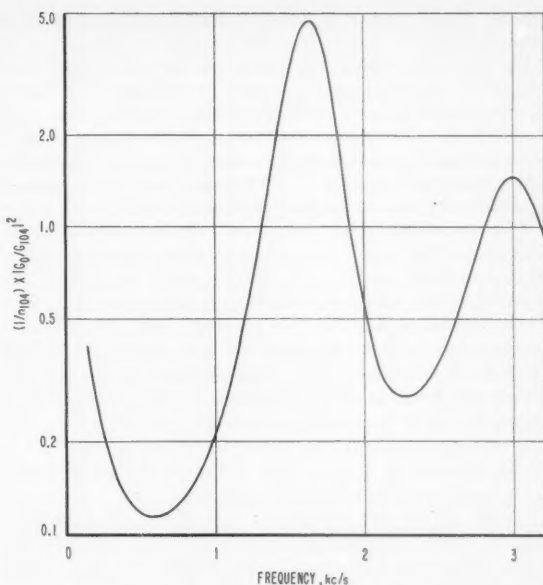


FIGURE 5. Ratio of the Poynting vectors on the ground and in the ionosphere for the profile of figure 4.

The graphical construction was used to derive the intensity variation of the descending wave. The ratio of the Poynting vectors on the ground and in 104 km height,  $(1/n_{104}) \times |G_0/G_{104}|^2$ , is plotted versus frequency in figure 5. The positions of the maxima and minima are not much different from those for a sharply bounded ionosphere (section 2.1), in 90 or 100 km height. The gradient of the electron concentration apparently is too steep to have much influence. A shallower gradient doubtless has some effect and must lead to diminished resonance frequencies as does a  $D$  layer below the  $E$  reflection level (next section). The greatest enhancement of the Poynting vector (fig. 5) is seen to amount to 5 (at 1.63 kc/s), the strongest reduction to 0.11 (at 0.60 kc/s).

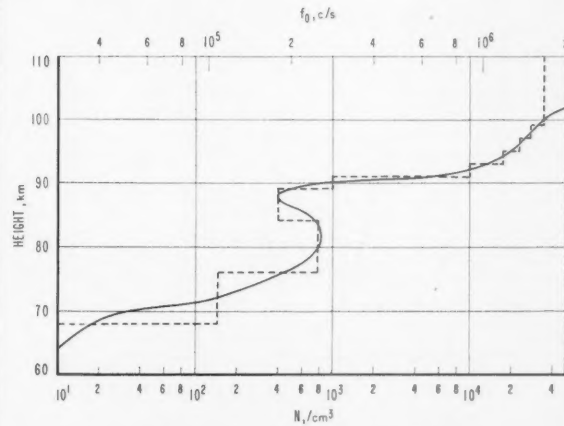


FIGURE 6. Profile of  $D$  layer and  $E$  layer.

### 3.2. D Layer and E Layer, Extraordinary Wave

In daytime, with presence of the *D* layer, the profile of the ionosphere may according to Pfister be that of figure 6 ([Poeverlein, 1959a], fig. 17, curve (b)). The step approximation of this profile leads to the Poynting vector ratio,  $(1/n_{100}) \times |G_0/G_{100}|^2$ , represented in figure 7. The maximum enhancement is 1.02, the strongest reduction 0.06.

The sequence of the resonance peaks seems to be irregular. In fact, the stratification of the ionosphere resembles the simplified model of section 2.2 for which two series of resonances were found. The first resonance peak in the present case (at 440 c/s) corresponds to the first peak of the simplified model (at 509 or 469 c/s) which was explained by the behavior of the field at the bottom of the *E* layer and the phase shift in passing through the *D* layer. In the further course of the resonance curve (fig. 7) it seems impossible to separate the two series of resonance peaks of the simplified model.

There is no pretension to accuracy of figure 7. At the higher frequencies, for which the subdivision of the step function (fig. 6) is not fine enough, some estimates were used in the values plotted.

### 3.3. Ordinary Wave

For the ordinary wave, which is obtained with the minus sign in eq (1), the refractive index is imaginary in most parts of the ionosphere. The graphical method of figure 2 is still usable for imaginary  $n$ ; however, the electric field strengths  $F$  and  $G$  become purely imaginary and have unequal amounts. The two waves ( $F$  and  $G$ ) are attenuated, each in progression in its direction of propagation.

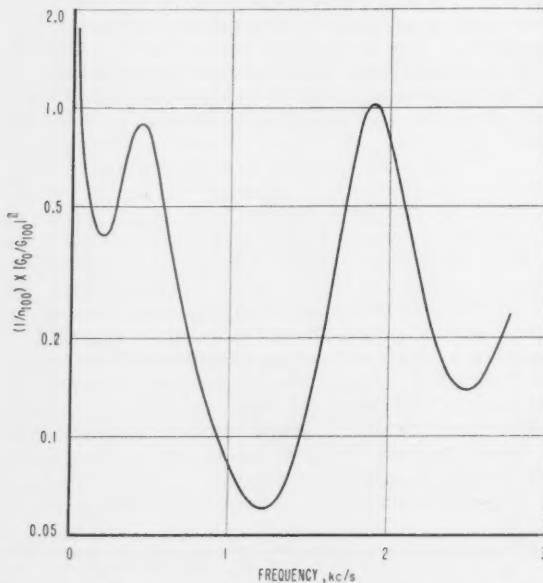


FIGURE 7. Ratio of the Poynting vectors on the ground and in the ionosphere for the profile of figure 6.

The resonance case now is the case of disappearance of *G* in higher altitudes, strictly speaking in the altitude in which the signal is generated. In this case the enhancement of the Poynting vector is infinite, because no initial Poynting vector is present. A finite enhancement would result from considering electron collisions in the refractive index formula. The present study in which collision losses are disregarded allows therefore only the computation of the resonance frequencies. The first resonance frequency in the case without *D* layer (fig. 4) is found to be 1.52 kc/s, nearly the same as for a sharply bounded ionosphere.

Whereas resonance of extraordinary waves may be excited by waves coming down from any altitude within the ionosphere, the ordinary-wave resonance requires emission of radiation not too far beyond the reflection level, in order to have the ordinary waves only slightly attenuated in traveling down. The radiation source may be somewhat above the reflection level of the ordinary waves or in the part of the ionosphere below the reflection level (lower tail of *E*, or *D* layer). The polarizations of ordinary and extraordinary waves show opposite senses of rotation.

### 4. Comparison With Observations

As noted in section 1.3, only an emission of white noise or short pulses in the ionosphere, fulfilling the coherence requirement, would lead to an observation of the derived resonance functions (figs. 5 and 7). In case of a given noise frequency the resonance function determines the enhancement or diminution of the signal on the ground compared with the noise intensity descending from higher altitudes.

The field observable on the ground should be a horizontal *H*. On a perfectly reflecting ground there should be no horizontal *E*. Imperfectness of the ground reflection, however, makes a horizontal *E* possible. Circular polarization as expected from extraordinary (or ordinary) waves would correspond to two horizontal *E* (or *H*) components with 90-deg phase shift.

Noise emissions exhibiting two or sometimes three peaks in the spectrum were observed in the auroral zone in connection with geomagnetic disturbances [Aarons, Gustafsson, and Egeland, 1960; Gustafsson, Egeland, and Aarons, 1960]. The observed spectrum resembles at least roughly the resonance functions. The noise peaks in most cases were near 750 c/s and between 2 and 3.5 kc/s. The peak near 750 c/s is rather stable in frequency. In one event of noise emission, for example, it is reported to have varied as little as  $\pm 150$  c/s. At other occasions there were, however, larger deviations. The observers suggest gyroresonance of protons as cause of the 750-c/s peak.

The second peak in the observed spectrum is more variable. It may be that this peak is caused by resonance enhancement of practically white noise and the first peak by gyroresonance radiation, possibly in near coincidence with our first resonance peak under the prevailing conditions. A clue to the nature of the noises could be obtained from observa-

tion of their polarization. In proton gyroradiation ordinary waves are emitted. Our standing-wave resonance, on the other hand, may preferably be excited by extraordinary waves, as the remarks in section 3.3 indicate. Simultaneous noise observations on the ground and in the ionosphere might also allow a decision about the character of the noises.

For a discussion of VLF and ELF noises with respect to characteristics and possible origin one may refer to Gustafsson, Egeland, and Aarons [1960].

### 5. Additional Remarks

From a *pulse-type signal* emitted in the ionosphere, a series of pulses will be received on the ground. The first pulse reaches the ground immediately after leaving the ionosphere and traveling down through the air space. The others traveled back and forth between earth and ionosphere once or several times.

As previously, only noise signals that have extensive horizontal wave fronts are considered. The spectrum of the received series of pulses is then necessarily identical with the resonance spectrum obtained from white noise emissions in the ionosphere, because a pulse (provided it is short) has the same spectrum as white noise. In the simplified model of a sharply bounded homogeneous ionosphere with a refractive index independent of frequency, there is no distortion of the pulse in the ionospheric reflection, only a reduction of the field strength by a factor  $(n-1)/(n+1)$ . The geometric series of pulses thus obtained has a Fourier spectrum corresponding to eq (4) of the above resonance theory. This proves the equivalence of the two considerations in this special case.

The question arises whether the *whistlers* observed in the audiofrequency band are also affected by resonance of the space between earth and ionosphere. Whistlers in coming down from high altitudes may have extensive wave fronts, but presumably not in a horizontal position. A possible variation of the resonance phenomena resulting from this inclination is not so much of interest now. The modification of the whistler by the resonance effect means nothing but a multiple repetition of the whistler signal, just the same as in the case of pulses. It will not be discussed now whether this repetition may or may not be recognizable in recordings. An important feature of the resonance spectrum is the first minimum, which appears in figure 5 at 600 c/s and will be slightly shifted towards higher frequencies in case of inclined wave fronts. This minimum may contribute to a low-frequency cutoff of the observable whistler spectrum.

The resonance effect this paper deals with refers to standing waves between two parallel reflectors. The *curvature* of the actual reflectors (earth and ionosphere) may necessitate some correction of the theory at the lowest frequencies.<sup>3</sup> The lateral extension of the field must be wide in terms of wavelengths, but does not have to include the entire spherical shell.

<sup>3</sup> For the general theory of VLF propagation between curved earth and ionosphere, refer to Wait [1960].

A resonance effect caused by the spherical shape of the earth is the *resonance of the zero-order mode propagated between earth and ionosphere* which results from winding-up of the waveguide to a spherical shell [Schumann, 1957; König, 1959; Wait, 1960]. The fundamental frequency of this resonance effect corresponds to a phase variation of  $2\pi$  along a path around the earth and amounts according to Schumann [1957] and König [1959] to approximately 9 c/s.

The fundamental frequency of our resonance effect in case of no leakage into the ionosphere is identical with the *cutoff frequency* of the first-order mode between earth and ionosphere, because this cutoff relates to vertically traveling waves. The higher-order resonance frequencies similarly represent the cutoff frequencies of the higher-order modes in this case.

### Appendix 1. Effect of Collisions

The quasi-longitudinal approximation of the refractive index derived from the Appleton-Hartree formula with inclusion of the collision frequency  $\nu$  of the electrons is<sup>4</sup> [Ratcliffe, 1959]

$$n^2 = 1 - \frac{\omega_0^2}{\omega(\omega - i\nu \pm \omega_H |\cos \alpha|)} \quad (14)$$

This approximation is usable at sufficiently high frequencies and at very low frequencies, provided the angle  $\alpha$  between wave normal and terrestrial magnetic field is not near 90 deg. In both cases the approximative formula can be further simplified.

The high-frequency approximation of  $n$  with the assumption of  $\omega \gg \omega_0$ ,  $\omega \gg \omega_H$ , and  $\nu \ll \omega$  is

$$n = 1 - \frac{1}{2} \frac{\omega_0^2}{\omega^2} - i \cdot \frac{1}{2} \frac{\omega_0^2 \nu}{\omega^3} \quad (15)$$

At sufficiently low frequencies we may assume  $\omega_0 \gg \omega$ ,  $\omega_0^2 \gg \omega \omega_H$ ,  $\nu \ll \omega_H$  and obtain then for the extraordinary wave

$$n = \left( \frac{\omega_0^2}{\omega \omega_H |\cos \alpha|} \right)^{\frac{1}{2}} \left( 1 - i \cdot \frac{1}{2} \frac{\nu}{\omega_H |\cos \alpha|} \right) \quad (16)$$

The absorption in ionospheric propagation is given by  $\exp \left( \int \frac{\omega}{c} \text{Imag}(n) \cdot ds \right)$ . The absorption coefficient thus is at high frequencies

$$\frac{\omega}{c} |\text{Imag}(n)| = \frac{1}{2} \frac{\omega_0^2 \nu}{\omega^2 c} \quad (17)$$

and at sufficiently low frequencies

$$\frac{\omega}{c} |\text{Imag}(n)| = \frac{1}{2} \frac{\omega_0 \omega^{\frac{1}{2}}}{(\omega_H |\cos \alpha|)^{3/2}} \frac{\nu}{c} \quad (18)$$

The absorption coefficient for high frequencies, eq (17), shows the familiar frequency dependence of

<sup>4</sup> Angular frequencies are written in place of the frequency quantities of eq (1).

the "nondeviative" absorption (with neglect of  $\omega_H$  compared with  $\omega$ ). The absorption coefficient for very low frequencies, however, decreases with decreasing frequency. This has the consequence that at our rather low frequencies the absorption in the lower ionosphere is only small.

A numerical evaluation based on eq (14) and daytime data of the  $D$  layer (fig. 6 and  $\nu$  as noted) gave the following amounts of the absorption coefficient of the extraordinary wave at 1 kc/s (for  $f_H |\cos \alpha| = 1.2 \cdot 10^6$  c/s):

0.021 per km in 72 km with  $\nu = 10^7$  per sec,

0.019 per km in 80 km with  $\nu = 2 \cdot 10^6$  per sec.

These values should lead to a considerable absorption on paths of 50 km length, but the absorption coefficient decreases rapidly above 80 km and the decisive vertical path lengths are shorter.

A closer investigation of the absorption and its influence on the resonance curve are still desirable, but the above estimate suggests that the absorption is small and may not deteriorate badly the resonance curves, particularly not at the lower frequencies. At night the absorption coefficients are much smaller than the ones derived for daytime and in daytime the lowest resonance frequency is below 1 kc/s, as figure 7 shows.

It may be pointed out that the absorption coefficients for high and very low frequencies are different not only in their variation with frequency but also in their dependence on  $\omega_0$ . The absorption coefficient, of course, is not in an immediate connection with the reflection coefficient of the lower ionosphere at very low frequencies.

## Appendix 2. Wave Theory Based on the Vector Method

The construction of the complex field strength vectors (fig. 2) can be used for a rigorous wave-theoretical treatment of propagation in a medium that varies continuously with one coordinate. It was seen that the method of constructing field vectors is applicable to a step approximation of a continuously varying medium. The start of the graphical procedure was at a perfect reflector, in our case the ground. The solution consequently is a standing-wave solution.

If propagation of plane waves in a continuously varying medium is to be studied, we replace the medium by an approximative step function and add a perfect reflector somewhere outside, thus creating conditions for the vector method and a standing-wave solution. A traveling-wave solution or any more general solution follows from superposition of two independent standing-wave solutions. These two standing-wave solutions may either be obtained by assuming the perfect reflector at two different locations or by assuming two alternative reflectors, one that does and one that does not reverse the electric field strength in reflection of the incident wave. The only approximation introduced is the step function.

By making the steps differentials the method becomes rigorous. Nevertheless, the method has certain limitations. Before showing them, a brief analytical formulation will be given.

The medium will be assumed to vary with the coordinate  $z$ . For waves propagated in the direction of the gradient, the field strengths may then be written

$$\left. \begin{aligned} E_x &= C(z) \sin [\int n(z) k_0 dz + \phi(z)] \\ H_y &= i \sqrt{\frac{\epsilon_0}{\mu_0}} n(z) C(z) \cos [\int n(z) k_0 dz + \phi(z)] \end{aligned} \right\}. \quad (19)$$

The time variation factor  $\exp(i\omega t)$  has been omitted. The amplitude function  $C(z)$  and the phase function  $\phi(z)$  are sought.  $E_x$  and  $H_y$  represent transverse field strengths only. An additional longitudinal electric field component  $E_z$  may however exist, due to the anisotropy of the medium. The polarization of the wave in the  $x, y$  plane must be constant in order to have the continuity considerations of the next paragraph valid. The polarization may be linear (with  $E_x$  and  $H_y$  only) or circular (for example with  $E_y = iE_x, H_z = -iH_y$ ).

The continuity of  $E_x$  and  $H_y$  at boundaries requires that at the steps of the step function

$$\left. \begin{aligned} \Delta(Cs) &= 0 \\ \Delta(nCc) &= 0 \end{aligned} \right\}. \quad (20)$$

Herein  $s$  and  $c$  are abbreviations for the sine and cosine appearing in eqs (19):

$$\left. \begin{aligned} s &= \sin [\int nk_0 dz + \phi] \\ c &= \cos [\int nk_0 dz + \phi] \end{aligned} \right\}. \quad (21)$$

The integral term in the argument of these functions varies continuously. Only  $\phi$  is supposed to jump at the steps of the step function. The differences of  $s$  and  $c$  needed in eqs (20) are therefore

$$\left. \begin{aligned} \Delta s &= c \Delta \phi \\ \Delta c &= -s \Delta \phi \end{aligned} \right\}. \quad (22)$$

Equations (20) together with eqs (22) yield

$$\left. \begin{aligned} \frac{\Delta C}{C} &= -\frac{\Delta n}{n} c^2 \\ \Delta \phi &= \frac{\Delta n}{n} sc \end{aligned} \right\}. \quad (23)$$

Making the steps differentials leads to the rigorous wave-theoretical differential equations for  $C$  and  $\phi$

$$\left. \begin{aligned} \frac{dC}{C} &= -\frac{dn}{n} c^2 \\ d\phi &= \frac{dn}{n} sc \end{aligned} \right\}. \quad (24)$$

It has to be noticed that the quantities  $s$  and  $c$  in eqs (24) are functions of  $\phi$  (eqs (21)). The last of eqs (24) allows the computation of the phase function  $\phi$  without considering the amplitude function, whereas the first equation involves both the amplitude function and the phase function. Equations (24) are also readily obtained from Maxwell's equations.

A set of equations closely related to eqs (24) has been derived by van Cittert [1939] [Kofink, 1947]. Van Cittert considered oblique incidence on a one-dimensionally stratified medium. His equations therefore are more general in this respect. The medium he assumes as isotropic. The equations are necessarily different for the two cases of (linear) polarization.

*Slow variation of the refractive index* suggests averaging the factors  $c^2$  and  $sc$  over many periods of  $c$  and  $s$ . Equations (24) then become approximately

$$\left. \begin{aligned} \frac{dC}{C} &= -\frac{1}{2} \frac{dn}{n} \\ d\phi &= 0 \end{aligned} \right\}, \quad (25)$$

whence we obtain

$$\left. \begin{aligned} C &\propto \frac{1}{\sqrt{n}} \\ \phi &= \text{const} \end{aligned} \right\}. \quad (26)$$

This is the behavior of amplitude and phase in the geometric-optical approximation.

The above study was limited to *normal* incidence on a one-dimensionally stratified medium. A generalization for *oblique incidence* (on a one-dimensionally stratified medium) may not be difficult, as van Cittert's formulation shows. The *more severe limitation* arises from the demand of constant polarization. In case of oblique incidence the polarization in the planes of the stratification has to stay constant. This is easily achieved in isotropic media. In anisotropic media constant polarization is obtained in normal incidence if the polarization can be assumed as circular, independent of the location in the layer. In more general cases of propagation in anisotropic media (oblique incidence or elliptic polarization) the polarization in the planes of the stratification varies. The continuity at the steps of our step function can then be preserved only by simultaneous consideration of ordinary and extraordinary waves with variable amplitude factors. This indicates the well-known phenomenon of coupling between the two types of waves.

The step method is not applicable near a *zero of the refractive index*. In approaching the zero, the required step length decreases towards zero. However, a rigorous expression for the refractive index that includes the collision frequency has no zero at any location.

*Complex refractive index* leaves the analytical formulations valid, but makes the graphical procedure of figure 2 more intricate.

The author thanks James R. Wait for a stimulating discussion and Thomas J. Birmingham for help in preparing the manuscript.

## References

Aarons, J., G. Gustafsson, and A. Egeland, Correlation of audio-frequency electromagnetic radiation with auroral zone micropulsations, *Nature* **185**, 148-151 (Jan. 1960).  
 Casey, J. P., Jr., and E. A. Lewis, Interferometer action of a parallel pair of wire gratings, *J. Opt. Soc. Am.* **42**, 971-977 (Dec. 1952).  
 Gallet, R. M., and R. A. Helliwell, Origin of "very-low-frequency emissions," *J. Research NBS* **63D** (Radio Prop.) 21-27 (July-August 1959).  
 Gustafsson, G., A. Egeland, and J. Aarons, Audio-frequency electro-magnetic radiation in the auroral zone, *J. Geophys. Research* **65**, 2749-2758 (Sept. 1960).  
 Kofink, W., Reflexion elektromagnetischer Wellen an einer inhomogenen Schicht, *Ann. Physik*, Ser. 6, **1**, 119-132 (1947).  
 König, H., Atmosphères geringster Frequenzen, *Zeit. angew. Physik* **11**, 264-274 (July 1959).  
 Poeverlein, H., Lang- und Längstwellenausbreitung, *Fortschritte der Hochfrequenztechnik* (Akademische Verlagsgesellschaft, Wiesbaden), **4**, pp. 47-101 (1959a).  
 Poeverlein, H., Transparency of the ionosphere and possible noise signals from high altitudes at extremely low frequencies, *AGARDograph 42* on the AGARD Symposium, Paris, May 1959, pp. 345-354 (1959b).  
 Potter, R. K., Analysis of audio-frequency atmospheres, *Proc. IRE* **39**, 1067-1069 (Sept. 1951).  
 Ratcliffe, J. A., The magneto-ionic theory and its applications to the ionosphere (Cambridge University Press), pp. 75-76 (1959).  
 Schumann, W. O., Über elektrische Eigenschwingungen des Hohlraumes Erde-Luft-Ionosphäre, erregt durch Blitzentladungen, *Zeit. angew. Physik* **9**, 373-378 (Aug. 1957).  
 Storey, I. R. O., An investigation of whistling atmospheres, *Phil. Trans. Roy. Soc. London A* **246**, 113-141 (July 1953).  
 van Cittert, P. H., On the propagation of light in inhomogeneous media, *Physica* **6**, 840-848 (Aug. 1939).  
 von Trentini, G., Partially reflecting sheet arrays, *IRE Trans. AP-4*, 666-671 (Oct. 1956).  
 Wait, J. R., Reflection from a wire grid parallel to a conducting plane, *Can. J. Phys.* **32**, 571-579 (Sept. 1954).  
 Wait, J. R., Terrestrial propagation of very-low-frequency radio waves, a theoretical investigation, *J. Research NBS* **64D** (Radio Prop.) 153-204 (March-April 1960).

(Paper 65D5-152)



# Observed Attenuation Rate of ELF Radio Waves

A. G. Jean, A. C. Murphy, J. R. Wait, and D. F. Wasmundt

Contribution from Central Radio Propagation Laboratory,  
National Bureau of Standards, Boulder, Colo.

(Received April 27, 1961)

Propagation attenuation rates for frequencies below 1 kc/s in the ELF region (30 c/s to 3,000 c/s) were calculated from the spectra of atmospherics observed at widely-spaced stations. Data are presented for east to west propagation under sunset approaching the eastern station. Under these conditions, the attenuation rates are about 1 db/1,000 km at 75 c/s and increase with increasing frequency, attaining about 3 db/1,000 km at 200 c/s. The attenuation rates observed seem to be consistent with a two-layered ionosphere model with its lower region 90 km above the earth.

## 1. Introduction

It is now accepted that radio waves in the ELF (extremely low frequency) region, extending from c/s to 3,000 c/s, propagate mainly in the waveguide bounded by the earth and ionosphere in the principal or zero-order mode. In recent years, a number of workers have investigated the propagation of ELF waves using atmospherics as signals, in lieu of more suitable man-made signals [Holzer and Deal 1956, Chapman and Macario 1956, Liebermann 1957, Pierce 1960, Smith 1960, and Watt 1960].

In most of the work carried out to date, observations were made at a single station of a large number of atmospherics having their origins in lightning discharges at different ranges from the receiver. The locations of individual lightning discharges were determined using direction finding systems or, in some cases, estimates of the storm locations were arrived at from meteorological information; thus, Chapman and Macario [1956] recorded waveforms at a single station while the locations of the lightning flashes were obtained from an atmospherics direction finding network. Propagation attenuation rates were then extracted from differences between the spectra of waveforms received at different ranges and from different sources. In this technique, some assumptions regarding the constancy of the radiation spectra of the sources must be made.

It would be of interest to determine propagation attenuation rates from waveforms of the same atmospherics observed at different ranges; especially with the observing stations lying approximately along a great circle path passing through the origin of the lightning discharges. In this favorable circumstance, fewer assumptions regarding the radiation spectra of the sources need be made.

Such observations were made recently through the cooperation of the USAF who supplied atmospheric direction finding records from which the locations

and times of occurrence of individual lightning discharges were determined.

In this paper some preliminary results of atmospheric waveforms in the ELF band are presented. Data are presented here resulting from fortunate alignments of storms and two recording stations approximately along great circle paths. The resultant attenuation rates are compared with theoretical and other experimentally-determined values.

The simultaneous recordings of atmospheric waveforms of the vertical electric field were carried out at Boulder, Colorado; Fairbanks, Alaska; and Maui, Hawaii in the spring of 1960. The equipment at each of the stations consisted of a 25 ft vertical antenna with an isolating cathode-follower connected directly to its base. The input impedance of the cathode-follower was approximately 400 meg. A coaxial transmission line connected the output of the cathode-follower with the amplifiers located in the recording building approximately 200 feet away from the antenna. The remainder of the equipment consisted of an amplifier, filters, oscilloscope and strip-film camera. The recording equipment and its performance were the same at each station.

The overall amplitude versus frequency response of the recording apparatus, including a capacitor of  $100 \mu\text{f}$  to simulate the antenna, is flat within 1 db between 30 c/s and 400 c/s and within 3 db between 15 c/s and 1 kc/s (see fig. 1). The decrease in amplitude response at the higher frequencies, to eliminate interference from transmitters operating in the VLF region, was accomplished through the use of RC filters. The decrease in response at frequencies below 45 c/s is a result of the time-constant of the interstage coupling capacitors and a reduction in voltage transferred from the capacitive antenna to the cathode-follower.

All of the receiving sites were located two miles or more from commercial power lines to minimize the reception of power line interference. Electrical

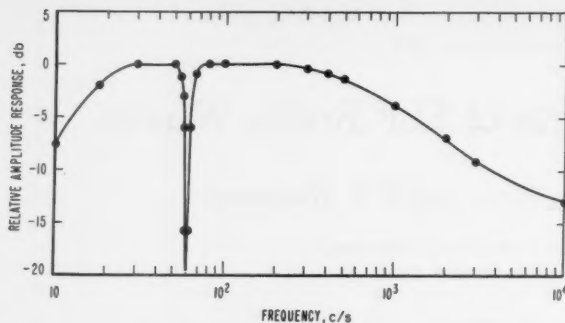


FIGURE 1. Amplitude versus frequency response of recording equipment.

power was supplied to the recording equipment by diesel-electric generators. After taking these precautions, it was found that the predominant interference was received from the distant power lines. At Maui and Boulder, the 60 c/s interference (before filtering) amounted to about 5 mv/m and 10 mv/m, respectively. By comparison, the amplitude of received signals varied over a range of about 5 mv/m to 100 mv/m. It was found advantageous to use a narrow-tuned filter to reject the 60 c/s power line interference. In plotting the spectra of the atmospherics, spectral components at 60 c/s were found by interpolating from components at frequencies either side of 60 c/s.

Recordings were made simultaneously at each station on continuously-moving film, which was advanced past the cathode-ray tube at a speed of 50 cm/sec. The film motion provided the sweep necessary to resolve the ELF components.

## 2. Theoretical Considerations

Let  $G(t,d)$  represent the amplitude variations of an atmospheric waveform in time,  $t$ , and at distance,  $d$ , such that

$$| G(t,d) = 0 \text{ for } t < 0 \text{ and } t > \tau, \quad (1)$$

where  $\tau$  is the duration of the waveform. The Fourier spectrum of the waveform is then

$$E(\omega, d) = \int_0^\infty G(t, d) \cdot e^{-i\omega t} dt = \int_0^\tau G(t, d) e^{-i\omega t} dt, \quad (2)$$

where  $\omega$  is the angular frequency. It is assumed that the source is equivalent to a vertical dipole and that the ELF waves of interest here propagate in the earth ionosphere waveguide in the zero-order mode. The spectrum amplitude of such a pulse, propagating in the zero-order mode, can be represented by an expression of the form

$$E(\omega, d) \cong A(\omega) [a \sin(d/a)]^{-1/2} e^{-\alpha(\omega)d}, \quad (3)$$

where  $A(\omega)$  represents the amplitude spectrum of the source function,  $a$  is the earth's radius in kilometers, and  $\alpha(\omega)$  is the attenuation in nepers per unit distance. Equation (3) is valid at ELF provided the sources are at least 1,000 km from the receiving antennas [Wait, 1960]. It is also necessary, of course, that the observer is not near the antipode of the source.

If the waveform of the same atmospheric is observed at two distances,  $d_1$  and  $d_2$ , where  $d_2 > d_1$ , it follows that

$$\exp[\alpha(\omega) \cdot (d_2 - d_1)] = \frac{|E(\omega, d_1)|}{|E(\omega, d_2)|} \cdot \left[ \frac{\sin d_1/a}{\sin d_2/a} \right]^{1/2}. \quad (4)$$

Using this expression, the attenuation rate as a function of frequency was obtained from the spectra of atmospherics observed simultaneously at distances  $d_1$  and  $d_2$ . Then the attenuation rate in decibels per 1,000 km of path length is given by

$$\alpha(\omega) = \left[ 20 \log \frac{|E(\omega, d_1)|}{|E(\omega, d_2)|} - 10 \log \frac{\sin d_2/a}{\sin d_1/a} \right] \cdot \frac{10^3}{d_2 - d_1}, \quad (5)$$

where the logarithms are to base 10.

The amplitude spectra of atmospheric number 1 observed at the three stations are shown in figure 2. The spectrum of highest amplitude represents observations made at Boulder, the shortest range; the spectrum of smallest amplitude represents observations made at Maui, the greatest range; while

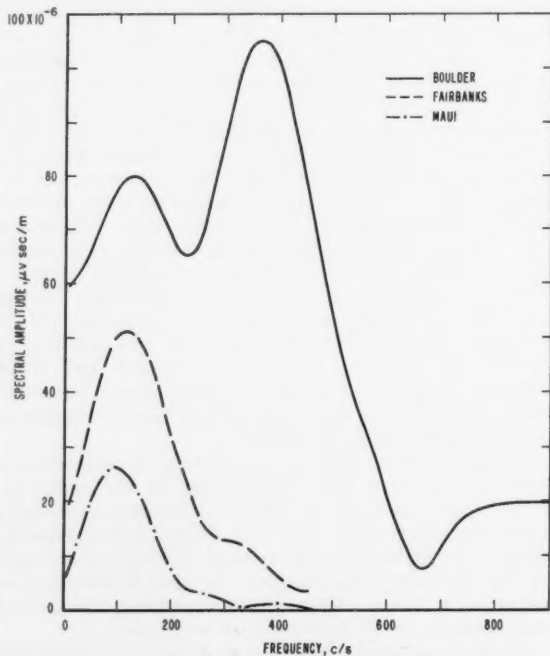


FIGURE 2. Amplitude spectra of atmospheric number 1 observed at Boulder, Fairbanks, and Maui.

the intermediate values represent the Fairbanks observations. It is evident from these spectra that the frequency of peak amplitude decreases with increasing distance. For example, the frequency of maximum energy of atmospheric number 1 is about 300 c/s at 4,500 km and 100 c/s at 9,600 km. It will be noted that the spectral width of the atmospheric narrows with increasing distance. The range of frequencies over which the attenuation can be calculated is limited to the width of the narrowest

spectrum. The spectra and bandpass characteristic of the receiver indicate that the attenuation rates for the Boulder to Maui path should be valid over a frequency range of about 50 c/s to about 250 c/s.

In a similar manner, the spectra of atmospherics numbers 2, 3, and 4, observed at Boulder, Fairbanks, and Maui, are given in figures 3, 4, and 5.

In figure 6, the propagation attenuation rates in db/1,000 km derived from atmospherics numbered 1, 2, 3, and 4 are plotted against frequency for the

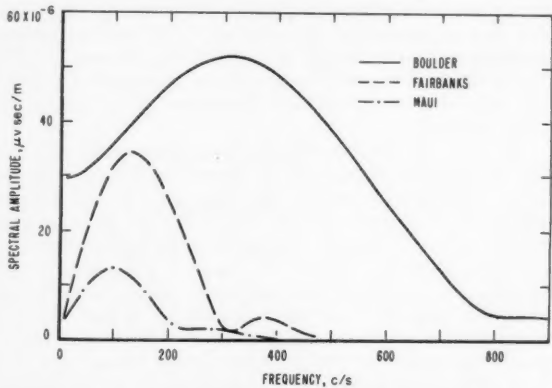


FIGURE 3. Amplitude spectra of atmospheric number 2.

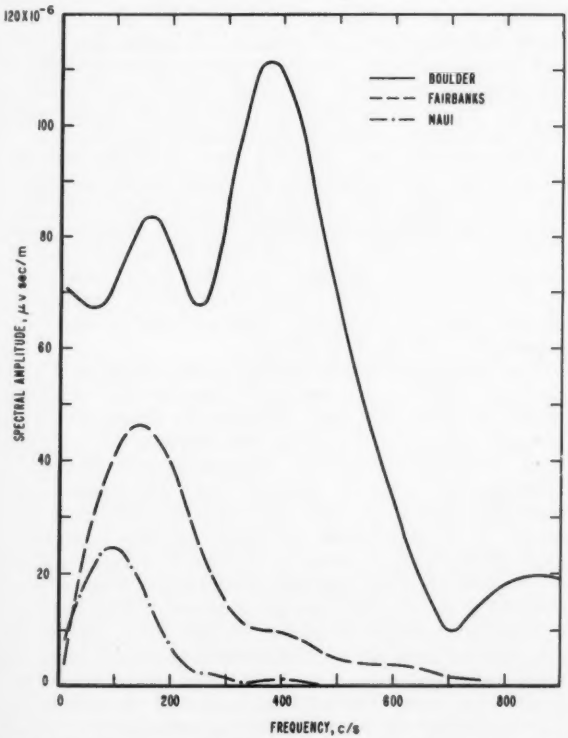


FIGURE 4. Amplitude spectra of atmospheric number 3.

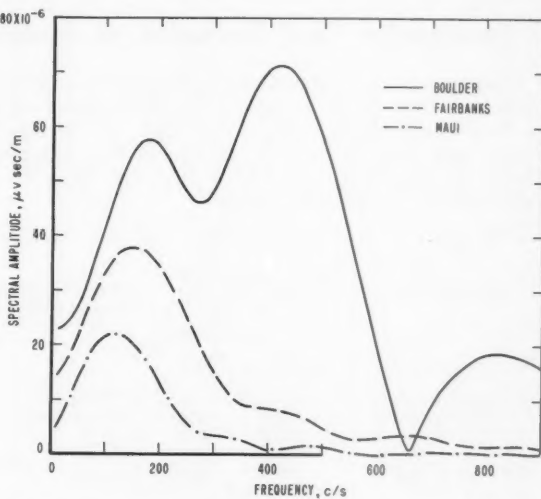


FIGURE 5. Amplitude spectra of atmospheric number 4.

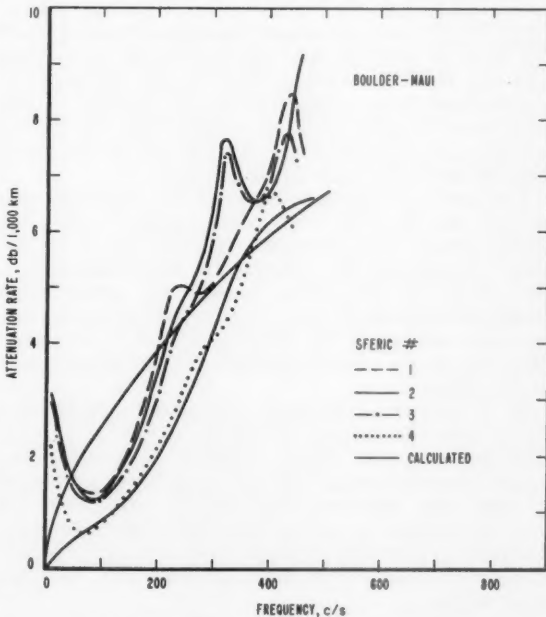


FIGURE 6. Propagation attenuation rates versus frequency derived from atmospherics 1-4 compared with calculated rates (see text).

Boulder to Maui pair. Attenuation rates derived from numbers 1, 2, and 3 were recorded when sunset was at the eastern end of the path (1835 MST) and have minimum values of about 1.25 db/1,000 km near 75 c/s. Somewhat lower rates are observed at 75 c/s for atmospheric number 4 which was recorded an hour later. It is tempting to attribute the lower attenuation rate observed at 1935 to the increased amount of darkness along the path—although the occurrence of sunset along the path complicates the situation.

### 3. Presentation and Discussion of Results

During two, 2-minute recording intervals beginning 1835 and 1935 MST on March 8, 1960, waveforms of five atmospherics were recorded at Boulder, Maui, and Fairbanks from storms in the Atlantic Ocean at approximately 39° N and 58° W. This information is tabulated below.

Atmospheric		Approximate range from source to		Time of reception of atmospheric at Boulder
No.	Location	Boulder	Maui	
1	39°N, 59°W	4500	9600	1835:52 MST
2	39°N, 65°W	3500	8700	1836:25
3	37°N, 61°W	3500	8800	1836:07
4	39°N, 58°W	4500	9600	1935:58

The propagation paths from the sources to Boulder were in darkness. At the time of the first observation (1835 MST), ground sunset was approximately 600 km west of Boulder and approximately 1,900 km west of Boulder during the second observation. In the first case, approximately 90 percent of the path from Boulder to Maui was in daylight; in the second case, approximately 75 percent of the path from Boulder to Maui was in daylight.

The paths of propagation from the lightning discharges to Boulder and Maui, respectively, are approximately east-to-west and transverse to the earth's magnetic field. Waveform observations were also made at Fairbanks, Alaska and attenuation rates were calculated from the Boulder and Fairbanks data also, although this is a less favorable situation since the paths of propagation are not along great circle paths.

As a matter of interest, calculated attenuation curves are also shown in figure 6. A two layer ionospheric model [Wait 1958] is employed; the height of the bottom of the reflecting layer is denoted  $h'$ , and the effective conductivity parameter is  $\omega'$ . At height  $d$  above this, the effective conductivity is assumed to jump to a new value of  $\omega''$ . The curves shown in figure 6 correspond to the two cases where

(i)  $\omega'=10^5$ ,  $h=90$  km,  $d=\infty$  (upper calculated curve)

(ii)  $\omega'=10^5$ ,  $h=90$  km,  $d=20$  km (lower calculated curve)

$$\omega''=10^6$$

The first of these cases corresponds, of course, to a homogeneous ionosphere. The resulting attenuation should be proportional to (frequency)<sup>4</sup>. This would lead to a convex curve which is clearly not in accord with the data. The second of these curves has the required form; the ionosphere is thus behaving as a stratified conductor. For the lower frequencies, the upper well-conducting layer is becoming effective and the attenuation is reduced. Of course, other combinations of  $d$  and  $\omega''$  could be chosen to fit the facts, but it would always be necessary to have the effective conductivity increase with height in some manner.

An average of the attenuation rates observed for the Boulder to Maui path is shown in figure 7 (solid line). There appears to be minimum in the attenuation rate of about 1.0 db/1,000 km of path length near 70 c/s. The rate increases with increasing frequency attaining values of about 1.5 db/1,000 km at 135 c/s, 2 db at 160 c/s, etc. The increase in observed attenuation at frequencies below 70 c/s is doubtful; it is thought that the data are influenced by noise at frequencies below about 70 c/s. However, it is possible to construct a layer model which does have an attenuation increase as the frequency becomes very much lower. Such a model might consist of a three-layer ionosphere with parameters  $\omega'$ ,  $\omega''$ , and  $\omega'''$ . If  $\omega'''$  is taken to be somewhat less than  $\omega''$  and  $\omega'$ , a lower frequency will be reached where the attenuation is controlled by the outermost layer of conductivity  $\omega'''$  [Wait 1957]. It is also possible that heavy ions may influence the results in frequencies below 100 c/s.

Attenuation rates derived from the Boulder to Fairbanks and Fairbanks to Maui data are also plotted in figure 7. These data are subject to additional limitations in interpretations; however, the rates are about the same as those presented for the largely sea-water Boulder to Maui path. In view of the theory for ELF propagation [Wait, 1960], the effects due to ground conductivity would be expected to be small if present.

The propagation attenuation rates in figure 7 are compared with more complete data for day and for night by Chapman and Macario in figure 8. The present data plots between the daytime and nighttime values reported by Chapman and Macario. Perhaps this is to be expected since the paths were partially dark at the east end, and in daylight to the west. It is of interest to recall that the Chapman and Macario data were recorded at ranges up to 4,000 km while the present data results from observations at a minimum range of about 4,000 km and a maximum range of about 10,000 km. Although the present data are not very comprehensive, they do confirm attenuation rates resulting from other experiments using different techniques. In addition, the feasibility of deriving propagation data at ELF from spectral analyses of atmospherics is established.

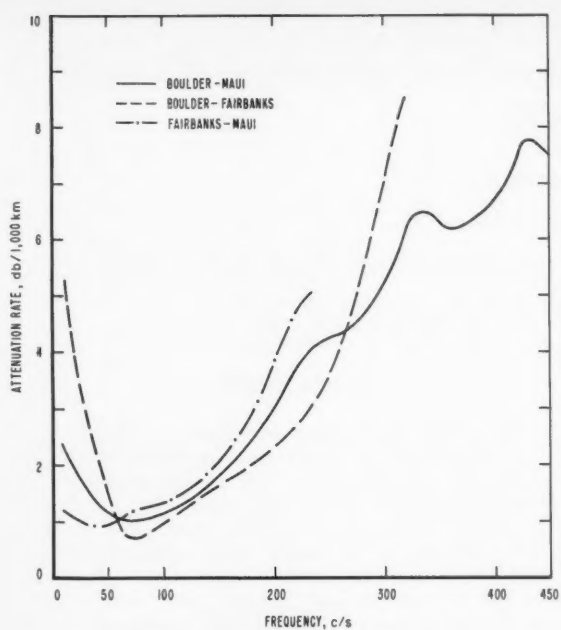


FIGURE 7. Average of propagation attenuation rates versus frequency for atmospherics 1-4.

#### 4. References

Chapman, F. W. and R. C. V. Macario, Propagation of audiofrequency radio waves to great distances, *Nature* **177**, 930 (1956).  
 Holzer, R. E. and O. E. Deal, Low audiofrequency electromagnetic signals of natural origin, *Nature* **177**, 536 (1956).  
 Liebermann, L., Anomalous propagation below 500 c/s, *Symp. Prop. VLF Radio Waves* **3**, No. 25, Boulder, Colo. (1957).  
 Pierce, E. T., Some ELF phenomena, *J. Research NBS* **64D**, No. 4, 383-386 (July-Aug. 1960).  
 Smith, E. J., The propagation of low-audio frequency electromagnetic waves, *Ph. D. dissertation*, Univ. of Calif. at Los Angeles, Feb. 1960.

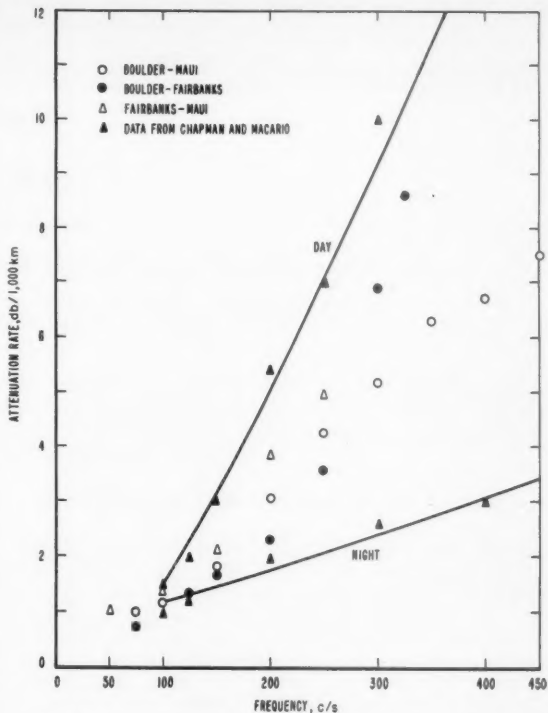


FIGURE 8. Comparison of figure 7 propagation attenuation rates with Chapman and Macario Data.

Wait, J. R., The mode theory of VLF ionospheric propagation for finite ground conductivity, *Proc. IRE* **45**, 760 (1957).  
 Wait, J. R., An extension to the mode theory of VLF ionospheric propagation, *J. Geophys. Research* **63**, 125 (1958).  
 Wait, J. R., Mode theory on the propagation of ELF radio waves, *J. Research NBS* **64D**, 387-404 (July-Aug. 1960).  
 Watt, A. D., ELF electric fields from thunderstorms, *J. Research NBS* **64D**, No. 5, 425-434 (Sept.-Oct. 1960).

(Paper 65D5-153)



# A Note Concerning the Excitation of ELF Electromagnetic Waves

James R. Wait

(Received March 30, 1961)

Contribution From Central Radio Propagation Laboratory, National Bureau of Standards, Boulder, Colo.

Previous solutions for the ELF mode series are discussed briefly. Particular attention is paid to the height-gain functions. The excitation of the modes for vertical and horizontal dipole excitation is also considered.

## 1. Introduction

In a number of earlier papers [Wait, 1960a and b] the author discussed the theory of electromagnetic wave propagation in the extremely low frequency range (i.e., 1.0 to 3000 c/s). The model adopted is a smooth homogeneous earth surrounded by a concentric reflecting layer which is to represent the ionosphere. The field was represented by a sum of modes for both vertical and horizontal electric dipole excitation. Essentially the same model has been used by Schumann [1954] but some of his results differ from those of Wait [1960a]. It is the purpose of this note to discuss certain extensions and limitations of the theory.

Initially the earth is taken to be flat. This idealization simplifies the discussion. Furthermore, for ELF, influence of sphericity can be introduced later in the analysis.

## 2. Formulation

Choosing the usual cylindrical coordinate system  $(\rho, \phi, z)$  the earth's surface is at  $z=0$  and the ionospheric reflecting layer is at  $z=h$ . Free space of electrical constant  $\epsilon_0, \mu_0$  occupies the space  $0 < z < h$ . At  $z=0$  and  $z=h$ , it is further assumed that the fields satisfy the Leontovich boundary conditions. Again this is not an essential restriction but it does simplify the discussion somewhat. Thus

$$\left. \begin{aligned} E_\rho &= -Z_g H_\phi \\ E_\phi &= Z_g H_\rho \end{aligned} \right\} \text{at } z=0 \quad (1)$$

and

$$\left. \begin{aligned} E_\rho &= Z_i H_\phi \\ E_\phi &= -Z_i H_\rho \end{aligned} \right\} \text{at } z=h \quad (2)$$

where

$$Z_g = (i\mu_0\omega/\sigma_g)^{\frac{1}{2}} = \Delta_g/\eta,$$

and

$$Z_i = (i\mu_0\omega/\sigma_i)^{\frac{1}{2}} = \Delta_i/\eta,$$

in terms of the (complex) conductivities  $\sigma_g$  and  $\sigma_i$  of the earth and the ionosphere, respectively. The preceding forms for  $Z_g$  and  $Z_i$  are valid at ELF

when the earth and the ionosphere are both equivalent to isotropic conductors [Wait, 1960b]. In the above,  $\eta \cong 120\pi$  ohms and  $\Delta_g$  and  $\Delta_i$  are dimensionless complex quantities.

## 3. General Form of the Mode Series

First the source is taken to be a vertical electric dipole (of current  $I$  and length  $ds$ ) located at  $z=z_0$ , where  $0 < z_0 < h$ . From a previous analysis the fields, in the space  $0 < z < h$ , are obtained from

$$\begin{aligned} E_z &= WE_0, \\ E_\rho &= -SE_0, \\ H_\phi &= -TE_0/\eta, \end{aligned} \quad (3a)$$

where

$$E_0 = i(\eta/\lambda) Ids(e^{-ik\rho})/\rho, \quad (3b)$$

is a reference field and  $W$ ,  $S$ , and  $T$  are dimensionless factors which are expressible as a sum of modes. In the usual notation, the latter are given explicitly by

$$W = -i\pi \frac{\rho}{h} e^{ik\rho} \sum_{n=0}^{\infty} \delta_n S_n^2 H_0^{(2)}(kS_n\rho) f_n(z_0) f_n(z) \quad (4)$$

$$S = \frac{\pi\rho}{h} e^{ik\rho} \sum_{n=0}^{\infty} \delta_n S_n H_1^{(2)}(kS_n\rho) f_n(z_0) g_n(z) \quad (5)$$

$$T = -\frac{\pi\rho}{h} e^{ik\rho} \sum_{n=0}^{\infty} \delta_n S_n H_1^{(2)}(kS_n\rho) f_n(z_0) f_n(z) \quad (6)$$

where

$$\delta_n = \left[ 1 + i \frac{\partial [R_i(C)R_g(C)]/\partial C}{2khR_i(C)R_g(C)} \right]_{C=C_n}^{-1}, \quad (7)$$

$$R_g(C) = \frac{C - \Delta_g}{C + \Delta_g}, \quad (8)$$

$$R_i(C) = \frac{C - \Delta_i}{C + \Delta_i}, \quad (9)$$

and

$$2f_n(z) = [R_g(C_n)]^{-\frac{1}{2}} e^{ikC_n z} + [R_g(C_n)]^{\frac{1}{2}} e^{-ikC_n z}, \quad (10)$$

$$2g_n(z) = C_n [R_g(C_n)]^{-\frac{1}{2}} e^{ikC_n z} - C_n [R_g(C_n)]^{\frac{1}{2}} e^{-ikC_n z}. \quad (11)$$

$H_0^{(2)}$  and  $H_1^{(2)}$  are the Hankel functions of the second kind of order zero and one.  $C_n$  are the solutions of the mode equation

$$R_g(C)R_i(C)e^{-i2khC} = e^{-i2\pi n} \quad (12)$$

and

$$S_n = (1 - C_n^2)^{\frac{1}{2}}.$$

#### 4. Height-Gain Functions

While the above result was given in previous papers [Wait, 1960a and b] its significance was not fully discussed there. Furthermore, the heights of source and observer above the ground were taken to be zero. It is of interest to look into the nature of the solution under more general conditions.

The function  $W$  is considered first. It is the ratio of the actual vertical electric field  $E_z$  to the reference field  $E_0$  of the same dipole source if it, and the observer, were on the surface of a flat perfectly conducting plane. If  $k\rho \gg 1$ , corresponding to the "far-zone", it follows that

$$W \approx \frac{(\rho/\lambda)^{\frac{1}{2}}}{h/\lambda} e^{i\left(\frac{2\pi\rho}{\lambda} - \frac{\pi}{4}\right)} \sum_{n=0}^{\infty} \delta_n S_n^{3/2} e^{-i2\pi S_n \rho/\lambda} f_n(z_0) f_n(z), \quad (13)$$

where  $\lambda$  is the free-space wavelength. The vertical field  $E_z$  is thus proportional to a sum of modes whose amplitudes are proportional to

$$\frac{1}{\rho^{\frac{1}{2}}} \exp[-\text{Im } 2\pi S_n \rho/\lambda].$$

At short distances, such that

$$\rho \ll h, \quad W \rightarrow \left(1 - \frac{i}{k\rho} - \frac{1}{k^2 \rho^2}\right), \quad (14)$$

provided  $z = z_0 = 0$ . This is the expected behavior for a dipole if the reflecting layer (at  $z = h$ ) was neglected. Numerical values of  $W$  were presented on previous occasions for the intermediate range where  $k\rho$  is unrestricted but  $z = z_0 = 0$  [Wait and Carter, 1960].

As can be seen from (4), the height dependence of the individual modes is described entirely by the function  $f_n(z)$ . When  $z = 0$ , we see that

$$[f_n(0)]^2 = \frac{C_n^2}{C_n^2 - \Delta_g^2}. \quad (15)$$

For most applications to ELF propagation,  $|C_n^2| \gg |\Delta_g^2|$ , and thus  $f_n(0)$  can be replaced by unity. This approximation is contained implicitly in earlier work. For present purposes it appears to be preferable to define a "height-gain function" in the manner

$$F_n(z) = \frac{f_n(z)}{f_n(0)}. \quad (16)$$

Using (10) this can be rewritten in the form

$$\begin{aligned} F_n(z) &= \frac{e^{ikC_n z} + R_g(C_n) e^{-ikC_n z}}{1 + R_g(C_n)} \\ &= 1 + i\Delta_g k z - \frac{(kC_n z)^2}{2} \\ &\quad + \text{terms in } (kz)^3, (kz)^4, \text{ etc.} \end{aligned} \quad (17)$$

Since

$$C_0^2 \approx i \frac{\Delta_t + \Delta_g}{kh} \approx i \frac{\Delta_t}{kh} \quad (18)$$

it is seen that for the zero mode

$$F_0(z) = 1 + i\Delta_g k z - \frac{ikz^2 \Delta_t}{2kh} + \dots \quad (19)$$

For most ELF applications  $F_0(z)$  departs only slightly from unity. Also, it should be noted that if the ground was a perfect conductor the linear term in height is absent. Similar remarks apply to the higher modes. In fact, if  $\Delta_g = 0$ , we have

$$F_n(z) = \cos kC_n z$$

for all  $n$ .

It is seen from (6) that the height-gain functions for the  $H_\phi$  component is identical to  $F_n(z)$ . In the case of the  $E_\rho$  field it is desirable to define a height factor  $G_n(z)$  as follows

$$G_n(z) = \frac{g_n(z)}{f_n(0)}. \quad (20)$$

For a given mode, this quantity is proportional to the ratio of the horizontal electric field at height  $z$  to the vertical electric field at height zero. From (11), it is seen that

$$\begin{aligned} G_n(z) &= \frac{g_n(z)}{f_n(0)} = \frac{C_n (e^{ikC_n z} - R_g e^{-ikC_n z})}{1 + R_g} \\ &= \Delta_g + ikC_n^2 z - \frac{(kC_n z)^2}{2} \Delta_g + \dots \end{aligned} \quad (21)$$

For mode zero

$$G_0(z) \approx \Delta_g - \Delta_g \frac{z}{h} - i\Delta_t \Delta_g \frac{kz^2}{2h} + \dots \quad (22)$$

Again, under most practical conditions, only the first term of this series need be retained. In fact, if  $z = 0$ , we have exactly that

$$G_n(0) = \Delta_g \quad (23)$$

which is simply a consequence of the Leontovich boundary condition imposed at  $z = 0$ . If the ground is perfectly conducting

$$G_n(z) = iC_n \sin kC_n z. \quad (24)$$

## 5. Excitation of the Modes

We now consider the excitation coefficient  $\delta_n$  defined by (7). Since

$$\begin{aligned} \frac{\partial}{\partial C} R_g R_i &= R_i \frac{\partial R_g}{\partial C} + R_g \frac{\partial R_i}{\partial C} \\ &= R_i \frac{2\Delta_g}{(C+\Delta_g)^2} + R_g \frac{2\Delta_i}{(C+\Delta_i)^2}, \end{aligned} \quad (25)$$

it readily follows that

$$\delta_n = \frac{1}{1 + \frac{i\Delta_g}{kh(C_n^2 - \Delta_g^2)} + \frac{i\Delta_i}{kh(C_n^2 - \Delta_i^2)}} \quad (26)$$

If  $|\Delta_g| \ll |\Delta_i|$ , which is the usual case, the second term in the denominator can be neglected. Then to the same approximation

$$\delta_n = \frac{1}{1 + \frac{\sin 2khC_n}{2khC_n}} \quad (27)$$

where use has been made of  $R_i = e^{2ikC_n h}$ . Actually, (27) is exact if  $\Delta_g = 0$  and it can be regarded as an excellent approximation provided  $|\Delta_g| \ll |\Delta_i|$ . For practical applications at ELF, this may be further approximated to

$$\delta_n \approx \frac{1}{2} \text{ since } khC_n \ll 1$$

and

$$\delta_n \approx 1 \text{ since } 2khC_n \approx 2n\pi.$$

## 6. Further Extensions

The extension to a vertical magnetic dipole source is very simple. In view of the symmetrical properties of Maxwell's equations we can write down the corresponding field expressions. Thus

$$H_z = W^* H_0 \quad (28)$$

$$H_\rho = -S^* H_0 \quad (29)$$

$$E_\phi = T^* H_0 \eta \quad (30)$$

where  $W^*$ ,  $S^*$  and  $T^*$  are dimensionless factors and

$$H_0 = i(1/\eta\lambda) K ds (e^{-ik\rho})/\rho \quad (31)$$

where  $K$  is the magnetic current in the vertical magnetic dipole of length  $ds$ . The explicit expressions for  $W^*$ ,  $S^*$ , and  $T^*$  are identical in form to those given by  $W$ ,  $S$ , and  $T$  (i.e., (4) to (6)). Now, however, the modes are solutions of the equation

$$R_g^h(C) R_i^h(C) e^{-i2khC} = e^{-i2\pi m} \quad (32)$$

where  $m$  is an integer and

$$R_g^h(C) = \frac{C - \Delta_g^h}{C + \Delta_g^h} \quad (33)$$

and

$$R_i^h(C) = \frac{C - \Delta_i^h}{C + \Delta_i^h} \quad (34)$$

where  $\Delta_g^h \approx \frac{1}{\Delta_g}$  and  $\Delta_i^h \approx \frac{1}{\Delta_i}$ . The superscript  $h$  is to denote the horizontally polarized nature of these reflection coefficients.

In this case we note that

$$[f_m^h(0)]^2 = \frac{C_m^2}{C_m^2 - (\Delta_g^h)^2} \approx -\Delta_g^2 C_m^2 \quad (35)$$

which is a very small quantity compared with unity. Consequently, the excitation of ELF waves by a vertical magnetic dipole on the ground plane is very poor. However, when the dipole is raised the situation is greatly improved. The height-gain function of the modes for this case is

$$\begin{aligned} F_m^h(z) &= \frac{e^{ikC_m z} + R_g^h(C_m) e^{-ikC_m z}}{1 + R_g^h(C_m)} \\ &= 1 + ikz/\Delta_g - \frac{(kC_m z)^2}{2} + \dots \end{aligned} \quad (36)$$

Since  $\Delta_g$  is a small quantity, the second term of this series may be quite large even for small heights.

The height-gain function  $F_m^h(z)$  describes the behavior of both the  $H_z$  and  $E_\phi$  components of the vertical magnetic dipole. The appropriate height-gain function for the horizontal magnetic field component  $H_\rho$  is defined by the function

$$G_m^h(z) = \frac{g_m^h(z)}{f_m^h(0)} = \frac{C_m (e^{ikC_m z} - R_g^h e^{-ikC_m z})}{1 + R_g^h} \quad (37)$$

in complete analogy to (21) for the electric dipole case.

The excitation of the waveguide modes for a horizontal electric dipole was treated previously [Wait, 1960a]. For an electric dipole of moment  $Ids$  situated at  $z=z_0$  and oriented in the direction  $\phi=0$ , it was shown that

$$E_z = \cos \phi E_0 S \quad (38)$$

where  $E_0$  and  $S$  are given by (3b) and (5), respectively. Also

$$\eta_0 H_z = -\sin \phi E_0 T^* \quad (39)$$

where, explicitly,

$$T^* = -\frac{\pi \rho}{h} e^{ik\rho} \sum_{m=0}^{\infty} \delta_m S_m H_1^{(2)}(kS_m \rho) f_m^h(z_0) f_m^h(z). \quad (40)$$

For most applications the fields derived from  $S$  (i.e., the vertically polarized waves) are only significant.

The fields associated with  $T^*$  (i.e., the horizontally polarized waves) are hardly excited at all when  $ka \ll 1$  which is the usual case.

The field of a horizontal *magnetic* dipole of moment  $Kds$  has the same structure as the fields of the horizontal electric dipole. Explicitly

$$H_z = \cos \phi H_0 S^* \quad (41)$$

and

$$E_z = \sin \phi H_0 T / \eta_0. \quad (42)$$

The solution for the horizontal magnetic dipole has been discussed recently by Galejs [1961]. He obtains his results by an application of the reciprocity theorem as outlined by Wait [1960a].

The remarks in the preceding section concerning the height-gain functions for the vertical dipoles can be carried over to the horizontal dipoles without modification.

The generalization of the foregoing results to include the effects of earth curvature is not difficult. Provided one stays away from the antipode of the source dipole it is only necessary to multiply the field expressions by

$$\left( \frac{\theta}{\sin \theta} \right)^{\frac{1}{2}}$$

where  $\theta$  is the central angle subtended by the source and observer at the center of the earth. The justification for this step was given previously. It might

be added, however, that in addition to the restriction in the neighborhood of the antipode it is also necessary that

$$C_n^2 \gg h/a \quad (43)$$

and

$$\left( \frac{ka}{2} \right)^{\frac{1}{3}} C_n \gg 1. \quad (44)$$

It is not difficult to verify that these conditions are well justified at ELF.

## 7. References

Galejs, J., Propagation of VLF and ELF radio waves excited by a horizontal magnetic dipole, *J. Research NBS 65D* (Radio Prop.), No. 3 (May-June 1961).

Schumann, W. O., Über die Oberfelder bei der Ausbreitung langer, elektrischer Wellen im System Erde-Luft-Ionosphäre und 2 Anwendungen (horizontaler und senkrechter Dipol), *Z. angew. Phys.* **6**, 34 (1954).

Wait, J. R., Terrestrial propagation of VLF radio waves, *J. Research NBS 64D* (Radio Prop.), No. 2, 153-204 (Mar.-Apr. 1960a).

Wait, J. R., Mode theory and the propagation of E.L.F. radio waves, *J. Research NBS 64D* (Radio Prop.), No. 4, 387-404 (July-Aug. 1960b).

Wait, J. R., and N. F. Carter, Field strength calculations for E.L.F. radio waves, *NBS Tech. Note No. 52* (PB-161553) (Mar. 1960).

(Paper 65D5-154)

# Computation of Whistler Ray Paths<sup>1</sup>

Irving Yabroff

Contribution From Stanford Research Institute, Menlo Park, Calif.

(Received May 8, 1961)

Calculations of whistler ray paths in the outer ionosphere are shown for a variety of electron density profile models including exponential, constant, and columnar profiles. The Haselgrove formulation of the ray equations was used with the magneto-ionic representation of the wave refractive index to develop a set of differential equations for ray tracing suitable for inhomogeneous, anisotropic medium. The variation of paths with frequency, latitude, initial wave-normal angle, and other variables are examined for the purpose of providing a preliminary basis for comparison of the theoretical with some of the experimental results.

## 1. Introduction

Little work has previously been done to describe the mechanics and physics of electromagnetic wave propagation in an inhomogeneous anisotropic medium. Of particular interest are certain phenomena taking place at frequencies below the plasma and gyrofrequencies of the ionosphere. The subject has become important during the last few years because of the increasing interest in VLF wave phenomena such as "whistlers."

Whistlers propagate in what is known as the "extraordinary" mode in magneto-ionic theory [Ratcliffe, 1959]. This mode of propagation is also described by the terms "whistler-mode" or "magneto-ionic duct." Details of the phenomena and additional references are given elsewhere [Helliwell and Morgan, 1953]. The basic theory of whistler propagation was first given by Storey [1953]; however, his description is valid only for a restricted set of conditions, many of which do not apply over the complete whistler path.

The work reported here is an attempt to demonstrate some of the complex phenomena of whistler propagation. The set of computations described here is in no sense complete or comprehensive; it is meant only to demonstrate a few interesting details of this mode of propagation and to stimulate further thought and work. Very little attempt has been made to interpret the form and shape of the results shown; such interpretations must arise from an examination of the form of the general solution of the ray path equations.

## 2. Discussion

### 2.1. General Procedure

Equations which are in a form useful for computation of ray paths in the ionosphere can be obtained from substitution of the familiar Appleton-Hartree expression for the complex refractive index into

ray equations derived by Haselgrove [1954]. The resulting equations in spherical coordinates  $r, \theta, \phi$  are

$$\frac{dr}{dt} = \frac{1}{\mu^2} \left( \rho_r - \mu \frac{\partial \mu}{\partial \rho_r} \right)$$

$$\frac{d\theta}{dt} = \frac{1}{r\mu^2} \left( \rho_\theta - \mu \frac{\partial \mu}{\partial \rho_\theta} \right)$$

$$\frac{d\phi}{dt} = \frac{1}{r\mu^2 \sin \theta} \left( \rho_\phi - \mu \frac{\partial \mu}{\partial \rho_\phi} \right)$$

$$\frac{d\rho_r}{dt} = \frac{1}{\mu} \frac{\partial \mu}{\partial r} + \rho_\theta \frac{d\theta}{dt} + \rho_\phi \frac{d\phi}{dt} \sin \theta$$

$$\frac{d\rho_\theta}{dt} = \frac{1}{r} \left( \frac{1}{\mu} \frac{\partial \mu}{\partial \theta} - \rho_\theta \frac{dr}{dt} + r \rho_\phi \frac{d\phi}{dt} \cos \theta \right)$$

$$\frac{d\rho_\phi}{dt} = \frac{1}{r \sin \theta} \left( \frac{1}{\mu} \frac{\partial \mu}{\partial \phi} - \rho_\phi \frac{dr}{dt} \sin \theta - r \rho_\theta \frac{d\theta}{dt} \cos \theta \right)$$

where

$\mu$ =the real part of the complex phase refractive index,

$\rho_r, \rho_\theta, \rho_\phi$ =the physical components of a vector of length  $\mu$ , and directed normal to the phase fronts (also called the wave normal or refractive index vector),

$t$ =time of phase travel along the ray (that is,  $(f\Delta t)/c$ =number of wavelengths in the medium along the ray path),

$f$ =wave frequency,

$c$ =speed of light.

The quantity  $\mu$  and its derivatives are calculated from the Appleton-Hartree formula as follows:

$$M^2 = (\mu - jK)^2 = 1 - \frac{2X(1-X-jZ)}{D}$$

$$D = 2(1-X-jZ)(1-jZ) - Y^2 \sin^2 \psi + S$$

$$S = \pm \sqrt{Y^4 \sin^4 \psi + 4Y^2(1-X-jZ)^2 \cos^2 \psi}$$

<sup>1</sup>Based on a report prepared by Stanford Research Institute for Stanford University under Prime Contract AF 18(603)-126 (Dec. 1959).

where

$M$ =complex phase refractive index= $\mu-jk$ ,

$X$ =normalized electron density= $(Ne^2)/(\omega^2 m \epsilon_0)$ ,

$Y$ =normalized magnitude of the earth's magnetic field vector,  $\vec{Y}=(\mu_0 \epsilon \vec{H}_e)/(\omega m)$ ,

$Z$ =normalized collision frequency= $(\nu_0)/\omega$ ,

$\psi$ =angle between  $\vec{\rho}$  and  $\vec{Y}=\cos^{-1}[(\rho_r Y_r + \rho_\theta Y_\theta + \rho_\phi Y_\phi)/(\mu Y)]$ ,

$N$ =electron density,

$e$ =charge on an electron,

$m$ =mass of an electron,

$\omega=2\pi f=2\pi \cdot$  wave frequency,

$\epsilon_0$ =dielectric constant of free space,

$\mu_0$ =permeability of free space,

$\nu_0$ =collision frequency in collisions per second,

$K$ =imaginary part of the complex phase refractive index.

The two values of  $M$  corresponding to the plus and minus sign on  $S$  represent the two modes of ionospheric propagation commonly called the "ordinary" and "extraordinary" modes.

The derivatives of  $\mu$  are

$$\frac{\partial \mu}{\partial \rho_i} = \frac{\partial \mu}{\partial \psi} \frac{\partial \psi}{\partial \rho_i} = \frac{\partial \mu}{\partial \psi} \left( \frac{\rho_i Y \cos \psi - \mu Y_i}{\mu^2 Y \sin \psi} \right)$$

where  $i$ =the coordinates  $r, \theta, \phi$ .

[NOTE: When  $\psi \rightarrow 0$ ,  $\partial \mu / \partial \psi \rightarrow 0$ ,  $\partial \psi / \partial \rho_i \rightarrow \infty$  but  $\partial \mu / \partial \rho_i \rightarrow 0$ .]

$$\frac{\partial \mu}{\partial \psi} = \text{Re} \frac{\partial M}{\partial \psi} = \text{Re} \left( \frac{(M^2 - 1) Y^2 \sin \psi \cos \psi}{MD} \right)$$

$$\left\{ 1 - \frac{1}{S} [Y^2 \sin^2 \psi - 2(1 - X - jZ)^2] \right\})$$

$$\frac{\partial \mu}{\partial i} = \frac{\partial \mu}{\partial X} \frac{\partial X}{\partial i} + \frac{\partial \mu}{\partial Y} \frac{\partial Y}{\partial i} + \frac{\partial \mu}{\partial Z} \frac{\partial Z}{\partial i} + \frac{\partial \mu}{\partial \psi} \frac{\partial \psi}{\partial i}$$

$$\frac{\partial \mu}{\partial X} = \text{Re} \frac{\partial M}{\partial X} = \text{Re} \left( \frac{1}{MD} \left\{ 2X - 1 + jZ + (M^2 - 1) \left[ 1 - jZ + \frac{2Y^2(1 - X - jZ) \cos^2 \psi}{S} \right] \right\} \right)$$

$$\frac{\partial \mu}{\partial Y} = \text{Re} \frac{\partial M}{\partial Y} = \text{Re} \left( \frac{(M^2 - 1) Y}{MD} \left\{ \sin^2 \psi - \frac{1}{S} [Y^2 \sin^4 \psi + 2(1 - X - jZ)^2 \cos^2 \psi] \right\} \right)$$

$$\frac{\partial \mu}{\partial Z} = \text{Re} \frac{\partial M}{\partial Z} = -\text{Im} \left( \frac{1}{MD} \left\{ X + (M^2 - 1) \left[ 2 - X - 2jZ + \frac{2Y^2(1 - X - jZ) \cos^2 \psi}{S} \right] \right\} \right)$$

where  $\text{Im}$ =imaginary part of.

[NOTE:  $\partial \psi / \partial i$  is calculated holding  $\rho$  constant and so measures the change in the direction of the earth's magnetic field in space.]

The quantities  $\partial X / \partial i$  and  $\partial Z / \partial i$  must be derived from the space variation of  $X$  and  $Z$  which are assumed. An arbitrary inhomogeneous ionosphere can be represented in this manner. If an earth-centered dipole field approximation is used for the magnetic field, then

$$Y = Y_e \left( \frac{r_0}{r} \right)^3 \sqrt{1 + 3 \cos^2 \theta}$$

where  $Y_e = Y$  at the equator at the surface of the earth  $\approx (8.7 \cdot 10^3)/f$ . The vector components of  $Y$  in spherical coordinates are

$$Y_r = \frac{Y}{\sqrt{1 + (1/4) \tan^2 \theta}} \quad \frac{\partial Y}{\partial r} = -\frac{3Y}{r}$$

$$Y_\theta = \frac{1}{2} Y_r \tan \theta \quad \frac{\partial Y}{\partial \theta} = \frac{-3Y \cos \theta \sin \theta}{1 + 3 \cos^2 \theta}$$

$$Y_\phi = 0 \quad \frac{\partial Y}{\partial \phi} = 0$$

where

$\theta$ =colatitude and

$\phi$ =longitude.

The derivatives of  $\psi$  for a dipole magnetic field are

$$\frac{\partial \psi}{\partial r} = 0$$

$$\frac{\partial \psi}{\partial \theta} = \frac{\partial \psi}{\partial \gamma} \frac{\partial \gamma}{\partial \theta}$$

where  $\gamma$ =angle between  $\vec{Y}$  and the radial (see fig. 1).

[NOTE:  $\gamma = \tan^{-1}(-1/2 \tan \theta)$  for the dipole field.]

$$\frac{\partial \psi}{\partial \phi} = 0$$

$$\frac{\partial \psi}{\partial \gamma} = \frac{\sigma_r Y_\theta - \sigma_\theta Y_r}{\sigma Y \sin \psi}$$

$$\frac{\partial \gamma}{\partial \theta} = \frac{1}{2 \cos^2 \theta + (1/2) \sin^2 \theta}$$

[NOTE: When  $\psi \rightarrow 0$ , both numerator and denominator of  $\partial \psi / \partial \gamma$  go to zero and  $\partial \psi / \partial \gamma \rightarrow 1$ .]

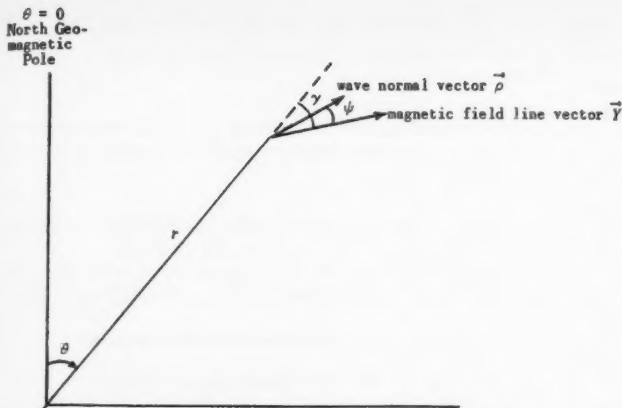


FIGURE 1. Coordinate system for two dimensions,  $r-\theta$ .

It is usually desired to compute the following additional quantities along with the ray path:

(1) Path length,  $S$

$$\frac{dS}{dt} = \frac{1}{\mu^2 \sqrt{1 + (\partial\mu/\partial\psi)^2}} = \frac{1}{\text{ray refractive index}} = \frac{1}{\mu \cos \alpha}.$$

(2) Time of travel,  $T$ , also called group delay

$$\frac{dT}{dt} = \frac{1}{c} \left( 1 + \frac{f}{\mu} \frac{\partial\mu}{\partial f} \right)$$

$$\frac{\partial\mu}{\partial f} = \text{Re} \frac{\partial M}{\partial f} = \text{Re} \left( \frac{1}{MDf} \left\{ X(2X+jZ) + (M^2-1) \right. \right.$$

$$\left. \left[ 2-2jZ-jZX + \frac{2}{S} Y^2 \cos^2 \psi \right. \right.$$

$$\left. \left. (1-X-jZ)(1+X) \right] \right\}$$

(3) Absorption,  $A$ , in nepers

$$\frac{dA}{dt} = -\frac{\omega}{c} \frac{K}{\mu}; \quad \omega = 2\pi f$$

## 2.2. Notes on the Method of Digital Computation Used

### a. Initial Conditions Needed

Initial values for  $r$ ,  $\theta$ ,  $\phi$ ,  $\rho_r$ ,  $\rho_\theta$ ,  $\rho_\phi$  are needed. To get  $\rho_r$ ,  $\rho_\theta$ , and  $\rho_\phi$ , the wave normal direction can be inserted as an initial condition.  $\mu$  is then calculated and the  $\rho$ 's obtained. For example, let  $x_t = (\rho_t/\rho) =$  direction cosines of wave normal with respect to the local coordinate axes. Then, since  $\rho = \mu$ ,  $\rho_t = \mu x_t$ .

### b. Stability Condition

The six basic ray differential equations contain one more degree of freedom than there are constraints explicitly expressed. That is, it only takes 5 quantities to define a vector field (three space coordinates and two direction cosines). The sixth

equation is implicit in the definition of  $|\rho| = \mu$ . The round-off errors involved in calculating  $\mu$  and in integrating  $d\rho_t/dt$  will result in  $|\rho| \neq \mu$  after a few steps of integration unless an additional constraint is imposed. Thus, to maintain the equality, we correct the  $\rho_t$ 's at each point in the manner

$$\rho_t \text{ corrected} = \rho_t \frac{\mu}{\rho}$$

This correction is made as early as possible in the derivative calculation, i.e., immediately after calculation of  $M$ . Since the magnitude of  $\rho$  is not used in the calculation of  $M$  (only the wave normal direction is used), no errors arising from  $|\rho| \neq \mu$  are allowed to accumulate by this procedure.

### c. Interval Size

The  $\Delta t$  to use depends upon the accuracy required, the frequency, the size of refractive index gradients encountered along the ray path, and the stability and accuracy of the numerical method of solution of the differential equations used. For the whistler ray paths, shown later in this report, the interval size was changed when the local truncation error became either too large or too small. The local truncation error was measured by noting the difference between the predicted values for the next point and the values obtained by application of the first corrector (an Adam's predictor-corrector method of solution of the D.E. equations was used). When this difference became less than  $5 \cdot 10^{-7}$ , the interval size was doubled using an extrapolation formula in a special subroutine. When the difference became greater than  $10^{-4}$ , the interval size was halved. The corrector was applied only once every 5 or 10 points and only a predictor was used for the in-between points. This was done because application of a corrector and subsequent doubling or halving costs several "points" worth of time. Thus it is undesirable to do this very often. The interval size used for these whistler calculations was approximately one-half an earth radius. Calculation was started at the top of the  $F_2$  layer.

#### d. Other Comments

The bulk of computation time is spent in calculating the derivatives of  $M$ ,  $\mu$ , etc. Only a small fraction of the total time is actually spent in the numerical method of solution calculations. Therefore, a method of solution should be chosen that minimizes the number of times the derivatives have to be calculated, and that makes maximum use of the derivatives already calculated. Thus the Runge-Kutta methods are long and cumbersome for these equations. A predictor-corrector method with a minimum number of corrector cycles applied seems to be about the best. Perhaps even a high-order predictor (5th or 6th order) might be best, since this would increase the interval size one could use without increasing the calculation time proportionately.

The main weakness of the program used for these calculations is the instability of the extrapolation formula used for doubling. This formula has to jump ahead two intervals. It would be better to carry more points along with the calculations and use a higher-order extrapolation formula that only jumps ahead one space—or better still, carry sufficient points to use no extrapolation formula at all.

If these equations are to be used for frequencies high enough that the earth's magnetic field can be ignored (frequencies much higher than the local gyrofrequency) then a separate routine should be written for this case, since the equations simplify to a much easier and faster computation. If the same routine is used, many of the expressions for the derivatives become indeterminate when  $Y=0$ . Most of these derivatives actually become zero, but special tests would have to be installed in the program to handle this case.

### 2.3. Computations

#### a. General Procedure

The differential equations were programmed for numerical solution on an Electrodata 205 computer. Only the two-dimensional case of propagation in the magnetic meridian was utilized in these computations. Also, no losses were included ( $\nu=0$ ). The calculation of a whistler path was begun with the assumed initial conditions at an altitude of 300 km. This altitude corresponds roughly with the maximum ionization level of the  $F_2$  layer.

An electron density profile was assumed for altitudes greater than this.

The computations are organized into the following categories according to the electron density profile used and the parametric variation examined:

- (1) Exponential model—variation of frequency,
- (2) Exponential model—variation of initial latitude,
- (3) Exponential model—variation of initial wave normal direction,
- (4) Constant density model, and
- (5) Miscellaneous.

The exponential model used in all of the first three categories is:

$$N=180,000 \exp [-4.183119 (r-1.0471)]$$

where

$N$ =electron density in electrons per cubic centimeter.  
 $r$ =radial distance from center of earth in earth radii.

( $r=1.0471=300$  km above the surface of the earth at the beginning of the path computation).

These particular values of electron density and scale height were obtained from Maeda and Kimura [1956].

#### b. Exponential Model—Variation With Frequency

Figure 2(a) gives the results of ray path computations at the frequencies 5, 10, 20, 25, 30, 50, 100, 200, 400, 1000 kc/s. Figures 2 (a) and (b) show the ray path for each of these frequencies. The initial wave normal direction for each of these paths is vertical (wave normal angle=0°). In order to exhibit the variation of certain variables in these computations, figures 2(c) to 2(i) have been plotted.

Some of the interesting features of these computations may be listed as follows:

#### c. Exponential Model—Variation With Latitude

Figure 3 gives the results of ray path computations initiating at north latitudes of 10, 20, 30, 35, 40, 45, 50, and 60°. Figures 3 (a) to (i) show the ray paths for each of these latitudes as well as the variation of wave normal direction over the path. Additional data from these computations have been plotted in figures 3 (j) to (o).

#### d. Exponential Model—Initial Wave Normal Variation

Figure 4 gives the results of ray path computations with initial wave normal angles 10, 5, -5, and -10° measured positively clockwise from vertical (along the radial). Figures 4 (a) to (d) show the ray paths and wave normal direction over these paths. The wave frequency is 10 kc/s. Additional data from these computations have been plotted in figures 4 (e) to (g).

The behavior of the wave normal over the path changes only negligibly with these changes in initial wave normal direction.

#### e. Constant Density Model

Figure 5 gives the results of ray path computations with constant electron density. The characteristics of a constant density model are as follows. Since there is no electron density gradient, the total refractive index gradient is formed by the magnetic field. Also, since the refractive index gradient determines the change in wave normal which in turn determines the bending of the ray path, the bending of the ray path is determined only by the guiding effect of the magnetic field, not by the electron density. Thus the ray path is the same regardless of the magnitude of the electron density.

#### f. Miscellaneous Computations

*Comparisons with Maeda's computations*—Maeda (1951) used a very approximate method of numerical integration as well as an approximation to the refractive index gradient which is only very roughly correct. In order to compare his computations with the more exact formulation of Haselgrave, one of Maeda's published ray paths was compared with a similar computation using the present program in figure 6. It can be seen that the difference is appreciable. The lack of comparison is not due to the quasi-longitudinal approximation of the refractive index function which was used by Maeda since this approximation was used also in Haselgrave's formulation for this particular computation. The difference between the Q. L. approximation and the full expression is too small to be shown. The differences between the two computed paths may be due to the relatively crude method of integration used by Maeda to numerically solve the differential equations.

*Field-aligned column model*—In a recent theoretical paper it has been shown that if the ionization is field-aligned it can act like a waveguide in trapping whistler energy [Smith, Helliwell, and Yabroff, 1960]. This would explain some of the very distinct and clear whistlers which have been recorded. In order to answer certain questions regarding the effects of field-alignment, the following models have been computed:

$$N = 180,000 \left\{ 1 + C \exp \left[ \frac{(b-b_0)^2}{2D^2} \right] \right\} \exp [-4.183119(r-1.0471)]$$

where

$b = r/\sin^2\theta$  (the equation of a field line is  $b = \text{constant}$ ),

$b_0 = 2.094$  (this is a field line corresponding to 300 km altitude at a latitude of  $45^\circ$  and is the center of the column),

$C$  = the modulation factor, i.e., the relative increase of maximum ionization at the center of the column over that of the surrounding background level of ionization, and

$D$  = the standard deviation of the column. (The column is of gaussian electron density distribution with the standard deviation measured in terms of the local distance between the field lines.) This makes more intuitive physical sense than making the thickness of the column constant at all points on the field line, since the individual electrons will tend to diffuse easily along the lines of force but not across them.

For these computations  $D = 0.029$  which corresponds to a standard deviation of about 35 km at an altitude of 300 km, and about 215 km at the top of the path.

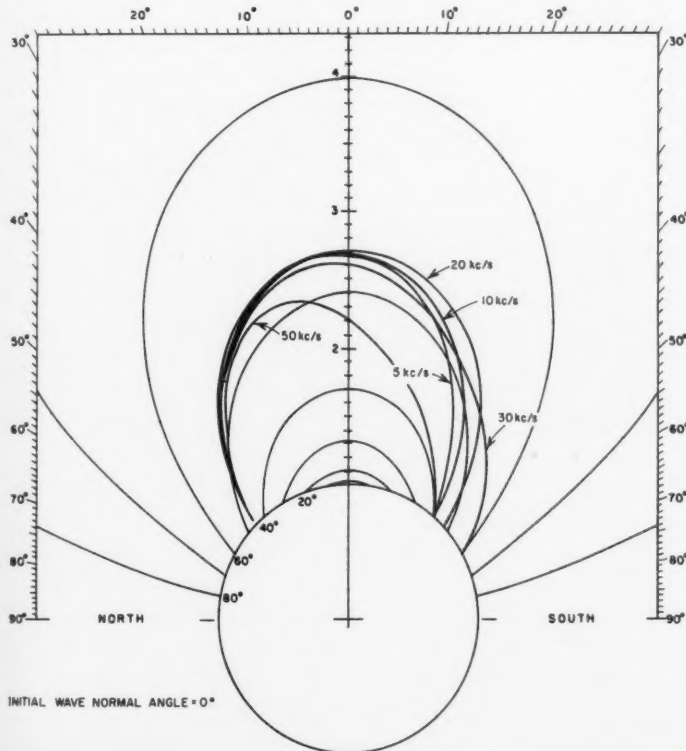


FIGURE 2(a). Ray paths at various frequencies.

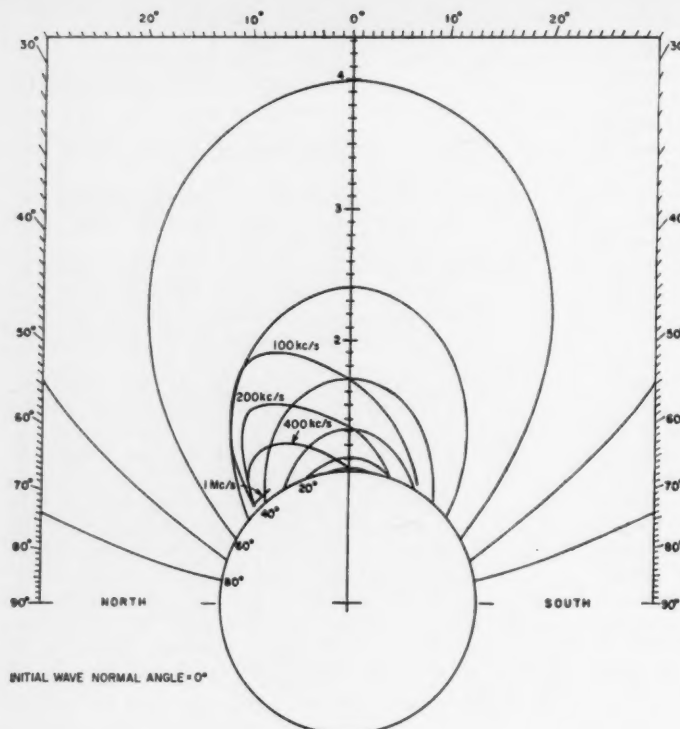


FIGURE 2(b). Ray paths at various frequencies.

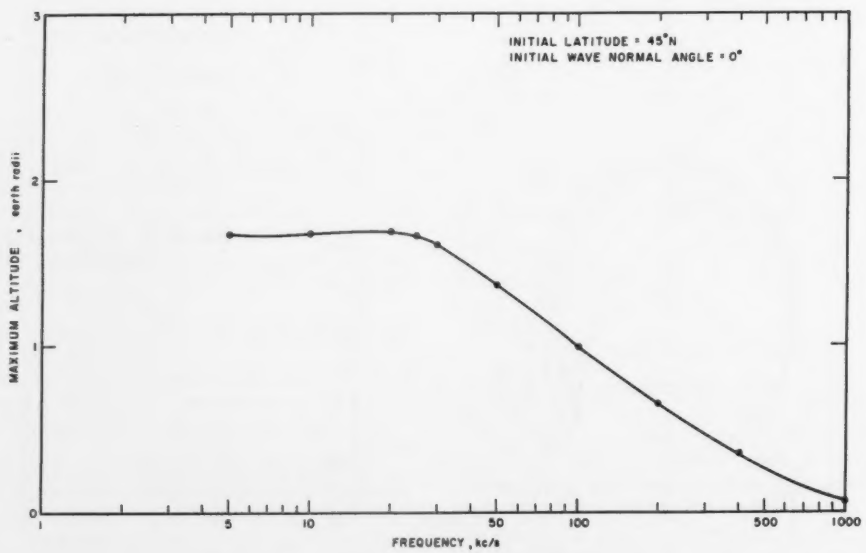


FIGURE 2(c). Maximum altitude versus frequency.

The maximum height of the path remains essentially constant up to the frequency of minimum time 'delay' [the nose frequency, which is seen to be at about 20 kc/s in fig. 2(d)] at which point the maximum path height begins decreasing.

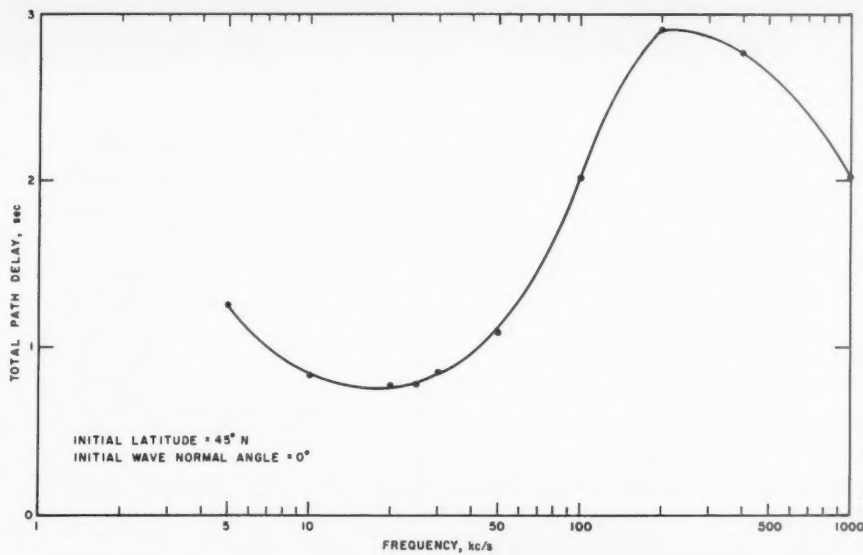


FIGURE 2(d). Total path delay versus frequency.

The time delay decreases in the expected "Eckersley" fashion until the nose region is reached. This region corresponds to the frequency reaching approximately 45 percent of the gyrofrequency at the top of the path. These calculations confirm this behavior. The time delay at higher frequencies increases until the effect of the shortening of the path length at high frequencies overbalances the decrease in group velocity to cause the time delay to begin to decrease again above 200 kc/s.

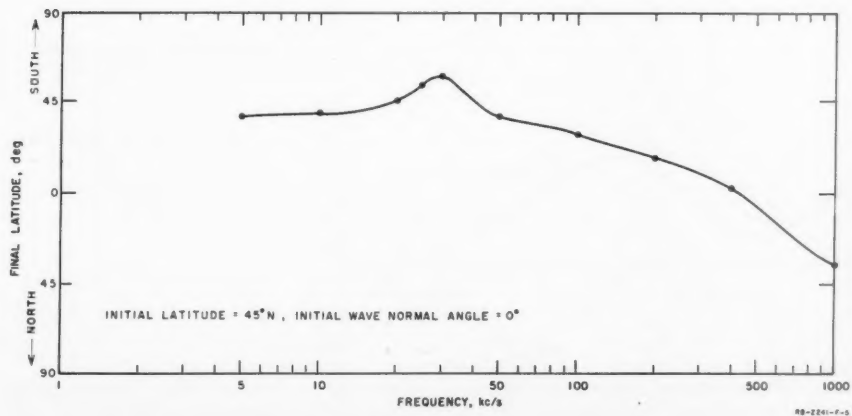


FIGURE 2(e). Final latitude versus frequency.

The final latitude remains fairly constant at frequencies up to the nose frequency. This suggests some latitude focusing in the "Eckersley" region. Above the nose frequency, the final latitude starts shifting toward the pole until the effect of the shortening path length at higher frequencies overcomes this tendency and results in a shift back toward the equator.

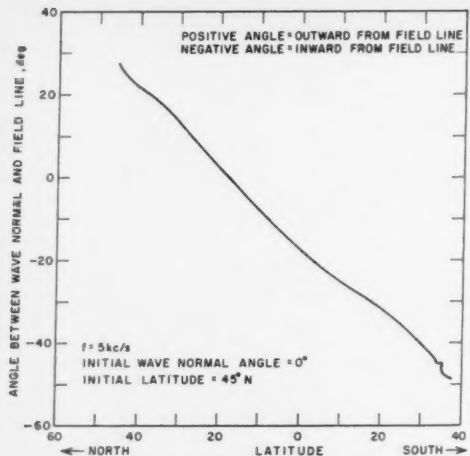


FIGURE 2(f). Wave normal—field line angle along the path.

At frequencies below the nose frequency, the wave normal swings steadily below the field line as the path progresses. As the nose frequency is approached, the wave normal tends to oscillate about a position approximately ten degrees above the field line. At higher frequencies, the wave normal swings outward after an initial dip toward the field line.

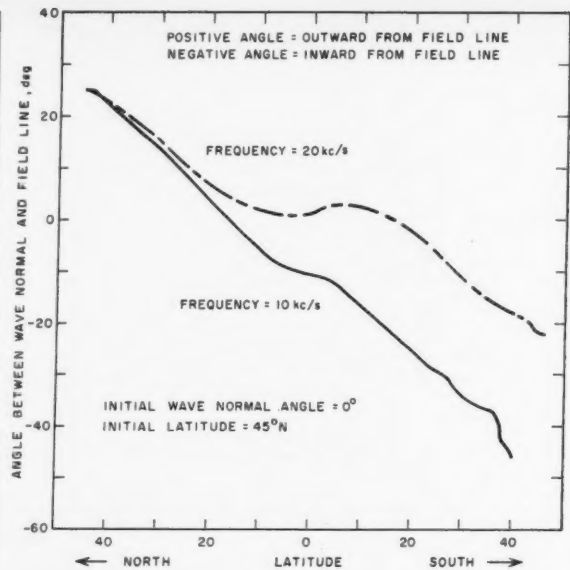


FIGURE 2(g). Wave normal—field line angle along the path.

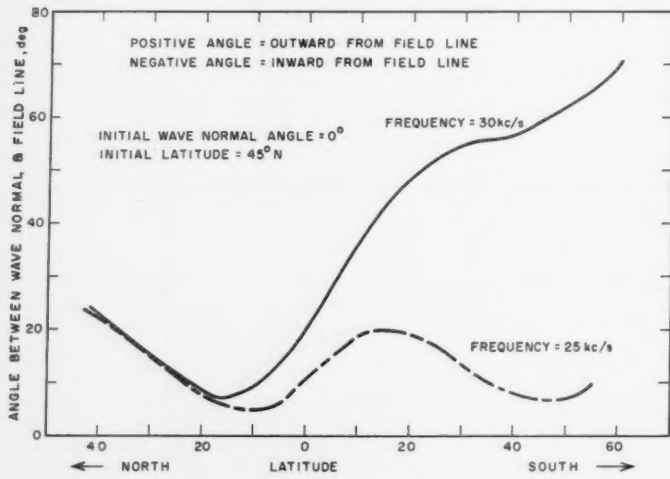


FIGURE 2(h). Wave normal—field line angle along the path.

In the first two computations shown in figures 7 and 8 the initial wave normal direction is vertical. When the modulation is 0.2, good guiding occurs. When the modulation is reduced to 0.1, the ray is not guided because the initial wave normal direction is far from the field-line direction and the ray gets pulled out of the column before the wave normal gets properly lined up with the field line. This is in agreement with theoretical predictions [Smith, Helliwell, and Yabroff, 1960]. In the third case shown in figure 9, the wave normal was set along the

field line. In that case, the guiding is even better than for the higher modulation of case 1. The final case shown in figure 10 shows the modulation reduced to zero with the initial wave normal direction on the field line. The guiding of this ray is still good, but less so than for the previous case of 0.1 modulation.

These calculations support the theoretical predictions [Smith, Helliwell, and Yabroff, 1960] that wave components whose wave normals lie within a certain angle with respect to the direction of the magnetic field will be trapped.

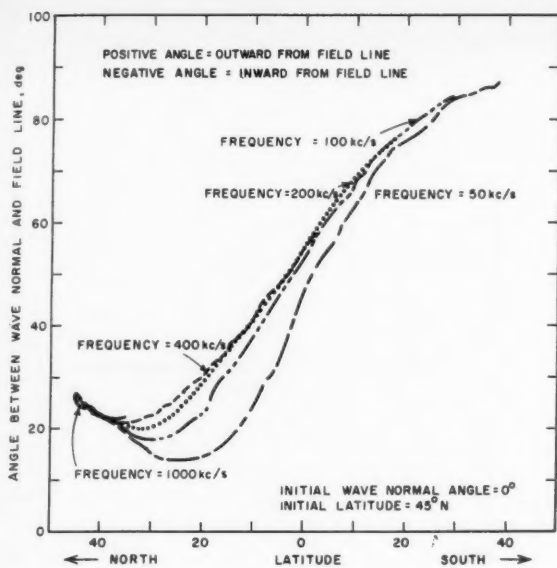


FIGURE 2(i). *Wave normal—field line angle along the path.*

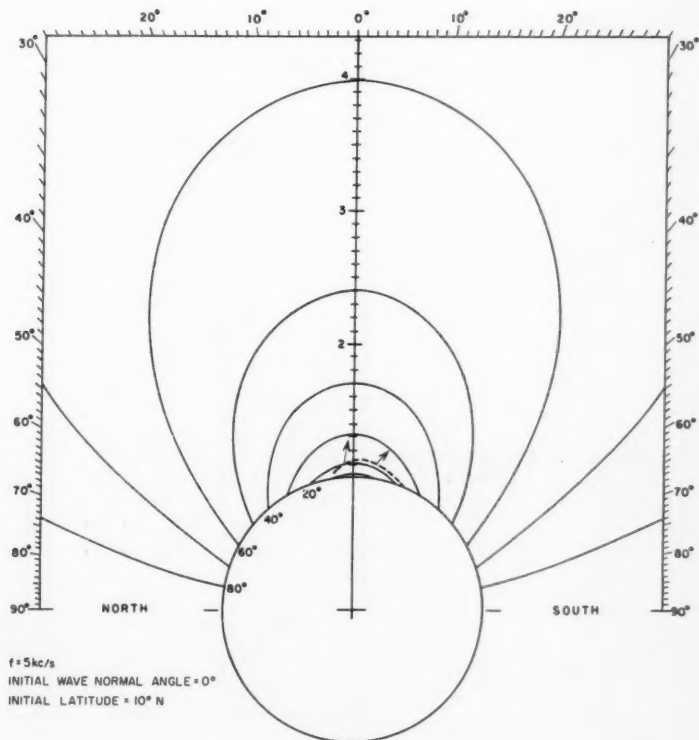


FIGURE 3(a). *Ray path initiating at 10°N latitude.*

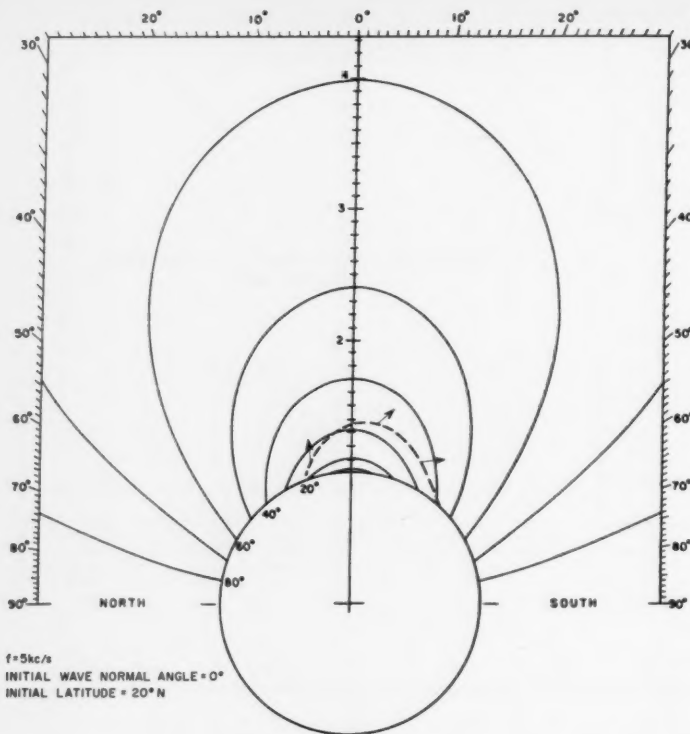


FIGURE 3(b). Ray path initiating at  $20^\circ \text{ N}$  latitude.

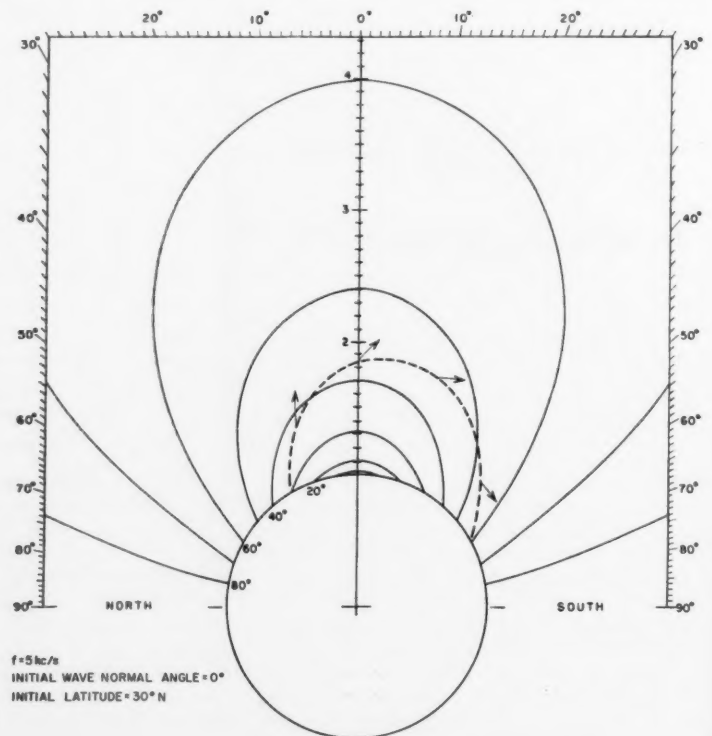


FIGURE 3(c). Ray path initiating at  $30^\circ \text{ N}$  latitude.

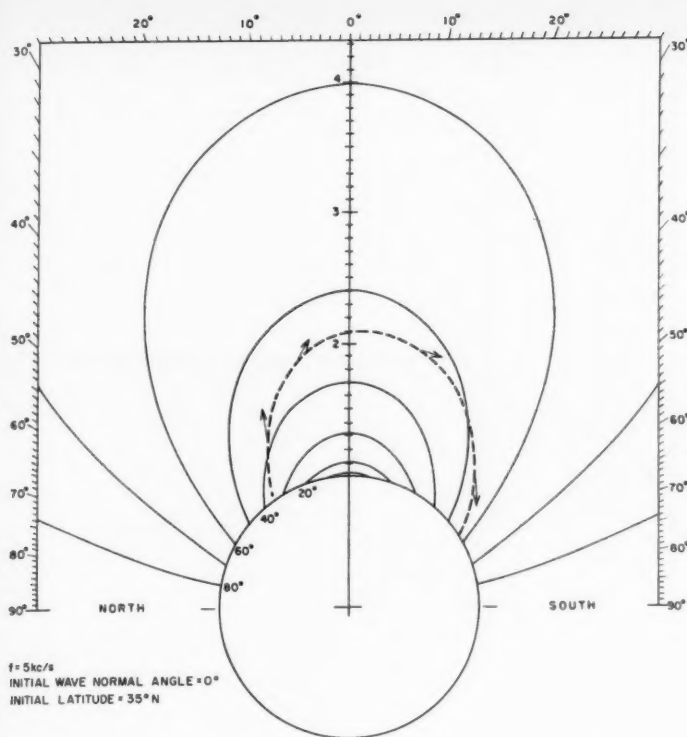


FIGURE 3(d). Ray path initiating at  $35^\circ \text{N}$  latitude.

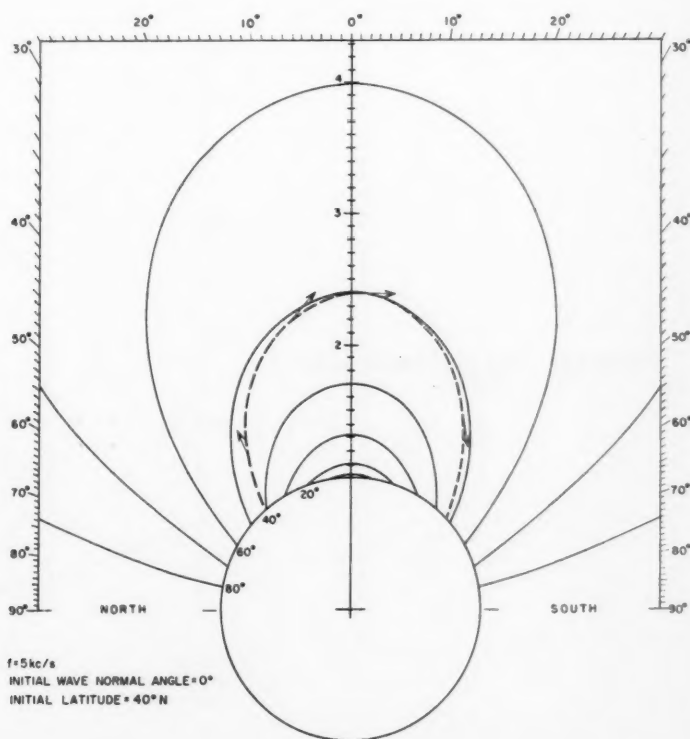


FIGURE 3(e). Ray path initiating at  $40^\circ \text{N}$  latitude.

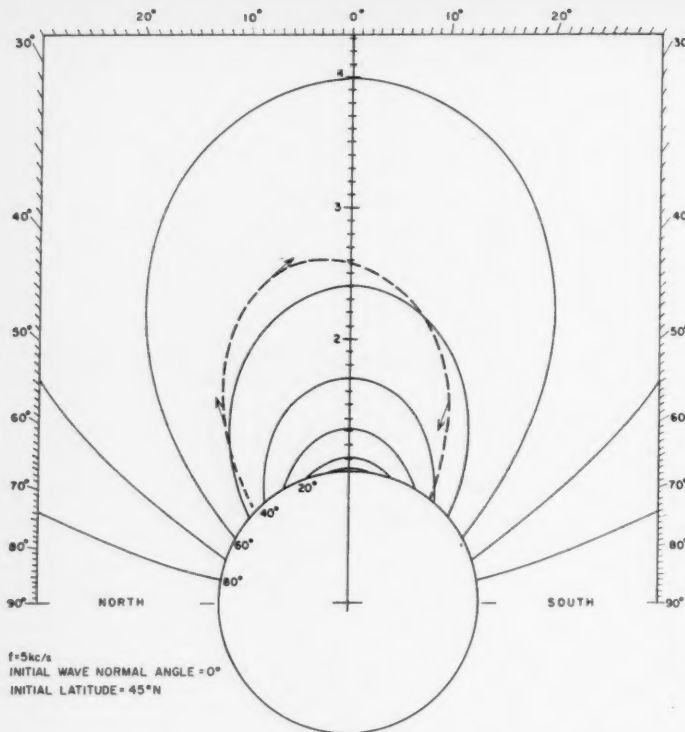


FIGURE 3(f). Ray path initiating at  $45^\circ \text{N}$  latitude.

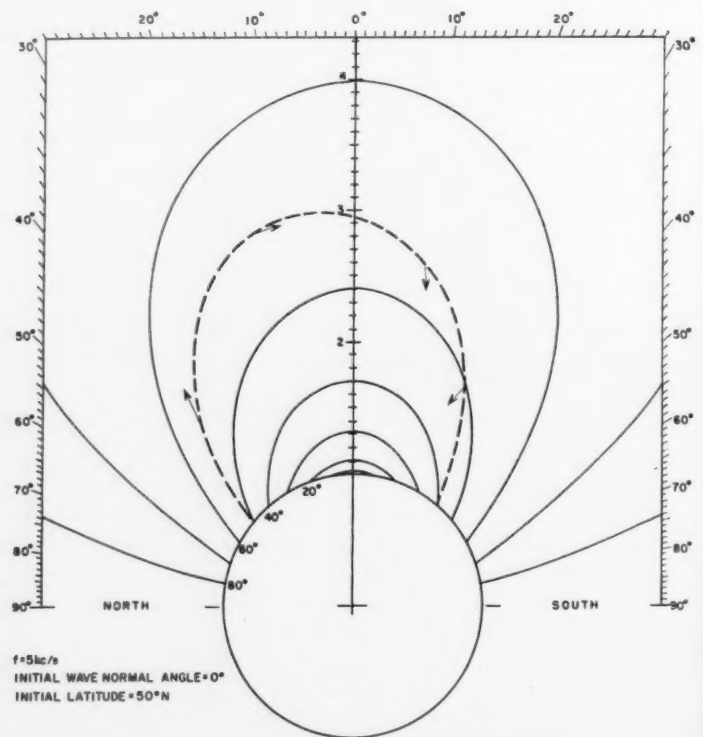


FIGURE 3(g). Ray path initiating at  $50^\circ \text{N}$  latitude.

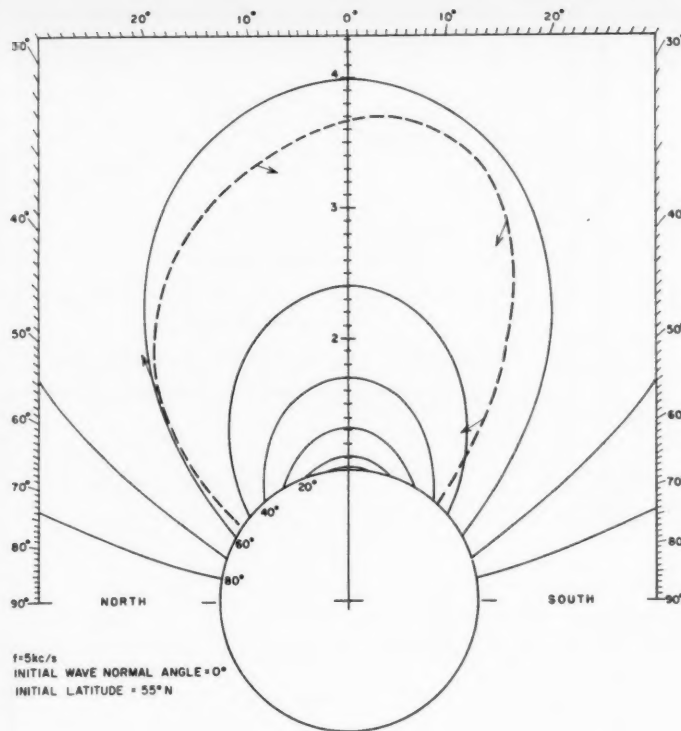


FIGURE 3(h). Ray path initiating at  $55^{\circ}$  N latitude.

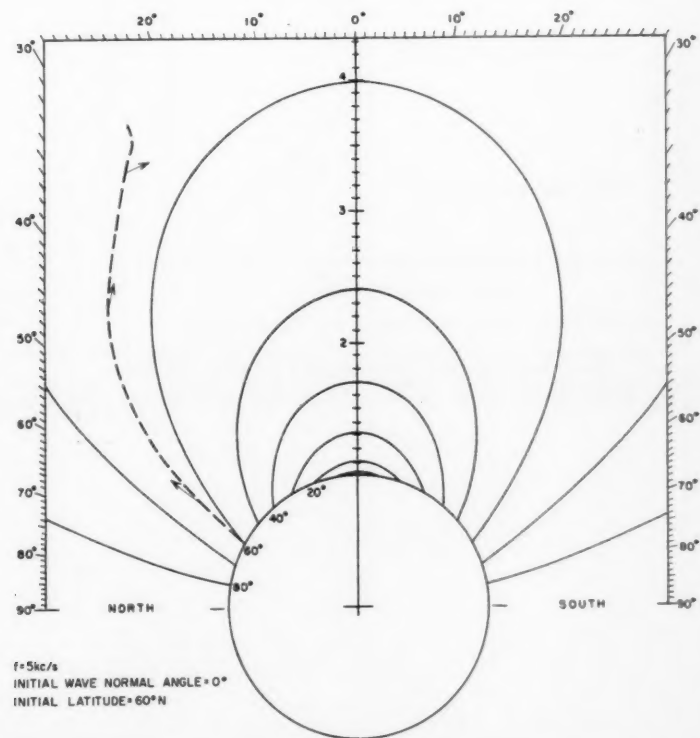


FIGURE 3(i). Ray path initiating at  $60^{\circ}$  N latitude.

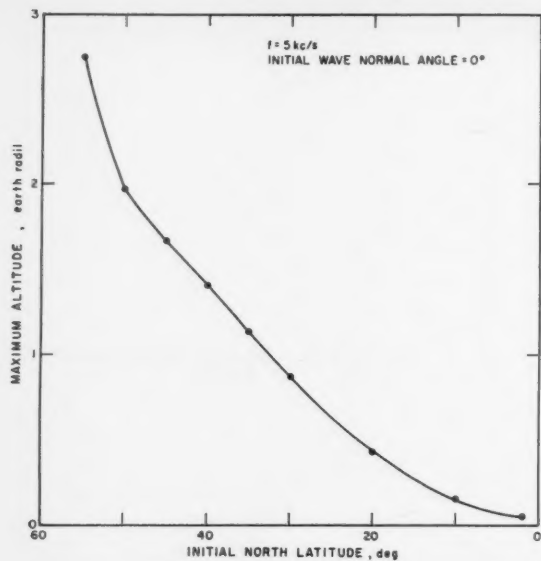


FIGURE 3(j). Maximum altitude versus initial latitude.

The maximum height of the path is seen to increase very rapidly with increasing initial latitude until an altitude is reached at which the plasma frequency becomes equal to the wave frequency. This represents the usual reflection level.

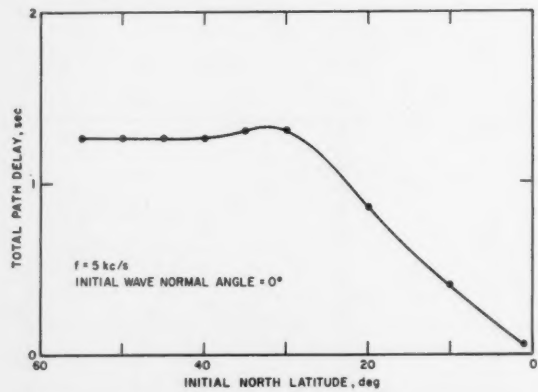


FIGURE 3(k). Total path delay versus initial latitude.

The total time delay is seen to be fairly constant over a wide range of initial latitude. This may be a bit surprising since it was previously observed that the path length changes very rapidly with initial latitude. Clearly the average group velocity must be much higher for the longer paths which are at a higher latitude.

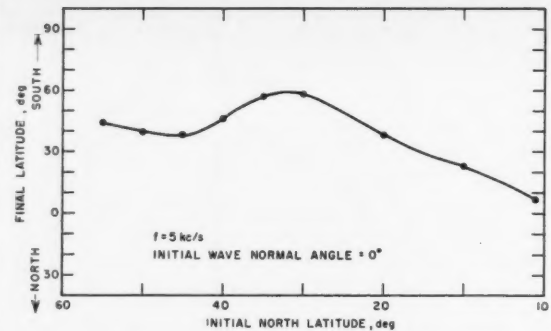


FIGURE 3(l). Final latitude versus initial latitude.

This plot of final latitude against initial value shows some focusing of rays in the region of  $45^\circ$  and  $33^\circ$  latitude.

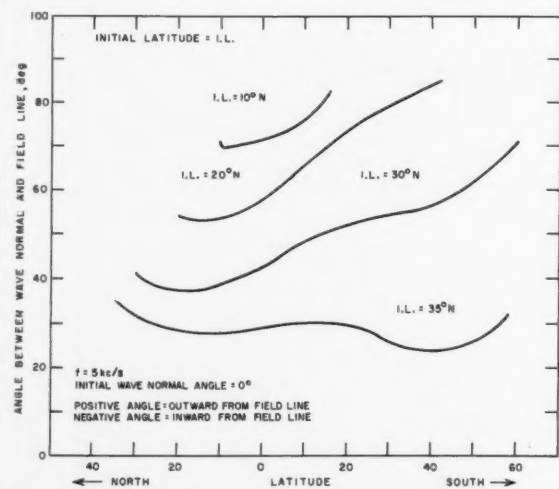


FIGURE 3(m). Wave normal—field line angle along the path.

At initial north latitudes greater than  $35^\circ$ , the wave normal swings from the outside to the inside of the field line along the path. For initial north latitudes less than  $35^\circ$ , the wave normal swings farther away from the field line.

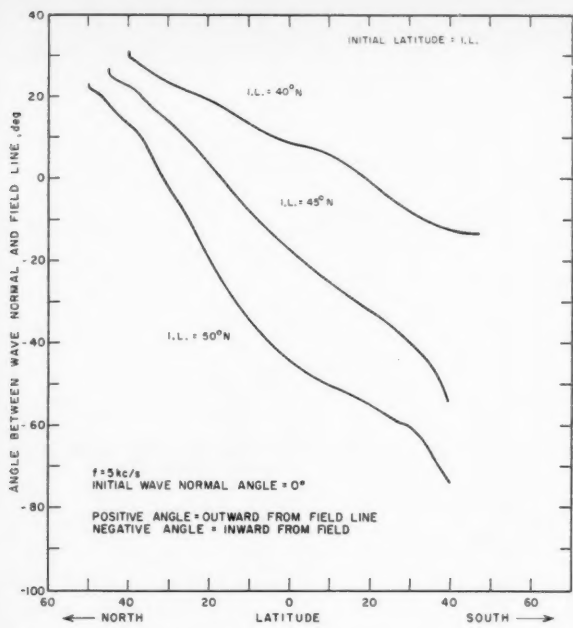


FIGURE 3(n). Wave normal—field line angle along the path.

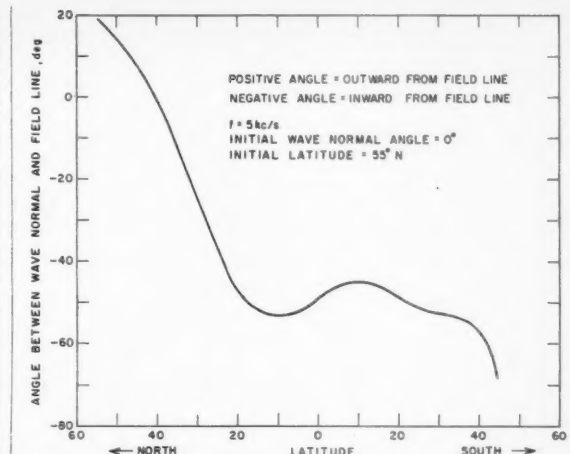


FIGURE 3(o). Wave normal—field line angle along the path.

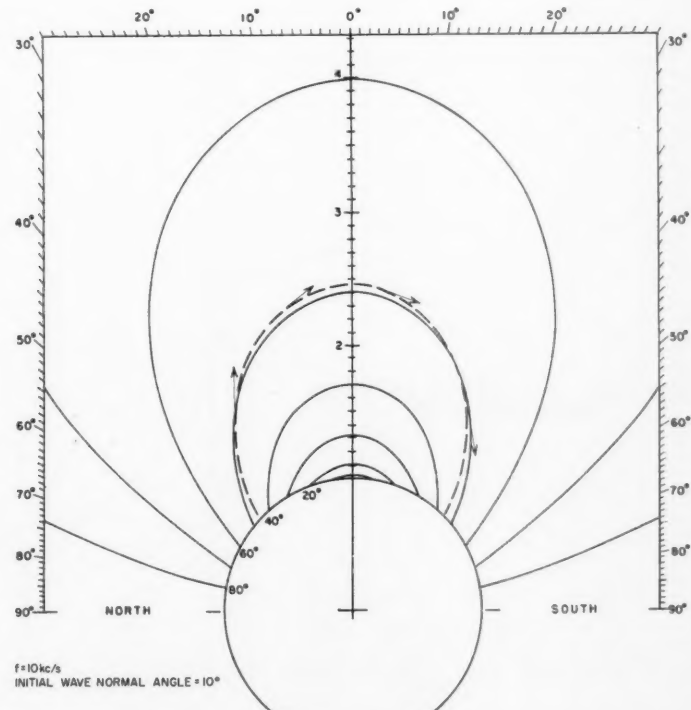


FIGURE 4(a). Ray path with initial wave normal angle = 10°.

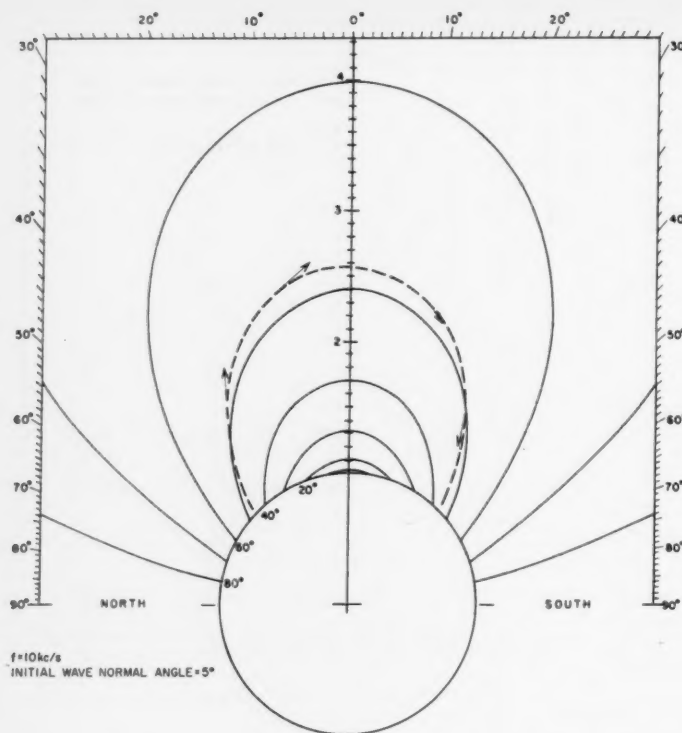


FIGURE 4(b). Ray path with initial wave normal angle =  $5^\circ$

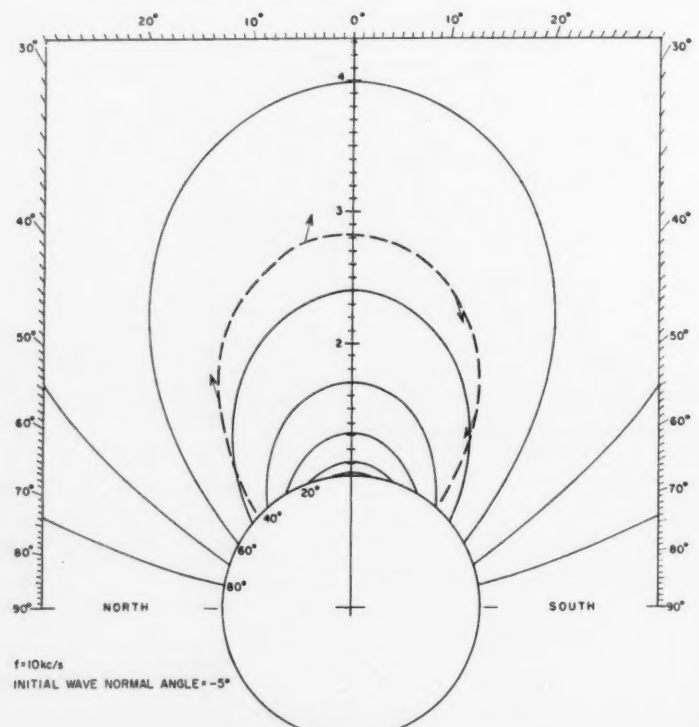


FIGURE 4(c). Ray path with initial wave normal angle =  $-5^\circ$ .

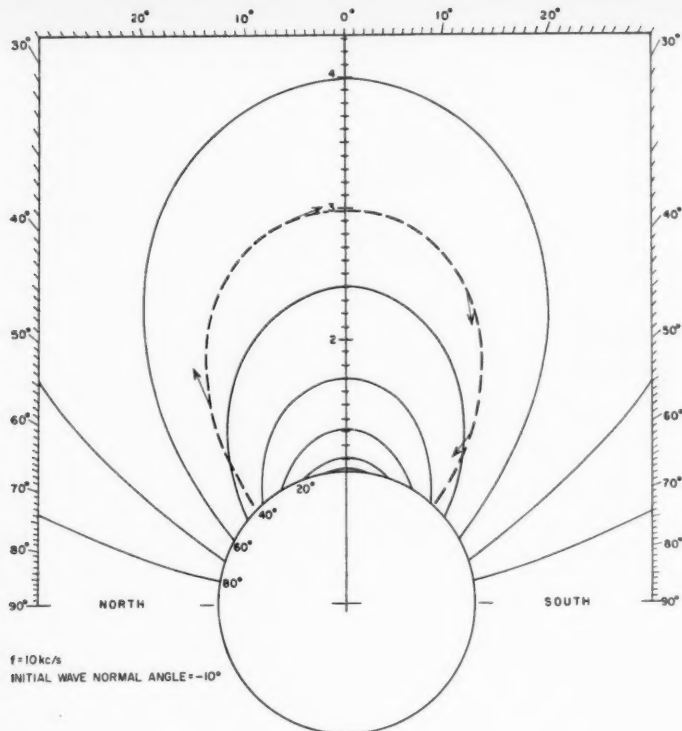


FIGURE 4(d). Ray path with initial wave normal angle =  $10^\circ$ .

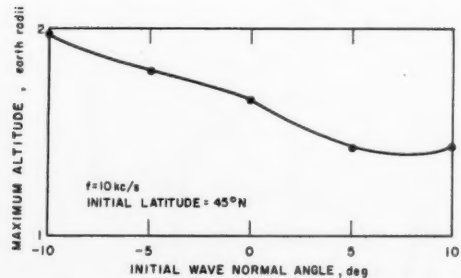


FIGURE 4(e). Maximum altitude versus initial wave normal angle.

Maximum path height is seen to decrease with increasing wave normal angle until the wave reaches between  $5^\circ$  and  $10^\circ$ .

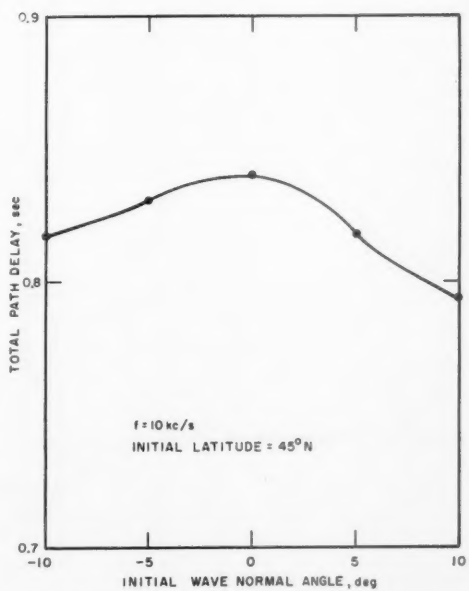


FIGURE 4(f). Total path delay versus initial wave normal angle.

The total time delay is also seen to remain roughly constant with changes in initial wave normal angle. This is again consistent with the idea of average group velocity being roughly proportional to path length.

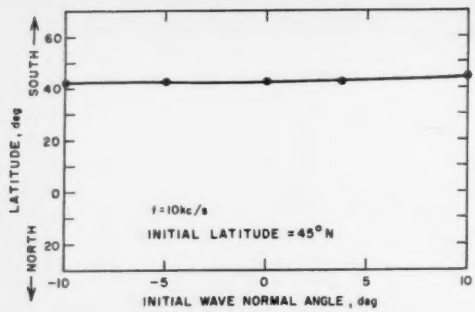


FIGURE 4(g). Final latitude versus initial wave normal angle.

The final latitude is seen to remain constant with initial wave normal variation even though maximum path height changes.

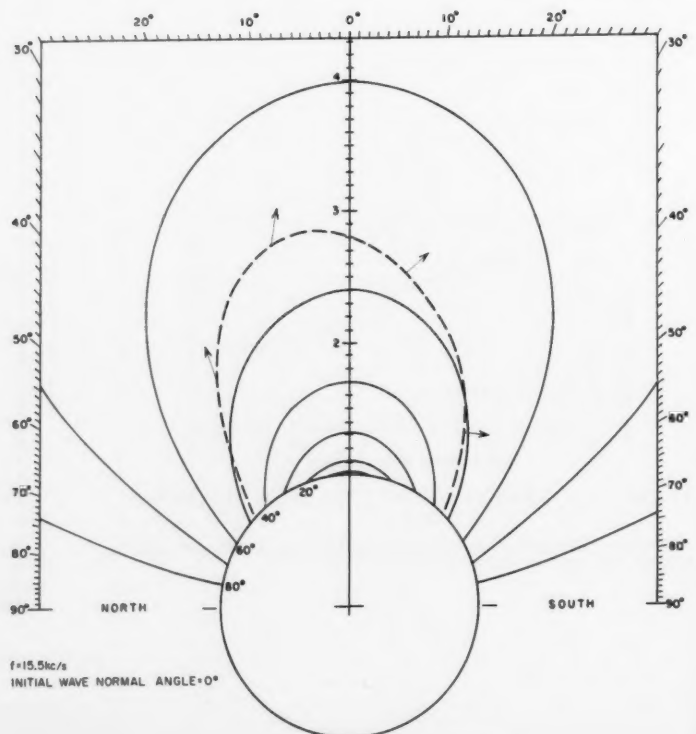


FIGURE 5. Constant density model.

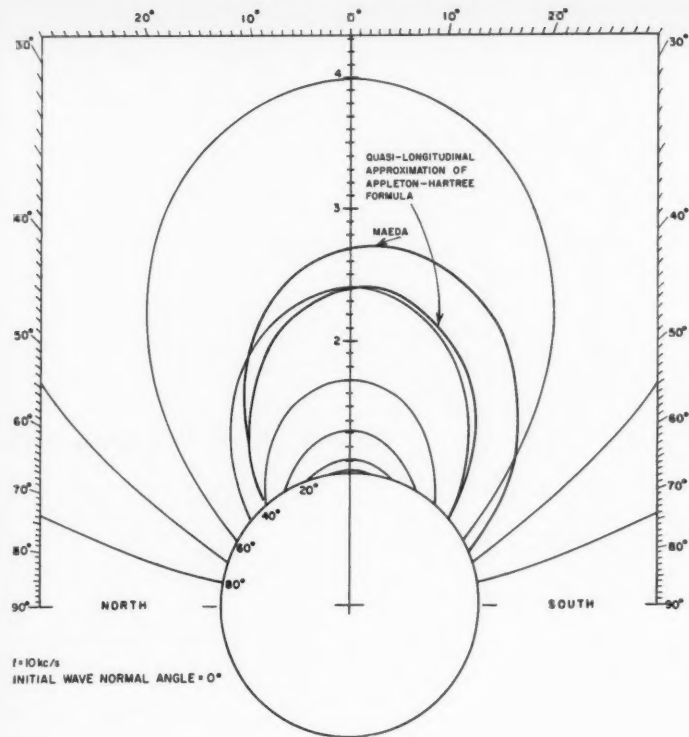
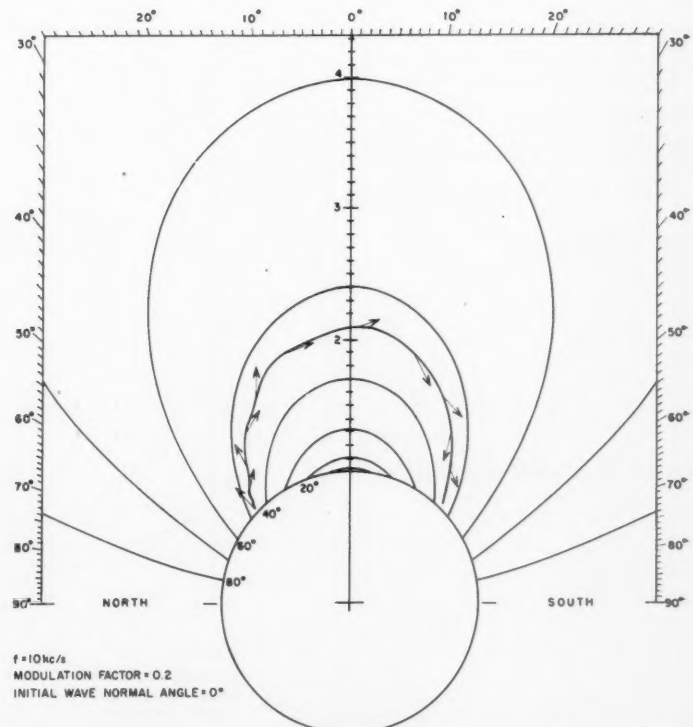


FIGURE 6. Comparison with Maeda's computation.

FIGURE 7. A field-aligned column model.



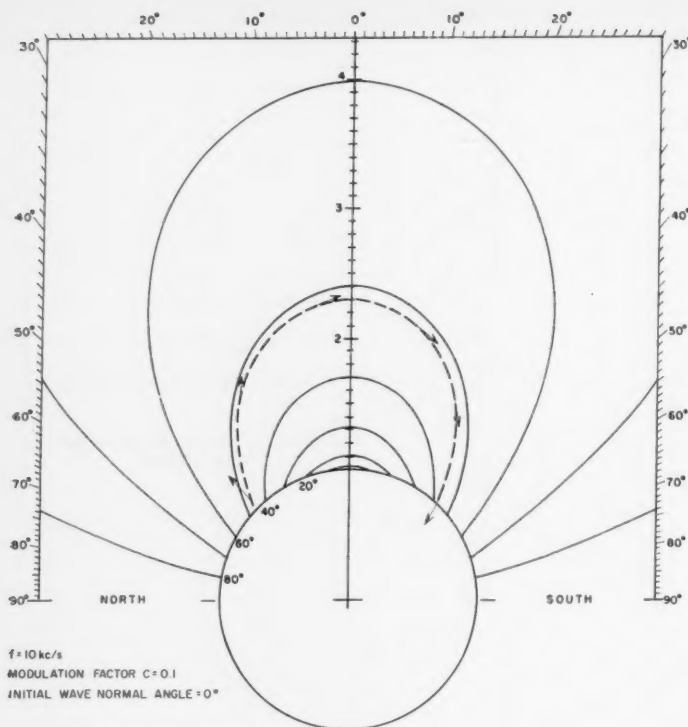


FIGURE 8. A field-aligned column model.

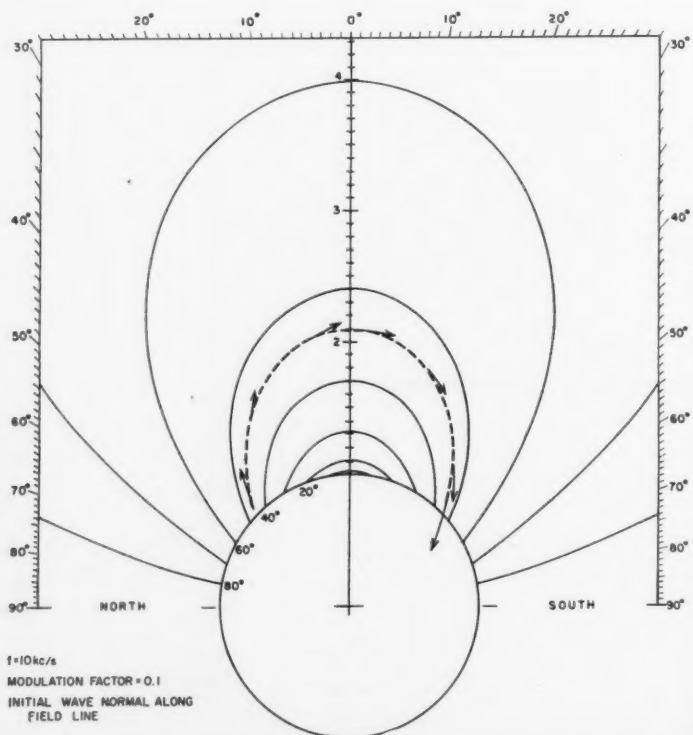


FIGURE 9. A field-aligned column model.

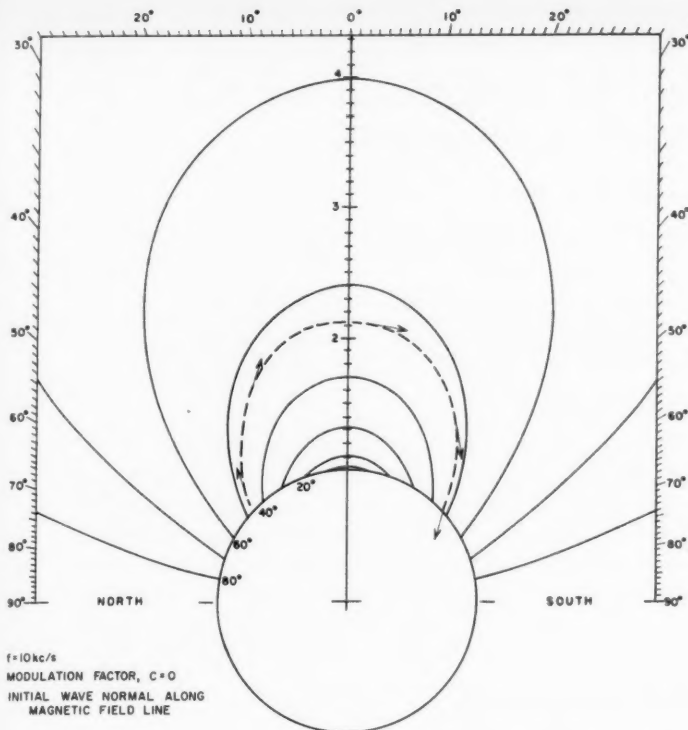


FIGURE 10. Ray path with initial wave normal along field line.

### 3. References

Haselgrave, J., Ray theory and a new method for ray tracing, Report of Phys. Soc. Conference on Physics of the Ionosphere, pp. 355-364, Cambridge (Sept. 1954).  
 Helliwell, R. A., and M. G. Morgan, Atmospheric whistlers, Proc. IRE **47**, No. 2, 200-210 (Feb. 1959).  
 Maeda, K., and I. Kimura, A theoretical investigation on the propagation path of the whistling atmospherics, Rpt. Ionospheric Research Japan **X**, No. 3, 105-123 (Sept. 1956).

Ratcliffe, J. A., The magneto-ionic theory and its application to the ionosphere (Cambridge University Press, Cambridge, Mass., 1959).

Smith, R. L., R. A. Helliwell, and I. W. Yabroff, A theory of trapping of whistlers in field-aligned columns of enhanced ionization, J. Geophys. Research **65**, No. 3, 815-823 (Mar. 1960).

Storey, L. R. O., Phil. Trans. Roy. Soc. [A] **246**, pp. 113-141 (1953).

(Paper 65D5-155



# On the Analysis of LF Ionospheric Radio Propagation Phenomena\*

J. Ralph Johler

Contribution From Central Radio Propagation Laboratory, National Bureau of Standards, Boulder, Colo.

(Received April 27, 1961)

Recent theoretical work which employs the classical magneto-ionic theory for a special model of the ionosphere applicable to transmission via the ionosphere at or close to grazing incidence is employed to analyze LF propagation data. The results of the analysis illustrate a practical model of the ionosphere by a detailed study of transmission via the first time-mode in particular.

## 1. Introduction

Recent contributions and extensions to the classical geometric-optical theory of propagation [Wait and Conda, 1958; Wait, 1960a; Johler and Walters, 1960, 1961] of LF waves about the earth provide a valuable analysis tool for the interpretation of various experimental data. This paper summarizes the mathematical formulas required to predict the field with particular emphasis on a type analysis most suitable for large scale electronic computers. Attention is focused on certain available experimental data and the results of the analysis are detailed with emphasis on technique. However, the physical phenomena which can be deduced as a result of the analysis of these data are given considerable attention to emphasize the value of the technique.

## 2. Mathematical Theory

A geometric-optical theory [Bremmer, 1949] can be employed with the aid of a sharply bounded model ionosphere [Johler and Walters, 1960, 1961] emplaced at various altitudes  $h$  above a spherical earth to describe the *cw* field,  $E(\omega, d)$ , radiated from a dipole source current moment,  $I_0 l$ . It is common engineering practice at LF to relate the amplitude of the field,  $|E(\omega, d)|$  to the well known concept of radiated power [Ballantine, 1924], neglecting earth losses,

$$P_r = 1.6(10^{-13})\omega^2(I_0 l)^2/Z_0, \quad (1)$$

where  $Z_0 \sim 120\pi$ , a constant. Such a field,  $E(\omega, d)$ , implies a similar Hertzian dipole receiver (vertical polarization). The total field,  $E(\omega, d)$ , is the sum of  $j+1$  reflected ionospheric waves,  $j=0, 1, 2, 3 \dots$ ,

$$E(\omega, d) = \sum_{j=0}^p E_j(\omega, d), \quad (2)$$

in which the zero order ( $j=0$ ) reflection,  $E_0(\omega, d)$  is the groundwave. Each skywave reflection,  $j=1, 2, 3 \dots$ , using the positive time function,  $\exp(i\omega t)$ , can be written,

$$E_j(\omega, d) = i\omega d D_j^{-1} C \exp(i\omega t_j) G_j^* G_j \alpha_j F_j C_j, \quad (3)$$

where [Johler, Kellar, and Walters, 1956],

$$E_0(\omega, d) = [E_0(\omega, d)] \exp[-i(\omega b + \phi_e)], \quad (4)$$

and where,

$$C = I_0 l b^2 / 4\pi \kappa d^3 = (10^{-7})/d, (I_0 l = 1). \quad (5)$$

The local time<sup>1</sup> for the groundwave,  $t'_0$  is,

$$t'_0 = t - b, \quad (6)$$

$$b = \eta_l d/c, \quad (7)$$

\*This is a revised version of a paper presented at the Avionics Panel Meeting of the Advisory Group for Aeronautical Research and Development (AGARD) NATO, Istanbul, Turkey, October 1960.

<sup>1</sup>The notion of local time was apparently introduced by Lorentz [1906, p. 57].

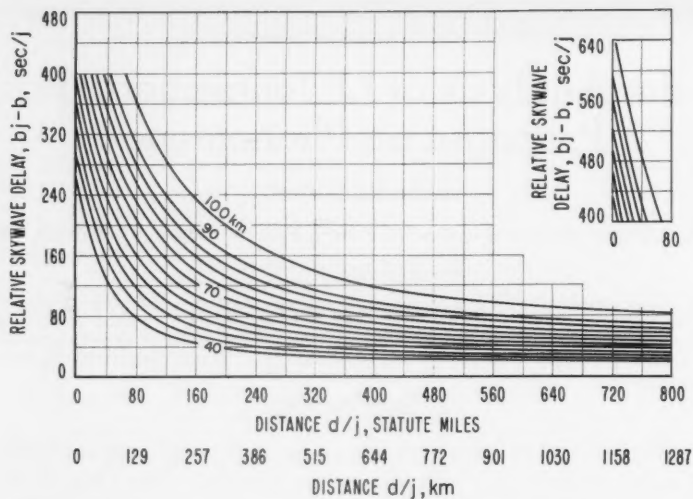


FIGURE 1. *Relative sky wave delay for various altitude,  $h$ , of the lower boundary of the model ionosphere.*

where  $c$  is the speed of light,  $c \sim 3(10^8)$  m/sec, and  $\eta_1$  is the index of refraction of air,  $\eta_1 \sim 1$ . Similarly, the local skywave time, or skywave delay,  $t'_j$  ( $j=1, 2, 3 \dots$ ) is,

$$t'_j = t - b_j, \quad (8)$$

$$b_j = \eta_1 D_j / c, \quad (j=1, 2, 3 \dots). \quad (9)$$

The quantity,  $b_j - b$ , is frequently called the relative skywave delay, figure 1 (relative to the groundwave). The physical length of the ray,  $D_j$ , can be evaluated geometrically for a reflection at an altitude,  $h$ , above the surface of the earth of radius,  $a$ ,

$$D_j = 2j [(a+h) \cos \phi_{t,j} - a \cos \tau_j], \quad (10)$$

where, figures 2, 3,  $\phi_t$  is the angle of incidence of the "ray" on the ionosphere and  $\tau_j$  is the

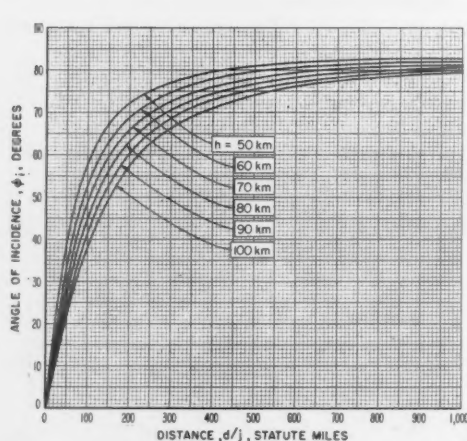


FIGURE 2. *Geometric-optical relation between the angle of incidence,  $\phi_i$ , distance from the source,  $d/j$  ( $j$  = order of sky wave hop or time-mode,  $j=1, 2, 3 \dots$ ) and altitude of the boundary of the model ionosphere,  $h$ .*

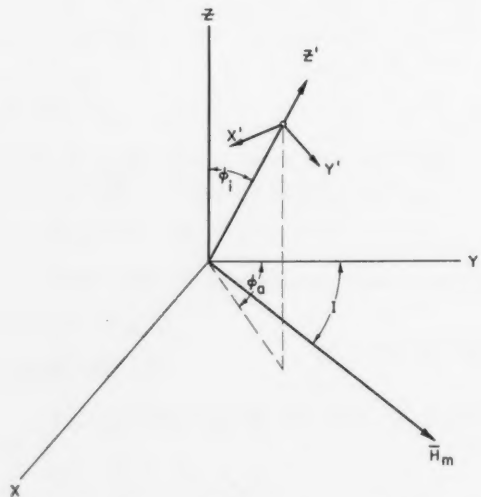


FIGURE 3. *Coordinate systems at the ionosphere boundary.*

corresponding angle of incidence on the earth and the subscript "j" reminds the reader that the equation refers to the particular ionospheric reflection under consideration. The angles  $\phi_i$  and  $\tau_j$  are evaluated quite simply from the geometry,

$$\sin \phi_{i,j} = \Delta_j^{-1} a \sin \frac{\theta}{2j}, \quad (11)$$

$$\cos \phi_{i,j} = \Delta_j^{-1} [a(1 - \cos \theta/2j) + h], \quad (12)$$

$$\sin \tau_j = \Delta_j^{-1} (a + h) \sin \theta/2j, \quad (13)$$

$$\cos \tau_j = \Delta_j^{-1} [a(\cos \theta/2j - 1) + h \cos \theta/2j], \quad (14)$$

$$\Delta_j = [2a(a + h)(1 - \cos \theta/2j) + h^2]^{\frac{1}{2}}, \quad (15)$$

where  $\theta$  is the angle at the center of the earth subtended by the distance,  $d$ , along the surface of a spherical earth, or, simply,

$$d = a\theta.$$

The factors,  $G_i^j$  and  $G_j^j$  refer to the transmitter and receiver complex antenna patterns respectively, and again the subscript, "j", is employed to designate the particular time-mode under consideration. The vertically polarized Hertzian dipoles considered in this paper reduce to,  $G_i^j = G_j^j = \sin \tau_j$ . Of course, other antenna complex pattern factors can be introduced.

Since plane reflection coefficients are employed in this analysis, the convergence-divergence coefficient,  $\alpha_j$ , is necessary to convert the plane reflection coefficients to spherical reflection coefficients or from the viewpoint of "ray theory" it is necessary to take account of ray focusing by the ionosphere and a corresponding defocusing of rays by the earth. The "classical" convergence-divergence is modified by a "convergence correction" [Wait, 1959],  $A_j$ , in this paper, since the values of the first time-mode studied are at distances close to the "caustic" of rays or geometric-optical horizon, and hence the complete expression,  $\alpha_j$ ,

$$\alpha_j = (1 + h/a)[(2j \sin \theta/2j)/\sin \theta]^{\frac{1}{2}} \times \{[a(1 - \cos \theta/2j) + h]/[(a + h) \cos \theta/2j - a]\}^{\frac{1}{2}} A_j, \quad (16)$$

in which  $A_j$  can be evaluated from the cylindrical Hankel function of order,  $n = \frac{1}{3}$ , of the second kind,

$$A_j \sim \left[ \frac{\pi}{2} k_1 a \cos^3 \tau_j / 3 \sin^2 \tau_j \right]^{\frac{1}{2}} H_{\frac{1}{3}}^{(2)} \left[ k_1 a \cos^3 \tau_j / 3 \sin^2 \tau_j \right] \times \exp \left\{ -i \left[ 5\pi/12 - k_1 a \cos^3 \tau_j / 3 \sin^2 \tau_j \right] \right\}. \quad (17)$$

The factor,  $|A_j|$ , approaches unity ( $A_j \sim 1$ ) at shorter distances, ( $\tau_j \ll \pi/2$ ). Near the geometric-optical-horizon,  $\tau_j \sim \pi/2$ , and beyond, the correction becomes quite appreciable. The Hankel functions,  $H_n^{(2)}(z)$  can be readily evaluated on an electronic computer by a consideration of the integral form,

$$H_n^{(2)}(z) = \frac{1}{\pi} \int_0^\pi \exp(-iz \sin \rho + in\rho) d\rho - \frac{1}{\pi i} \int_0^\infty \exp(-z \sinh \rho) \{ \exp n\rho + \exp(-n\rho + in\pi) \} d\rho, \quad (18)$$

where the order,  $n = \frac{1}{3}$ , and the argument,  $z = k_1 a \cos^3 \tau_j / 3 \sin^2 \tau_j$ , in which the wave number,  $k_1 = \omega \eta_1 / c \sim \omega / c$ , for the case under consideration are real numbers. Nevertheless, it is interesting to note that the method is also applicable to complex argument,  $z$ , and complex order,  $n$ , provided the multiple branches of the Hankel function are carefully considered. The following substitution is made,

$$\beta = \exp(-\rho),$$

and a resultant expression for the Hankel function.

$$H_n^{(2)}(z) = \frac{1}{\pi} \int_0^\pi \exp(-iz \sin \rho + in\rho) d\rho - \frac{1}{\pi i} \int_0^1 \left[ \beta^{-n-1} + \beta^{n-1} \exp(in\pi) \right] \exp\left[-\frac{z}{2}\left(\frac{1}{\beta} - \beta\right)\right] d\beta, \quad (19)$$

or,

$$H_n^{(2)}(z) = \int_0^\pi f(z, \rho, n) d\rho - \int_0^1 f(z, \beta, n) d\beta, \quad (20)$$

is found to comprise integrals with finite limits. These integrals can then be evaluated in terms of Gaussian quadrature,<sup>2</sup>

$$H_n^{(2)}(z) = \sum_{m=1}^M W_m^\rho [\operatorname{Re} f(z, \rho_m, n) + i \operatorname{Im} f(z, \rho_m, n)] - \sum_{m=1}^M W_m^\beta [\operatorname{Re} f(z, \beta_m, n) + i \operatorname{Im} f(z, \beta_m, n)] + \epsilon(M) \quad (21)$$

$m = 1, 2, 3, \dots, M$ , where,  $\epsilon(M)$  can be made arbitrarily small by increasing  $M$ ,

where,

$$\begin{aligned} W_m^\rho &= \pi H_m / 2, \\ W_m^\beta &= H_m / 2, \\ \rho_m &= \pi x_m / 2 + \pi / 2, \\ \beta_m &= x_m / 2 + 1/2, \end{aligned}$$

and the constants,  $x_m$ , of the theory of Gaussian quadrature can be evaluated as the roots of the Legendre polynomials defined by,

$$\frac{d^M}{dx^M} (x^2 - 1)^M - 2^M M! P_M(x) = 0, \quad (22)$$

or,

$$P_0(x) = 1,$$

$$P_1(x) = x,$$

$$P_2(x) = \frac{3}{2}x^2 - \frac{1}{2},$$

$$P_3(x) = \frac{5}{2}x^3 - \frac{3}{2}x,$$

$$P_4(x) = \frac{35}{8}x^4 - \frac{15}{4}x^2 + \frac{3}{8},$$

...

(23)

where polynomials of higher degree are determined by the use of the recursion formula,

$$(M+1)P_{M+1}(x) + MP_{M-1}(x) - (2M+1)xP_M(x) = 0. \quad (24)$$

The weight coefficients,  $H_m$ , are evaluated from the roots,  $x_m$ ,

$$H_m = 2 / (1 - x_m^2) [P_M'(x_m)]^2. \quad (25)$$

The factor,  $F_j$ , accounts for the presence of the earth at the transmitter (source) and receiver. If it can be assumed that the "ray" reflected by the earth is not too close or beyond the geometric-optical horizon, the Fresnel approximation of the ground reflection coefficient suffices to determine  $F_j$ , or,

$$F_j \sim [1 + R_e^s(\tau_j)][1 + R_e^r(\tau_j)], \quad (26)$$

<sup>2</sup>This type analysis has been used extensively by the author in previous papers to evaluate Fourier integrals [Johler and Walters, 1959].

where the superscripts,  $t$  and  $r$ , refer to the transmitter and receiver respectively and the subscript,  $e$ , refers to vertical polarization, and,

$$R_e(\tau_j) = \{k_2^2 \cos \tau_j/k_1^2 - [k_2^2/k_1^2 - \sin^2 \tau_j]^{1/2}\} / \{k_2^2 \cos \tau_j/k_1^2 + [k_2^2/k_1^2 - \sin^2 \tau_j]^{1/2}\}, \quad (27)$$

or for horizontal polarization,

$$R_m(\tau_j) = \{\cos \tau_j - [k_2^2/k_1^2 - \sin^2 \tau_j]^{1/2}\} / \{\cos \tau_j + [k_2^2/k_1^2 - \sin^2 \tau_j]^{1/2}\}, \quad (28)$$

where,

$$k_2 = \frac{\omega}{c} \left[ \epsilon_2 - i \frac{\sigma \mu_0 c^2}{\omega} \right]^{1/2} \quad (29)$$

and  $\epsilon_2$  is the dielectric constant of the earth ( $\epsilon_2 \sim 15$ ) and  $\sigma$  is the conductivity of the earth ( $\sigma \sim 0.005$  for land). Since the examples considered in this paper involve distances which, for the first time-mode, were close to the geometric-optical horizon, it was found necessary to replace the Fresnel reflection coefficients with a more rigorous treatment.

Close to the geometric-optical horizon a calculation of  $F_j = F_j^t F_j^r$  can be accomplished by a numerical evaluation of the contour integral, [Wait and Conda, 1958],

$$F_j^{t,r} \sim (\pi)^{-1/2} \exp[-ik_1 a \theta'] \int_{\infty \exp[-i2\pi/3]}^{\infty} \exp[-i(k_1 a/2)^{1/2} \theta' \rho] / [W_1'(\rho) - q W_1(\rho)] d\rho, \quad (30)$$

$\theta' = (d - d_H)/a$ , where  $d_H$  is the distance <sup>3</sup> from transmitter to the geometric-optical horizon ( $\tau_j \sim \pi/2$ ) and,

$$q = -i \left( \frac{k_1 a}{2} \right)^{1/2} \frac{k_1}{k_2} \sqrt{1 - \frac{k_1^2}{k_2^2}}, \quad (31)$$

in which  $\sigma = \sigma_2$  is the ground conductivity at either transmitter  $F_j^t$  or receiver  $F_j^r$  and  $\epsilon_2$  is the corresponding dielectric constants (relative to a vacuum), and,

$$W_1(\rho) = \exp[-2\pi i/3] \sqrt{\pi/3} (-\rho)^{1/2} H_{1/2}^{(2)}[2/3(-\rho)^{1/2}], \quad (32)$$

$$W_1'(\rho) = \exp[-2\pi i/3] \sqrt{\pi/3} \left\{ -\frac{1}{2} (-\rho)^{-1/2} H_{1/2}^{(2)} \left[ \frac{2}{3}(-\rho)^{1/2} \right] + \rho H_{1/2}^{(2)} \left[ \frac{2}{3}(-\rho)^{1/2} \right] \right\},$$

$$W_1'(\rho) = \exp[-i4\pi/3] \sqrt{\pi/3} \rho H_{1/2}^{(2)} \left[ \frac{2}{3}(-\rho)^{1/2} \right] \quad (33)$$

$$H_{1/2}^{(2)}(Z) = \frac{d}{dZ} H_{1/2}^{(2)}(Z) = \exp[-i2\pi/3] H_{1/2}^{(2)}(Z) - \frac{1}{3Z} H_{1/2}^{(2)}(Z). \quad (34)$$

The Hankel functions  $H_{1/2}^{(1,2)}(Z)$  can be calculated by previously described quadrature methods (20-27). The contour integral can be written [Wait, 1960b],

$$F_j^{t,r} = (\pi)^{-1/2} \exp[-ik_1 a \theta'] \left\{ \int_0^{\infty} \frac{\exp[-i(k_1 a/2)^{1/2} \theta' \alpha]}{W_1'(\alpha) - q W_1(\alpha)} d\alpha - \int_0^{\infty} \frac{\exp[-i(k_1 a/2)^{1/2} \theta' \alpha']}{W_1'(\alpha') - q W_1(\alpha')} d\alpha' \right\}, \quad (35)$$

$\alpha' = \alpha \exp(-i2\pi/3)$ . These integrals can then be evaluated with a Gaussian quadrature.

Close to but beyond the geometric-optical horizon ( $\tau_j \sim \pi/2$ ) [Wait and Conda, 1958], a calculation can be performed as a residue series summation,

$$F_j^{t,r} \sim -2i\sqrt{\pi} \exp[-ik_1(d - d_H)] \sum_{s=0}^{\infty} \frac{\exp[-i(k_1 a)^{1/2} \theta' \tau_s^*]}{(2i\tau_s^* - q^2) W_1(2i\tau_s^*)} \quad (36)$$

<sup>3</sup>  $a \sim 6.367 (10^6)$  m. In diffraction problems it is common practice to account for the vertical lapse of the permittivity of air at the earth's surface by use of an "effective earth radius",  $a_s$  in place of  $a$  such that  $\frac{a}{a_s} \sim 0.75 - 0.85$ , [Bremmer, 1949, p. 145].

where the complex conjugate  $\tau_s$  of  $\tau_s^*$  comprises the special roots of the differential equation of Riccati tabulated by Johler, Walters, and Lilley [1959], employing the time function,  $\exp(-i\omega t)$ ,

$$\frac{d\delta_e}{d\tau_s} - 2\tau_s \delta_e^2 + 1 = 0, \quad (37)$$

where

$$\delta_e = \frac{ik_2^2 \alpha^4 / k_1^2}{(k_1 a)^{\frac{1}{2}} \left[ \frac{k_2^2}{k_1^2} - 1 \right]^{\frac{1}{2}}} \sim i \frac{Z_0}{(k_1 a)^{\frac{1}{2}} \left[ \frac{-i\mu_0 \omega}{\sigma - i\omega_e} \right]^{\frac{1}{2}}} \quad (38)$$

and,  $k_1 = \frac{\omega}{c} \eta_1 \sim \frac{\omega}{c}$ ,  $k_2^*$ , implies the complex conjugate of  $k_2$ , (3), and the limiting roots are found from the equations,

$$\begin{aligned} H_{\frac{1}{4}}^{(1)} \left[ \frac{1}{3} (-2\tau_s)^{\frac{1}{2}} \right] &= 0, \quad \delta_e = \infty, \\ H_{\frac{1}{4}}^{(1)} \left[ \frac{1}{3} (-2\tau_s)^{\frac{1}{2}} \right] &= 0, \quad \delta_e = 0, \\ s &= 0, 1, 2, 3 \dots \end{aligned}$$

Finally, the effective reflection coefficient of geometric-optics,  $C_j$ , can be evaluated for vertical polarization,

$$C_j = \frac{1}{j! R_e} \frac{d^j}{dx^j} \left[ \frac{1 + A_1 x}{1 - A_2 x - A_3 x^2} \right]_{x=0}, \quad (39)$$

where,

$$\begin{aligned} A_1 &= -R_m T_{mm} \\ A_2 &= R_e T_{ee} + R_m T_{mm} \\ A_3 &= R_e R_m [-T_{ee} T_{mm} + T_{em} T_{me}]. \end{aligned} \quad (40)$$

Thus, the essential nature of the propagation about the earth via the ionosphere can be described in terms of four reflection coefficients,  $T_{ee}$ ,  $T_{em}$ ,  $T_{me}$ , and  $T_{mm}$ . The reflection coefficient,  $T_{ee}$ , refers to the vertical electric polarization of the incident plane wave and a similar vertical electric polarization of the reflected wave. The coefficient,  $T_{em}$ , describes the generation of the abnormal component by the incident vertical polarization (reflected horizontal polarization for vertical excitation). Similarly,  $T_{mm}$  refers to the incident horizontal electric polarization and the corresponding reflected horizontal electric polarization. Also, the abnormal component generated by the horizontal electric polarization (reflected vertical polarization for horizontal excitation) is described by the coefficient,  $T_{me}$ . Thus, figure 3,

$$T_{ee} = E'_{y'ri} / E_{y'i}, \quad T_{mm} = E'_{x'ri} / E_{x'i}, \quad T_{em} = E'_{x'ri} / E_{y'i}, \quad T_{me} = E'_{y'ri} / E_{x'i} \quad (41)$$

where the subscripts  $i$  and  $r$  refer to incident and reflected wave respectively at the ionosphere boundary. The calculation of these reflection coefficients has been previously described in detail and the results of various computations have been tabulated [Johler and Walters, 1960].

The reflection coefficients are completely specified by the angle of incidence,  $\phi_i$ , figures 2, 3, electron density  $N(\text{El/cm}^3)$ , figure 4, collision frequency  $\nu(\text{c/s})$ , figure 5, magnetic field intensity  $H_m$  (gauss), magnetic dip  $I$  and magnetic azimuth  $\phi_a$ . The effective reflection coefficients,  $C_j$ , can then be written in terms of the ionosphere reflection coefficients,  $T$ , and the ground reflection coefficients,  $R$ , for each local ionosphere or ground reflection,

$$\begin{aligned} C_1 &= C_1(\tau_1) = T_{ee}, \\ C_2 &= C_2(\tau_2) = T_{ee_1} T_{ee_2} R_{e_1} + R_{m_1} T_{em_1} T_{me_2}, \\ C_3 &= C_3(\tau_3) = R_{e_2} R_{m_1} T_{ee_3} T_{em_1} T_{me_2} + R_{e_1} R_{m_2} T_{ee_1} T_{em_1} T_{me_3} + R_{e_1} R_{e_2} T_{ee_1} T_{ee_2} T_{ee_3} + R_{m_1} R_{m_2} T_{mm_2} T_{em_1} T_{me_3}, \end{aligned} \quad (42)$$

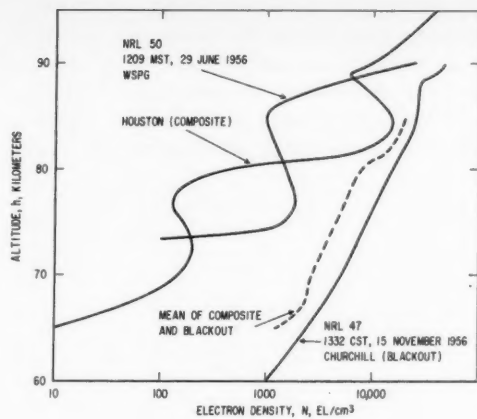


FIGURE 4. Electron density-altitude,  $N(h)$ , profiles of the lower ionosphere deduced from various radio and rocket measurements.

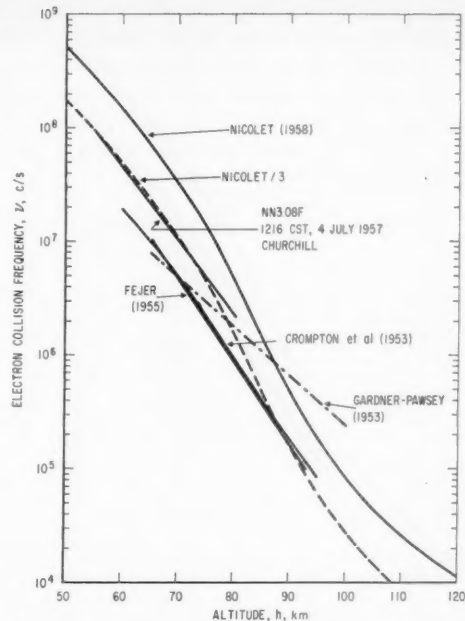


FIGURE 5. Collision frequency-altitude,  $\nu(h)$ , profiles of the lower ionosphere deduced from theory and various rocket measurements.

$$\begin{aligned}
 C_4 = C_4(\tau_4) = & R_{e_1} R_{e_2} R_{e_3} T_{ee_4} T_{ee_3} T_{ee_1} + R_{e_1} R_{e_2} R_{m_3} T_{me_4} T_{em_3} T_{ee_2} T_{ee_1} + R_{e_1} R_{m_2} R_{e_3} T_{ee_4} T_{em_3} T_{em_2} T_{ee_1} \\
 & + R_{e_1} R_{m_2} R_{m_3} T_{me_4} T_{mm_3} T_{em_2} T_{ee_1} + R_{m_1} R_{e_2} R_{e_3} T_{ee_4} T_{ee_3} T_{me_2} T_{em_1} + R_{m_1} R_{e_2} R_{m_3} T_{me_4} T_{em_3} T_{me_2} T_{em_1} \\
 & + R_{m_1} R_{m_2} R_{e_3} T_{ee_4} T_{me_3} T_{mm_2} T_{em_1} + R_{m_1} R_{m_2} R_{m_3} T_{me_4} T_{mm_3} T_{mm_2} T_{em_1},
 \end{aligned} \quad (43)$$

where the subscripts 1, 2, 3, 4 . . . refer to the first, second, third, fourth, etc., reflection regions of the ionosphere with corresponding separate values for electron density,  $N$ , collision frequency,  $\nu$ , and the intensity and direction of the earth's magnetic field vector,  $\bar{H}_m$ , or, for the ground, refer to the separate values of conductivity,  $\sigma$ , and dielectric constant,  $\epsilon_2$ .

For a homogeneous ionosphere and ground with a single set of values,  $N$ ,  $\nu$ ,  $\bar{H}_m$ ,  $\sigma$ , and  $\epsilon_2$ , the effective reflection coefficients,  $C_j$ , reduce as follows:

$$\begin{aligned}
 C_1 &= T_{ee} \\
 C_2 &= T_{ee}^2 R_e + R_m T_{em} T_{me} \\
 C_3 &= 2R_e R_m T_{ee} T_{em} T_{me} + R_e^2 T_{ee}^3 + R_m^2 T_{mm} T_{em} T_{me}, \\
 C_4 &= R_e R_m^2 T_{em}^2 T_{me}^2 + 3R_e^2 R_m T_{ee}^2 T_{em} T_{me} + 2R_e R_m^2 T_{ee} T_{mm} T_{em} T_{me} + R_m^3 T_{mm}^2 T_{em} T_{me} + R_e^3 T_{ee}^4,
 \end{aligned} \quad \dots \quad (44)$$

The wave number of the ionosphere propagation medium,

$$\begin{aligned}
 k_3 &= \frac{\omega}{c} \eta_0, \\
 &= \frac{\omega}{c} \eta_e,
 \end{aligned} \quad (45)$$

implies two upgoing waves excited in the model ionosphere with index of refraction,  $\eta_0$ , for

of the calculations was the altitude,  $h$ , of the assumed sharply bounded model ionosphere. This implies a variation of the electron density according to the  $N(h)$  profile as the variable  $h$  is changed. Also, small adjustments in the angle of incidence,  $\phi_i$ , are implied.

Geophysical data on the ionosphere employed in the calculation are shown, tables 1, 2. The magnetic data, shown in table 2, were scaled from Magnetic Charts [1954, 1957]. Apparently a nominal intensity value  $H_m=0.5$  gauss (table 2) is an adequate assumption for many practical cases.

TABLE 1

$h$	$\nu$	$N_g$	$N_d$	$N_b$
km	$c/s \times 10^{10}$	$El/cm^3$	$El/cm^3$	$El/cm^3$
55	175	-----	-----	10
60	50	-----	-----	1000
65	24	10	1205	2400
67.5	16	56	-----	-----
70	10.9	150	2675	5200
71	9.2	180	-----	-----
72.5	7	200	-----	-----
75	4.5	160	4505	8850
77.5	2.6	140	-----	-----
80	1.6	500	7980	15400
81	1.2	3500	10550	-----
82.5	0.88	11000	16100	-----
85	.465	15000	20500	26000
90	.155	10000	-----	-----

TABLE 2.—Magnetic field,  $H_m$ , data

Adak-Nome, $d=965.5$ statute miles (1,550 km)				
	Reflection number	$H_m$	$I$	$\phi_a$
1	1st	0.5187	68.68	12.27
2	1st	.4996	65.75	12.52
2	2d	.5329	71.52	11.72
2	1st	.4952	64.82	12.63
3	2d	.5187	68.68	12.27
3	3d	.5388	72.46	11.66
Adak-Kodiak, $d=1040.1$ statute miles (1,670 km)				
	Reflection number	$H_m$	$I$	$\phi_a$
1	1st	0.5035	67.18	51.08
2	1st	.4950	65.15	52.84
2	2d	.5170	69.04	49.73
3	1st	.4923	64.42	53.42
3	2d	.5085	67.18	51.08
3	3d	.5262	69.64	49.35

The modal (skywave time-mode) and the total (including the groundwave) calculated fields (amplitude and phase) for quiescent, disturbed, and blackout conditions of the ionosphere are presented, figures 6 to 9. The effect of the ionosphere focusing corrections,  $A_j$ , is also illustrated, and, indeed, was found to be appreciable, both for the total field,  $E(\omega, d)$ , and the first modal field,  $E_j(\omega, d)$ ,  $j=1$ . The diffraction correction  $F_j$  was also modified from the classical Fresnel reflection coefficient as discussed with the aid of calculated data of Wait and Conda [1958] which was installed in the electronic memory of a small computer.<sup>5</sup>

The ground wave,  $E_0(\omega, d)$ , which was calculated with the classical Bremmer-van der Pol theory [Johler, Kellar, and Walters, 1956] and corrected for land-sea boundaries with the aid of the Millington [1949] method is not shown alone graphically, since the groundwave is not a function of the emplacement altitude,  $h$ , but can be summarized as follows:

TABLE 3

	$E_0(\omega, d)$		$\arg E_0(\omega, d)$
	$I_0 d = 1$	$I_0 d = 2050$	
Nome	$v/m$ 7.56( $10^{-6}$ )	$v/m$ 1.55( $10^{-6}$ )	$Radians$ 2.30
Kodiak	$v/m$ 4.64( $10^{-6}$ )	$v/m$ 9.51( $10^{-6}$ )	$Radians$ 2.43

<sup>5</sup> IBM-650.

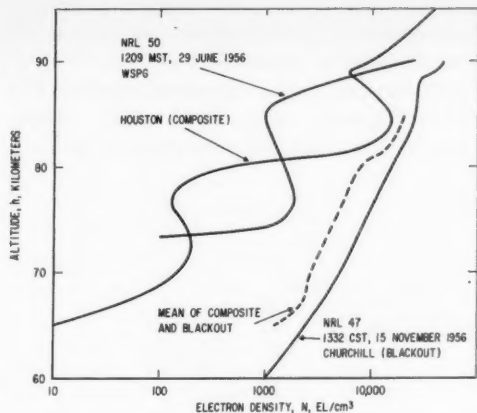


FIGURE 4. Electron density-altitude,  $N(h)$ , profiles of the lower ionosphere deduced from various radio and rocket measurements.

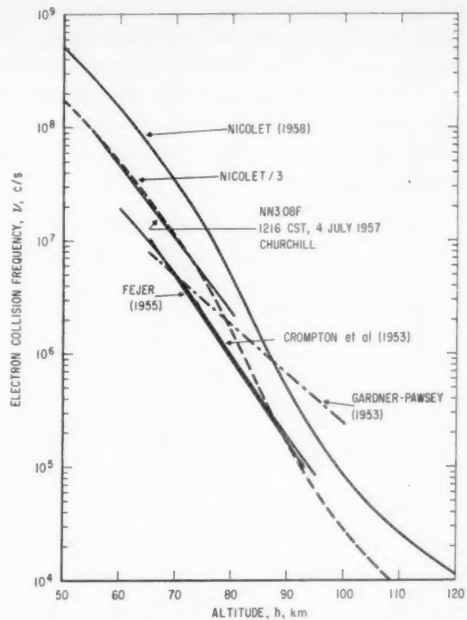


FIGURE 5. Collision frequency-altitude,  $\nu(h)$ , profiles of the lower ionosphere deduced from theory and various rocket measurements.

$$\begin{aligned}
 C_4 = C_4(\tau_4) = & R_{e_1} R_{e_2} R_{e_3} T_{ee_4} T_{ee_3} T_{ee_2} T_{ee_1} + R_{e_1} R_{e_2} R_{m_3} T_{me_4} T_{em_3} T_{ee_2} T_{ee_1} + R_{e_1} R_{m_2} R_{e_3} T_{ee_4} T_{me_3} T_{em_2} T_{ee_1} \\
 & + R_{e_1} R_{m_2} R_{m_3} T_{me_4} T_{mm_3} T_{em_2} T_{ee_1} + R_{m_1} R_{e_2} R_{e_3} T_{ee_4} T_{ee_3} T_{me_2} T_{em_1} + R_{m_1} R_{e_2} R_{m_3} T_{me_4} T_{em_3} T_{me_2} T_{em_1} \\
 & + R_{m_1} R_{m_2} R_{e_3} T_{ee_4} T_{me_3} T_{mm_2} T_{em_1} + R_{m_1} R_{m_2} R_{m_3} T_{me_4} T_{mm_3} T_{mm_2} T_{em_1}
 \end{aligned} \quad (43)$$

where the subscripts 1, 2, 3, 4 . . . refer to the first, second, third, fourth, etc., reflection regions of the ionosphere with corresponding separate values for electron density,  $N$ , collision frequency,  $\nu$ , and the intensity and direction of the earth's magnetic field vector,  $\bar{H}_m$ , or, for the ground, refer to the separate values of conductivity,  $\sigma$ , and dielectric constant,  $\epsilon_2$ .

For a homogeneous ionosphere and ground with a single set of values,  $N$ ,  $\nu$ ,  $\bar{H}_m$ ,  $\sigma$ , and  $\epsilon_2$ , the effective reflection coefficients,  $C_j$ , reduce as follows:

$$\begin{aligned}
 C_1 &= T_{ee} \\
 C_2 &= T_{ee}^2 R_e + R_m T_{em} T_{me} \\
 C_3 &= 2R_e R_m T_{ee} T_{em} T_{me} + R_e^2 T_{ee}^3 + R_m^2 T_{mm} T_{em} T_{me}, \\
 C_4 &= R_e R_m^2 T_{em}^2 T_{me}^2 + 3R_e^2 R_m T_{ee} T_{em} T_{me} + 2R_e R_m^2 T_{ee} T_{mm} T_{em} T_{me} + R_m^3 T_{mm}^2 T_{em} T_{me} + R_e^3 T_{ee}^4, \\
 &\dots
 \end{aligned} \quad (44)$$

The wave number of the ionosphere propagation medium,

$$\begin{aligned}
 k_3 &= \frac{\omega}{c} \eta_0, \\
 &= \frac{\omega}{c} \eta_e,
 \end{aligned} \quad (45)$$

implies two upgoing waves excited in the model ionosphere with index of refraction,  $\eta_0$ , for

of the calculations was the altitude,  $h$ , of the assumed sharply bounded model ionosphere. This implies a variation of the electron density according to the  $N(h)$  profile as the variable  $h$  is changed. Also, small adjustments in the angle of incidence,  $\phi_i$ , are implied.

Geophysical data on the ionosphere employed in the calculation are shown, tables 1, 2. The magnetic data, shown in table 2, were scaled from Magnetic Charts [1954, 1957]. Apparently a nominal intensity value  $H_m=0.5$  gauss (table 2) is an adequate assumption for many practical cases.

TABLE 1

$h$	$\nu$	$N_e$	$N_d$	$N_b$
km	$c/s \times 10^{10}$	$E1/cm^3$	$E1/cm^3$	$E1/cm^3$
55	175			10
60	50			1000
65	24	10	1205	2400
67.5	16	56		
70	10.9	150	2675	5200
71	9.2	180		
72.5	7	200		
75	4.5	160	4505	8850
77.5	2.6	140		
80	1.6	500	7950	15400
81	1.2	3500	10550	
82.5	0.88	11000	16100	
85	.465	15000	20500	26000
90	.155	10000		

TABLE 2.—Magnetic field,  $\bar{H}_m$ , data

Adak-Nome, $d=965.5$ statute miles (1,550 km)				
	Reflection number	$H_m$	$I$	$\phi_e$
1	1st	0.5187	68.68	12.27
2	1st	.4996	65.75	12.52
2	2d	.5329	71.52	11.72
2	1st	.4852	64.82	12.63
3	2d	.5187	68.68	12.27
3	3d	.5888	72.46	11.66
Adak-Kodiak, $d=1040.1$ statute miles (1,670 km)				
1	1st	0.5035	67.18	51.08
2	1st	.4950	65.15	52.84
2	2d	.5170	69.04	49.73
3	1st	.4923	64.42	53.42
3	2d	.5035	67.18	51.08
3	3d	.5262	69.64	49.35

The modal (skywave time-mode) and the total (including the groundwave) calculated fields (amplitude and phase) for quiescent, disturbed, and blackout conditions of the ionosphere are presented, figures 6 to 9. The effect of the ionosphere focusing corrections,  $A_j$ , is also illustrated, and, indeed, was found to be appreciable, both for the total field,  $E(\omega, d)$ , and the first modal field,  $E_j(\omega, d)$ ,  $j=1$ . The diffraction correction  $F_j$  was also modified from the classical Fresnel reflection coefficient as discussed with the aid of calculated data of Wait and Conda [1958] which was installed in the electronic memory of a small computer.<sup>5</sup>

The ground wave,  $E_0(\omega, d)$ , which was calculated with the classical Bremmer-van der Pol theory [Johler, Kellar, and Walters, 1956] and corrected for land-sea boundaries with the aid of the Millington [1949] method is not shown alone graphically, since the groundwave is not a function of the emplacement altitude,  $h$ , but can be summarized as follows:

TABLE 3

	$E_n(\omega, d)$		$\arg E_0(\omega, d)$
	$I_0 d = 1$	$I_0 d = 2050$	
Nome	$\mu/m$	$\mu/m$	$Radians$
Kodiak	$7.56(10^{-6})$ $4.64(10^{-6})$	$1.55(10^{-6})$ $9.51(10^{-6})$	2.30 2.43

<sup>5</sup> IBM-650.

All computations were made with the assumption of a dipole current moment,  $I_0 l = 1$ . The total radiated power,  $P_r = 1.3$  kw, for the arctic data considered was found to correspond to a dipole current moment,  $I_0 l = 2050$  amp-m; therefore, the calculated field amplitude,  $[E(\omega, d)]$ , or  $[E_j(\omega, d)]$ , has been increased by this factor for comparison with the data.

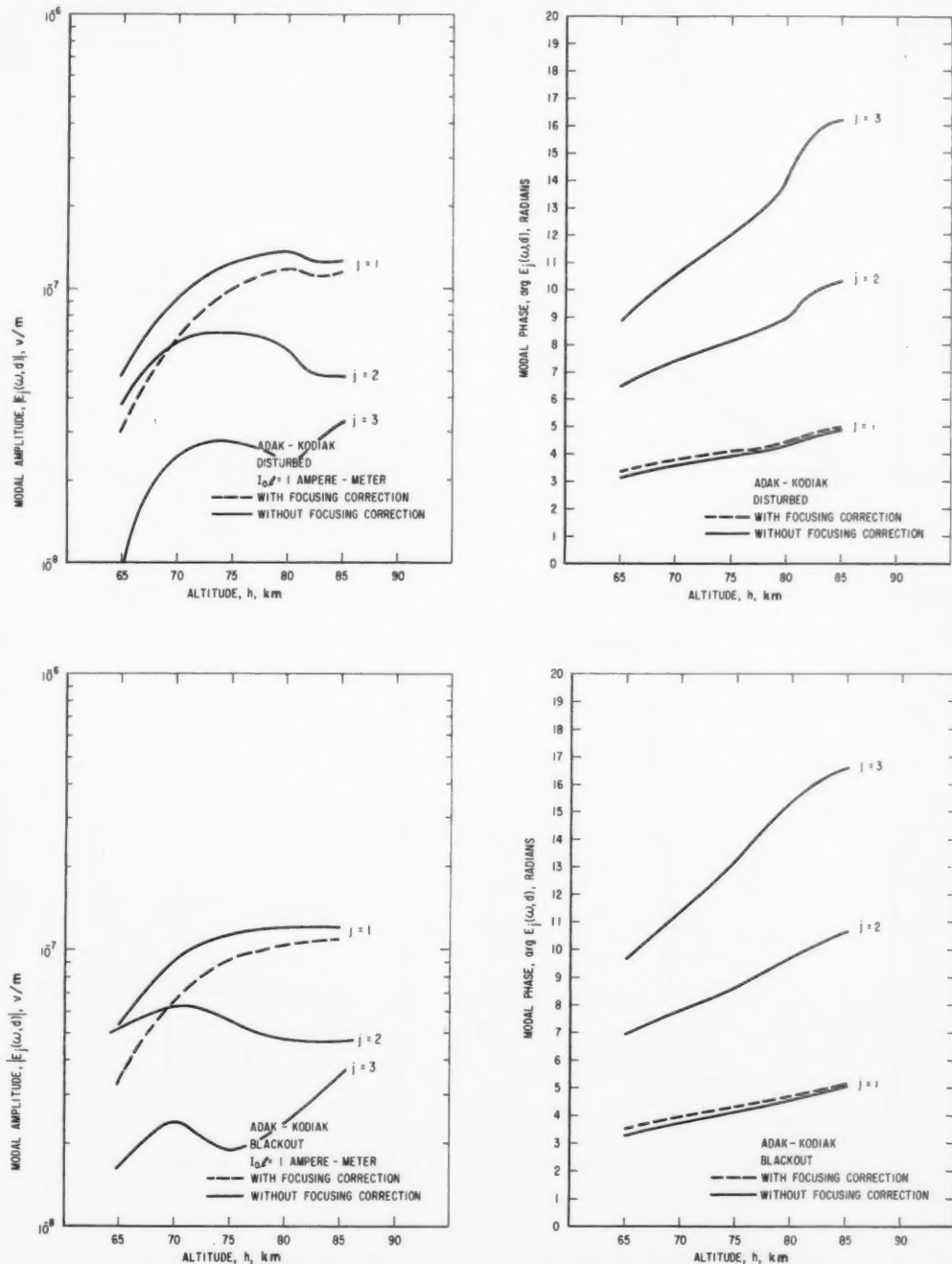


FIGURE 7. Disturbed-blackout theoretical field  $E(\omega, d)$  for various fixed heights,  $h$ , of sharply bounded model ionosphere for LF transmissions from Adak to Kodiak, Alaska.

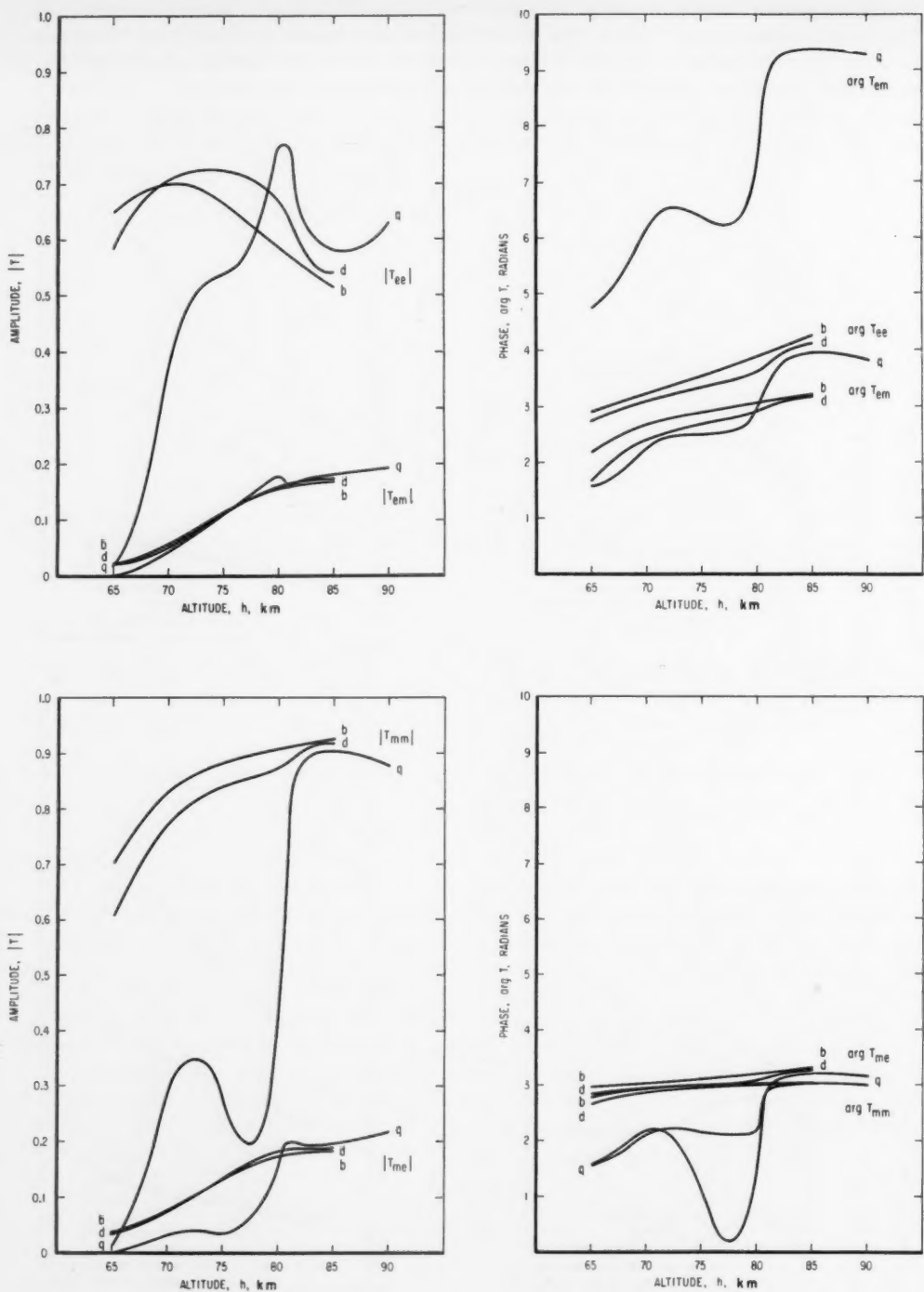


FIGURE 10. Comparison of quiescent and disturbed-blackout conditions of theoretical reflection coefficient,  $T_j$  ( $j=1$ ), for various fixed heights,  $h$ , of sharply bounded model ionosphere for LF transmissions from Adak to Kodiak, Alaska.

$H_m = 0.5035$ ,  $\phi_a = 51.08^\circ$ ,  $I = 67.18^\circ$

All computations were made with the assumption of a dipole current moment,  $I_0 l = 1$ . The total radiated power,  $P_r = 1.3$  kw, for the arctic data considered was found to correspond to a dipole current moment,  $I_0 l = 2050$  amp-m; therefore, the calculated field amplitude,  $[E(\omega, d)]$ , or  $[E_j(\omega, d)]$ , has been increased by this factor for comparison with the data.

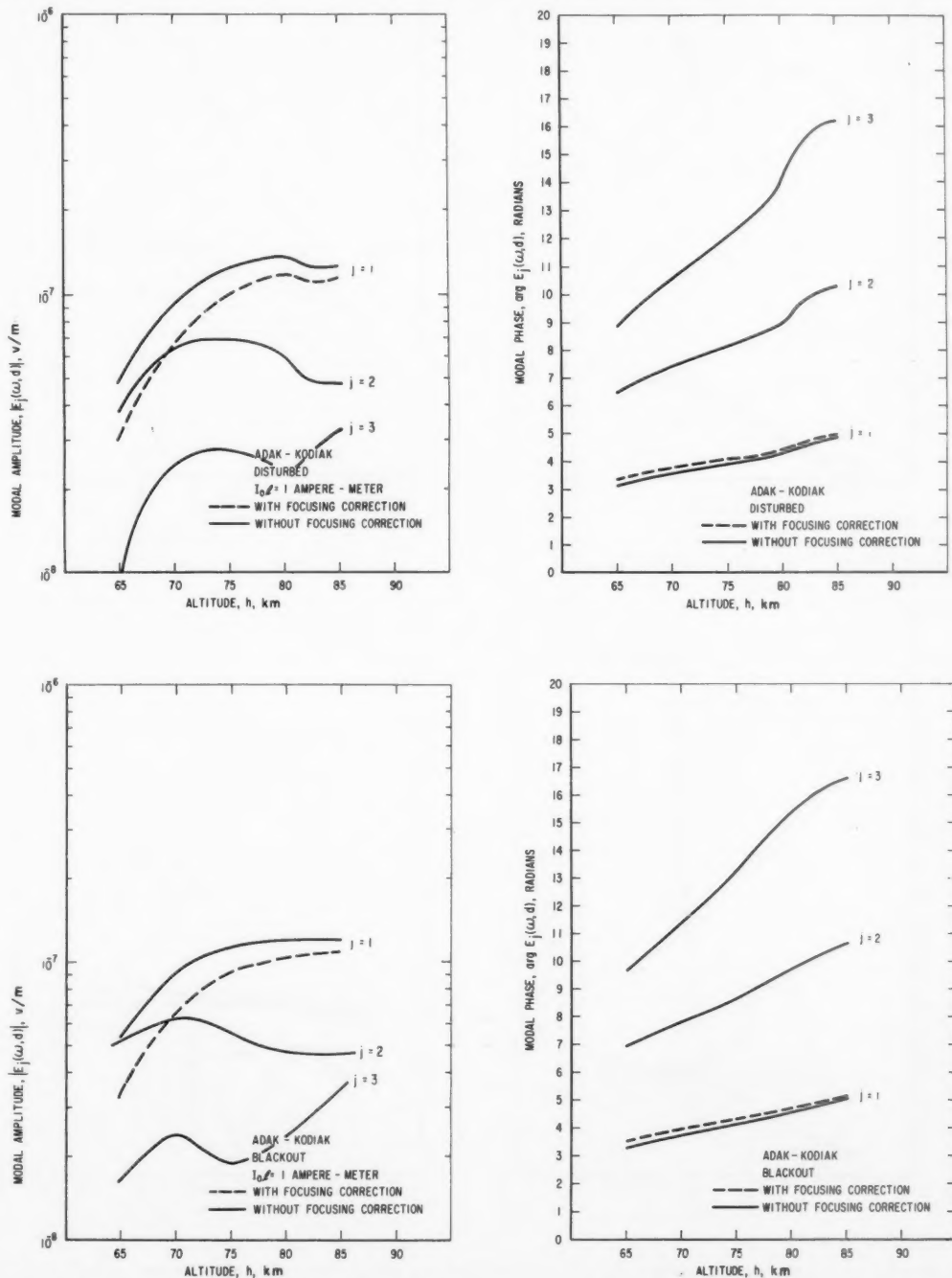


FIGURE 7. Disturbed-blackout theoretical field  $E(\omega, d)$  for various fixed heights,  $h$ , of sharply bounded model ionosphere for LF transmissions from Adak to Kodiak, Alaska.

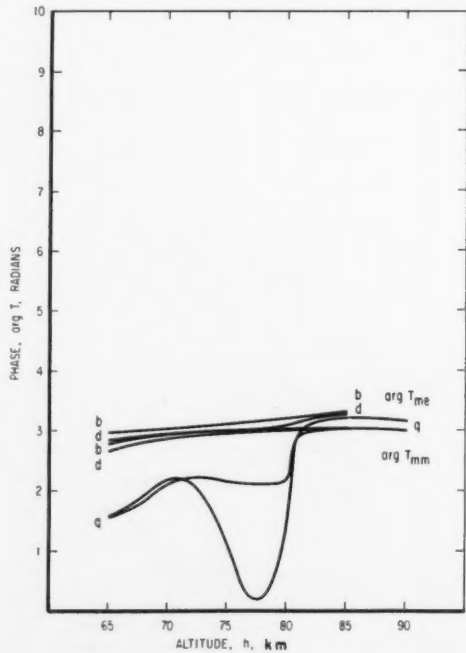
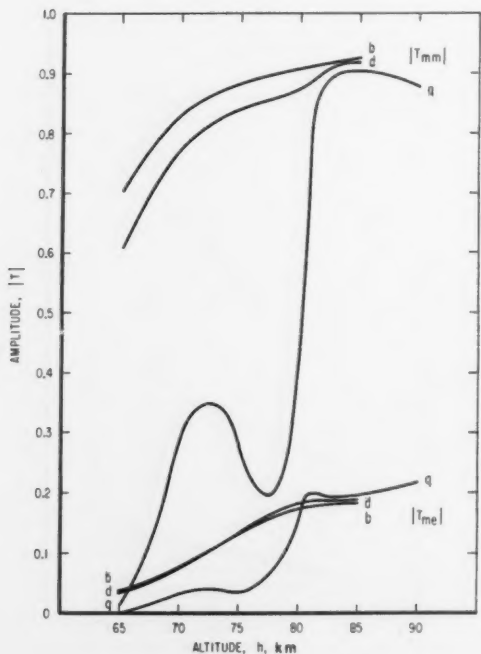
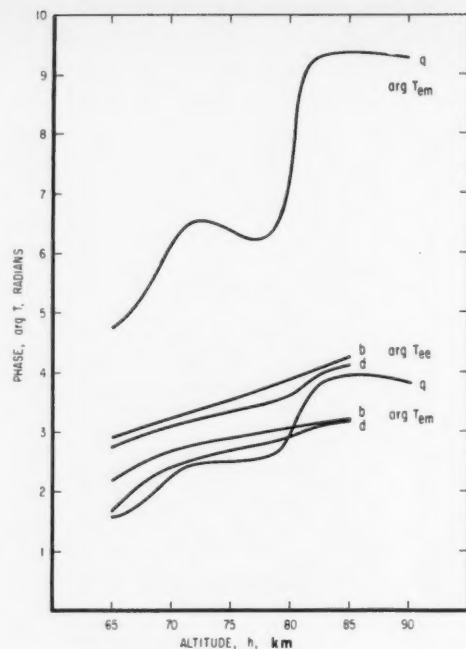
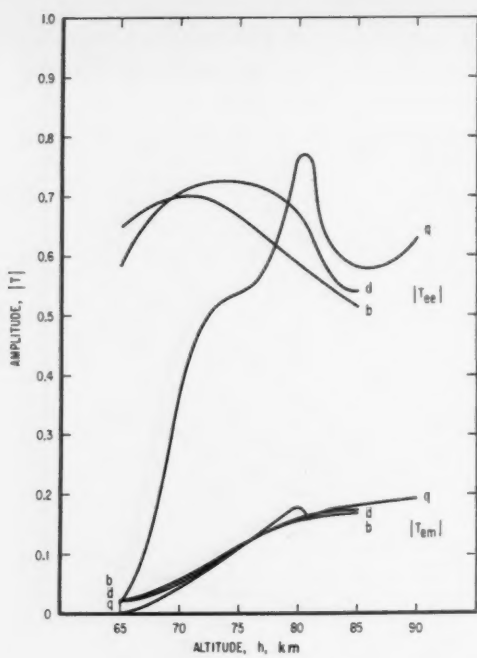


FIGURE 10. Comparison of quiescent and disturbed-blackout conditions of theoretical reflection coefficient,  $T$ , ( $j=1$ ), for various fixed heights,  $h$ , of sharply bounded model ionosphere for LF transmissions from Adak to Kodiak, Alaska.

$H_m = 0.5035$ ,  $\phi_a = 51.08^\circ$ ,  $I = 67.18^\circ$

In addition to the total field,  $E(\omega, d)$ , and the modal field,  $E_j(\omega, d)$ , figures 6 to 9, the reflection coefficients,  $T$ , (horizontal and vertical polarization; normal and abnormal components), figures 10 to 11, and the transmission data of the ordinary and extraordinary upgoing

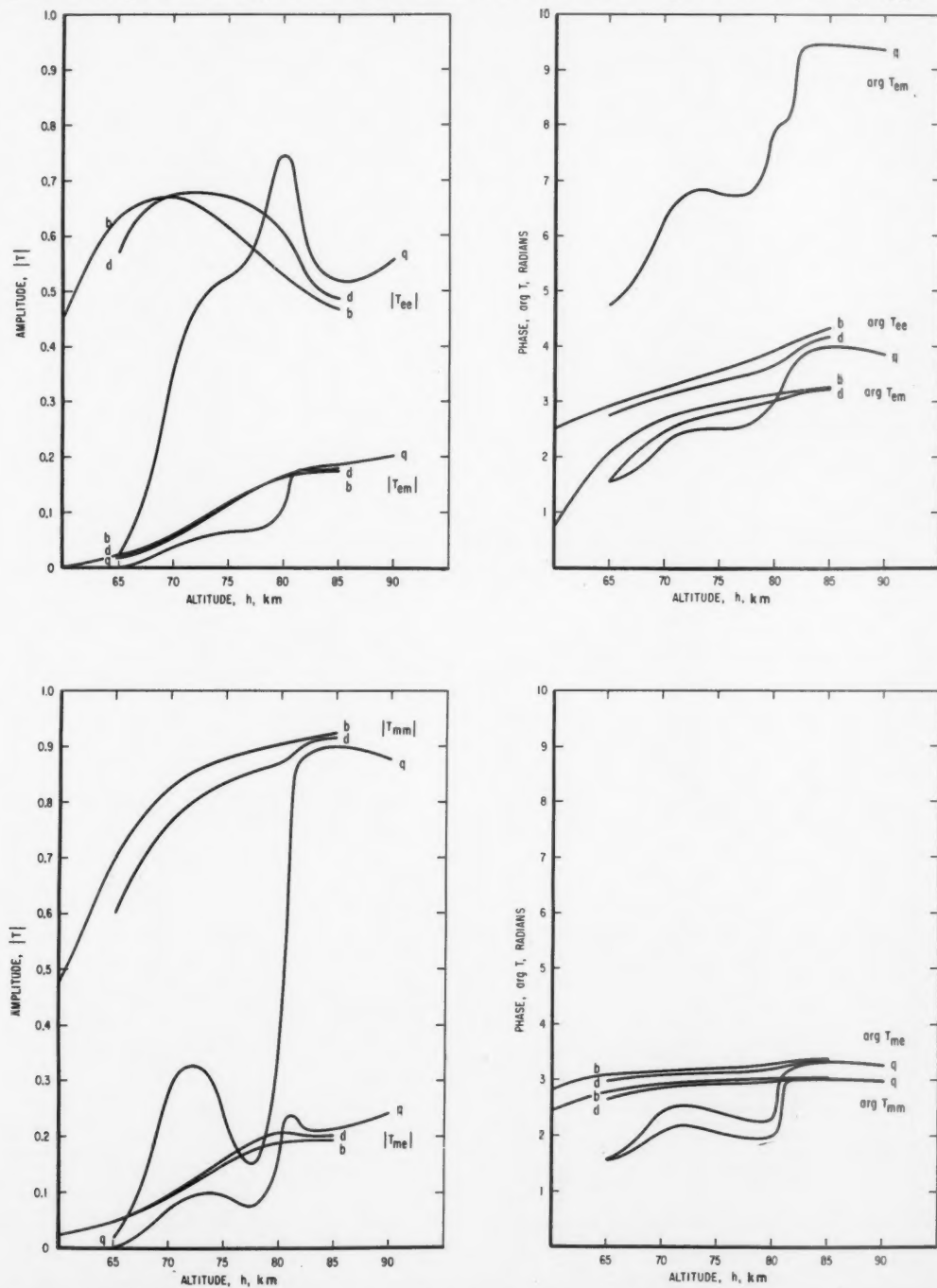


FIGURE 11. Comparison of quiescent and disturbed-blackout conditions of theoretical reflection coefficient,  $T$ , ( $j=1$ ), for various fixed heights,  $h$ , of sharply bounded model ionosphere for LF transmissions from Adak to Nome, Alaska.

$H_m = 0.5187$ ,  $\phi_m = 12.27^\circ$ ,  $I = 68.68^\circ$ .

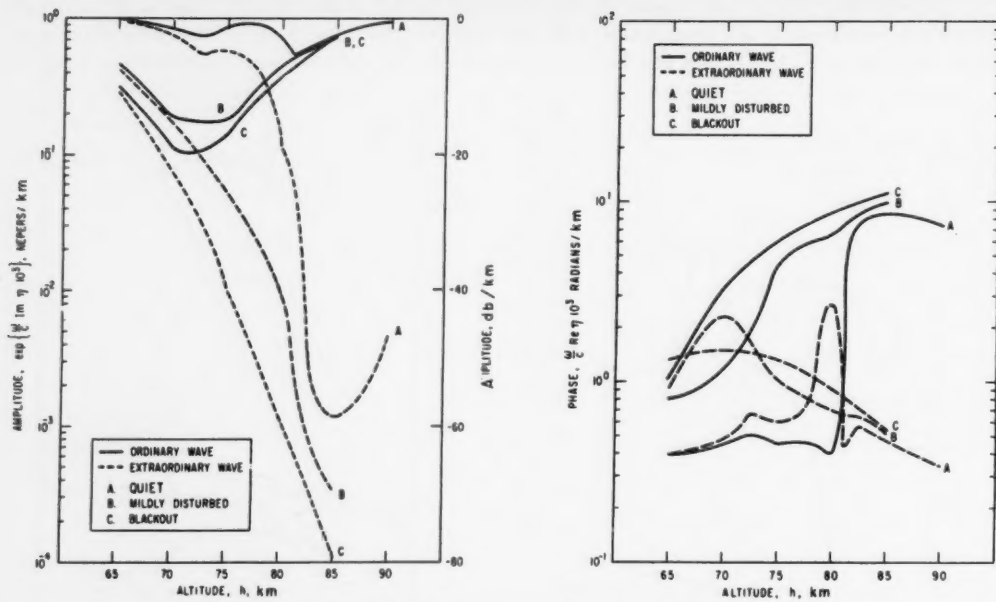


FIGURE 12. Attenuation rate and phase lag rate at various emplacement altitudes,  $h$ , for upgoing "ordinary" and "extraordinary" waves excited in the model ionosphere by Adak to Kodiak, Alaska transmissions during quiescent and disturbed-blackout conditions.

First time-mode:  $H_m = 0.5035$ ,  $\phi_a = 51.08^\circ$ ,  $I = 67.18^\circ$ .

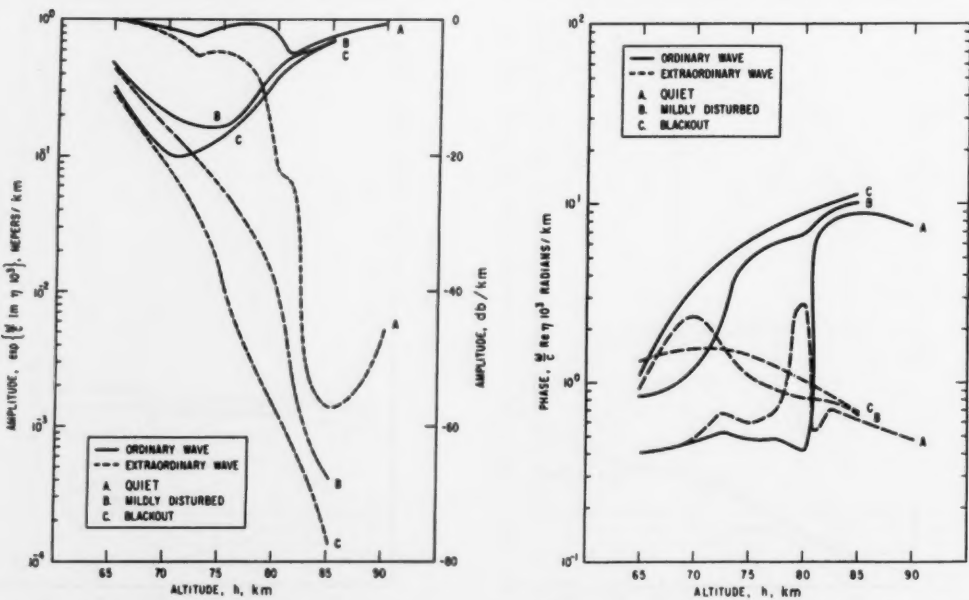


FIGURE 13. Attenuation rate and phase lag rate at various emplacement altitudes,  $h$ , for upgoing "ordinary" and "extraordinary" waves excited in the model ionosphere by Adak to Nome, Alaska transmissions during quiescent and disturbed-blackout conditions.

First time-mode:  $H_m = 0.5187$ ,  $\phi_a = 12.27^\circ$ ,  $I = 68.68^\circ$ .

waves excited in the ionosphere by the reflection process, figures 12, 13, were evaluated. The unabsorbed modal field,  $E_j(\omega, d)/C_j$ , and the effective reflection coefficients,  $C_j$ , are separately illustrated, figures 14 and 15, respectively.

The emplacement height,  $h$ , of the model ionosphere was deduced by comparison of the computed field strength,  $E(\omega, d)$ , with the measured value. The corresponding four reflection coefficients,  $T_{ee}$ ,  $T_{em}$ ,  $T_{mm}$ ,  $T_{me}$ , (amplitude and phase) were then evaluated from the theory. The results of this process which were readily scaled from graphs such as illustrated, figures 10, 11, are presented in table 4, and the reflection coefficients deduced for the first time-mode only are presented.

The higher order time-mode,  $j=2, 3$ , reflection coefficients are obviously quite numerous since a separate set exists for each ionosphere reflecting region. These reflection coefficients are determined by the analysis by reference to the emplacement altitude,  $h$ , table 5, deduced from the field,  $E(\omega, d)$ .

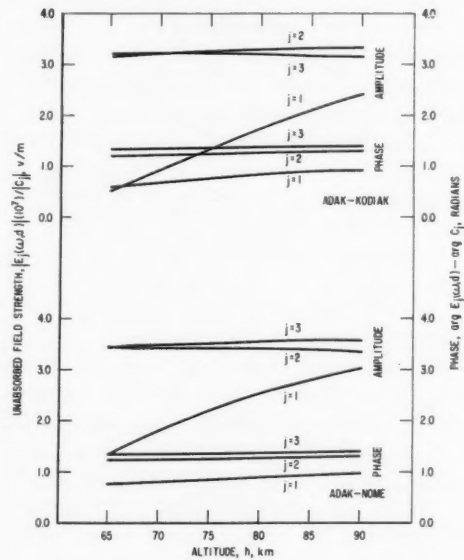


FIGURE 14. Unabsorbed modal field,  $E_j(\omega, d)/c$ , at various model ionosphere altitude emplacements,  $h$ , for Adak to Nome and Kodiak, Alaska transmissions  $I_0 = 1$  ampere-meter.

TABLE 4

Adak-Kodiak (Daytime)

% Time Field $ E $ exceeded	Season and year	Observed $ E(\omega, d) $	$h$	$\arg E(\omega, d)$	$ E_1(\omega, d) $	$\arg E_1(\omega, d)$	$ T_{ee} $	$\arg T_{ee}$	$ T_{em} $	$\arg T_{em}$	$ T_{mm} $	$\arg T_{mm}$	$ T_{me} $	$\arg T_{me}$	$ T_{em} $	$\arg T_{em}$		
10.....	Winter 1953-54...	$\mu V/m$	$km$	<i>Radians</i>	$\mu V/m$	<i>Radians</i>	.27	.21	.03	.02	.23	.16	.03	.02	.20	.02		
50.....		33	69	10.4	56	2.8					5.8	5.7	2.0	1.9	2.0	2.1		
90.....		12	68	9.5	35	2.6					5.7	5.7	1.9	1.9	2.0	2.0		
10.....	Autumn 1954....	4.8	<65	<5.0	<2.0	<2.1	<.02	<1.6	0	<4.8	<.02	<1.6	0	<1.6	<1.6	<1.6	<1.6	
50.....		20	69	10.4	56	2.8					5.8	5.8	.23	.20	.03	.03	.21	.21
90.....		7.1	<65	<5.0	<2.0	<2.1					<4.8	<4.8	<.02	<1.6	0	<1.6	<1.6	<1.6
10.....	Autumn 1954....	2.6	<65	<5.0	<2.0	<2.1	<.02	<1.6	0	<4.8	<.02	<1.6	0	<1.6	<1.6	<1.6	<1.6	
50.....																		
90.....																		

Adak-Nome (Daytime)

% Time Field $ E $ exceeded	Season and year	Observed $ E(\omega, d) $	$h$	$\arg E(\omega, d)$	$ E_1(\omega, d) $	$\arg E_1(\omega, d)$	$ T_{ee} $	$\arg T_{ee}$	$ T_{em} $	$\arg T_{em}$	$ T_{mm} $	$\arg T_{mm}$	$ T_{me} $	$\arg T_{me}$	$ T_{em} $	$\arg T_{em}$
10.....	Winter 1953-54...	$124$	$69$	$9.8$	$94$	$3.0$	$0.29$	$2.1$	$0.03$	$5.95$	$0.23$	$1.95$	$0.055$	$2.25$		
50.....		56	68	9.0	60	2.7	.18	1.9	.02	5.55	.15	1.8	.04	2.0		
90.....		22	65.5	6.4	9.0	2.4	.04	1.6	.01	4.8	.035	1.6	.01	1.6		
10.....	Autumn 1954....	64	68.5	9.3	70	2.8	.22	1.95	.025	5.7	.18	1.9	.045	2.1		
50.....		28	66.5	7.4	22	2.5	.08	1.65	.01	5.0	.065	1.65	.015	1.75		
90.....		11	<65	<5.7	<5.0	<2.3	<.02	<1.55	0	<4.75	<.02	<1.6	0	<1.6		
10.....	Spring 1954....	34	67	7.8	36	2.6	.11	1.75	.015	5.2	.09	1.7	.02	1.8		
50.....		19	<65	<5.7	<5.0	<2.3	<.02	<1.55	0	<4.75	<.02	<1.6	0	<1.6		
90.....		10	<65	<5.7	<5.0	<2.3	<.02	<1.55	0	<4.75	<.02	<1.6	0	<1.6		

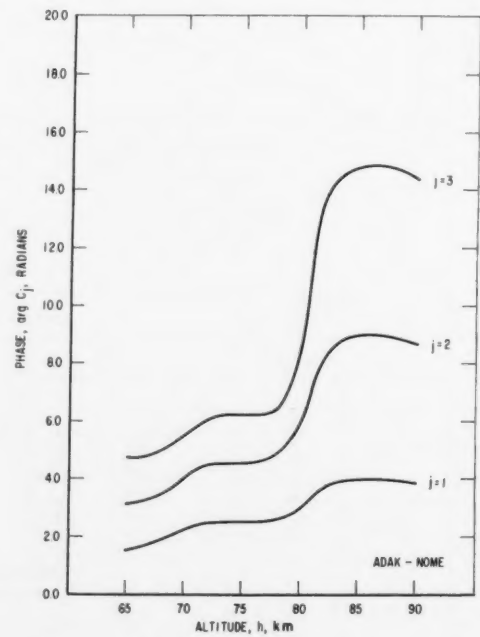
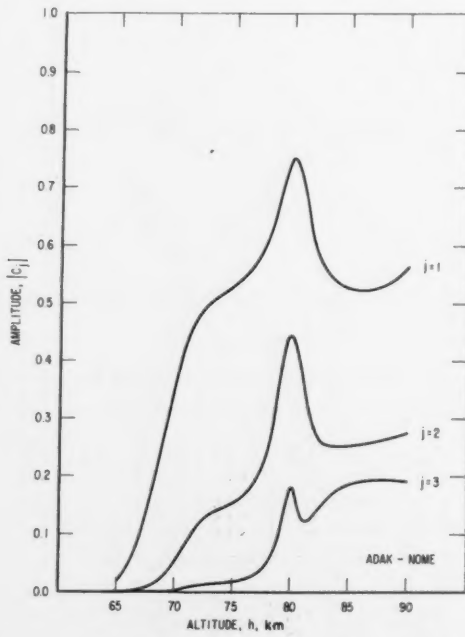
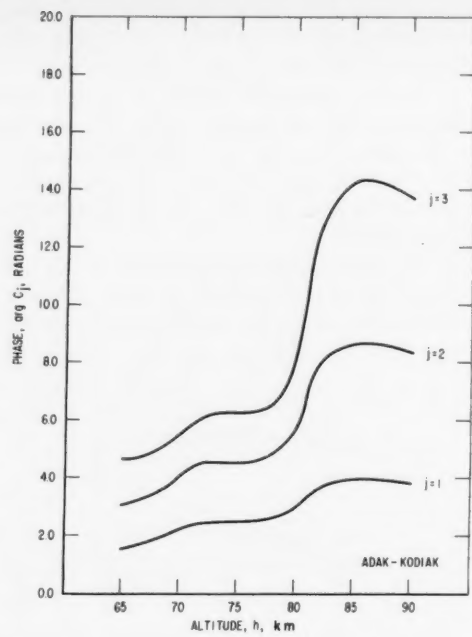
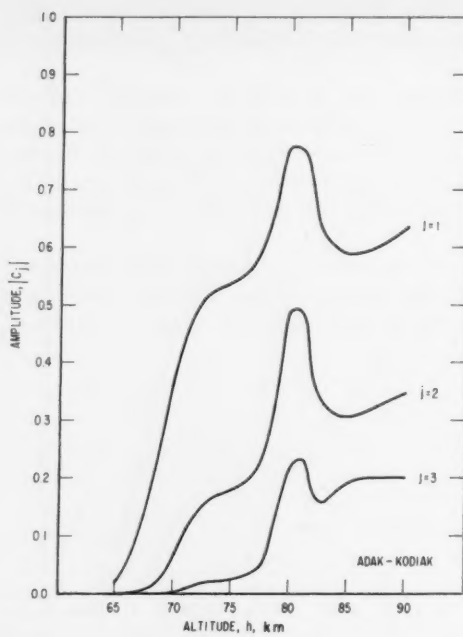


FIGURE 15. Effective reflection coefficient,  $c_j$ , for Adak to Nome and Kodiak, Alaska, transmissions under quiescent ionosphere conditions.

TABLE 5

Condition	Mode	$N$	$h$	$ E(\omega, d) $	$\arg E$
		El/cm <sup>3</sup>	km	v/m	radians
$b$ -----	Total	10	55	7.59 (10 <sup>-9</sup> )	5.54
$b$ -----	Total	1000	60	6.60 (10 <sup>-9</sup> )	2.84
$b$ -----	$j=1$	10	55	1.18 (10 <sup>-10</sup> )	2.10
$g$ -----	Total	10	65	9.77 (10 <sup>-9</sup> )	5.66
$g$ -----	$j=1$	10	65	2.42 (10 <sup>-9</sup> )	2.33

It is interesting to note emplacement altitudes,  $h$ , less than 65 km under quiescent conditions. Indeed, the highest altitude for these daytime values was 69 km (winter 1954). A good nominal daytime emplacement altitude is 67.5 km. The low value ( $|T| < 0.1$ ) reflection coefficients are also quite interesting. Note the highest value,  $|T| \sim 0.27$ . Note also, the median value at Nome (1954 equinox),  $|T_{ee}| = 0.08$ . A low value  $|T| < 0.1$ , and "black",  $|T| \sim 0$  appearance of the ionosphere indicates a low level absorbing region in the lower ionosphere at grazing incidence. A region of low electron density,  $N = 10-100$  El/cm<sup>3</sup>, is indicated by the model employed, figure 4. The transmission into such a region at grazing incidence,  $\phi_i \sim 80^\circ$ , figures 11, 12, indicates almost complete absorption of both the "ordinary" and the "extraordinary" rays if a "virtual height,"  $h + \Delta h$ , is assumed of the order of 70 km. The transmission curves, figures 11, 12, demonstrate that the "extraordinary" ray is very highly attenuated such that it is necessary to consider only the "ordinary" ray. Assuming 1 db/km, for example, figures 11, 12, and a virtual height,  $h + \Delta h$ , of 70 km, noting that appreciable attenuation rate begins at 65 km, the total attenuation can be estimated; total decibels  $\sim 2\Delta h/\cos \phi_i \sim 57$  db. This, of course, neglects a reflection absorption at the 70 km virtual height plus the transmission absorption back into the region below the ionosphere. The values,  $\Delta h$ , can be decreased and a corresponding decrease in the attenuation noted. But a repetition of the process leads to the interesting conclusion that most of the ray reflection must occur in a fraction of a kilometer, and, hence, the sharply bounded model can be reasonably applied under these conditions to predict the LF field,  $E(\omega, d)$ . A similar examination of the second and third time-modes leads to an almost similar reflecting region since the angle of incidence,  $\phi_i$ , figure 2, does not change rapidly until the distance,  $d/j$ , is sufficiently short. It is, nevertheless, conceivable that the amplitude of the skywave reflections,  $j=4, 5, 6, \dots$  at shorter distances could become quite large as a result of reflection from a high level "virtual height,"  $h + \Delta h = 70$  to 85 km. Under these conditions, however, the sharply bounded model would not be valid and it would be necessary to develop theoretical techniques for a diffusely bounded model ionosphere.

Information on the lower ionosphere  $N(h)$  profile during nighttime conditions is quite sparse and hence the theoretician can only speculate on its nature. However, under certain reasonable assumptions, a possible explanation of the increase in field strength experienced at night may be deduced from the daytime model ionosphere employed.

Despite the seeming "evaporation" of the lower regions of the ionosphere at night with a corresponding abrupt increase of the electron density to a large finite value, it seems reasonable to assume that this abrupt increase does not occur within  $\lambda/10$  or 0.22 km at 135.6 kc/s. This makes it possible to utilize the present sharply bounded model ionosphere, if it is emplaced at a higher level. Recent work [Ellyett and Watts, 1959] indicates a height of 80 to 85 km is not unreasonable.

Since the change of the angle of incidence,  $\phi_i$ , figure 2, with ionosphere height,  $h$ , is not great at this range, we may neglect its effect on the field strength, figures 6 to 9, and the effective reflection coefficients, figure 15. The only factor changed, therefore, is the unabsorbed field, figure 14. It therefore seems reasonable to expect the first time mode,  $|E_1(\omega, d)|$ , to increase on the order of at least twice, whereas, reference to the arctic data and figure 16, "Battle Lake data" (to be discussed below), indicates an increase of perhaps 4 to 10 times. This could easily be explained by a slight change of slope in the  $N(h)$  profile employed as evidenced by the steep slope of the  $C_1$  curves ( $j=1$ ), figure 15, in the region involved. On this basis, it is reasonable to expect a nighttime reflection coefficient,  $|T| \sim 0.3, 0.4$ . Indeed, at temperate latitude, these values are confirmed [Ross, 1959].

It is not surprising that a large phase change could be expected during the sunset-sunrise transition periods, figures 6 and 8. Indeed, such phase changes were described at 100 kc/s by Doherty [1957], while operating the Loran-C on the first time-mode of the skywave.

The behavior of the LF propagation during disturbed and blackout conditions which are especially frequent in the arctic-auroral region is not quite so clear. Figures 7 and 9 illustrate disturbed-blackout conditions based on the geophysical measurements of electron density profiles,  $N(h)$ , of the lower ionosphere, figure 4. The corresponding reflection coefficients, figures 10, 11, and the transmission of upgoing ordinary and extraordinary waves excited by the reflection process are also illustrated, figures 12, 13. The disturbance of the earth's magnetic field during extreme blackout conditions is negligible since the total field,  $H_m \sim 0.5$  gauss and the fluctuations are of the order of 0.001 gauss [Chapman, 1940]. The most significant change in the propagation is caused by the drastic change in the electron density profile,  $N(h)$ , figure 4. Unfortunately, the shape of the lower levels,  $< 60$  km, of the "blackout"  $N(h)$  profile is unknown. Since the analysis under quiescent conditions indicates low-electron density reflections, the curve, figure 4, was extrapolated, and the corresponding field,  $E(\omega, d)$ , calculated for Adak to Nome transmission. The results are tabulated in table 5.

Note the  $j=1$  mode for a region of  $N=10$  El/cm<sup>3</sup> has undergone a 26 db decrease and the total field is therefore almost entirely groundwave. Appreciable as the decrease is, it is still well within the range of observations of arctic data. Notice, figure 16 "Battle Lake data" (to be discussed below), that the range of observations in temperate latitudes is approximately 18 db. The additional fluctuation may then, reasonably, be attributed to the change in electron density of the extreme lower ionosphere. If this change were to be so abrupt as to reach  $N=1000$  El/cm<sup>3</sup> in, say,  $\lambda/10$  km, the field strength would show a considerable increase, instead of decrease. It is reasonable to expect that a more realistic value of somewhat less than  $N=1000$  El/cm<sup>3</sup> would also produce an increase in the received field strength. The shape of the  $N(h)$  profile, thus, becomes quite important.

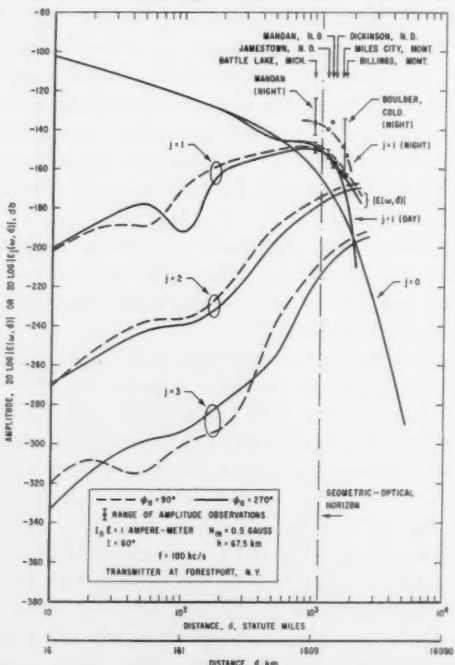


FIGURE 16. Amplitude of theoretical total field  $|E(\omega, d)|$  as a function of distance,  $d$ , from the source illustrating a comparison of experimental pulse amplitude measurements with theoretical first time-mode in the diffraction zone beyond the geometrical-optical horizon.

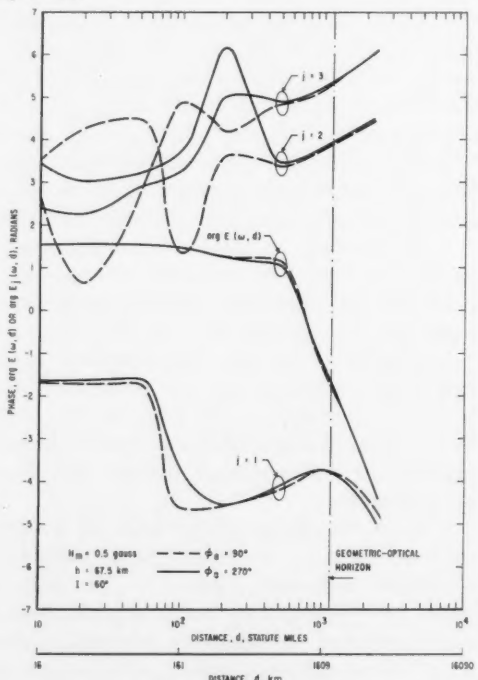


FIGURE 17. Phase of theoretical field  $\arg E(\omega, d)$  as a function of distance.

The calculation of the amplitude and phase of the total field,  $E(\omega, d)$  as a function of distance is illustrated in figures 16 and 17. The corresponding reflection coefficient  $T_{ee}$  (vertical polarization, normal component) is illustrated in figure 18.

Amplitude measurements<sup>6</sup> during the day which illustrate the diffraction of the first time-mode ( $j=1$ ) near and beyond the geometric-optical horizon are illustrated in figure 16. The agreement with the theoretical curve  $j=1$  appears to be quite close except at the range of 1,800 miles. It is interesting to note the apparent decrease in the range of amplitude observations in the daytime, indicating greater amplitude stability with range in the diffraction zone.

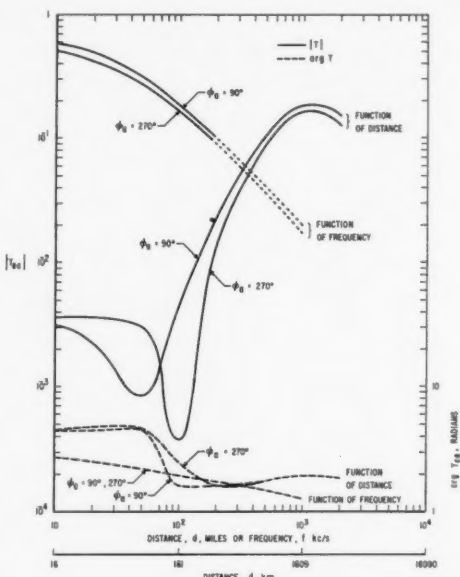


FIGURE 18. Amplitude and phase of the normal component reflection coefficient  $T_{ee}$  (vertical polarization) as a function of distance and frequency for east-to-west  $\phi_0 = 270^\circ$  and west-to-east  $\phi_0 = 90^\circ$  propagation.

#### 4. Conclusion

The analysis of these data demonstrates the application of propagation theory together with a suitable model for the ionosphere to the prediction of LF phenomena. The precision of the model for the case of transmission via the ionosphere at or close to grazing incidence is considered to be adequate upon considering the state of knowledge of the many parameters which influence such propagation. Nevertheless, the absence of an abundance of specific information does not deter the author from certain general conclusions which can be made as a result of this research.

At oblique incidence on the ionosphere, a condition which is certainly met under most practical situations, the reflection of LF waves during the daytime occurs in a region of very low electron density and high absorption, with corresponding low values of reflection coefficients,  $|T| < 0.1$ . The dominant skywave time-mode is, in general, the first; however, the second, third and higher order time-modes may offer appreciable contribution to the total field as the angle of incidence decreases as a result of reflection from higher levels and shorter transit distance in the ionized medium.

Periods of ionospheric disturbance (blackout) can produce a decrease in the field as a result of a reduction in the amplitude of the ionospheric time-modes. However, it is equally possible for the skywave mode to be incremented. This phenomenon is dependent upon the slope of

<sup>6</sup> From the author's personal notes on the 1953-1954 testing of the Loran-C (Cytae) System.

the electron density-altitude profile,  $N(h)$   $h$ . However, if ordinary communication is an engineering objective, LF seem to be quite reliable since the characteristic high absorption of HF waves does not appear to exist.

Since the writing of this paper the extensive theoretical work of Barron [1961] and the extensive experimental and engineering work of Belrose et al., [1959] have come to the attention of the author. It is interesting to note quite good agreement, figure 18, between the reflection coefficients deduced from the sharply bounded model presented in this paper and those presented as a result of Barron's full wave computations. Barron's data does, however, indicate, as might be expected, higher attenuation at the higher frequencies ( $>150$  kc/s).

It should be noted in conclusion that the adequacy of the sharply bounded model is subject to severe limitations, especially at the higher frequencies and the results of this paper suggest also the introduction into this geometric optical analysis of more rigorous or flexible models for the reflection coefficient which would treat a more diffuse ionosphere lower boundary.

## 5. References

Ballantine, S., On the radiation resistance of a simple vertical antenna at wave lengths below the fundamental, Proc. IRE **12**, 823-829 (Dec. 1924).

Barron, D. W., The numerical solution of differential equations governing the reflexion of long radio waves from the ionosphere, IV, Proc. Roy. Soc. **260**, Ser. A, No. 302, 393-408 (March 1961).

Belrose, J. S., W. L. Hutton, C. A. McKerrow, and R. S. Thain, The engineering of communication systems for low radio frequencies, Proc. IRE **47**, No. 5, pt. 1, 661-680 (May 1959).

Bickel, J. E., A method for obtaining LF oblique incidence reflection coefficient and its application to 135.6 kc data in the Alaska area, J. Geophys. Research **62**, No. 3, 373-381 (Sept. 1957).

Bremmer, H., Terrestrial radio waves—theory of propagation (Elsevier Publishing Co., New York, N.Y., 1949).

Chapman, S., and J. Bartels, Geomagnetism, Vol. I (Oxford at the Clarendon Press, 1940).

Crompton, R. W., L. G. H. Huxley, and D. J. Sutton, Experimental studies of the motions of slow electrons in air with applications to the ionosphere, Proc. Roy. Soc. London **218**, Ser. A, 507-519 (July 1953).

Davis, P., and P. Rabinowitz, Abscissas and weights for Gaussian quadratures of high order, J. Research NBS **56**, 35-37 (Jan. 1956).

Doherty, R. H., private communication (1957).

Ellyett, C., and J. M. Watts, Stratification in the lower ionosphere, J. Research NBS **63D** (Radio Prop.). No. 2, 117-134 (Sept.-Oct. 1959).

Fejer, J. A., The interaction of pulsed radio waves in the ionosphere, J. Atmospheric and Terrest. Phys. **7**, 322-332 (Dec. 1955).

Gardner, F. F., and J. L. Pawsey, Study of the ionospheric D-region using partial reflections, J. Atmospheric and Terrest. Phys. **3**, 321-344 (July 1953).

Johler, J. R., Magneto-ionic propagation phenomena in low- and very low-radiofrequency waves reflected by the ionosphere, J. Research NBS **65D**, (Radio Prop.), No. 1, 53-61 (Jan.-Feb. 1961).

Johler, J. R., W. J. Kellar, and L. C. Walters, Phase of the low radiofrequency ground wave, NBS Circ. 573, U.S. Government Printing Office, Washington 25, D.C. (June 26, 1956).

Johler, J. R., and L. C. Walters, Propagation of a ground wave pulse around a finitely conducting spherical earth from a damped sinusoidal source current, IRE Trans. on Antennas and Propagation **AP-7**, No. 1, 1-10 (Jan. 1959).

Johler, J. R., and L. C. Walters, On the theory of reflection of low- and very low-radio-frequency waves from the ionosphere, J. Research NBS **64D** (Radio Prop.), No. 3, 269-285 (May-June 1960).

Johler, J. R., L. C. Walters, and J. D. Harper, Jr., Low- and very low-radiofrequency model ionosphere reflection coefficients, NBS Tech. Note 69 (PB161570), U.S. Dept. of Commerce, Office of Technical Services, Washington 25, D.C. (July 1, 1960).

Johler, J. R., L. C. Walters, and C. M. Lilley, Low- and very low-radiofrequency tables of ground wave parameters for the spherical earth theory: The roots of Riccati's differential equation, NBS Tech. Note 7 (PB 151366), U.S. Dept. of Commerce, Office of Technical Services, Washington 25, D.C. (Feb. 1, 1959).

Johler, J. R., L. C. Walters, and C. M. Lilley, Amplitude and phase of the low- and very low-radiofrequency ground wave, NBS Tech. Note 60 (PB161561), U.S. Dept. of Commerce, Office of Technical Services, Washington 25, D.C. (June 1, 1960).

Lorentz, H. A., The theory of electrons and its applications to the phenomena of light and radiant heat (G. E. Stechert and Co., New York, N.Y., 1906, 1923).

Magnetic Chart 1706 N, The variation of the compass for the year 1955 North Polar area, U.S. Navy Hydrographic Office, Washington, D.C. (1946); 3rd edition (1954).

Magnetic Chart 1700 N, The magnetic inclination or dip for the year 1955 North Polar area, U.S. Navy Hydrographic Office, Washington, D.C. (1946); 3rd edition (1954).

Magnetic Chart 1703 N, The total intensity of the Earth's magnetic field for the year 1955 North Polar area, U.S. Navy Hydrographic Office, Washington, D.C., (1947); 2nd edition (1954).

Millington, G., Ground-wave propagation across a land/sea boundary, *Nature* **164**, 114-115 (July 1949); *Nature* **163**, p. 128 (June 1949).

Millington, G., Ground-wave propagation over an inhomogeneous smooth earth, *Proc. IRE* **46**, pt III, 53-63 (1949).

Nicolet, M., Aeronomic conditions in the mesosphere and lower ionosphere, *Science Report No. 102*, Pennsylvania State University, University Park, Pennsylvania (April 1958).

Rabinowitz, P., and G. Weiss, Tables of abscissas and weights for numerical evaluation of integrals of the form

$$\int_0^{\infty} e^{-x} x^n f(x) dx,$$

*Mathematical Tables and Other Aids to Computation*, Vol. 13, No. 68, p. 285 (Oct. 1959).

Ratcliffe, J. A., Ionizations and drift in the ionosphere, *J. Geophys. Research* **64**, No. 12, 2102-2111 (Dec. 1959).

Ross, J. M., Propagation field test, Appendix D (uncl.), Navigation, guidance and control system for drone aircraft, 6th Quarterly Progress Report to U.S. Army Signal Research and Development Laboratory, Ft. Monmouth, N.J. (Sept.-Nov. 1959), Contract No. DA 36-039 SC-78020, Motorola, Inc., Scottsdale, Arizona.

Seddon, J. C., and J. E. Jackson, Rocket arctic ionospheric measurements, *IGY Rocket Report Series*, No. 1, pp. 140-148 (July 1958).

Wait, J. R., Diffractive corrections to the geometrical optics of low frequency propagation, *Electromagnetic wave propagation*, pp. 87-101 (Academic Press, New York, N.Y., 1960a).

Wait, J. R., private communication, eq. (37), (1960b).

Wait, J. R., A diffraction theory for LF sky wave propagation, *J. Geophys. Research* **66**, No. 6, 1713-1730 (June 1961).

Wait, J. R., and A. M. Conda, Pattern of an antenna on a curved lossy surface, *IRE Trans. on Antennas and Propagation* **AP-6**, No. 4, 348-359 (October 1958).

Watt, A. D., E. L. Maxwell, and E. H. Whelton, Low-frequency propagation paths in arctic areas, *J. Research NBS* **63D** (Radio Prop.), No. 1, 99-112 (July-Aug. 1959).

Waynick, A. H., The present state of knowledge concerning the lower ionosphere, *Proc. IRE* **45**, No. 6, 741-749 (June 1957).

(Paper 65D5-156)



## Publications of the staff of the National Bureau of Standards\*

### Selected Abstracts

**Mean electron density variations of the quiet ionosphere 3—May 1959.** J. W. Wright, L. R. Wescott, and D. J. Brown, *NBS Tech. Note 40-3 (PB151399-3)* (1960) \$1.50.

The CRPL has initiated a program for large-scale computation of electron density profiles from ionospheric vertical soundings. Scaling is performed at field stations permitting computation of hourly profiles at the Central Laboratory. These profiles are combined to form hourly mean quiet profiles for each station and month. The results of this program for the month of May are illustrated graphically. This report is the third of a series illustrating the electron density variations in the mean quiet ionosphere between latitudes 15°N and 50°N along the 75°W meridian.

**On the nature of equatorial spread -F.** R. Cohen and K. L. Bowles, *J. Geophys. Research* **66**, No. 4, 1081–1106 (April 1961).

Ionospheric propagation via scattering from the *F* region was sought at 50 Mc/s over a transequatorial path (with midpoint near Huancayo, Peru) employing a 2580-km transmitter-receiver separation. Propagation via *F* scatter was present over this path about 10 per cent of the time, though only at night. A condition closely related to the occurrence of *F* scatter was the presence of equatorial spread-*F* configurations on the Huancayo ionograms. The height of the propagation medium supporting this *F* scatter was usually identifiable with the lowest height of the associated equatorial spread *F* on the ionograms. On the basis of an interpretation of experimental results, equatorial spread *F* is shown to arise from scattering by relatively thin sheets of irregularities in electron density which occur at the bottom of the *F* layer or as much as 100 km lower. The thickness of these patches is estimated at the order of 50 km. The scattering irregularities comprising these patches are found to be elongated along the earth's magnetic lines of force. Electron irregularities of scale 10 meters or smaller measured in at least one dimension transverse to the magnetic field lines, and 1,000 meters or longer measured along the magnetic field lines, are shown to exist as high as 450 km in the nocturnal equatorial *F* region during equatorial spread-*F* conditions. Equatorial spread-*F* echoes observed at Huancayo are demonstrated to be arriving at all elevation angles in the magnetic east-west plane. The geographical extension of a given scattering sheet in the magnetic east-west direction was at times as great as 1000 km. An observational procedure is suggested for distinguishing two fundamental varieties of spread-*F* echoes appearing on the equatorial ionograms. A necessary condition, that the contours of mean electron density be parallel to the magnetic lines of force, is proposed as a controlling factor for the occurrence of spread *F* in the equatorial ionosphere.

**On the analysis of polarization rotation recordings of satellite radio signals.** R. S. Lawrence and C. G. Little, pp. 391–399 of *Some ionospheric results obtained during the International Geophysical Year*; *Proc. symp. organized by the URSI/AGI committee, Brussels, 1959*, edited by W. J. G. Beynon (Elsevier Publ. Co., Amsterdam, 1960).

At frequencies as low as 20 mc/s the rotation of the plane of polarization of satellite signals cannot be assumed to be proportional to  $\int N B \cos \theta \, dl$  along the line of sight. A method of analysis is presented which eliminates this assumption and permits accurate estimates of total electron content below the satellite height to be obtained from 20 mc observations. Some of the results obtained using the method to determine the sub-satellite electron content, throughout a satellite pass, are presented. These analyses permit the study of ionospheric tilts, and have revealed the presence of large-scale irregularities in the ionospheric electron content. The deviation in sub-satellite content of these irregularities is of the order

2% of the running mean value; the lateral extent of the irregularities is of the order of a few hundred kilometers. The effects of such irregularities upon ionospheric refraction and satellite Doppler curves are briefly discussed.

**Prolonged space-wave fadeouts in tropospheric propagation.** A. P. Barsis and M. E. Johnson, *NBS Tech. Note 88 (PB161585)* (1961) \$2.00.

This paper contains the results of studies performed during the last several years on the short-term variability of tropospheric signals received over within-the-horizon paths. Signal variations of this type have been termed "prolonged space-wave fadeouts," as they are mainly characterized by reductions in signal level to many decibels below presumably constant values determined from geometrical optics methods. The data described here were obtained from measurements over propagation paths in the Pacific Coast region of Southern California, and the continental region of Eastern Colorado. Fadeouts are analyzed as a function of carrier frequency, path characteristics, and meteorological parameters. The study also includes an evaluation of fadeouts observed over a path using a mountain peak as a diffracting knife-edge like obstacle between transmitter and receiver.

**The relationship of low-height ionosonde echoes to auroral-zone absorption and VHF D scatter.** J. K. Olesen and J. W. Wright, *J. Geophys. Research* **66**, No. 4, 1127–1134 (April 1961).

Weak diffuse HF reflections at heights between 75 and 95 km in the auroral zone are designated *E<sub>d</sub>*. Diurnally, *E<sub>d</sub>* occurs most frequently at noon at all seasons, and shows a pronounced minimum of occurrence around 2000 hours local time. There is little evidence for a seasonal variation from the year's data presented here. It is suggested that *E<sub>d</sub>* is related to the anomalies of auroral-zone absorption and that it is the layer responsible for VHF forward scatter.

**The Ephi system for VLF direction finding.** G. Hefley, R. F. Linfield, and T. L. Davis, *J. Research NBS 65C (Eng. and Instr.)*, No. 1, 43–49 (Jan.–Mar. 1961).

A new system of VLF direction finding has been developed and tested by the National Bureau of Standards, Boulder, Colorado. The system has been named "Ephi" (*E*- $\phi$ ) because the bearing of the transient signal is determined from the relative phase ( $\phi$ ) of the vertical electrical field (*E*) received at spaced antennas. The advantage of this scheme compared to conventional crossed-loop techniques is that it minimizes siting and polarization errors. A minimum of three antennas must be used to resolve directional ambiguity, and the preferred antenna location is at the vertices of an equilateral triangle with baselines equal to  $1/2$  to  $1/10$  wavelength (at 10 kc/s). Appropriate phase detectors, delay lines and coincidence circuits are used to obtain a directional code in preset sectors. Within practical instrumentation limits any number of sectors of variable widths can be operated simultaneously and each can be rotated in azimuth.

**Integrated starlight over the sky.** F. E. Roach and L. R. Megill, *Astrophysical J.* **133**, No. 1, 228–242 (Jan. 1961). Calculations are made of the total integrated starlight over the entire sky based on the star counts in Groningen Pub., No. 43. The results are given in both the photographic and the visual magnitude scales in tabular and graphical form.

**Resonators for millimeter and submillimeter wavelengths.** W. Culshaw, *IRE Trans. Microwave Theory and Tech. MTT-9, No. 2*, 135–144 (Mar. 1961).

Further considerations on the mm-wave Fabry-Perot interferometer are presented. Computed *Q* values for parallel metal plate resonators indicate that at spacings around 2.5 cm, values ranging from 60,000 at 3 mm, to 300,000 at 0.1 mm wavelengths are possible. The plates must, however, be

quite flat. These results are important for many investigations, and in particular for mm and sub-mm wave maser research. For the aperture per wavelength ratios possible here, diffraction effects should be small. Consideration is given to using curved reflectors or focused radiation in applications where the fields must be concentrated. For this purpose, re-entrant conical spherical resonators are treated in detail, as regards operation in the TEM mode at high orders of interference. Expressions for the  $Q$  and shunt impedance are given, and high values are possible at mm and sub-mm wavelengths. Quasi-optical methods of coupling into and out of such a resonator are proposed, and the higher modes possible in such a resonator are considered. Results indicate that it could have application to the mm-wave generation problem, and that it represents a good resonant cavity for solid-state research at mm and sub-mm wavelengths, and for maser applications in particular.

**The electromagnetic fields of a dipole in the presence of a thin plasma sheet,** J. R. Wait, *Appl. Sci. Research, Section B, 8, 397-417 (1960).*

The problem of electric and magnetic dipoles located near a thin planar slab or sheet of ionized material is considered. A constant and uniform magnetic field is impressed on the slab. Under the assumption that the thickness of the slab is very small, expressions for the resultant fields are obtained. As a result of the anisotropy of the sheet it is indicated that the fields are elliptically polarized in general. On carrying out a saddle-point evaluation of the integrals in the formal solution it is shown that the far fields may be split into "radiation" and "surface wave" components. The dependence of the radiation pattern and the surface wave characteristics on electron density, collision frequency and the impressed magnetic field is illustrated.

**The Nation's electronic standards program: Where do we now stand?** Harvey W. Lance, *IRE Trans. Instrumentation I-9, No. 2, 94-100 (Sept. 1960).*

Recently increased standards activities throughout the nation have resulted in a large increase in the calibration services requested from the National Bureau of Standards and in a number of related problems. Several of these are discussed, including desirable criteria for the staffing and instrumentation of electronic standards laboratories, the choice of inter-laboratory standards to be submitted to NBS, and the use of these standards before and after calibration. An attempt is made to clarify the concept of "traceability of calibrations to NBS," and conditions under which a calibration may be called traceable are discussed. Suggestions are made regarding the use of available calibration services and the action to be taken when needed calibration services are not available. The need for an association of standards laboratories is pointed out, and many areas are noted in which such an association could make valuable contributions.

**Propagation of error in a chain of standards,** A. G. McNish and J. M. Cameron, *IRE Trans. Instrumentation I-9, No. 2, 101-104 (Sept. 1960).*

There is a widespread belief that in a chain of standards traceable back to a central laboratory, each standard must be calibrated in terms of a standard 10 times as accurate. Conversely, this implies a 10-fold degradation in accuracy in each successive calibration. If this were true, accuracy would be intolerably degraded at the working level. A more realistic view is that accuracy in a chain of standards is as good as its weakest link. This can be demonstrated by experimental data on the errors obtained in calibrations and can be explained by examining the factors which affect accuracy in calibration.

**An analysis of the accumulated error in a hierarchy of calibrations,** E. L. Crow, *IRE Trans. Instrumentation I-9, No. 2, 105-114 (Sept. 1960).*

Calibrations of many types are performed in a hierarchy of calibration laboratories fanning out from a national standard. Often the statement is made that the accuracy of each echelon of the hierarchy should be 10 times the accuracy of the immediately following echelon. The validity of such statements is examined by deriving formulas for the total error accumulated

over the entire sequence when systematic and random errors may occur in each echelon, and by determining how a given total error may be achieved at minimum total cost under reasonable assumptions for the form of the cost-error functions.

**Atomic beam frequency standards,** R. C. Mockler, R. E. Beehler, and C. S. Snider, *IRE Trans. Instrumentation I-9, No. 2, 120-132 (Sept. 1960).*

A general qualitative description of atomic beam devices is given, with particular emphasis upon cesium atomic frequency standards.

The various uncertainties in frequency measurements are discussed including the effects of the uniform  $C$  field, the effect of a phase difference between the two oscillating fields that excite the atomic transition, and the effect of exciting an atomic transition with signals that are not monochromatic. The two cesium beam devices constructed at the National Bureau of Standards are described in some detail. The various tests are described for determining the uncertainties in the frequency measurements. The results of these tests are given.

The accuracy of these rather dissimilar machines is considered to be  $\pm 1.5 \times 10^{-11}$ , and the precision of measurement is  $2 \times 10^{-12}$ . The latter figure represents the standard deviation of the mean for measurement times of a few hours, or, about 100 separate measurements.

**The power spectrum and its importance in precise frequency measurements,** J. A. Barnes and R. C. Mockler, *IRE Trans. Instrumentation I-9, No. 2, 149-155 (Sept. 1960).*

The power spectral density functions of a frequency multiplier chain, driven by several different crystal oscillators, were obtained by comparing the output with a second chain which was stabilized with an ammonia maser. The frequency of the maser stabilized chain was demonstrated to be relatively fixed; the power spectrum of the other chain was determined by two different methods. The results are compared. Possible errors and uncertainties introduced by the methods are discussed. An analysis is made that relates the instantaneous frequency fluctuations of a signal with the power spectral density function.

Analysis predicts that when frequency modulation occurs in the first stages of frequency multiplication or in the primary frequency oscillator, the output power spectrum is, in general, not symmetrical. Furthermore, the sidebands are increased in intensity by the multiplication process. This is, in fact, observed to be the case. It is shown that a frequency counter will measure the frequency of the center of gravity of the power spectrum.

If signals having a complex power spectrum are used in precise frequency measurements, errors may result.

**Standards and measurements of microwave surface impedance, skin depth, conductivity and  $Q$ ,** H. E. Bussey, *IRE Trans. Instrumentation I-9, No. 2, 171-175 (Sept. 1960).*

The metal walls of a cavity resonator become standards of skin depth when the internal  $Q$  is determined, if the walls are uniform and if contact loss is eliminated as in the circular  $TE_{01}$  mode. An end plate standardized in this way may be replaced by another flat piece of material and its unknown skin depth easily determined. A copper cavity in use has 94 per cent of theoretical  $Q$ . Deoxidization of the surface raises the value to 97 per cent. Surface roughness and mode conversion may account for the remaining  $Q$  departure. Accuracy of  $Q$  measurement ( $\pm 3$  per cent) will be discussed and preliminary results on several metals will be given.

**A radio-frequency permittimeter,** R. C. Powell and A. L. Rasmussen, *IRE Trans. Instrumentation I-9, No. 2, 179-184 (Sept. 1960).*

A coaxial RF impedance transformer in which the secondary is a single turn of the material to be measured is used with two-terminal impedance bridges to determine the complex permittivity or complex conductivity of low-impedance materials. No electrodes are needed, and many conductors, semiconductors, electrolytes and high-permittivity materials can be evaluated to about 1 per cent, since errors due to electrode impedance and interaction as well as first-order series induct-

ance are eliminated. The design, calibration, range, and accuracy are given along with measured values of such materials as ferrites and strong electrolytic solutions, showing complex conductivities differing considerably from those previously observed by other methods.

**A transfer instrument for the intercomparison of microwave power meters, G. F. Engen, *IRE Trans. Instrumentation* **I-9**, 202-208 (Sept. 1960).**

In the intercomparison of two microwave power standards, or in the calibration of a microwave power meter by means of a second or "standard" power meter, the measurement of microwave impedance has played a major role.

Through an extension of the reflectometer concept, it is now possible to devise a four-arm junction which, when properly adjusted, makes possible the intercomparison or calibration of such power meters with little or no regard for their impedance characteristics. In addition, the method is substantially independent of the impedance discontinuity which may be present at the input flange or connector. This latter result is of particular value in coaxial systems.

**Absolute measurement of temperatures of microwave noise sources, A. J. Estin, C. L. Trembath, J. S. Wells, and W. C. Daywitt, *IRE Trans. Instrumentation* **I-9**, 209-213 (Sept. 1960).**

In recent years, the requirement for noise-figure measurements of low-noise devices has led to a need for more precise knowledge of temperatures of noise sources. A system has been developed which is capable of measuring the absolute noise temperature of a gas discharge tube in WR-90 waveguide to within 0.01 db. The comparison circuit is a modified Dicke radiometer. The standard noise source is a black body radiator at approximately 1000°C. Preliminary measurements of noise temperatures of a set of nine laboratory equivalents of a commonly used argon discharge tube indicate an excess noise temperature of 15.90 db at 200 ma discharge current with a variation between tubes of 0.03 db.

**A modulated subcarrier technique of measuring microwave phase shifts, G. E. Schafer, *IRE Trans. Instrumentation* **I-9**, 217-219 (Sept. 1960).**

This paper describes a technique for comparing phases of two microwave signals which employs amplitude modulation in one channel of a two-channel system. This modulated subcarrier technique produces a null response in a two-channel system for all ratios of the amplitudes of the waves traversing the separate channels. Therefore, high precision is maintained for all ratios of amplitudes. A practical application of this technique using readily available components achieved a precision of phase measurements of a tenth of a degree for a change of attenuation of 50 db of component under test.

**Measurement of reflections and losses of waveguide joints and connectors using microwave reflectometer techniques, R. W. Beatty, G. F. Engen, and W. J. Anson, *IRE Trans. Instrumentation* **I-9**, 219-226 (Sept. 1960).**

The reflection and loss of a waveguide joint are quantified by its VSWR and efficiency, respectively. These are conveniently and accurately determined by techniques which employ a reflectometer with auxiliary tuners and an adjustable sliding termination. Depending upon the stability and gain of the associated apparatus, measurements of VSWR's of 1.001 and lower, and of efficiencies of 99.99 per cent and higher may be obtained. The attenuations of short lengths of waveguide may be determined at the same time that the efficiency measurement is made.

**A precision RF attenuation calibration system, C. M. Allred and C. C. Cook, *IRE Trans. Instrumentation* **I-9**, 268-274 (Sept. 1960).**

A new precision attenuation calibrating system with greatly increased sensitivity, stability, and measurement range has been completed at the National Bureau of Standards, Boulder Laboratories. The increased stability and sensitivity are achieved by the use of a highly accurate piston attenuator and precision phase shifter combined into a null system. The extended attenuation measurement range has been ob-

tained by using a new mode launching system which is excited by essentially a constant current source of very high magnitude. The padding necessary for correct impedance matching is kept at a minimum by use of a special noninteractive combining network.

**A precision RF power transfer standard, P. A. Hudson, *IRE Trans. Instrumentation* **I-9**, 280-283 (Sept. 1960).**

A fast-reading, precision RF power transfer standard is described which is usable at fixed frequencies in the range 10 Mc to 1000 Mc. The dynamic range is 1 watt to 1000 watts with a resolution of 0.1 per cent to 0.01 per cent. Stability is 0.1 per cent per year. The standard consists of three directional couplers to cover the frequency range and a series of vacuum thermoelement detectors matched to 50 ohms at each frequency interest. The thermoelements are connected to the secondary line of the appropriate coupler and provide a dc output voltage which is calibrated in terms of RF power in the coupler main line.

A series of small, portable wattmeters employing vacuum thermoelements are also described.

### Other NBS Publications

**Journal of Research, Vol. 65A, No. 4, July-August 1961. 70 cents.**

Electrical properties and kinetics of electrode reactions. R. J. Brodd.

Effect of hydrostatic pressure upon the relaxation of birefringence in amorphous solids. R. M. Waxler and L. H. Adams.

Vapor pressures of platinum, iridium, and rhodium. R. F. Hampson, Jr., and R. F. Walker.

Crystallization of bulk polymers with chain folding: theory of growth of lamellar spherulites. J. D. Hoffman and J. I. Lauzen, Jr.

Phase equilibrium relations in the binary system barium oxide-niobium pentoxide. R. S. Roth and J. L. Waring. Solid state reactions involving oxides of trivalent cations. S. J. Schneider, R. S. Roth, and J. L. Waring.

Gamma irradiation of fluorocarbon polymers. R. E. Florin and L. A. Wall.

Inhibition of diffusion flames of methyl bromide and trifluoromethyl bromide applied to the fuel and oxygen sides of the reaction zone. E. C. Creitz.

Atomic energy levels in crystals, J. L. Prather, NBS Mono. 19 (1961) 60 cents.

A spectrophotometric atlas of the spectrum of CH from 3000A to 5000A, A. M. Bass and H. P. Broida, NBS Mono. 24 (1961) 20 cents.

Development of high-temperature strain gages, J. W. Pitts and D. G. Moore, NBS Mono. 26 (1961) 20 cents.

Bibliography of temperature measurement—January 1953 to June 1960, C. Halpern and R. J. Moffat, NBS Mono. 27 (1961) 15 cents.

Corrected optical pyrometer readings, D. E. Poland, J. W. Green, and J. L. Margrave, NBS Mono. 30 (1961) 55 cents.

Units of weight and measure (United States customary and metric) definitions and tables of equivalents, L. V. Judson, NBS Misc. 233 (1960) 40 cents.

Quarterly radio noise data, September, October, November 1960, W. Q. Crichlow, R. T. Disney, and M. A. Jenkins, NBS TN18-2 (PB151377-8) (1961) \$1.75.

A survey of computer programs for chemical information searching, E. C. Marden and H. R. Koller, NBS TN85 (PB161586) (1961) \$2.25.

Standards and testing, the key to quality, B. E. Foster, Eng. Bull., Purdue Univ. **XLIV**, No. 6, 54-62 (Nov. 1960). Subgroups of the modular group and sums of squares, M. Newman, Am. J. Math. **82**, No. 4, 761-778 (Oct. 1960).

Phase equilibria in the system cadmium oxide-niobium oxide, R. S. Roth, J. Am. Ceram. Soc. **44**, No. 1, 49-50 (Jan. 1961).

Redetermination of the chromium and nickel solvuses in the chromium-nickel system, C. J. Bechtoldt and H. C. Vacher, Trans. Metallurgical Soc., Am. Inst. Mining Engrs. **221**, 14-18 (Feb. 1961).

Hydrogen-bonding in calcium-deficient hydroxyapatites. A. S. Posner, J. M. Stutman, and E. R. Lippincott, *Nature* **188**, No. 4749, 486-487 (Nov. 1960).

Hydrogen sulfide precipitation of the elements from 0.2-0.5 normal hydrochloric acid, J. I. Hoffman, *Chemist Analyst* **50**, No. 1, 30 (Mar. 1961).

Dielectric constant and dielectric loss of  $TiO_2$  (Rutile) at low frequencies, R. A. Parker and J. H. Wasilik, *Phys. Rev.* **120**, No. 5, 1631-1637 (Dec. 1960).

Generating functions for formal power series in non-commuting variables, K. Goldberg, *Proc. Am. Math. Soc.* **11**, No. 6, 988-991 (Dec. 1960).

Tests for regression coefficients when errors are correlated, M. M. Siddiqui, *Ann. Math. Stat.* **31**, No. 4, 929-938 (Dec. 1960).

Application of the method of polarized orbitals to the scattering of electrons from hydrogen, A. Temkin and J. C. Lamkin, *Phys. Rev.* **121**, No. 3, 788-794 (Feb. 1961).

A recommended standard resistor-noise test system, G. T. Conrad, Jr., N. Newman, and A. P. Stansbury, *IRE Trans. Component Parts* **CP-7**, No. 3, 71-88 (Sept. 1960).

On the absorption spectrum of  $CF_2$  and its vibrational analysis, D. E. Mann and B. A. Thrush, *J. Chem. Phys.* **33**, No. 6, 1732-1734 (Dec. 1960).

Plating gun bores, V. A. Lamb and J. P. Young, *Ordnance XLV*, No. 245, 725-727 (Mar.-Apr. 1961).

Low temperature static seals using elastomers and plastics, D. H. Weitzel, R. F. Robbins, G. R. Bopp, and W. R. Bjorklund, *Rev. Sci. Inst.* **31**, No. 12, 1350-1351 (Dec. 1960).

FM and SSB radiotelephone tests on a VHF ionospheric scatter link during multipath conditions, J. W. Koch, W. B. Harding, and R. J. Jansen, *IRE Trans. Commun. Systems* **CS-8**, No. 3, 183-186 (Sept. 1960).

Electron scattering in high magnetic field, A. H. Kahn, *Phys. Rev.* **119**, No. 4, 1189-1192 (Aug. 1960).

Microwave spectrum of *cis*-difluoroethylene, V. W. Laurie, *J. Chem. Phys.* **34**, No. 1, (Jan. 1961).

Surface roughness of gold castings, J. J. Barone, R. L. Huff, and G. Dickson, *Dental Progr.* **1**, No. 2, 78-84 (Jan. 1961).

The sensitivity of photographic film to 3-mev neutrons and to thermal neutrons, M. Ehrlich, *Health Phys.* **4**, 113-128 (1960).

A prototype rubidium vapor frequency standard, R. J. Carpenter, E. C. Beaty, P. L. Bender, S. Saito, and R. O. Stone, *IRE Trans. Instrumentation* **I-9**, No. 2 (Sept. 1960).

Low even configurations in the first spectrum of thorium (Th  $\alpha$ ), R. E. Trees, *Physica* **26**, 353-360 (1960).

Comparison measurements with intensity standards for high energy bremsstrahlung, J. S. Pruitt and W. Pohlit, *Z. Naturforschung* **15b**, No. 9, 617-619 (1960).

High-dispersion spectra of Jupiter, C. C. Kiess, C. H. Corliss, and H. K. Kiess, *Astrophys. J.* **132**, No. 1, 221-231 (July 1960).

Propagation of electromagnetic waves along a thin plasma sheet, J. R. Wait, *Can. J. Phys.* **38**, 1586-1594 (1960).

Preparation and properties of aromatic fluorocarbons, W. J. Pummer and L. A. Wall, *J. Chem. Engrs. Data* **6**, No. 1, 76-78 (Jan. 1961).

Stability of thermoset plastics at high temperatures, S. L. Madorsky and S. Straus, *Modern Plastics* **38**, 134-140 (Feb. 1961).

Immiscibility and the system lanthanum oxide boric-oxide, E. M. Levin, C. R. Robbins, and J. L. Waring, *J. Am. Ceram. Soc.* **44**, No. 2, 87-91 (Feb. 1961).

On the properties of the vapor pressure curve, E. H. Brown, *Cryogenics* **1**, No. 1, 37-40 (Sept. 1960).

Absorption and scattering of photons by holmium and erbium, E. G. Fuller and E. Hayward, *Proc. Intern. Conf. Nuclear Structure*, 761-766 (Kingston, Canada, 1960).

Spectroscopy of fluorine flames. I. Hydrogen-fluorine flame and the vibration-rotation emission spectrum of HF, D. E. Mann, B. A. Thrush, D. R. Lide, J. J. Ball, and N. Acquista, *J. Chem. Phys.* **34**, No. 2, 420-431 (Feb. 1961).

The absorption spectra of magnesium and manganese atoms in solid rare gas matrices, O. Schnapp, *J. Phys. Chem. Solids* **17**, Nos. 3/4, 188-195 (1961).

The Franck-Condon factor ( $q_v, q''$ ) array to high vibrational quantum numbers for the  $O_2(B^3\Sigma_u^+ - X^3\Sigma_g^+)$  Schumann-Runge band system, R. W. Nicholls, *Can. J. Phys.* **38**, 1705-1711 (1960).

NBS—source of American Standards, W. A. Wildhack, *ISA J.* **8**, No. 2, 45-50 (Feb. 1961).

Ionospheric mapping by numerical methods, W. B. Jones and R. M. Gallet, *Telecommun. J.* **12**, 260-264 (Dec. 1960).

The activation energy for hydrogen atom addition to propylene, M. D. Scheer and R. Klein, *J. Phys. Chem.* **65**, 375-377 (1961).

Intramolecular rearrangements. I. *sec*-butyl acetate and *sec*-butyl formate, R. Borkowski and P. Ausloos, *J. Am. Chem. Soc.* **83**, No. 5, 1053-1056 (Mar. 1961).

Titanium (III) chloride and titanium (III) bromide (titanium trichloride and titanium tribromide), J. M. Sherfey, Chapter **IVB**, Sec. 17, p. 57-61, Book, *Inorganic Syntheses*, by E. G. Rochow (McGraw-Hill Book Co., New York, N.Y., 1960).

Science news writing, D. M. Gates and J. M. Parker, *Science* **133**, No. 3447, 211-214 (Jan. 1961).

Elastomers for static seals at cryogenic temperatures, D. H. Weitzel, R. F. Robbins, G. R. Bopp, and W. R. Bjorklund, *Rev. Sci. Insts.* **31**, No. 12, 1350-1351 (Dec. 1960).

New standards for the space age, A. T. McPherson, *Aeronautics* **6**, No. 1, 24-25; 50-54 (Jan. 1961).

Near infrared atmospheric transmission to solar radiation, D. M. Gates, *J. Opt. Soc. Am.* **50**, No. 12, 1299-1304 (Dec. 1960).

Determination of crystallite size distributions from X-ray line broadening, A. Bienenstock, *J. Appl. Phys.* **32**, No. 2, 187-189 (Feb. 1961).

Correlation of visual and subvisual auroras with changes in the outer Van Allen radiation zone, B. J. O'Brien, J. A. Van Allen, F. E. Roach, and C. W. Gartlein, *IGY Bull.*, No. 45, 1-16 (Mar. 1961).

Arc source for high temperature gas studies, J. B. Shumaker, Jr., *Rev. Sci. Instr.* **32**, No. 1, 65-67 (Jan. 1961).

The dependency of the melting temperature of bulk homopolymers on the crystallization temperature, L. Mandelkern, *J. Polymer Sci. XLVII*, issue **149**, 494-496 (July 1960).

Spiral patterns in geophysics, V. Agy, *J. Atmospheric and Terrest. Phys.* **19**, 136-140 (1960).

Iron (99.9+), G. A. Moore and T. R. Shives, *Metals Handb.* **1**, 1206-1212 (1961).

The interfacial properties of polyesters at glass and water surfaces, R. R. Stromberg, *Soc. Plastic Engr.* **15**, 882-886 (Oct. 1959).

Ionospheric absorption at times of auroral and magnetic pulsations, W. H. Campbell and H. Leinback, *J. Geophys. Research* **66**, No. 1, 25-34 (Jan. 1961).

Some properties of new or modified excitation sources, M. Margoshes, *Am. Soc. Testing Materials, Spec. Tech. Publ.* **250**, 46-58 (1959).

Seasonal and day-to-day changes of the central position of the  $S_a$  overhead current system, S. Matsushita, *J. Geophys. Research* **65**, No. 11, 3835-3839 (Nov. 1960).

Hydrogen sulfide precipitation of the elements from 0.2-0.5 normal hydrochloric acid, J. I. Hoffman, *Chemist-Analyst* **50**, No. 1, 30 and 32 (Mar. 1961).

The mechanism of electrolytic deposition of titanium from fused salt media, W. E. Reid, *J. Electrochem. Soc.* **108**, No. 4, 393-394 (Apr. 1961).

Studies of elevated temperature corrosion of type 310 stainless steel by vanadium compounds, H. L. Logan, *Corrosion* **17**, 109-111 (Apr. 1961).

Deep penetration of radiation, U. Fano and M. J. Berger, *Proc. Symp. Appl. Math.* **XI** 43-59 (1961).

Deposition of iron from salts of fluoro-acids, J. H. Connor and V. A. Lamb, *Plating* **48**, No. 4, 388-389 (Apr. 1961).

Calculation of properties of magnetic deflection systems, S. Penner, *Rev. Sci. Instr.* **32**, No. 2, 150-160 (Feb. 1961).

A simple low-temperature specimen holder for an X-ray diffractometer, D. K. Smith, *Norelco Reporter* **VII**, No. 1, 11-12 (Jan.-Feb. 1961).

Stepless variable resistor for high currents, C. R. Yokley and J. B. Shumaker, Jr., *Rev. Sci. Instr.* **32**, No. 1, 6-8 (Jan. 1961).

Microbalance techniques for high temperature application, R. F. Walker, Book, Vacuum Microbalance Techniques, edited by M. J. Katz, I, 87-110 (Plenum Press Inc., New York, N.Y., 1961).

Investigation of bond in beam and pull-out specimens with high-yield-strength deformed bars, R. G. Mathey and D. Watstein, *J. Am. Concrete Inst.* **32**, No. 9, 1071-1090 (Mar. 1961).

Vacuum ultraviolet photolysis of ethane: Molecular detachment of hydrogen, H. Okabe and J. R. McNesby, *J. Chem. Phys.* **34**, No. 2, 668-669 (Feb. 1961).

Shielding calculations for civil defense, C. Eisenhauer, *Health Phys.* **4**, No. 2, 129-132 (1960).

Hydrogen atom reactions with propene at 77° K. Disproportionation and recombination, R. Klein and M. D. Scheer, *J. Phys. Chem.* **65**, 324-325 (1961).

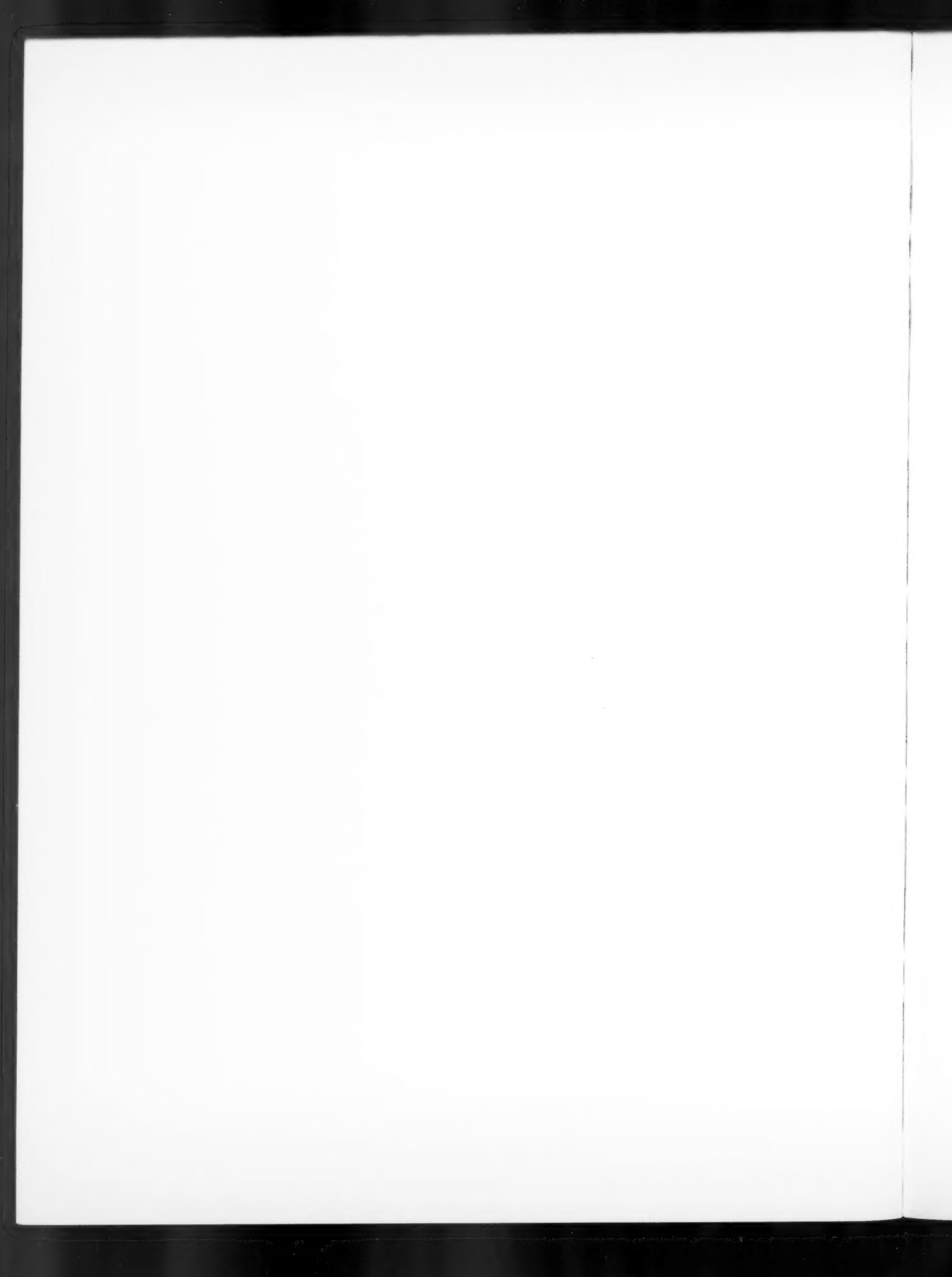
The effect of solvents of the  $\gamma$ -ray radiolysis of methyl acetate and acetone, P. Ausloos, *J. Am. Chem. Soc.* **83**, No. 5, 1056-1060 (Mar. 1961).

On the nature of the crystal field approximation, C. M. Herzfeld and H. Goldberg, *J. Chem. Phys.* **34**, No. 2, 643-651 (Feb. 1961).

A study of auroral coruscations, W. H. Campbell and M. H. Rees, *J. Geophys. Research* **66**, No. 1, 41-55 (Jan. 1961).

\* Publications for which a price is indicated (except for Technical Notes) are available only from the Superintendent of Documents, U.S. Government Printing Office, Washington 25, D.C. (foreign postage, one-fourth additional). Technical Notes are available only from the Office of Technical Services, U.S. Department of Commerce, Washington 25, D.C. (order by PB number). The Technical News Bulletin and Basic Radio Propagation Predictions are available on a 1-, 2-, or 3-year subscription basis, although no reduction in rates can be made. Reprints from outside journals and the NBS Journal of Research may often be obtained directly from the authors.





## Notice

The papers listed below will appear in early issues of *Radio Propagation*:

The solar wind. E. N. Parker.

Attenuation coefficients for propagation at very low frequencies (VLF) during a sudden ionospheric disturbance (SID). E. T. Pierce.

Dipole radiation in a conducting half-space. R. K. Moore and W. E. Blair.

Reliability of atmospheric radio noise predictions. John R. Herman.

The effects of the ionosphere on VLF navigational aids. W. T. Blackband.

On the spectrum of terrestrial radio noise at extremely low frequencies. Harold R. Raemer.

The nonsingular embedding of transition processes within a more general framework of coupled variables. John Heading.

Worldwide VLF standard frequency and time signal broadcasting. A. D. Watt, R. W. Plush, W. W. Brown, and A. H. Morgan.

Design of panoramic ionospheric recorders. L. H. Heisler and L. D. Wilson.

A quick method for estimating the stage of the mean sunspot cycle. W. B. Chadwick.

Measurements of low-angle radiation from a monopole. A. C. Wilson.

JOURNAL OF RESEARCH of the National Bureau of Standards  
D. Radio Propagation

Vol. 65D, No. 5

September-October 1961

## Contents

	Page
Frequency dependence of <i>D</i> -region scattering at VHF. J. C. Blair, R. M. Davis, Jr., and R. C. Kirby.	417
Theoretical scattering coefficient for near vertical incidence from contour maps. H. S. Hayre and R. K. Moore.	427
Mutual interference between surface and satellite communication sys- tems. William J. Hartman and Martin T. Decker.	433
VHF and UHF signal characteristics observed on a long knife-edge diffraction path. A. P. Barsis and R. S. Kirby.	437
Experimental study of inverted L-, T-, and related transmission-line antennas. Sheila Prasad and Ronold W. P. King.	449
Reflection from a sharply bounded ionosphere for VLF propagation perpendicular to the magnetic meridian. Douglass D. Crombie.	455
Resonance of the space between earth and ionosphere. H. Poeverlein.	465
Observed attenuation rate of ELF radio waves. A. G. Jean, A. C. Murphy, J. R. Wait, and D. F. Wasmundt.	475
A note concerning the excitation of ELF electromagnetic waves. James R. Wait.	481
Computation of whistler ray paths. Irving Yabroff.	485
On the analysis of LF ionospheric radio propagation phenomena. J. Ralph Johler.	507
Publications of the staff of the National Bureau of Standards.	531

